Aspects of Ionophore-Mediated Ion Transport Monitored by NMR

being a thesis by

Mark Francis Agacan

Submitted for the degree of

Doctor of Philosophy (Chemistry)

in the Faculty of Science of the

University of St. Andrews

February 2002

St Leonard's College

Declaration

I, Mark F. Agacan, hereby certify that this thesis, which is approximately 30,000 words in length, has been written by me and is a record of the work carried out by me and it has not been submitted in partial or complete fulfilment of any previous application for a higher degree.

Signed..... February 2002

I was admitted as a research worker in October 1998 and as a candidate for the degree of Ph.D. in October 1998, the higher study for which this is a record was carried out in the University of St. Andrews between 1998 and 2001.

Signed..... February 2002

Certification

I hereby certify that the candidate has fulfilled the conditions of the Resolution and Regulations appropriate for the degree of Doctor of Philosophy in the University of St. Andrews

Signed..... February 2002

Acknowledgements

There are several people I have worked with during my time in St Andrews who deserve thanks. Firstly I am indebted to my supervisor, Dr Frank Riddell ('the boss'), for all the help and time he gave me. I feel I have learnt a lot more than just Chemistry and NMR from Frank, and this will stand me in good stead for some time to come. I'd also like to thank all the members of the Riddell research group with whom I became acquainted just as they were leaving: Roger, Diane, and Jukka. Also, Jenny and Craig, I spent most of my working time with you both, thanks for listening to my ravings, I'm glad to have worked with you!

I must say a big thank you to Melanja Smith, the NMR boss, and Dr Charlie Weller. They both got me started and Melanja showed me how to operate the NMR machines throughout my studies and helped me set-up a lot of the experiments. Dr Dave Richens also helped me confirm the structures of cobalt (II) triglycine.

To Professor Geoff Hunter and Dr Sandy Chudek from the Department of Chemistry at the University of Dundee – thank you for opening my eyes to the world of NMR.

Finally I'd like to thank the staff of the Department of Chemistry at the University of St Andrews, who assisted me and made my time in St Andrews a very pleasant experience.

Dedication

I dedicate this Thesis to my Mum, Gran and Babane, I love you. Others certainly deserve my love and respect, which is gratefully acknowledged. May all beings be well, happy and peaceful!

To Rena.

"If these be vague words, then seek not to clear them.

Vague and nebulous is the beginning of all things, but not their end,

And I fain would have you remember me as a beginning.

Life, and all that lives, is conceived in the mist and not in the crystal.

And who knows, but a crystal is mist in decay?"

K.G., 'The Prophet'

Contents

Chapter 1

Chapter 2

Chapter 3

Chapter 4

Chapter 5

Chapter 6

Figures & Tables

Chapter 1

Chapter 2

Chapter 3

Chapter 4

Chapter 5

Chapter 6

Table of Abbreviations

Broderick 1- Eicosyl-3a-(p-nitrophenylsulfonylamino)-7a,12a-(nitrophenylamino-carbonyloxy) cholanate

CF - Cystic Fibrosis

COSY - Correlated Spectroscopy

DEPT - Distortionless Enhancement by Polarisation Transfer

EFG - Electric Field Gradient

EPC - Egg Lipid Phosphatidylcholine

EXSY - Site Exchange Spectroscopy

FID - Free Induction Decay

GCOSY - Gradient Correlated Spectroscopy

Ionophore 1 – Sodium (cyclopentadienyl) tris (diethylphosphite) cobaltate

Ionophore 2 - Cis-N,N,N',N'-tetraisobutylcyclohexane-1,2-dicarboxamide

k_f - Complex formation rate constant

k_d - Complex dissociation rate constant

K_s - Stability constant for the complex in the membrane

LUV - Large Unilamellar Vesicles

NMR - Nuclear Magnetic Resonance

NOE - Nuclear Overhauser Effect

NOESY - Nuclear Overhauser Effect Spectroscopy

PC - Phosphatidylcholine

RBC - Red Blood Cell

ROESY - Rotating Frame Overhauser Effect Spectroscopy

TOCSY - Total Correlation Spectroscopy

Abstract

The first part of this Thesis relates to ionophore-mediated ion transport studies across egg-lipid phosphatidylcholine (EPC) vesicular membranes monitored with NMR. The rates of transport for two synthetic lithium-selective ionophores and for a highly selective chloride anionophore were studied in detail using ^{7}Li, ^{23}Na, and ^{35}Cl NMR, across a range of salt concentrations. The stability constants and the complex formation and dissociation rate constants were calculated where applicable.

The second section involves the preparation and characterisation of a new series of NMR shift reagents for anions based on cobalt (II) triglycine. They were tested over varying concentrations, through most of the physiological pH range, and in conjunction with EPC membranes prepared for anion transport.

The third and final part of this thesis is the results of a structural / conformational study on the polyether antibiotic *Nigericin*. Proton chemical shift assignments for the lithium, sodium, potassium, rubidium and cesium salts of nigericin at 500MHz were derived from a combination of one and two-dimensional NMR experiments including COSY and NOESY.

Chapter 1

Introduction

Chapter 1

Introduction

1.1 Membrane Structure and Permeability

Biological membranes are of vital importance in living organisms. Membranes form boundaries around cells and the structures contained within (organelles) and at the same time regulate the flow of molecules and ions into and out of cells and organelles. The transport of materials across membranes is fundamental to cellular metabolic processes, including transmission of nerve impulses. To understand how this is achieved, it is necessary to take a closer look at the composition of membranes and the materials they permit or prevent passage to.

1.1.1 Membrane Composition

Membranes are composed of lipids, proteins, carbohydrates and water. A typical biological membrane is around 5nm thick. Phospholipid, the most abundant lipid found in biological membranes, comprises a hydrophilic (polar) head group, connected to a phosphate ester group, which is in turn linked via a glycerol unit to two long chain hydrophobic fatty acid (hydrocarbon) chains (Figure 1.1). When the maximum numbers of hydrogen atoms are bound to the carbons

of the chain, the fatty acid is said to be *saturated.* If some of the hydrogen atoms are missing the fatty acid is termed *unsaturated.* Double bonds are present when hydrogen atoms are missing from adjacent carbons in the chain. When a hydrocarbon chain has many double bonds, the fatty acid is *polyunsaturated.* Phospholipids are amphipathic, as they contain both 'water-loving' and 'water-fearing' moieties in the same molecule.

Lipids tend to form micelle-like bilayer sheets when exposed to an aqueous environment (Figure 1.2). The edges of such sheets can spontaneously fold and seal to form spherical shapes or *vesicles,* whereby the hydrophobic interior is kept from contact with the polar medium, e.g. water, and the charged phosphate groups face outward into the hydrophobic environment. The entire assemblage is held together by non-covalent interactions such as Van der Waals and hydrophobic interactions.

Lipid bilayers are commonly used as models of membranes. Being easier to obtain and use in practical terms, they share many properties normally associated with biological membranes, such as the hydrophobic interior and the ability to control the passage of small molecules and ions.

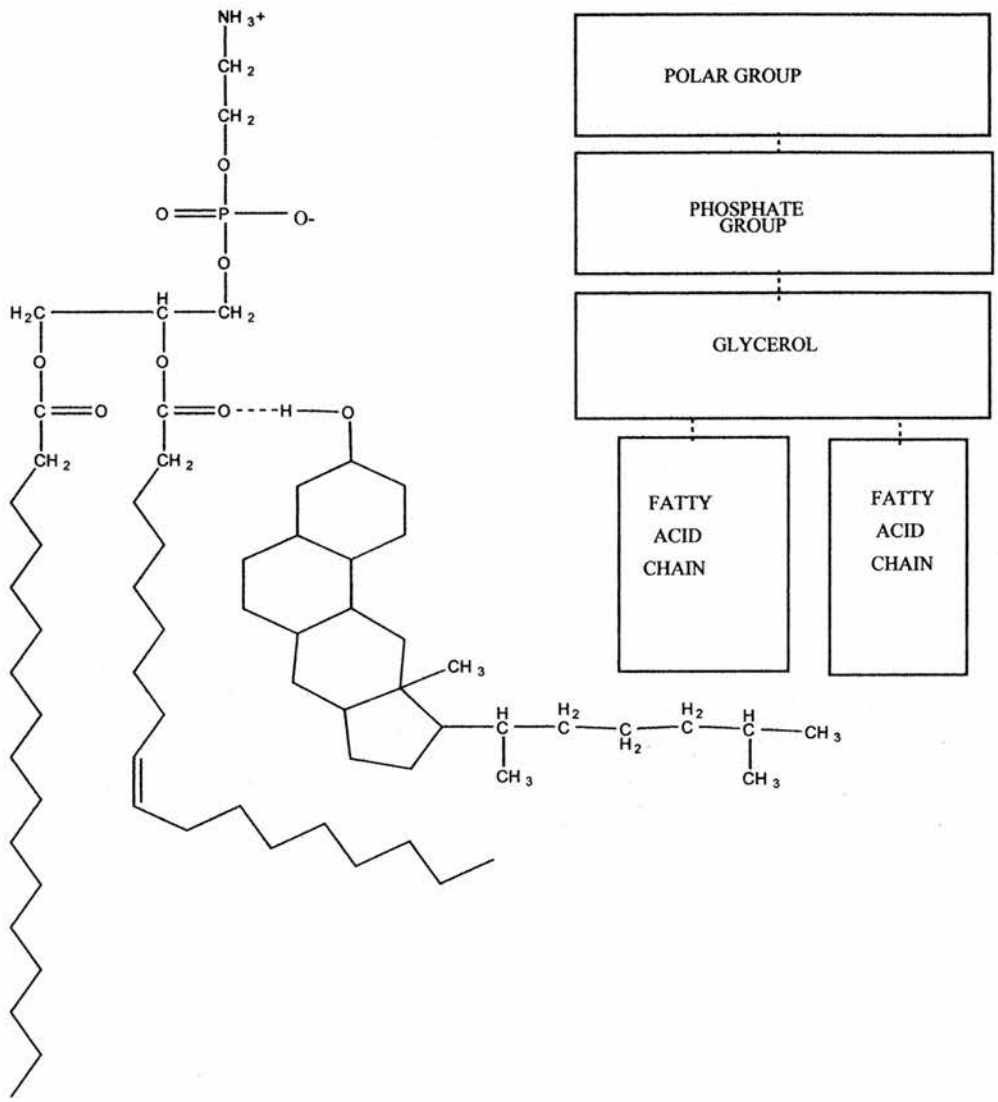

Figure 1.1 On the left, the structure of a typical phosphoglyceride, phosphatidylethanolamine. A double bond in the *cis* configuration in one of the hydrocarbon chains produces a kink. Cholesterol is connected by its own –OH group to the oxygen of the ester linkage On the right, a schematic diagram showing the subunits of the phospholipid.

Since the lipid bilayer in a membrane is not flat, but curved, the distribution of lipids in the inner and outer layers is not equal. Lipids in the inner layer are generally more tightly packed than lipids in the outer layer.

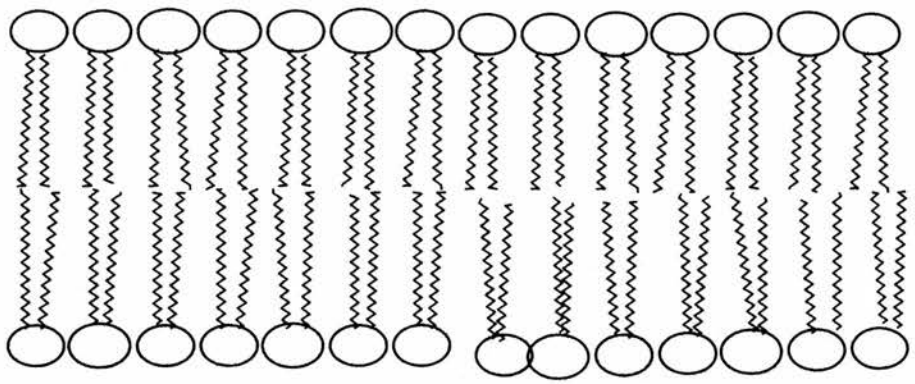

Figure 1.2 A lipid bilayer, in which circle and jagged lines represent polar phosphate head groups and saturated fatty acid chains (no kinks). On either side of the membrane is a hydrophobic environment, whilst the membrane interior is hydrophobic.

Phospholipid bilayers are highly impermeable to very large or charged molecules and those with prominent polar substituents, (e.g. amides, alcohols, ethers, ketones), whilst uncharged molecules and those with non-polar substituents (e.g. alkyl, aryl, chloro, and bromo) show greater membrane solubility. Molecules that can diffuse through the membrane do so at varying rates depending on their size and their *lipophilicity*, which describes the preference of a molecule to

be in a lipid phase compared to an aqueous phase. Uncharged, non-polar compounds generally have higher lipophilicities than charged polar compounds, and are therefore more likely to diffuse through a membrane than charged polar compounds.

Phospholipids consist of three sections. Phosphatidate (diacylglycerol-3-phosphate) is connected to two long hydrocarbon chains, and to another polar functionality. Five common phospholipids are given below in Figure 1.3:

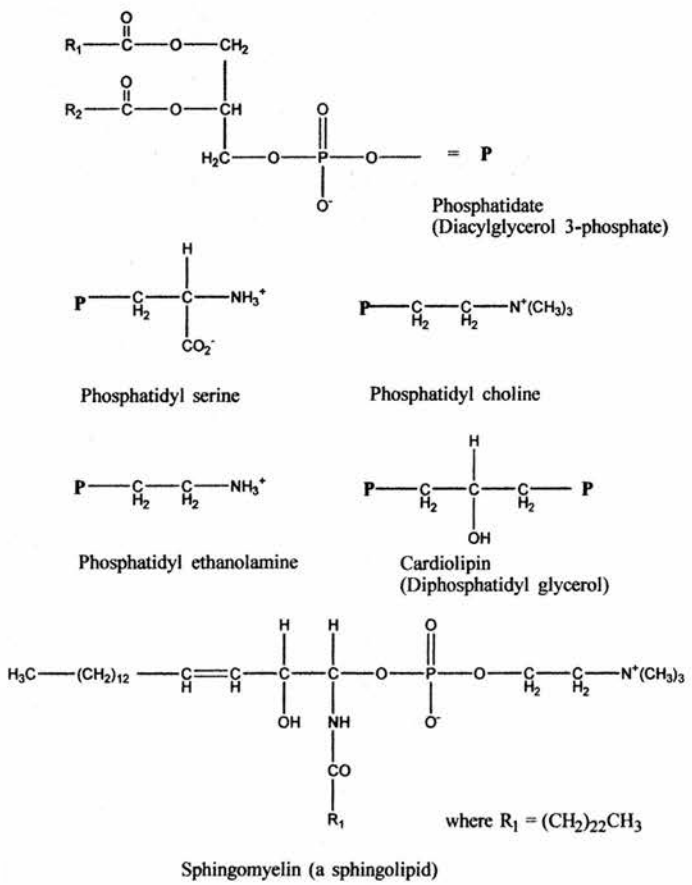

Figure 1.3 Commonly encountered phospholipids

1.2 The Fluid Mosaic Model

The currently accepted representation of biological membranes, the fluid mosaic model of membrane structure, was published in 1972.[1] The authors, Singer and Nicholson, observed "*a mosaic structure of alternating globular proteins and phospholipid bilayer was the only membrane model... that was consistent with thermodynamic restrictions and with all the experimental data available.*" Since then the study of the role of membranes has developed into a major research topic in its own right.[2-5] A particular feature of this model was that the membrane itself was deemed to be in a highly fluid condition under physiological regimes. The model also allowed for the possibility of substantial rearrangement of lipids within layers, and between layers via the *flip-flop* mechanism. This type of rearrangement was predicted to be uncommon, as the rate constants for rearrangement within a layer is very much greater than the rate constant for flip-flop rearrangement between layers.

The hydrocarbon interior of a bilayer has a degree of rigidity or fluidity, depending on its composition. Bilayers composed of saturated fatty acids lead to close packing of the straight hydrocarbon chains, whilst the kink in the hydrocarbon chain of unsaturated fatty acids raises the level of disorder in the packing, and hence increases

the fluidity of the bilayer. Cholesterol molecules can strengthen the bilayer by taking up some of this extra space.

1.3 Physical Properties of Natural and Artificial Membranes

Both ^{1}H and ^{31}P NMR have been used to characterise the phospholipid content of membranes, [6-10] and a variety of methods exist to produce artificial membranes.[11-14] It has been shown that proteins and phospholipid are unevenly distributed across the membrane[14], including those prepared from phosphatidylcholine (lecithin) and phosphatidylethanolamine. Some commonly encountered phospholipids include phosphatidate, phosphatidylserine, phosphatidylcholine, phosphatidylethanolamine, cardiolipin, and sphingomyelin (See Figure 1.3). The exact amount of lipid in a membrane varies, but usually the content is between 40 and 90%. [2, 6,7]

Figure 1.4 below shows a saturated and an unsaturated hydrocarbon chain. The reaction of glycerol to form diglyceride in the presence of fatty acids is also shown.

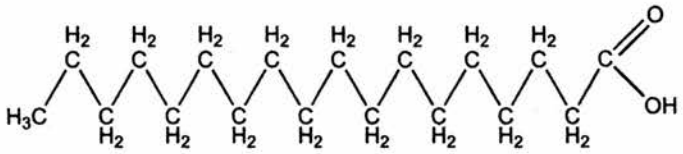

Stearic Acid, $CH_3(CH_2)_{16}COOH$

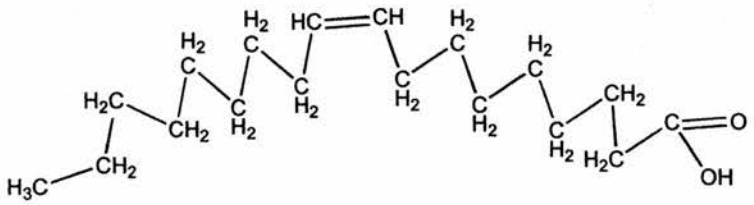

Oleic Acid, $CH_3(CH_2)_7CH{=}CH(CH_2)_7COOH$

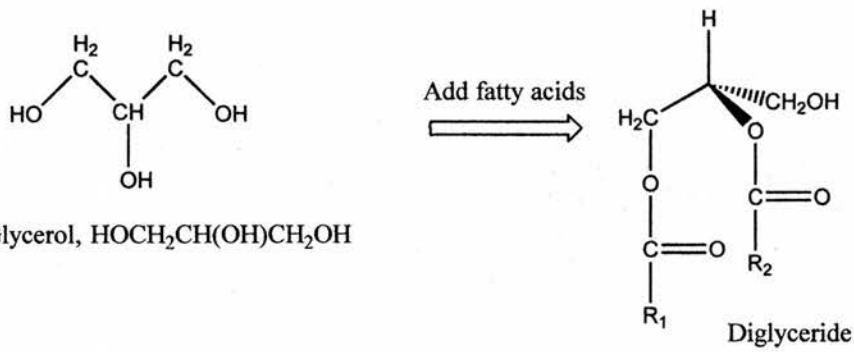

Glycerol, $HOCH_2CH(OH)CH_2OH$

Diglyceride

Figure 1.4 Stearic Acid (saturated) Oleic acid (unsaturated, with a double bond), and glycerol. Two of the three-hydroxyl groups of glycerol can react with the carboxyl groups of fatty acids to form diglycerides. The third hydroxyl group connects to a phosphate group, as shown in Figure 1.1.

The table below illustrates the variations of the composition of animal and bacterial membranes.[6] The different types of lipid found in a membrane will typically have a range of fatty acids associated with it (See Table 1.1).

	Myelin	Erythrocyte	Mitochondria	Micro-some	Escherichia coli
Cholesterol	25	25	5	6	0
PE	14	20	28	17	100
PS	7	11	0	0	0
PC	11	23	48	64	0
PI	0	2	8	11	0
PG	0	0	1	2	0

Table 1.1 – Percentage composition of animal and bacteria membranes (values from Korn 1966)[6] ; PE = phosphatidylethanolamine; PS = phosphatidylserine; PC = phosphatidylcholine; PI = phosphatidylinositol; PG = phosphatidylglycerine;

1.4 Proteins and Membranes

The fluid mosaic model defines protein molecules as being associated with cell membranes two possible ways. Proteins attached to the surface of the membrane can be removed intact by appropriate solvents and are known as *peripheral* membrane proteins. Proteins embedded within the membrane either fully or partially are much harder to remove without denaturing. These are known as *integral*

membrane proteins. Initially it was thought that integral proteins may be capable of significant movement within the lipid bilayer, but there are anchor points (arranged in a form of lattice) for these proteins on the membrane surface. It has been estimated that around 40% of the human genome codes for membrane proteins, emphasizing the importance of membrane transport processes for life.

Both types of proteins may be involved in transport processes[2, 3] by acting as *channels* (passive transport), *gates* (facilitated transport), and *pumps* (active transport). Channels can be thought of as tunnels through which the diffusion of materials across the membrane can occur. Gates require specific conditions to open and close, allowing only certain molecules to cross the membrane. Channels and gates allow diffusion along concentration gradients, thereby minimising the energy input from the cell. Pumps require energy to facilitate the transport process.

Proteins active as enzymes may also be involved in transport processes. Studies of both integral and peripheral proteins have focussed on identifying sites to which ions may co-ordinate and to which the protein itself binds to the substrate, and structural / conformational studies. Thus proteins and membranes are involved in transport, catalysis, and also as receptors.

Protein components involved in transport processes can be identified using any characteristic that proves reliable, although this type of study is hindered by the requirement for these proteins to be in a very pure state. The molecular conformation, in part responsible for the observed action of the protein, may in many cases be different *in-situ* than in the isolated state because of protein-lipid interactions. Crystal packing factors may dominate in crystalline proteins. This may change the conformation of the protein and is of great importance when x-ray crystallographic studies are carried out. The conformation may also be greatly affected by the choice of solvent in NMR experiments.

Protein-to-lipid ratios in bacterial membranes[14] are generally higher than those found in other biological membranes[15], except for the inner mitochondrial membrane.[16] Bacterial membranes have very few if any steroids incorporated into their structures. Cholesterol, for example, is only found in such membranes when the bacteria are grown in a cholesterol-containing medium. Eukaryotic cells, however, contain cholesterol as an essential structural component, reinforcing the membrane by restricting the movement of the lipids in the bilayer.

1.5 Types of Transport

Ions and molecules are constantly moving across cellular membranes. Metabolites enter the cell from outside and waste materials are purged from the inside. There are two basic mechanisms by which materials may cross cell membranes.

1.5.1 Passive Transport

Passive transport occurs when the natural differences in concentrations on either side of the membrane lead to the movement of a substance along a *concentration gradient.* The result of passive transport is a more even distribution of molecules or ions throughout the available space. This form of transport requires no expenditure of energy. An example of passive diffusion is that of *osmosis*, whereby water moves from a region of high concentration to a region of lower concentration across a semi-permeable membrane.

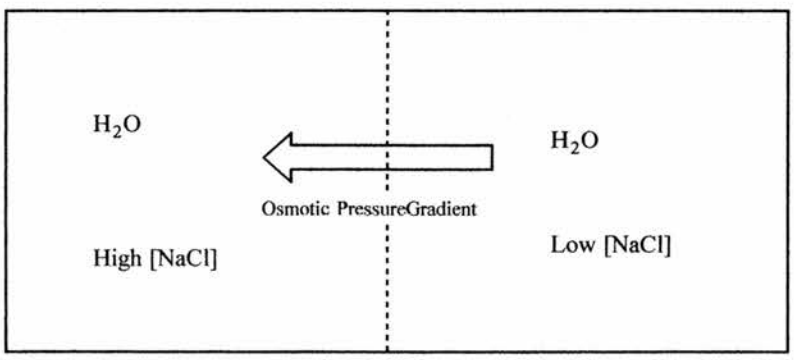

Figure 1.5 Schematic representation of osmosis.

Simple diffusion across a biological membrane obeys Fick's first law (Equation 1.1) in which the flux per unit area of a compound through the membrane (J) depends only on the diffusion coefficient of the compound (D) and its concentration gradient across the membrane (dc/dx).

$$J=D(dc/dx) \qquad \text{Equation 1.1}$$

1.5.2 Active Transport

Active transport of molecules or ions occurs against a concentration gradient or electrical potential, and therefore requires the consumption of metabolic energy. This process must be coupled to a system responsible for the required energy input. Active transport processes require a 'pump' to push the substances across the membrane, and these pumps are usually protein molecules. Perhaps the best-documented case of active transport is the Na^+ / K^+ - ATPase pumps, responsible for the removal of sodium and the intake of potassium against concentration gradients. An electrical gradient is brought about by the Na^+ / K^+ - ATPase pump, as three Na^+ ions are pumped out of the cell, while only two K^+ ions enter the cell. The voltage generated provides a basis for the conduction of electrical impulses by nerve and muscle cells. Up to a third of the energy expended by a resting mammal may be used by this system. There is

no equivalent to the Na^+ / K^+ - ATPase pump in bacteria, fungi or plants.

The kind of active transport known as facilitated diffusion requires a carrier protein, specific for each substrate, which can bind and transport a solute molecule across the lipid bilayer. The mechanism of carrier protein mediated diffusion is similar to the enzyme-substrate mechanism. There are three types of carrier protein. Uniport carriers can transport a single solute in one direction from one side of the membrane to the other. Symport carrier proteins mediate transport of one solute only in the presence of a second solute molecule, which is also transported across the membrane. Antiport carrier proteins can transport one solute molecule in one direction and one solute in the opposite direction.

The three types of carrier proteins are represented below in Figure 1.6.

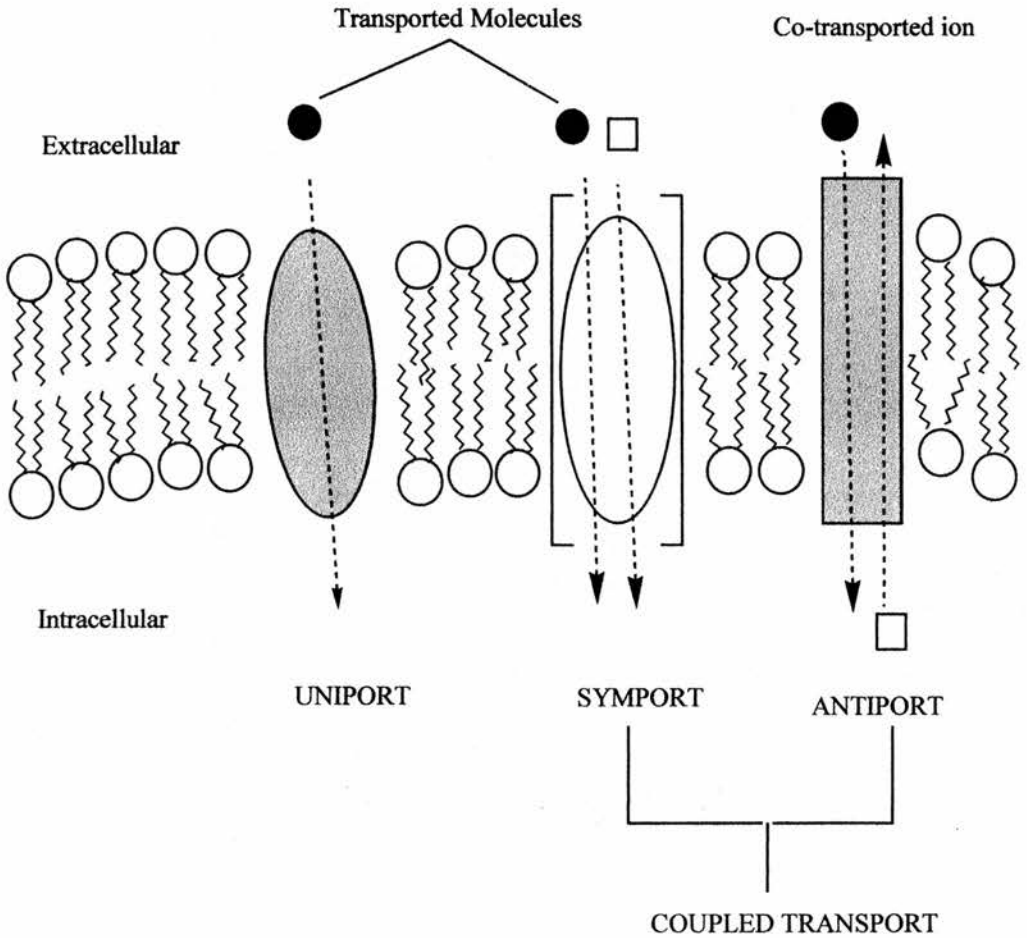

Figure 1.6 Schematic diagram of carrier proteins as uniports, symports and antiports.

1.6 Artificial Membranes and Transport Studies

Artificial membranes have supplied a great deal of fundamental information about the nature and characteristics of biological membrane transport systems. Much of what is known about membranes has been elucidated from studies of simplistic membrane systems in which all the components are carefully controlled. The

environment of such systems can then be modified and the response of the artificial membrane can be observed. There are three main types of artificial membrane: the *lipid monolayer*, the *lipid bilayer*, and *lipid-based vesicles* or *liposomes*. Each has a particular advantage in certain studies.

Arguably the most versatile preparation is the vesicle, a spherical self-sealing structure into which it is possible to trap materials during the formation stages. This simple system is used as a model for an artificial and highly simplified cell. Kinetic and pharmacological data can be obtained through monitoring the leakage or transport of materials from one side of a lipid bilayer to another[17-28] in the presence of ionophores or drugs. It is also possible to incorporate protein molecules into bilayers and hence into vesicles, although this inevitably complicates the transport rate equations. Artificial membranes are, for this reason, often prepared without protein incorporation. Many more factors can affect leakage and transport *in-situ* than in the model system, including the presence of proteins. The cytoplasmic membrane for example, would generally have a much wider variety of substances on either of its sides than even the most complex artificial membrane model system.

Both natural and artificial membranes undergo temperature-defined phase transitions, whereby they 'melt' into a more fluid phase, or 'freeze' into a more rigid phase. Phase transitions in phospholipid bilayers occur when there is a change in the mobility of the hydrocarbon chains as a consequence of increasing or decreasing temperature. The exact temperature at which the phase transition occurs depends on the length and the degree of saturation of the hydrocarbon chain. Shorter chains generally have a lower phase transition temperature due to there being fewer stabilising H-bond and van der Waals sites.

The kinks introduced into hydrocarbon chains by double bonds further lower the temperature of the phase transition by inhibiting close and orderly packing of the chains. This allows such membranes to maintain their fluid characteristics even at lower temperatures. The role of cholesterol in the strengthening of the membrane is already in evidence. In relation to phase transitions, cholesterol has two functions. At low temperatures the presence of cholesterol increases membrane fluidity by preventing close packing of the chains whilst at high temperature cholesterol decreases fluidity by restricting rapid movements of the lipids.

1.7 Ionophores

Not all materials are transported across cell membranes by the action of proteins. Ionophores[29, 30] are also important in ion transport studies. Typical ionophores are of moderate weight and size, forming lipid-soluble complexes with biologically important ions or other small charged species.

Some of the naturally occurring carboxylic ionophores, which include the polyether antibiotic family, are shown in Figure 1.7. Carboxylic ionophores have the ability to manipulate their backbones into a position in which they can trap a small cation. It is thought that the cation is sequestered within the cage formed by the macrocyclic molecule so that the polar cation is wrapped up in a non-polar jacket and can diffuse through the non-polar membrane interior.

It is the degree to which the backbone can be manipulated that determines the likelihood of complex formation and dissociation between an ionophore and a particular cation. The 'snugness-of-fit' between a cation and ionophore effectively confers selectivity, or an ability to recognize different cations, to the ionophore. Carboxylic ionophores assume a conformation that encapsulates an ion, which may in turn co-ordinate to 5 or more oxygen atoms of the ionophore.[31, 32] The oxygen atoms can come from a variety of sources

including carboxylate, ether, carbonyl and hydroxyl groups within a molecule. Several common families of ionophores (polyether antibiotics, crown ethers, cyclic polypeptides) are made up of cyclic ring systems with lipophilic outwards pointing side chains, a combination which shields the polar or charged moieties from the hydrophobic membrane interior.

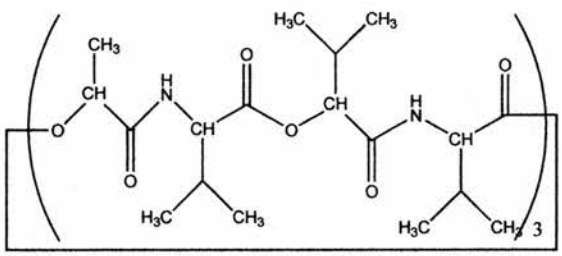

Valinomycin

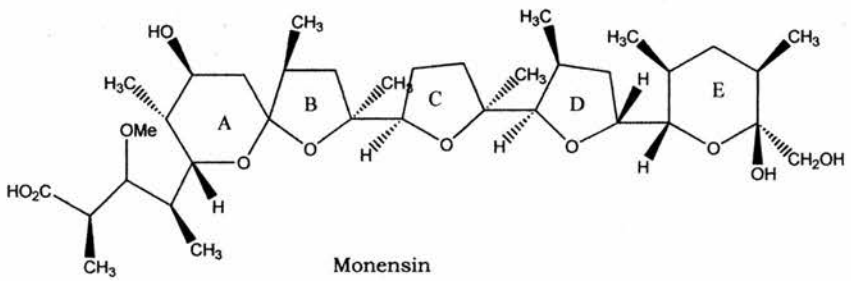

Monensin

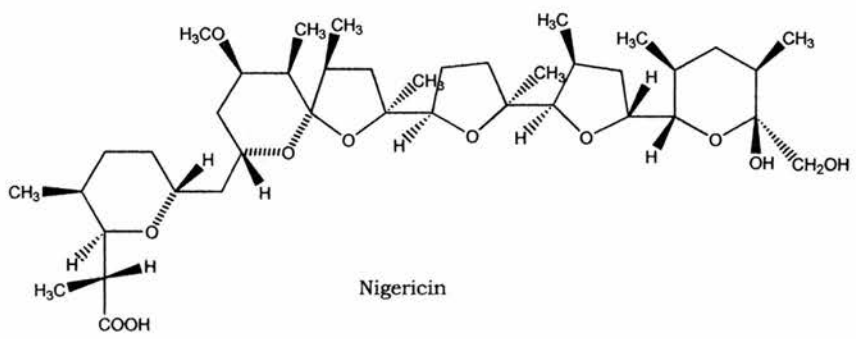

Nigericin

Figure 1.7 Naturally-occurring polyether antibiotic (carboxylic) ionophores

Carboxylic Ionophore	Molecular Weight (g mol^{-1})
Nigericin	725
Monensin	671
Tetronasin	602
Cationomycin	851

Table 1.2 Molecular weights of selected carboxylic ionophores

A specific class of ionophores known as channel- or pore-forming antibiotics, are comprised of cyclic polypeptides (e.g. gramicidin A, Figure 1.8 and Figure 1.12). Such molecules form channels all the way through the membrane. These channels can be filled with water and permit the passage of small monovalent cations, protons, and unlike diffusing ionophores, the transport of intact water molecules through these structures may also occur. Gramicidin A can also form dimers with itself.

OCH-NH-Val-Gly-Ala-Leu-Ala-Val-Val-Val-Trp-Leu-

Trp-Leu-Trp-Leu-Trp-CO-NH-CH_2-CH_2-OH

Figure 1.8 The fifteen amino acid sequence of the cyclic polypeptide gramicidin A showing terminal N and C groups. See also Figure 1.12.

Ion transport by diffusing ionophores is inhibited when the temperature at which the transport takes place is below the gel to liquid-crystalline phase transition temperature of the particular membrane lipid system. Decreasing the temperature in this manner has little or no effect on channel forming ionophores such as the gramicidins, as illustrated below in Figure 1.9:

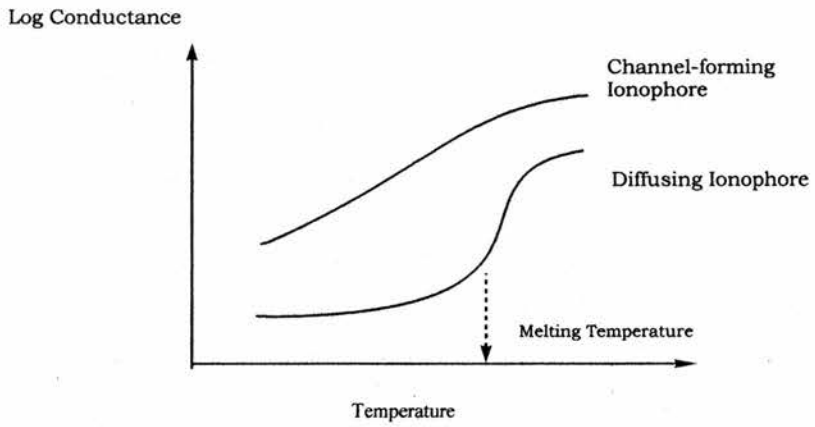

Figure 1.9 Variations between channel-forming and diffusing ionophores with temperature.

Diffusing ionophores can be classified on the basis of the mode of transport adopted, and are believed to behave as ligands with which an ion forms a lipid soluble complex. This complex may be neutral or charged. Neutral complexes form when an *ionic* ionophore interacts with a cation of equal and opposite charge, such as an alkali metal

(see Figure 1.10). *Nigericin* and *monensin* are ionic or *carboxylic* ionophores.

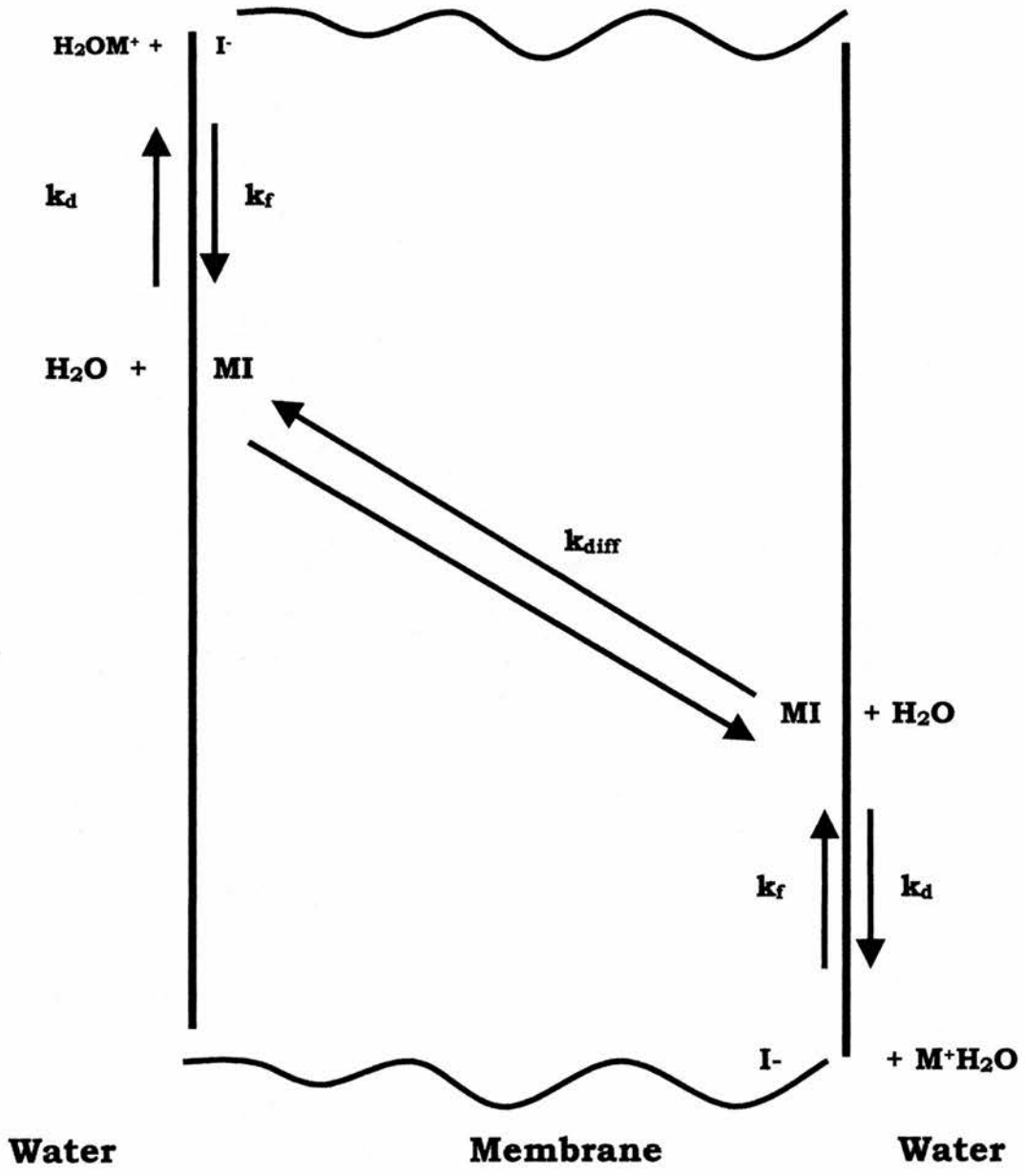

Figure 1.10 Schematic of the transport process for a cation by an ionic or carboxylic ionophore.[30]

In anionic form, these molecules co-ordinate with a singly charged metal cation through stepwise ligation to form a zwitterionic complex, which then diffuses through the membrane to the opposite interface where the metal cation is released. A cation may be carried back by the ionophore, or it may simply diffuse back through the membrane.

Charged complexes arise when there is a difference in charge between an ionophore and a cation, for example when a *neutral* ionophore binds with a cation (See Figure 1.11). *Valinomycin*, an antibiotic shown in Figure 1.7, is a neutral ionophore, capable of arranging six of its ester carbonyls around a central alkali cation. Studies have shown valinomycin to favour the larger potassium cation to the smaller sodium cation by a factor of ten thousand.

Stepwise solvation binds the metal cation to the ionophore, which can now diffuse across the membrane, eventually releasing M^+ at the opposite surface. The ionophore can then diffuse into the membrane or transport an ion in the reverse direction to complete the cycle. The charged complexes can upset electrical potentials as they move across the membrane[22, 23, 33, 34] and affect the rates of the transport process.

The ionophoric complex is formed either as IM or as IM^+ at a rate represented by the overall rate constant k_f. Once formed, the complex

diffuses across the membrane at a rate represented by k_{diff}, the rate constant for diffusion.

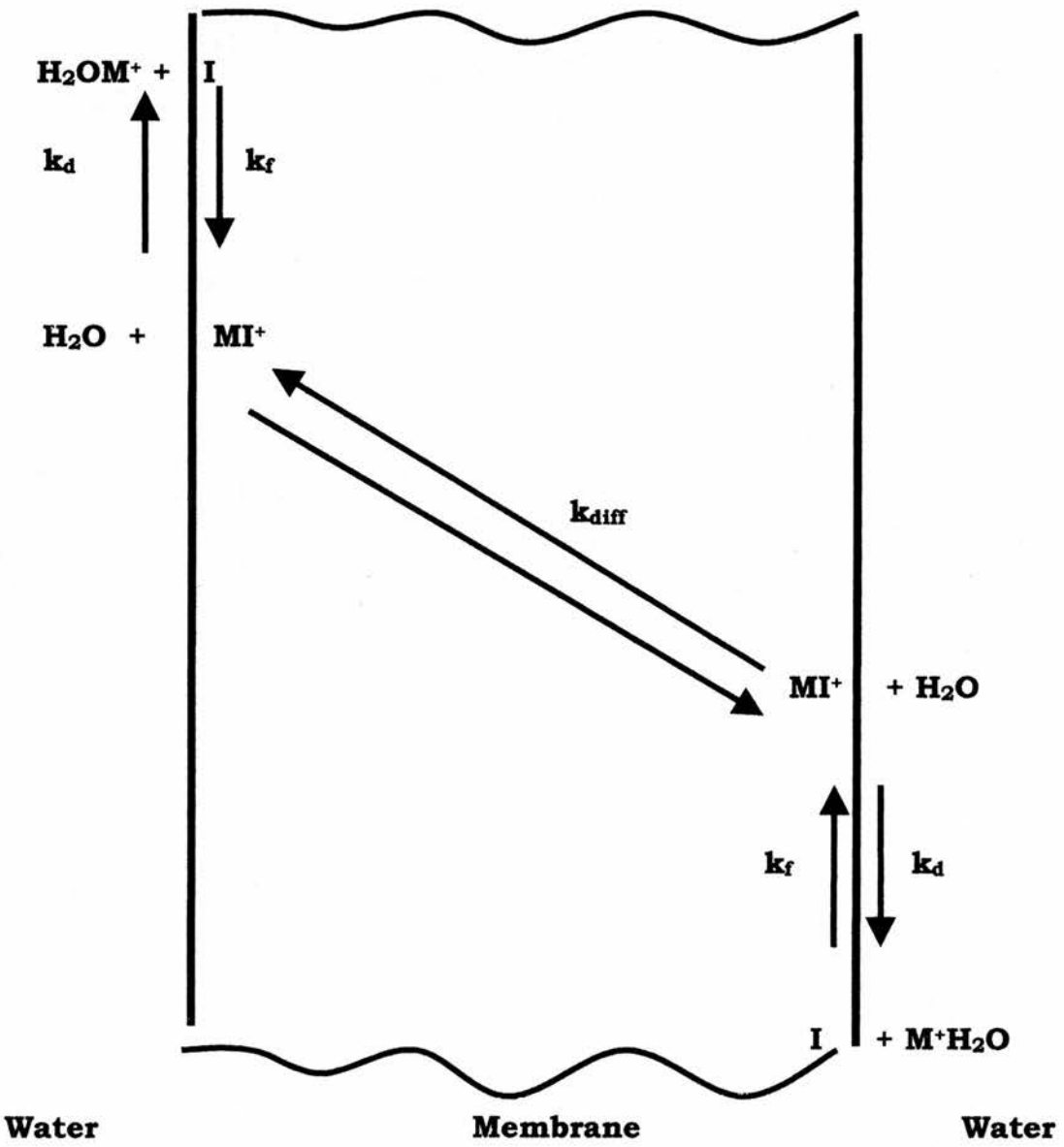

Figure 1.11 Schematic of the transport process for a cation by a neutral ionophore.[30]

At the other side of the membrane, the ion dissociates from the ionophore (at a rate that can be represented by the overall rate constant k_d) and is released into aqueous medium. The ionophore may then form another complex with a new ion (again, at a rate represented by the rate constant k_f), regenerating the charge of the complex, and allowing the ionophore to make its return to the side of the membrane it started at. The formation and dissociation steps are multi-step processes combined to give a single rate constant for formation and a single rate constant for dissociation.

In many biological processes the ion carried back from within the cell is as important as the ion transported across. In most cases, for an ionophore to be a good transporter, it should have high formation and dissociation rate constants. If k_f is very low, then the complex will never form at an appreciable rate. If k_d is very low, then the complex, once formed, will not readily dissociate. The stability constant K_s is in this case determined by k_f/k_d. Thus, a similar stability constant can be obtained for complexes with low k_f and low k_d as for complexes with a high k_f and high k_d. The best transporters are between 10% and 90% associated and the rate constants k_f and k_d are high.

1.8 Biological Ion Transport

Medical applications for some of the biologically useable polyether ionophores have been few to date, as their hydrophobicity prevents them from becoming evenly distributed into biological membranes, and there are also toxicity issues. Several of the polyether antibiotics such as nigericin and monensin are used as anti-coccidiostats, and fed to poultry to control infections.[35, 36] The antibiotic activity is thought to be a result of interaction with the cytoplasmic membrane and resultant leakage of alkali metal cations. Cell death can occur through the loss of these cations, by acidification of the cytoplasm, or by, for example, M^+ / H^+ exchange leading to a catastrophic increase in osmotic pressure inside the cell. The carboxylic ionophores also increase the rate at which ruminant animals gain weight by controlling the bacteria in the rumen (or stomach).

However, the application of these compounds as model biological carriers has enabled studies of membranes and transport systems.[26-28] The transport turnover rates for many ionophores are greater than the turnover rates of many transport-linked enzymes.

Various illnesses and diseases are believed to arise through excesses or deficiencies of ions in specific regions of the body; cystic fibrosis (CF), for one, is associated with abnormal chloride transport

processes.[37] CF is a common genetic disorder occurring mainly in Caucasians, and the defective chloride transporter protein is known as CFTR (cystic fibrosis transmembrane conductance regulator). People with two recessive CF genes can experience severe medical problems due to the way in which chloride ions pass through the plasma membranes of their epithelial cells. In a CF patient's sweat glands, chloride ions are not reabsorbed into the cells but are excreted in sweat, leading to a reduction in extracellular chloride concentrations. Since there is a higher concentration of chloride inside the cell, water molecules do not diffuse out of the cell. This makes the excreted mucus too thick, as it is not mixed with water.

The significance of cellular lithium transport is reflected through the use of lithium in the treatment of manic-depressive symptoms.[38-41] In USA 1 in 1000 people regularly ingest lithium to treat symptoms of bipolar affective disorders (manic depressive psychosis). Such substances have well documented side effects, including lethargy. Most of these medicines are designed for administration on a daily basis. Lithium is the primary choice of medicine for manic-depressives, who must maintain intake permanently to prevent the onset of mania or depression. People suffering from manic depression are often reluctant to take medicine. The dose is usually 1-2g lithium carbonate per day, making a slow-release drug desirable. Sufferers of

bipolar affective disorders and manic depression being treated with lithium show changes in the levels of lithium in blood plasma.

The synthesis of ionophores or molecules that can regulate the release of lithium across the blood-brain barrier more effectively than existing drugs may lead to a more effective use of lithium in psychiatric medicine. Membrane transport has been linked to the response of a depressive to therapeutic doses of lithium, as higher erythrocyte to plasma lithium concentrations in responsive patients compared to those unresponsive to the treatment have been observed.[42, 43] Lithium is assumed in one theory to exert its various actions partly by resembling other cations, including Na^+, K^+, Mg^{2+}, and Ca^{2+}, all of which are believed to be related to membrane functioning. Alternatively, it has been suggested that the inhibition of inositol monophosphatase by lithium may account for its activity.

Both chloride and lithium ion transport in erythrocytes and biological membranes have been studied using $^{35\&37}Cl$ and $^{6\&7}Li$ NMR.[42-45] An obvious clinical use for ionophores is to restore or mediate a natural and balanced transport regime in systems that have in some way become unbalanced, although this is difficult due to their inherent toxicity.

Biological ion transport studies using ionophores with mitochondria, photosynthetic vesicles, erythrocytes and liposomes show a general increase in membrane permeability after addition of the ionophore.[22, 26, 29-30] In mitochondria, cation uptake and resultant lowering of pH as protons are released, increase in volume, and increase in respiratory rates due to increased transport can be observed using ion-sensitive electrodes. Erythrocytes are usually readily available and convenient to use experimentally, as ionophore-mediated ion flux can readily be made to exceed the transport of the Na^+/K^+ pump in the membrane.[42, 43]

Many antibiotic agents are thought to act by producing aqueous pores in membranes.[29] The linear gramicidins, previously referred to, consist of linear pentadeca-peptides containing alternating D and L hydrophobic amino acid residues. These are believed to exist in helical conformations, which form barrel-like channels in membranes through which certain univalent ions such as the alkali metals can pass (See Figure 1.12 below).

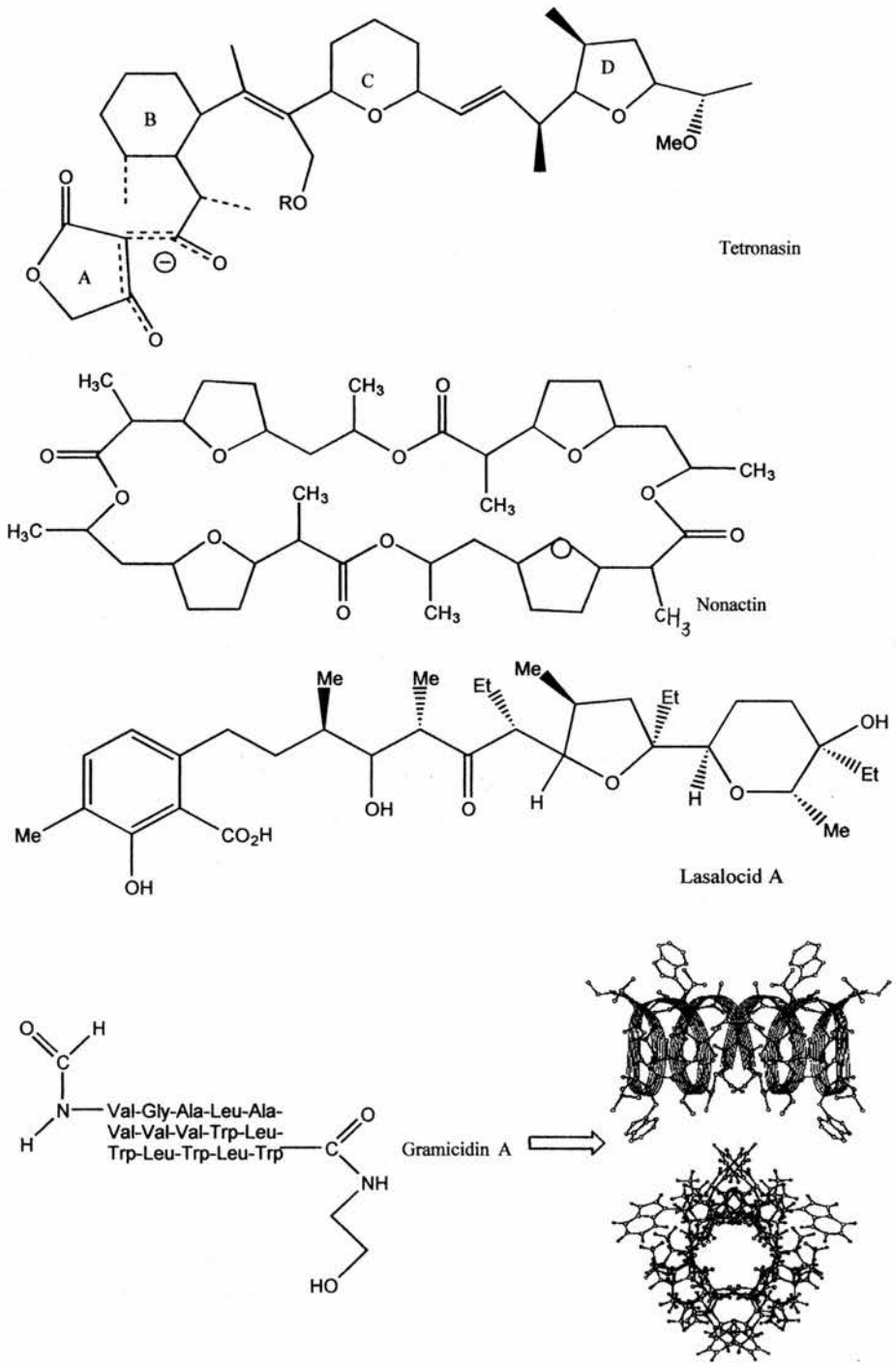

Figure 1.12 Some naturally-occurring ionophores

Pressman observed a similar 'channel-forming' action for gramicidin and valinomycin in mitochondria, and both showed dependence for K^+, Rb^+ or Cs^+, and inorganic phosphate.[30] Valinomycin, shown in Figure 1.7, causes K^+-dependent release of H^+ from mitochondria. The main difference between the two transporters is that whilst gramicidin is effective for any alkali metal cation, valinomycin is only active for the larger K^+, Rb^+ or Cs^+, and not Li^+ or Na^+. The overall conformation and size of the cavity formed by an ionophore can determine the ion-selectivity sequence. Such sequences for several important ionophores are presented below:

Ionophore	Selectivity Sequence for Cations
Valinomycin	Rb>K>Cs>Ag>>NH_4>Na>Li
Monactin	NH_4>K>Rb>Cs>Na>Ba
Monensin	Na>>K>Rb>Li>Cs
Nigericin	K>Rb>Na>Cs>>Li
Gramicidin A	H>Cs>Rb>NH_4>K>Na>Li

Table 1.3 Selectivity sequences indicating the preference of a particular ionophore for a cation.[30]

1.9 Uses of Ion Transport by Ionophores

The design and synthesis of highly selective ionophores for cations continues unabated. The primary use of synthetic ionophores is as ion-selective electrodes or sensors.[46-48] Valinomycin, noted in 1967 by Pressman[30] for its ability to selectively facilitate the transport of potassium cations through mitochondria, is still the active component in potassium-selective sensors. The potassium / sodium selectivity of valinomycin was until recently[49] greater than that of any subsequent potassium ionophores.

An emerging alternative to the ion-selective electrode lies in the development of chelating materials for the separation of toxic heavy metal ions from waste and processing solutions.[50-52] Selective removal of Pb (II) from the natural environment remains an important objective. The lipophilic di-ionizable ionophore shown in Figure 1.13 below can act as an extractant for lead (II) in solvent extraction experiments involving the transport of the ionophore-Pb (II) complex across a plasticizer membrane. The molecule has a crown-type arrangement of 5 oxygen atoms that connect to a chiral carbon at either end. This work raises the possibility of an environmental protection role for ionophores.

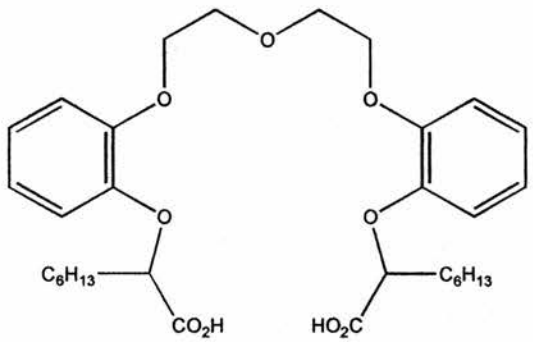

Figure 1.13 Lipophilic di-ionizable ionophore *1,5-Bis[2-(2'-carboxylheptyloxy)phenoxyl-3-oxapentane)* for selective solvent extraction of Pb(II) from Cu(II).

1.10 Lithium-Specific Ionophores

Lithium-specific ionophores find employment in several areas. The first is lithium-selective electrodes.[48] These devices are used mostly in laboratory situations, to detect concentrations of lithium in various samples. The active component in Li^+-selective electrodes is usually a crown ether[53-54] or cryptand[55-56] derivative.

Lithium electrodes have also found use in medical and clinical fields, as they can, for example, allow the continuous monitoring of lithium in the bloodstream of manic-depressive patients prescribed lithium as a medicine. Although there is little environmental damage caused by lithium, there are still uses for lithium-selective ionophores as tools in analysis or separation of biological and environmental systems.

There may be potential for ionophores to mediate the penetration of lithium ions into the human central nervous system[57], but toxicological issues have so far prevented this application. Such molecules should have low selectivity for other cations such as Na^+ or K^+, a necessity before inclusion into biological systems. In almost all situations, the main competitor for lithium would be sodium.

Since lithium is the smallest of the alkali metal cations, it is also very strongly solvated in aqueous environments, i.e. there is a strong interaction between M^+ and H_2O molecules, as shown in Table 1.4 below. Many attempts to synthesise lithium-selective ionophores ended up generating sodium-selective ionophores instead. This is a major consideration for the design and synthesis of such molecules.

Ionophore design can often be rationalised in terms of the diameter of the ion in question and the size of the proposed cavity in which the ion is to be held. It has been shown that the size-fit concept can adequately account for the observed results.

Lithium specific ionophores recognised to date belong to the cryptand, spherand,[45] dioxadiamide, macrocyclic crown ether[53, 55] and acyclic polyether families.[29, 30] Selectivity measurements are often made using potentiometric selectivity coefficients for polymeric membranes containing the ionophore.

	Li	Na	K	Rb	Cs
Ionic Radius (Pauling, nm)	0.060	0.095	0.133	0.148	0.169
$H^0(kj/mol)_{sol}$	552	443	359	334	301
$S^0(J/K.mol, K)_{sol}$	0.141	0.110	0.074	0.062	0.059
$G^0(kj/mol)_{sol}$	510	410	337	316	282

Table 1.4 Some properties of Group 1A elements. The absolute standard thermodynamic functions of hydration of M^+ are given at 298 K.

1.10.1 Crown Ethers

Crown ether molecules are used as phase-transfer catalyts and can transport ionic compounds into an organic phase. The whole system forms a ring, hence the name crown. Crown ethers are named as *x*-crown-*y* where x is the total number of atoms in the ring and y is the number of oxygen atoms.

In ion recognition, crown ethers play the 'host', and the cavity formed by the ring allows a small cation to become trapped and held tight by hydrogen bonding from the oxygen atoms. The 'lock and key' manner in which crown ethers form complexes with certain ions is thought to mimic the functioning of enzymes. Ultimately the study of crown ethers, and ionophores in general, aids the understanding and

design of molecules designed for molecular recognition, particularly of ions.

Kitazawa et al[54] demonstrated that lipophilic 14-crown-4 ether derivatives (Figure 1.14 below) show high preference for lithium in favour of sodium. They also found that addition of a methyl group geminal to the long aliphatic chain enhanced the lithium selectivity of the original crown ether, and that lipophilic 14-crown-4 derivatives incorporating a nitrophenol substituent showed extremely high selectivity ratios for lithium over sodium.[53, 58]

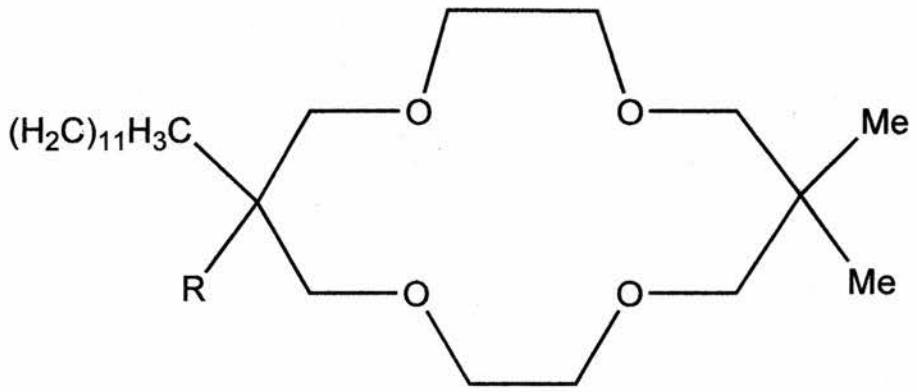

where R = H or CH_3

Figure 1.14 The structure of a 14-crown-4 cyclic ether showing preference for lithium over sodium.

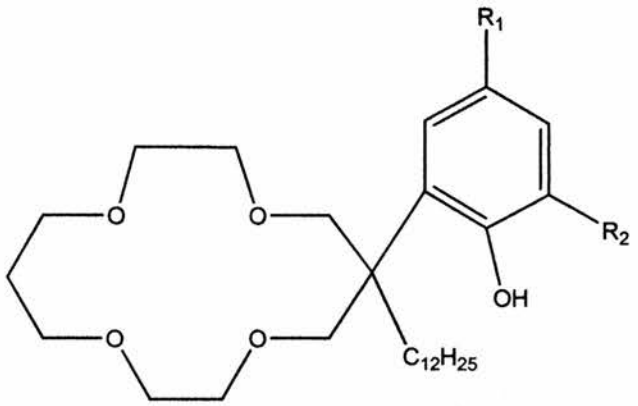

where R_1 and R_2 = H or NO_2

Figure 1.15 A phenol-substituted 14-crown-4-ether derivative that shows very high lithium selectivity.

The phenol substituted crown-4 derivatives in Figure 1.15 above display highest lithium selectivity as crown-*o*-nitrophenol or crown-dinitrophenol, whilst crown-phenol alone displayed no proton-driven transport of alkali-metal ions. For the dinitrophenol-crown derivative, the lithium / sodium selectivity ratio was determined to be at least 20, i.e. lithium is favoured over sodium by at least twenty times.

Crown ethers are among other families of ionophores to find use as 'scavengers', in which they selectively separate ions, or regulate their movements.

1.11 Anion Transport

Previous reference to ionophores has so far been with respect to cation transport, but another type of transport is equally important. Jean-Marie Lehn was co-awarded the Nobel Prize for Chemistry for his development and use of molecules with structure-specific interactions of high selectivity, which laid the foundations for anion co-ordination chemistry.

Stable anion complexes of organic ligands are much less common than cationic complexes. The first examples arrived in the 1960s, when anion cryptates (see Figure 1.16 below) were developed.[59] The cavity formed by the cryptate is lined with appropriate anion binding sites, e.g. sites able to form ionic hydrogen bonds, such as N^+-H---X^-.

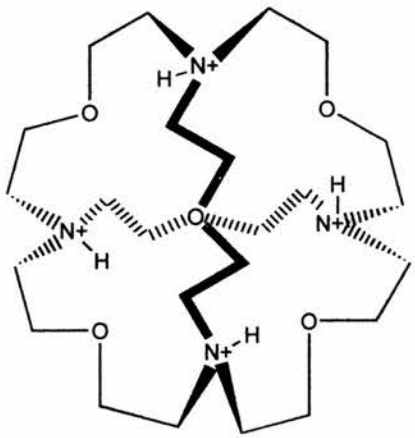

Figure 1.16 A stable and selective anion cryptate that carries halide anions as its tetraammonium salt.

Studies have since focussed on the development of new molecules designed with high specificity for anions such as perchlorate ClO_4^-, thiocyanate SCN^-, nitrate NO_3^-, and the halogens.[60-62] Suitable molecules can be used as receptors or anion-selective organic ligands.

Anions can be transported across membranes by the mechanisms of passive and active transport systems, proteins and ionophores. Some aspects of biological chloride ion transport were discussed in Section 1.8. The major protein responsible for chloride membrane transport in mammals is Band III protein. The role of Band III protein is to exchange HCO_3^- inside the cell for Cl^- outside, thereby facilitating the removal of CO_2. Other animal transport proteins known simply as *anion carriers* facilitate the diffusion of negatively charged inorganic groups such as phosphate and carbonate.

The anion transporting system of the red blood cell (RBC) provides a useful model for anion transport in general.[63] Physiologically, anion transport in RBCs occurs to promote the rapid distribution of bicarbonate (formed from tissue CO_2 by carbonic anhydrase) into the plasma as well as the cell water. In the lungs, the reverse reaction occurs as a response to the lowered CO_2 concentration.

Anion ionophore or anionophore mediated chloride / bromide exchange using a new and powerful ionophore is examined in more detail in Chapter 4.

References

1. Singer, S.J., Nicholson, G.L., *Science*, **175**, 720-731, (1972)
2. Berden, J. A., Barker, R. W., Radda, G. K., *Biochimica et Biophysica Acta*, **375**, 186-208, (1975)
3. Kyte, J., *Nature*, **292**, 201-202, (1981)
4. Nagle, J. F., Tristram-Nagle, S., *Biochimica et Biophysica Acta*, **1469**, 159-195, (2000)
5. Bretscher, M. S., *Science*, **181**, 622-629, (1973)
6. Korn, E.D., *Science*, **153**, 1491-1498, (1966)
7. Fettiplace, R., Andrew, D. M., Haydon, D. A., *Journal of Membrane Biology*, **5**, 277-296, (1971)
8. Huang, C., Mason, J. T., *Proceedings of the National Academy of Science, USA*, **75**, 1, 308-310, (1978)
9. Hemminga, M. A., Berendsen, H. J. C., *Journal of Magnetic Resonance*, **8**, 133-143, (1972)
10. Gent, M. P. N., Cottam, P. F., Ho, C., *Biophysical Journal*, **33**, 211-224, (1981)
11. Sumida, Y., Masuyama, A., Maekawa, H., Takasu, M., Kida, T., Nakatsuji, Y., Ikeda, I., Nojima, M., *Chemical Communications*, 2385-2386, (1998)
12. Hauser, H., Shipley, G. G., *Journal of Biological Chemistry*, 256, **22**, 11377-11380, (1981)
13. Mimms, L. T., Zampighi, G., Nozaki, Y., Tanford, C., Reynolds, J. A., *Biochemistry*, **20**, 833-840, (1981)
14. Blume, A., *Biochemistry*, **22**, 5436-5440 (1983)

15. Higgins, C., *Nature*, **341**, 103-104 (1989)

16. Prabhananda, B. S., Kombrabail, M. H., *Biochimica et Biophysica Acta*, **1370**, 41-50 (1998)

17. Waldeck, A.R., Lennon, A. J., Chapman, B. E., Kuchel, P. W., *Journal of the Chemical Society, Faraday Transactions*, **89** *15*, 2807-2814, (1993)

18. Taylor, R., Kauffman, R. F., Pfeiffer, D. R., In "*Polyether Antibiotics: Naturally Occurring Acid Ionophores*"; Westley, J. W., Ed.; Marcel Dekker; New york, 1982, Vol.1, pp. 103-184

19. Riddell, F. G., Cox, B. G., *Journal of the Chemical Society, Chemical Communications*, 1890-1891, (1987)

20. Riddell, F. G., Arumugam, S., Cox, B. G., *Biochimica et Biophysica Acta*, **944**, 279-284, (1987)

21. Riddell, F. G., Arumugam, S., Patel, A., *Journal of the Chemical Society, Chemical Communications*, 74-76, (1990)

22. Hladky, S. B., Haydon, D. A., *Biochimica et Biophysica Acta*, **318**, 464-468, (1973)

23. Riddell, F. G., Arumugam, S., *Biochimica et Biophysica Acta*, **945**, 65-72, (1988)

24. Riddell, F. G., Arumugam, S., *Biochimica et Biophysica Acta*, **984**, 6-10 (1989)

25. Benz, R., Lauger, P., *Journal of Membrane Biology*, **27**, 171-191 (1976)

26. Mronga, S., Muller, G., Fischer, J., Riddell, F. G., *Journal of the American Chemical Society*, **115**, 8414-8420, (1993)

27. Riddell, F. G., Arumugam, S., Brophy, P. J., Cox, B. G., Payne, M. C. H., Southon, T. E., *Journal of the American Chemical Society*, **110**, 734-738, (1988)

28. Riddell, F. G., Hayer, M. K., *Biochimica et Biophysica Acta*, **817**, 313-315, (1985)

29. Pressman, B.C. Harris, E. J., Jagger, W. S., Johnson, J. M., *Proceedings of the National Academy of Science, USA*, **58**, 1949-1956, (1967)

30. Pressman, B. C., *Annual Review of Biochemistry*, **45**, 501-530, (1976)

31. Kasuga, N. C., Kuboniwa, H., Nakahama, S., Yamaguchi, K., *Journal of the American Chemical Society*, **117**, 7238-7244, (1995)

32. Martinek, T., Riddell, F. G., Wilson, C., and Weller, C. T., *Journal of the Chemical Society, Perkin Transactions II*, 34-41, (2000)

33. Lehn, J. M., *Pure & Applied Chemistry*, **51**, 979-997, (1979)

34. Fossel, E. T., Sarasua, M. M., Koehler, K. A., *Journal Of Magnetic Resonance*, **64**, 536-540 (1985)

35. Shummard, R. F., and Callender, M. E., *Antimicrobial Agents in Chemotherapy*, 369-379 (1968)

36. Anteunis, M. J. O., Seto, H., and Otake, N., *Polyether Antibiotics: Naturally Occurring Acid Ionophores*, (J. W. Westley, ed.), 1982, Marcel Dekker, New York, pp. 245-334

37. Higgins, C., *Nature*, **341,** 102-103, (1989)

38. Ehrlich, B. L., Diamond, J. M., *Journal of Membrane Biology*, **52**, 187-200, (1980)

39. Schou, M., *European Journal of Pharmacology*, **27**, *324*, 231-243, (1976)

40. Dunham, P. B., Senyk, O., *Proceedings of the National Academy of Science, USA*, **74**, *7*, 3099-3103, (1977)

41. Pandey, G. N., Sarkadi, B., Haas, M., Gunn, R. B., Davis, J. M., Tosteson, D. C., *Journal of General Physiology*, **72**, 233-247, (1978)

42. Espanol, M. C., Mota de Freitas, D., *Inorganic Chemistry*, **26**, 4356-4359, (1987)

43. Pettigrew, J. W., Post, J. F., Panchalingham, K., Withers, G., Woessner, D. E., *Journal of Magnetic Resonance*, **71**, 504-519, (1987)

44. Tseng, L. F., Loh, H. H., Li, C. H., *Nature*, **263**, 237-238, (1976)

45. Zeevi, A., Margalit, R., *Journal of Membrane Biology*, **86**, 61-67, (1985)

46. Suzuki, K., Yamada, H., Sato, K., Watanabe, K., Hiasmoto, H., Tobe, Y., Kobiro, K., *Analytical Chemistry*, **65**, *23*, 3404-3410, (1993)

47. Suzuki, K., Sato, K., Hisamoto, H., Siswanta, D., Hayashi, K., Kasahara, N., Watanabe, K., Yamamoto, N., Sasakura, H., *Analytical Chemistry*, **68**, *1*, 208-215, (1996)

48. Paquette, L. A., Tae, J., Hickney, E. R., Rogers, R. D., *Angewande Chemie International Edition*, **38**, *10*, 1409-1411, (1999)

49. Casnati, A., Pochini, A., Ungaro, R., Bocchi, c., Ugozzoli, F., Egbrink, R. J. M., Struijk, H., Lugtenberg, R., de Jong, F., Reinhoudt, D. N., *Chemistry in Europe Journal*, **2**, 4, 436-445, (1996)

50. Hiratani, K., Sugihara, H., Kasuga, K., Fujiwara, K., Hayashita, T., Bartsch, R. A., *Journal of the Chemical Society, Chemical Communications*, 319-323, (1994)

51. Hayashita, T., Fujimoto, T., Morita, Y., Bartsch, R. A., *Chemistry Letters*, 2385-2388, (1994)

52. Kantipuly, C., Katragadda, S., Chow, A., Gesser, H. D., *Talanta*, **37**, 491-496 (1990)

53. Bartsch, R. A., Czech, B. P., Kang, S. I., Steq=wart, L. E., Walkowiak, W., Charewicz, W. A., Heo, G. S., Son, B., *Journal of the American Chemical Society*, **107**, 4997-4998 (1985)

54. Kitazawa, S., Kimura, K., Yano, H., Shono, T., *Journal of the American Chemical Society*, **106**, 6978-6983 (1984)

55. Tsukube, H., Adachi, H., Motosawa, S., *Journal of Organic Chemistry*, **56**, 7102-7108 (1991)

56. Marchand, A. P., Alihodzic, S., McKim, A. S., Kumar, K., *Tetrahedron Letters*, **39**, 1861-1864 (1998)

57. Margalit, R., Shanzer, A., *Biochimica et Biophysica Acta*, **649**, 441-448 (1981)

58. Kimura, K., Sakamoto, H., Kitazawa, S., Shono, T., *Journal of the Chemical Society, Chemical Communications*, 669-671, (1985)

59. Graf, E., Lehn, J.M., *Journal of the American Chemical Society,* **98**, *20*, 6403-6405 (1967)

60. Pedersen, C. J., *Journal of the American Chemical Society,* **89**, *10*, 2495-2496 (1967)

61. Dietrich, B., Fyles, T. M., Wais Hosseini, M., Lehn, J. M., Kaye, K. C., *Journal of the Chemical Society, Chemical Communications*, 691-692 (1988)

62. Cabantchik, Z. I., Knauf, P. K., Rothestein, A., *Biochimica at Biophysica Acta,* **515**, 239-302 (1978)

63. Tsukube, H., Hori, K., Inoue, T., *Tetrahedron Letters*, **34**, *42*, 6749-6752 (1993)

Chapter 2

NMR and Ion Transport

Chapter 2

The Use of NMR to Investigate Ion Transport Phenomena

2.1 Introduction

This chapter is devoted to NMR and the way in which it is used in this project. First is a description of the use of NMR in ionophore-mediated ion transport processes with large unilamellar phosphatidylcholine vesicles and a variety of quadrupolar nuclei (alkali metals and halogens). These were basic one-dimensional experiments repeated at regular time intervals (the 'timecourse' experiment) to allow rate data to be obtained through the variation in signal intensities when ionophore-mediated transport occurs. A shift agent (for Li^+/Na^+ exchange) and a relaxation agent (for Cl^-/Br^- exchange) were employed to separate intra and extravesicular signals.

The 1D NMR experiment was also used in the development of a new contrast reagent for anions based around cobalt (II) triglycine. These materials have been shown to allow the discrimination of NMR signals from partitioned samples of chloride, bromide, nitrate and nitrite. Again, these were relatively simple one-dimensional NMR experiments, using ^{35}Cl, ^{81}Br, and ^{14} & ^{15}N nuclei, in which chemical shifts and half-

height line widths were measured. Contrast reagents are discussed in detail in Chapter Five.

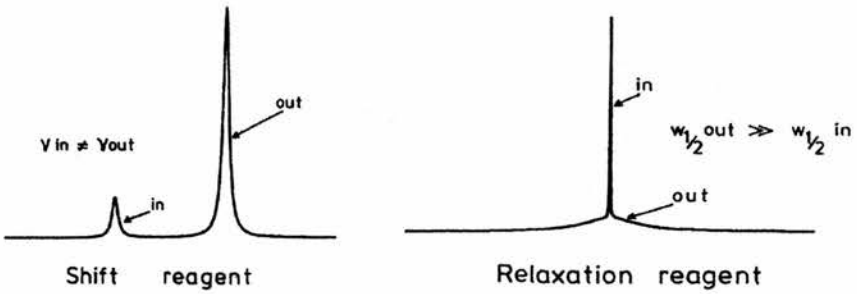

Figure 2.1 The effects of a contrast agent on signals from partitioned NMR active nuclei.

Lastly, the theory behind the two dimensional NMR studies of the five alkali metal salts of the polyether antibiotic nigericin is explained. The two-dimensional experiment in its simplest form is equivalent to a series of two-pulse experiments acquired with variable delay between the pulses. This work involved Correlated Spectroscopy (COSY) and Nuclear Overhauser Spectroscopy (NOESY), and both techniques are discussed.

This Chapter begins with a brief discussion of the underlying concepts of the one-dimensional NMR, starting with the origins of the NMR signal and moving on to the manipulation of the magnetisation vector through the use of radio-frequency pulses. The effect of

different pulse sequences on the magnetisation is described, as is the nature of the resulting NMR signals.

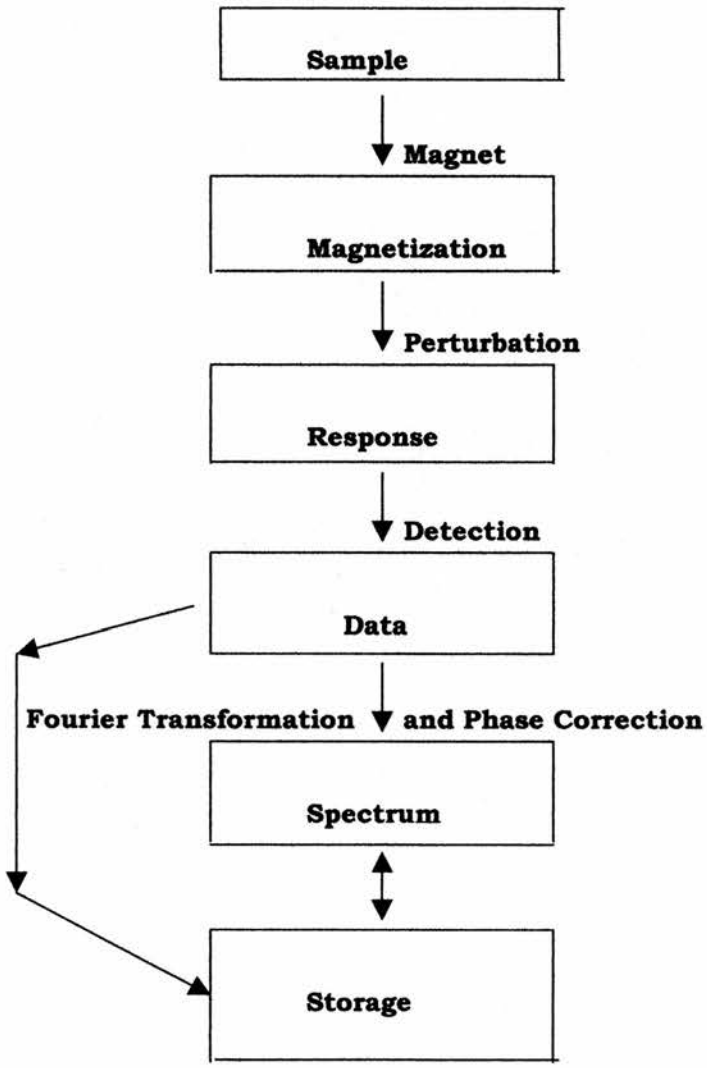

Figure 2.2 The various stages of a pulsed Fourier Transform NMR experiment.

2.1.1 Basic NMR Theory

The signals obtained in the NMR experiment arise from interactions of radio-frequency (RF) radiation with the magnetic moments (μ) of magnetically active nuclei in the presence of a strong magnetic field. The laws of electromagnetic theory state that a magnetic field is created when a charged particle moves. In atoms and molecules electrons and nuclei are sources of electrical movement, as both spin about their respective axes. Quantum mechanics predicts that nuclei with odd mass numbers have ½ integral spins, i.e. I=n/2. Nuclei with even mass and even charge numbers have 0 spin, i.e. I=0, and nuclei with even mass and odd charge numbers have integral spins, i.e. I=n.

NMR-active nuclei (with half or integral spins) interact with magnetic fields by aligning their magnetic moments in parallel or antiparallel arrangements with respect to the field itself. Each type of nucleus has a number of discrete energy levels, represented by the residual nuclear spin quantum number m_I. These energy levels are occupied by the magnetic moments of magnetically active nuclei and are degenerate, or of the same energy in the absence of a magnetic field. In a magnetic field, however, the degeneracy is removed, and there are generally $2I+1$ available energy levels or orientations that the nuclear magnetic moments (spin systems) can adopt.

In the simplest case of a proton, (I = ½), there are two energy levels; (α) m_I=+½, the lower energy state, in which the magnetic moment is aligned parallel to the applied field; and (β) m_I=-½, the higher energy state, when the magnetic moments are antiparallel to the applied field. The energy difference between them, ΔE, is related to B_o, the strength of the applied magnetic field, h, Planck's constant, and γ, the magnetogyric ratio:

$$\Delta E = h\gamma B_o / 2\pi \qquad \text{Equation 2.1}$$

Once a sample has been placed in the main magnetic field, the magnitude of which is represented by B_o, the application of an RF field at an appropriate frequency can induce transitions between these quantised energy levels that are characteristic of particular nuclei. This is a phenomenon known as *resonance*, whereby oscillating nuclei change their energy levels through interactions with other sources exhibiting similar oscillating frequencies. For resonance to occur, the energy must be applied from a direction perpendicular to the magnetic moment and at the exact precessional frequency of the nuclei. The frequency at which resonance occurs, υ, in Hertz, depends on B_o and γ:

$$\upsilon = \gamma B_o / 2\pi \qquad \text{Equation 2.2}$$

This defines the resonance frequency of different nuclei υ. The frequencies required for a given spin system to resonate fall in the radiofrequency (RF) region of the electromagnetic spectrum. The selection rule below dictates that only transitions between adjacent energy levels are possible.

$$\Delta m_I = \pm 1 \qquad \text{Equation 2.3}$$

The Boltzmann Equation describes the ratios of the populations of the various spin states at equilibrium:

$$N_{UPPER} / N_{LOWER} = exp\ (-\Delta E/kT) \qquad \text{Equation 2.4}$$

N_{upper} is equivalent to energy level β and N_{lower} is equivalent to energy level α as described in Figure 2.3. The differences in energy ΔE between two energy levels is equivalent to the resonance or Larmor frequency (υ) multiplied by h.

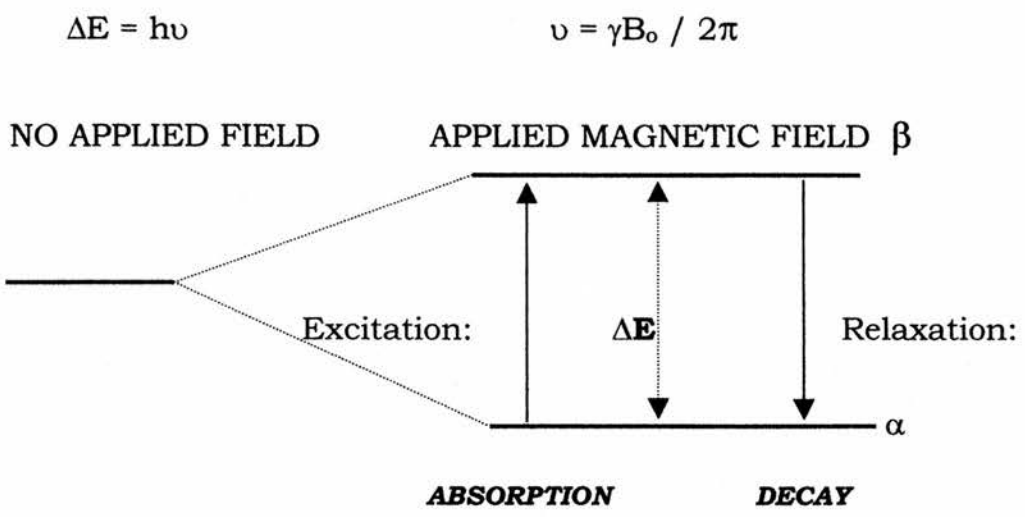

Figure 2.3 The two energy levels of a dipolar spin I=1/2 nucleus (i.e. ^1H), are degenerate in the absence of an applied magnetic field.

At equilibrium, the populations of energy levels α and β as described by the Boltzmann equation are not equal. If resonance of the collective magnetic moments of a sample occurs, then the population difference between α and β changes, then gradually returns to the equilibrium position. Through the resonance process, a very small excess of nuclei (around six per million in a 100 MHz ^1H field) are present in the lower energy levels at room temperature. Their net magnetic moments produce a magnetic vector that precesses about its equilibrium position, designated as the z-axis, co-incident with the main magnetic field axis, B_o. This precession is a result of B_o

itself. Two counter-rotating RF vectors are also present in the x-y or transverse plane.

2.1.2 The Manipulation of the Magnetisation Vector

The concept known as the *rotating frame of reference* allows the precessional motion of the net sample magnetisation to be simplified. This involves adopting a viewpoint based on a set of co-ordinates that rotate in synchronisation with the nuclear precession. In this way the individual magnetic moments appear static, i.e. it appears as if there is no precession about B_o (see Figure 2.4 below). It is conventional to rename the axes x', y', and z', to distinguish them from the *laboratory frame of reference*, in which there is precession around B_o. The rotating frame was originally devised as a means of simplifying the equations regarding motion in the system, and has been adapted to allow better visualisation and aid understanding of the behaviour of the vectors. In the rotating frame of reference, the z' axis remains parallel to the B_o field direction, and the x' and y' axes rotate about the z' axis at the angular frequency γB_o (in radians sec^{-1}) or $\gamma B_o/2\pi$ (in Hertz). From here on, all co-ordinates mentioned will refer to the rotating frame.

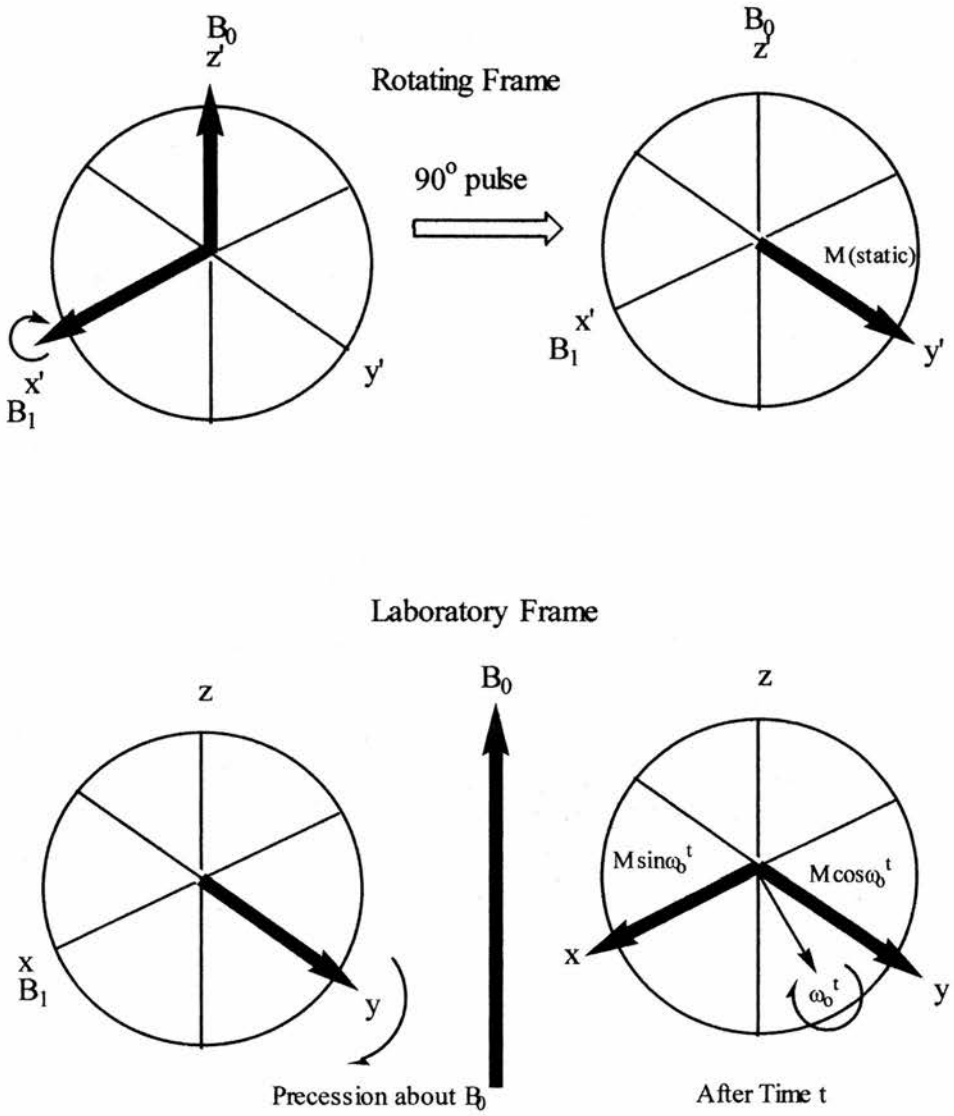

Figure 2.4 The laboratory frame of reference below shows the static field, the sample magnetisation and the two counter-rotating vectors arising through interaction with the RF field. The rotating frame above eliminates the static field and freezes one of the RF vectors.

A useful demonstration of the simplifications introduced through the rotating frame of reference follows. Imagine a record is spinning on a turntable at 33 or 45rpm, how can you read the label? From a stationary viewpoint, the writing on the label may be too difficult to read, but if the observer 'jumps' onto the turntable platter (representing the x'-y' plane) and begins to spin at the same speed (33 or 45 rpm) as the record, the writing appears stationary. Further, if the observer happens to jump onto the turntable when the writing is the correct way up (in-phase), it will be even easier to read than if it was upside down (out-of-phase).

A $90°_x$ RF pulse B_1, applied in a direction perpendicular to the main field B_o (see Figure 2.5 below) at the Larmor frequency ϖ is absorbed by nuclei causing the magnetisation vector to align with and precess about the y'-axis. The *flip angle* through which the magnetisation moves from its equilibrium position is proportional to the duration of the RF pulse, t_p, and is expressed as:

$$\theta = \gamma B_1 t_p \qquad \text{Equation 2.5}$$

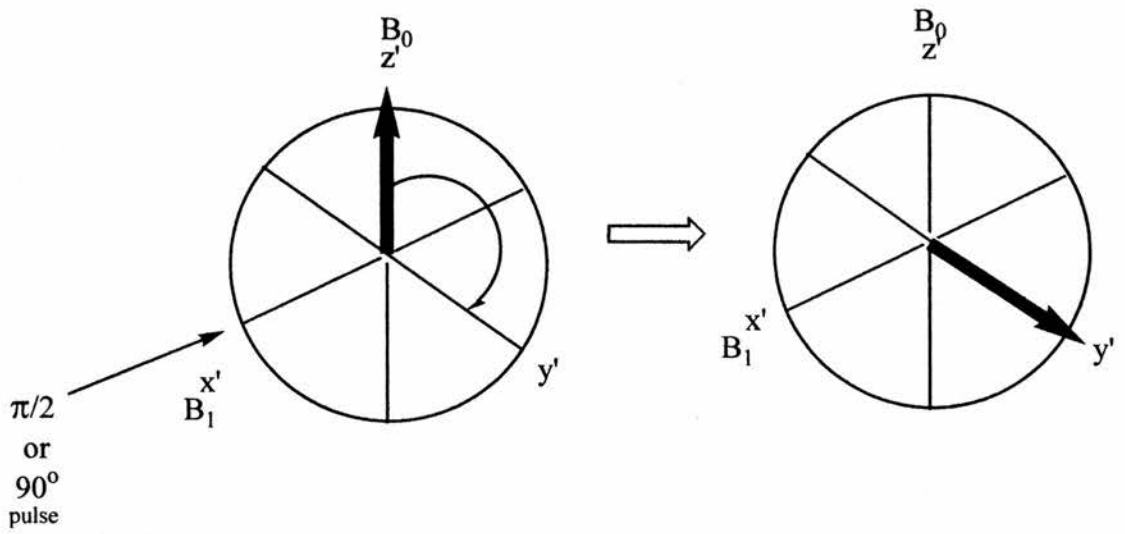

Figure 2.5 The effects of a ($\pi/2$) or $90°_x$ pulse.

The nuclear magnetisation vector is now said to be in-phase (coherent), as the magnetic moments comprising the vector are in the same position at the same moment in time through their precessional route. Voltages are induced in receiver coils located in the transverse plane when coherent magnetisation passes over the coil. This is the NMR signal.

2.1.3 Relaxation

After a certain period, these excited nuclei lose the extra energy they have absorbed and return to their equilibrium positions, through processes collectively known as *relaxation*, and the signal ceases. As the nuclei relax, the magnetisation vector slides from the y'-axis back to the z'-axis. There are two methods by which the excited nuclei can

lose energy; it can either be dispersed to the surrounding environment (the lattice) or to another nearby nucleus, providing both nuclei have the same precessional frequencies.

Two time constants are used to define the time periods involved throughout relaxation. The *spin lattice relaxation* time constant T_1, is a measure of the rate at which the equilibrium magnetisation along the z'-axis is restored. Spin lattice relaxation processes correspond to a change in energy of the system. Typical T_1 values (for example, ^1H or ^{13}C in solution) can range from very much less than a second to over 100 seconds. Quadrupolar nuclei often have very short T_1 values, allowing rapid pulsing, but can also produce very broad lines (several kHz) in spectra. The inverse of T_1, $(T_1)^{-1}$, is also known as the *longtitudinal relaxation rate*, and is often quoted or used in preference to the spin lattice relaxation time itself. The *spin-spin relaxation* time-constant, T_2, is also a measure of the rate at which the phase coherence in the x-y plane is lost. Spin-lattice relaxation corresponds to an energy change, whereas spin-spin relaxation corresponds to a change in the disorder (entropy) of the system.

2.1.4 Signal Detection, Collection, and Processing

The signal detected by the receiver coils in the x-y (transverse) plane comes from relaxing nuclei, and can be rapidly Fourier

transformed by computer to give a peak. Thus the time domain response of the system, or FID, is collected in analogue form, and quickly converted to digital form using an analogue to digital converter (ADC) and stored as data points on computer. The rate at which these data points are accumulated determines the spectral width of frequencies that will be present in the spectrum.

The free induction decay (FID) can be described as a periodic function of time, i.e. a signal that exhibits periodicity (+1 through 0 through –1) and time dependence (see Figure 2.6). In pulsed FT NMR experiments each FID contains information about the entire frequency range. The addition of successive FIDs leads to an improvement in the signal to noise ratio (s/n). Since the real signals from a spectrum appear at the same frequencies in each FID, they accumulate. The random noise that appears at varying frequencies in each FID accumulates much more slowly than the real signal does. Thus if n spectra are added together, the signal increases in intensity n times, but the noise only increases by $\sqrt{n}$. Thus the signal to noise ratio increases by a factor of $\sqrt{n}$.

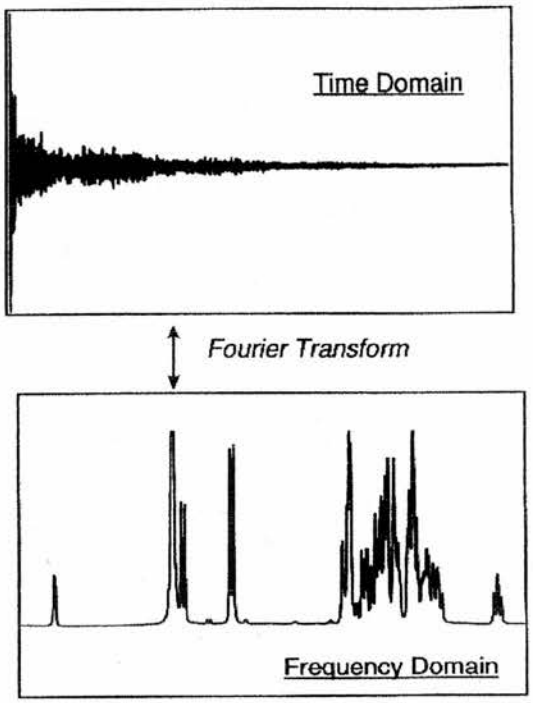

Figure 2.6 The Free Induction Decay (FID) is collected as a function of time (time domain) and the actual spectrum is a function of frequency (frequency domain). Fourier transformation is used to convert between the two domains.

The ADC or digitizer simply converts an analogue signal (e.g. voltage) into a digital signal (binary 1's and 0's). According to Nyquist theorem, the sampling rate (Hz) must be at least twice the signal frequency, or in this case, twice the entire width of the spectrum (Hz). If the sampling rate is too low, peaks may become folded over in the spectrum and appear at incorrect chemical shift positions.

For example, CD quality music is sampled at 44.1 kHz, that is, 44100 samples per second. Compare this to plain old telephony, which uses around 11 kHz as a sampling rate, and the difference is obvious - higher sampling rates more accurately reflect the original analogue signal.

The signal intensity in the NMR spectrum is limited by the *dynamic range* capacity of the digitizer. When the dynamic range of a digitizer is exceeded, the signals in a spectrum may no longer be accurate representations of the real thing. An 8-bit digitizer has 2^8 or 256 discrete levels (0-255). A very strong signal may correspond to, say 255. If there are signals in the spectrum that are more than 255 times lower in intensity, the digitizer will not have the capacity to represent the differences between these signals, which leads to improper representation of the signals.

2.2 Two-dimensional NMR

The one-dimensional NMR spectra of complex mixtures or large molecules can often contain many overlapping resonances. Such spectra can be difficult to interpret, even when selective decoupling techniques are employed, and so an additional dimension is introduced and the signals dispersed throughout both dimensions.

The two-dimensional NMR technique was proposed by Jeener[1] in 1971. The technique he described made use of two $\pi/2$ or 90^0 pulses. A two-dimensional pulse sequence contains a delay period t_1 between the 90^0 pulses, which is incremented upon each successive repetition, typically 512 or 1024 times. The signals are acquired as a function of time, denoted by t_2.

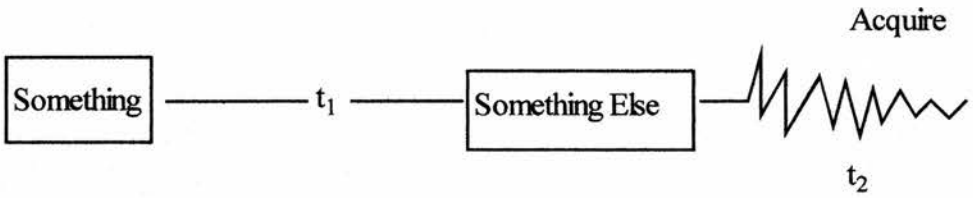

Figure 2.7 Schematic diagram of a two-dimensional pulse sequence.

The result is an array of FIDs, each of which represents a variation in the detected signal as a function of time. This is equivalent to a series of sequential 1D experiments. In general, the magnetisation of the sample evolves at a particular frequency υ_1 during the first delay period t_1 and becomes 'labelled' with this frequency. After the second pulse and during t_2 the evolution of the sample magnetisation occurs at a different frequency υ_2. Fourier transformation of the 2D array is carried out, with respect to t_2 and t_1. In the 2D spectrum, the 1D spectrum runs diagonally from bottom left to top right. Also present in the 2D spectrum, are the cross-peaks[2] at (υ_1, υ_2) where υ_1 is not

equal to υ_2. The 2D spectrum is often displayed as a contour plot with axes f_1 and f_2.

2.2.1 Two Dimensional NMR Time Periods

2D NMR experiments have four distinct time periods. The first is the *preparation* period, which is a delay before the experiment actually starts (designed to allow the magnetisation to equilibrate) followed by the pulse sequence to be applied for a particular experiment. The next time period is *evolution*, during which the magnetisation is allowed to evolve as a function of time. During this period the magnetisation of nuclei in a sample remains in a stable environment.

In the *mixing* period there is interaction between nuclear magnetisation, as the spins are allowed to affect each other in controlled manner, using delays or specific pulses. In COSY experiments nuclei that are spin-spin coupled can exchange magnetisation, whilst in NOESY experiments nuclei involved in dipolar relaxation or site exchange (EXSY) can undergo magnetisation transfer. The *mixing* period has a special time constant, τ, usually of the order of hundreds of milliseconds. The last time period is the *detection* or *acquisition*, during which magnetisation in the transverse plane is recorded as a FID.

2.2.2 Coupling Interactions in 2D NMR

The two main 2D NMR experiments make use of different kinds of coupling between nuclei. Spins that are *spin-spin, J,* or *scalar-coupled* permit the process of coherence (magnetisation) transfer, and this forms the basis for the COSY experiment. Scalar couplings give rise to the observed multiplets in 1D NMR. Scalar coupling between nuclei decreases as the number of bonds separating the nuclei increases. The magnitude of scalar coupling is affected by torsion angles about single and double bonds. This information can be used to derive data related to structure.

Dipolar-coupling is the dominant relaxation mechanism in spin=1/2 systems. Energy is lost to the lattice (surrounding molecules) in the form of heat through the mutual spin-flipping behaviour (direct dipole-dipole interaction) of the polarised nuclear magnetisation. The interaction of nuclear magnetic dipoles causes fluctuating local fields, and allows the dissipation of the energy absorbed from the pulse(s). This can in turn generate intramolecular cross-relaxation between nuclei that are close in space. Cross-relaxation is the source of the nuclear Overhauser effect (nOe), which alters the intensity of the detected signal through a disturbance in the energy level populations of other nuclei. The nOe is crucially

dependent on the distance between cross-relaxing nuclei, and gives rise to nOe spectroscopy (NOESY).

2.3 Correlated Spectroscopy (COSY)

2.3.1 COSY (COrrelated SpectroscopY) or Homonuclear Shift Correlation Through J-Coupling Using Jeener's Sequence

Jeener performed the first COSY (COrrelated SpectroscopY) in 1971.[1, 3] This makes use of the J-couplings between nuclei that are connected by bonds. COSY is a two-dimensional experiment in which the spin-spin (scalar) coupled nuclei in a molecule can be related to each other. Since the interaction occurs through connected atoms, it can be thought of as a *through-bond* effect. The 2D spectrum consists of what is basically a 1D spectrum along a diagonal axis representing the frequencies of nuclei in the sample. This arises as the intensity of each transition varies at υ_1 during t_1 and the frequency detected in t_2 is also at υ_1. The off-diagonal 'cross peaks' link spin-spin coupled or connected chemical shifts as the intensity of the υ_1 transition is modulated during t_1 by all the transitions to which it is connected.

Immediately after the initial 90^{o}_{x} pulse, the net magnetisation lies along the y'-axis, in the transverse plane. Although coherent (in-phase) for a small time, the magnetisation vectors begin to dephase in

the transverse plane in a fan-like motion. The second 90^{o}_{x} pulse applies a torque from the x'-axis to all vectors. Magnetisation that lay along the x'-axis before the pulse remains there, but vectors that lay between the y'-axis and the x'-axis (the transverse plane) get twisted through 90^{o} and move to give a component along the + z' and –z'-axes. Vectors lying along the + z'-axis have effectively returned to their equilibrium positions, and correspond to normal population distribution of energy levels. Vectors lying along the – z'-axis have undergone inversion of their population distributions for that pair of energy levels, and for all connected transitions in other resonances to which the proton is coupled.

A simplified pulse sequence for such an experiment can be explained as follows. A variable delay period, t_1, separates the first and second 90^{o}_{x} pulses before the signals are accumulated over a period t_2. These periods should not be confused by T_1 and T_2, the spin-lattice and spin-spin relaxation times. If this basic sequence is repeated many times, whilst increasing the delay t_1, we can obtain a signal that is modulated as a function of t_1 and detected as a function of t_2. A plot of signal versus t_1 gives rise to a FID-like structure, generated point-by-point as a function of t_1, also known as an interferogram. The accumulation of a two-dimensional data set requires two-dimensional processing, in this case Fourier transform.

When used on a set of data $f(t_1, t_2)$, an $f(n_1, n_2)$ frequency domain spectrum is obtained, as shown in Figure 2.8 below.

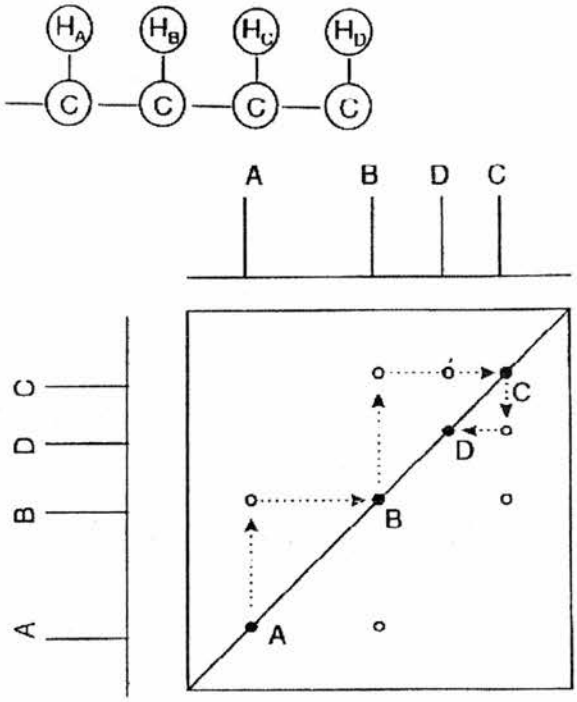

Figure 2.8 Schematic representation of a COSY experiment. Cross-peaks are indicated by hollow circles. The 1D spectrum lies along the diagonal and is also projected along the *f1* and *f2* axes.

The second pulse is also known as the *mixing* pulse. In a coupled system this pulse redistributes the magnetisation that arose from one of all possible transitions during t_1 among the coupled nuclei, and effectively frequency encodes them with information about all the

other coupled nuclei. The magnetisation from all transitions is eventually mixed together at the same time, enabling the transfer of information between coupled nuclei to occur. Thus a signal (line) picked up during the acquisition period t_2 may be amplitude modulated as a function of all the frequencies of all the other transitions. The two-dimensional spectrum will show cross-peaks to these lines. A typical 2D COSY spectrum has two frequency axes, ν_1 and ν_2. The 1D equivalent is displayed in the 2D spectrum, and usually runs diagonally from bottom left to top right. The chemical shift in ppm is also given along the bottom of the spectrum, enabling assignment of the peaks as usual. The so-called 'cross-peaks' represent nuclei lying on the diagonal that are connected by relatively strong couplings, and thus it is possible to move sequentially through a 2D COSY spectrum, identifying the coupled nuclei.

Significantly, strong couplings are rarely seen between nuclei separated by more than 3 bonds (^3J). This is lucky for us; if the effect travelled much further than 3 bonds, we would be swamped in information as longer range couplings would be picked up, and if the effect travelled less than 3 bonds, we would not get much useful information.

2.3.2 COSY Pulse Sequences

A typical COSY experiment consists of two 90^0 pulses separated by the time period t_1 (see Figure 2.9 below). In an AX proton spin system with no coupling, (i.e. J (A, X)=0), the initial pulse flips the magnetisation vector into the transverse plane where it begins to dephase at the Larmor frequency of A. The second pulse (mixing pulse) literally mixes the vectors comprising the transverse magnetisation by causing coherence transfer between coupled nuclei. Since J (A, X)=0, there are no coupled spins in this system, so the mixing pulse has no effect on the transverse magnetisation. In this case, the corresponding 2D spectrum shows only diagonal peaks with coordinates (δ_A, δ_A), and (δ_X, δ_X).

When J (A, X) is not equal to zero, there is coupling between A and X, and the mixing pulse has a different effect. The magnetisation vectors of A, precessing at υ_A, can mix with those of X, precessing at υ_X. The result is a transfer of spin information from A to X. The 2D spectrum of this system shows diagonal peaks at (δ_A, δ_A), and (δ_X, δ_X), and off diagonal or cross peaks at (δ_A, δ_X), and (δ_X, δ_A), which represents the coupling between A and X.

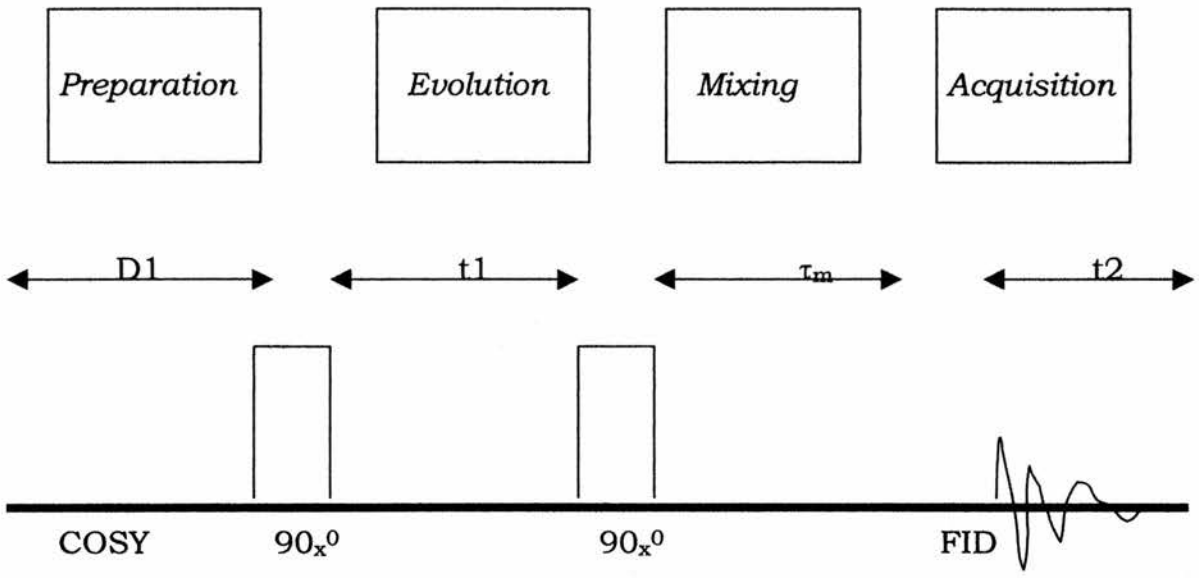

Figure 2.9 A standard COSY pulse sequence consisting of two 90⁰ pulses separated by a delay time t_1, and with a mixing time τ_m after the second pulse.

2.4 The Nuclear Overhauser Effect (nOe)

When the resonance of a particular nucleus is selectively saturated, the NMR signals from other nuclei in the same molecule can undergo changes in intensity due to a phenomenon known as the nuclear Overhauser effect (nOe),[4] and gives rise to nuclear Overhauser effect correlation spectroscopy, or NOESY.[5]

The nOe occurs through direct dipole-dipole interactions between saturated and observed nuclei, and, unlike COSY, nOe is a *through-space* effect. The magnetic dipole interactions that generate the nOe are in turn generated as a response of the system trying to maintain

its own thermal equilibrium.[4] Through the process of spin-lattice relaxation, excess energy passes to the surroundings as a result of dipole-dipole interaction between the magnetic moments of nuclei in diamagnetic molecules. The overall rate of dipole-dipole relaxation depends on the strength and frequency of fluctuating magnetic fields, and this is in turn dependent on the distance between interacting nuclei and molecular motion.

The magnitude of the nOe also depends on the distance between interacting nuclei (r), since it arises through dipole-dipole relaxation processes which themselves depend on how far apart in *spatial* terms the nuclei are. The nOe reduces as the sixth power as r increases, and the maximum nOe enhancement is given as:

$$\text{Maximum nOe enhancement} = \gamma_{sat} / 2\gamma_{obs} \qquad \text{Equation 2.7}$$

In a homonuclear experiment, the maximum enhancement is 0.5, or 50%, since both nuclei will have the same γ, but the intensities from low γ nuclei can be dramatically increased if there is nOe transfer from a nucleus with a higher γ, as illustrated in Table 2.1 (Page 77). The nOe can also give a negative enhancement (i.e. a decrease) in NMR signals from some important nuclei with negative magneto-gyric

ratios γ (e.g. ^{15}N, ^{29}Si) when protons in the same molecule are saturated. The evolution of the nOe is also dependent on molecular motion in solution. In situations where there is very little molecular motion in solution, i.e. for proteins, the observed signal may reduce to zero.

As the distance between two spins A and X increases, the intensity of the field produced through their interaction decreases and the efficiency of the dipole-dipole relaxation mechanism. Protons are the primary source of dipole-dipole interaction for ^{13}C, and carbons with two or more protons directly attached (i.e. secondary of tertiary carbons) have a faster relaxation rate than quarternary carbons.

The nOe arises through changes in energy level populations through dipole-dipole cross-relaxation mechanisms, demonstrated in Figure 2.10 below. There are two types of energy levels that must be considered:

(a) ω_{2AX} – a double quantum transition. ω_{2AX} transitions only occur when the local field fluctuates at the sum frequency ($\omega_A + \omega_X$).

(b) ω_{0AX} – a zero quantum transition. ω_{0AX} transitions only occur when the local field fluctuates at the difference frequency ($\omega_A - \omega_X$).

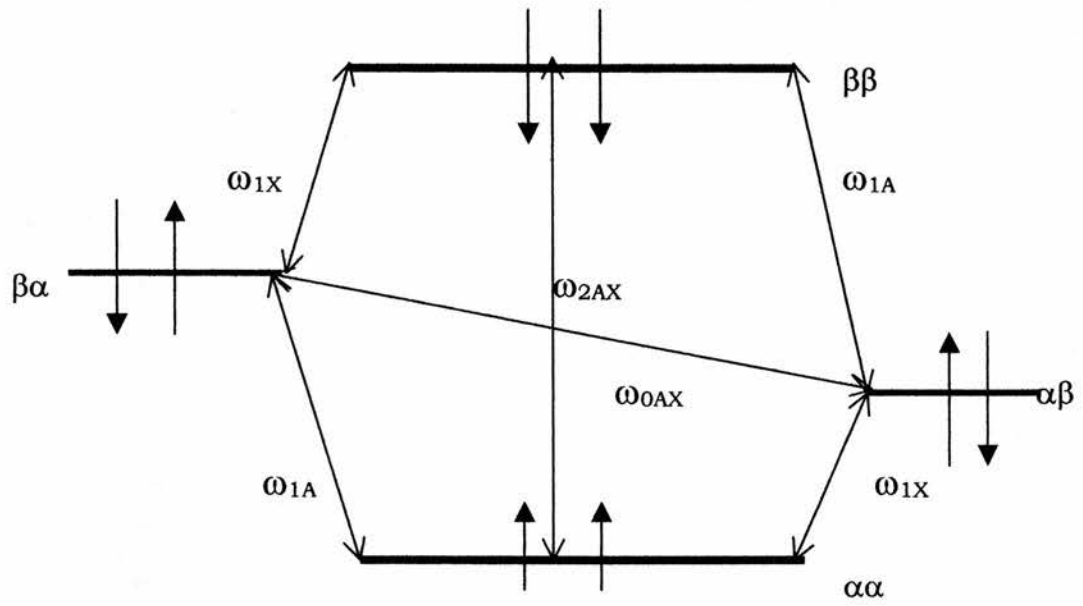

Figure 2.10 Energy level for an AX two-spin system. The transition probabilities ω_0, ω_1, and ω_2 are shown with spin states ($\alpha\alpha$, $\alpha\beta$, $\beta\alpha$, $\beta\beta$).

If spin X is selectively saturated, there will be an excess of high to low energy transitions, as there are more spins in a high energy state than there would be at equilibrium. The saturation of X equalises the populations of levels $\alpha\alpha$ and $\alpha\beta$, and also equalises the populations of levels $\beta\alpha$ and $\beta\beta$. The additional single quantum transitions (ω_1) of X have no effect on the intensity of the A signal.

In double quantum transitions (ω_2), when X moves from a high energy state to a low energy state, spin A must also flip downwards.

This increases the population differences across all A transitions. If ω_2 transitions are made to exceed ω_0 transitions, the saturation of X will cause the intensity of A to increase, as there are more spins engaged in transitions between energy levels, and hence more spins comprising the NMR signal. This corresponds to a positive nOe enhancement.

Observed Nucleus	γ / 10^7 rad T^{-1} s^{-1}	Maximum nOe enhancement after proton saturation (%)
^{1}H	26.751	50
^{13}C	6.726	199
^{15}N	-2.711	-493
^{19}F	25.166	53
^{29}Si	-5.314	-252
^{31}P	10.829	124

Table 2.1 Maximum nOe enhancements for selected nuclei with proton saturation.

In zero quantum transitions, when X flips downwards, A flips up, and the population difference across all A transitions decreases. If ω_0 transitions exceed ω_2 transitions, the saturation of X will cause the

intensity of A to decrease, as there are fewer spins engaged in transitions between energy levels, and fewer spins comprising the signal. This corresponds to a negative nOe enhancement.

When the rates of ω_0 and ω_2 transition are equal, there are no population disturbances and no nOe.

The NOESY (nOe Spectroscopy) experiment is used to identify pairs of protons involved in cross-relaxation (arising through dipole-dipole coupling). NOESY and variant forms are valuable tools in conformational studies of proteins, as the structural-geometrical information derived can be used in molecular dynamics and mechanics. In protein NMR, the common conformations adopted by proteins, such as α-helices or β-sheets, give a distinctive pattern of NOESY cross-peaks. This is taken to mean that the two groups correlated through the cross-peaks are close to each other in terms of distance.[6, 7]

The information obtained through NOESY experiments is complementary and often used in conjunction with that from the COSY spectrum.

2.4.1 NOESY Pulse Sequence

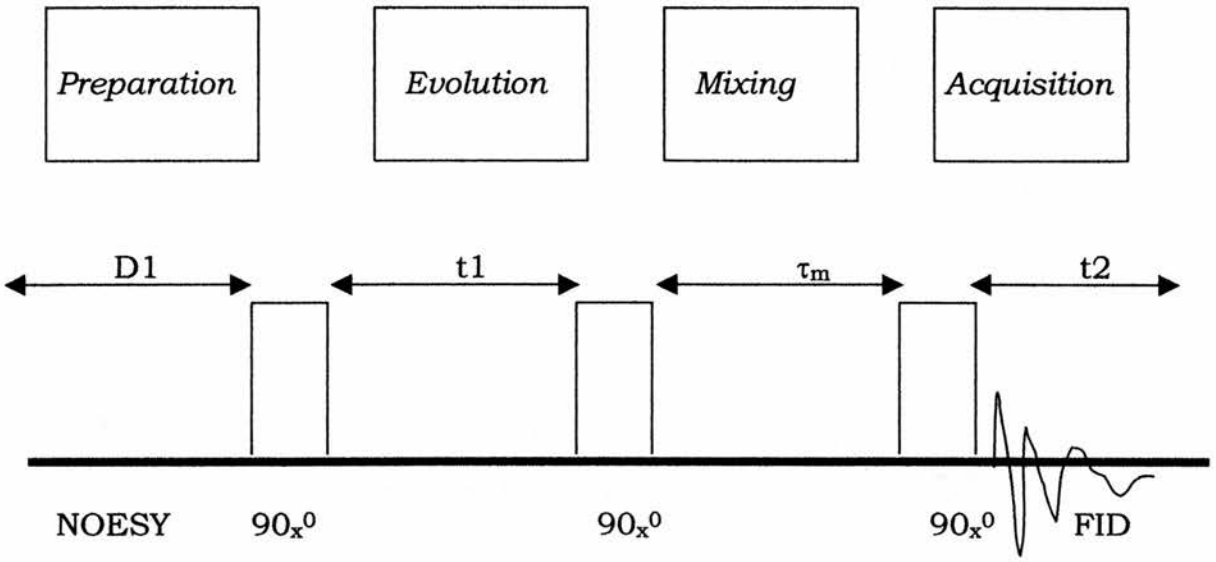

Figure 2.11 A standard NOESY pulse sequence consists of three 90^0_x pulses.

At its most basic the pulse sequence, shown in Figure 2.11 above, consists of three 90^o_x pulses separated by two delays, t_1 (variable), and τ_{mix} (constant). As with the COSY experiment, the collected FIDs are displayed in a 2D array, although the cross peaks in the case of NOESY arise only when two nuclei are close together in space.

A characteristic feature of the NOESY pulse sequence is the mixing time τ_{mix}, during which magnetisation transfer between dipolar-coupled spins takes place. The value of τ_{mix} must be proportional to the rate of magnetisation transfer. A NOESY build-up experiment (see Figure 2.12 below) allows the optimum τ_{mix} to be determined.

When τ_{mix} is plotted against nOe intensity, the mixing time at the maximum of the initial linear region of the nOe intensity is usually the optimum.

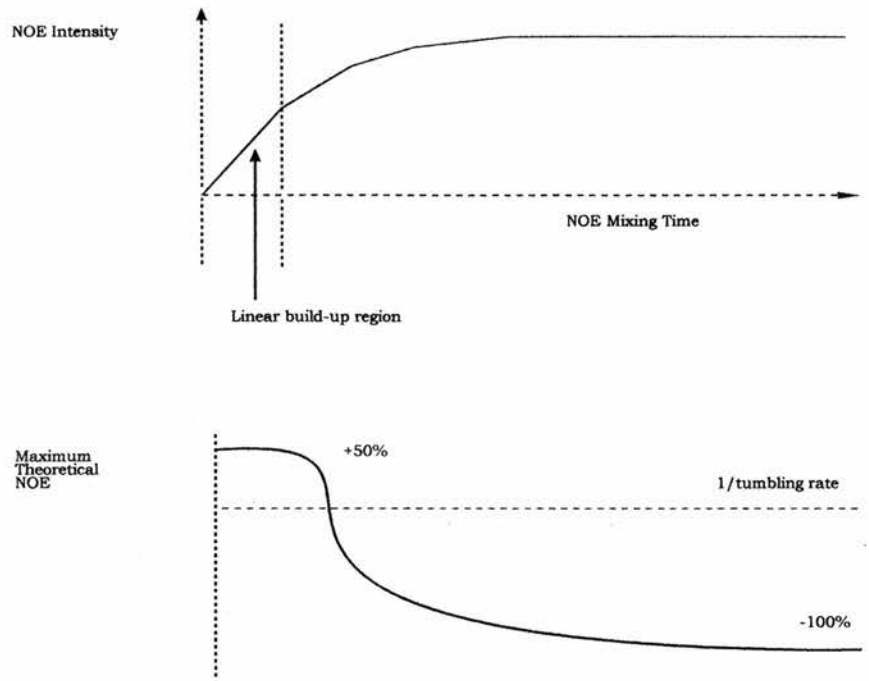

Figure 2.12 A NOESY build-up experiment follows the intensity of a certain peak at different mixing times (τ_{mix}) in order to find the optimum time. The tumbling rate of a molecule in solution must also be taken into consideration.

For a pair of dipolar coupled but not scalar coupled spins A and X, the first $90°_x$ pulse flips the equilibrium magnetisation of A to the y'-axis, where it precesses for a time t_1 at frequency ν_A. In a similar manner to the COSY experiment, the second $90°_x$ pulse returns the magnetisation left in the transverse plane to the z'-axis. During the

mixing time τ_{mix}, the spins A and X cross relax each other, and magnetisation from A can be transferred to X via the nOe. The third $90°_x$ pulse rotates the X magnetisation back to the y'-axis, where it precesses at frequency υ_X during t_2.

The intensity of the NOESY cross-peaks at $(\omega_1, \omega_2) = (\upsilon_A, \upsilon_X)$ and (υ_X, υ_A) depends on the effectiveness with which z magnetisation is transferred during τ_{mix}. The diagonal peaks in the NOESY spectrum at $(\omega_1, \omega_2) = (\upsilon_A, \upsilon_A)$ and (υ_X, υ_X) arise from excess spin A z-magnetisation that remains after τ_{mix} and gets flipped to the y'-axis by the third $90°_x$ pulse.

2.5 Nuclei Studied By NMR in Transport Experiments

The nuclei studied by NMR were the alkali metals ^{6}Li, ^{7}Li, ^{23}Na, and the halogens ^{35}Cl and ^{81}Br. Much of the chemistry of alkali metals and halogens can be rationalised in terms of the +1 and −1 charges present on the cations and anions respectively. All of these nuclei are quadrupolar, which has significant yet similar effects on the relaxation behaviour of most of the nuclei used.

2.5.1 The Alkali Metals

All of the alkali metals that make up Group IA of the Periodic Table are NMR active nuclei. The natural abundance for isotopes of the alkali metal ions are summarised in Table 2.2 below. Generally the isotope with highest abundance is preferentially used except in the case of rubidium, as ^{87}Rb has a greater magnetogyric ratio than ^{85}Rb. The main difference between alkali metal NMR and routine proton and carbon-13 NMR is that all of the alkali metals are quadrupolar nuclei ($I > 1/2$).

Nucleus	**^{6}Li**	**^{7}Li**	**^{23}Na**	**^{39}K**
Spin-Quantum Number	1	3/2	3/2	3/2
Natural Abundance (%)	7.42	92.58	100	93.1
Receptivity (c.f. $^{13}C=1$)	3.58	1.54×10^{2}	5.25×10^{2}	2.69
Frequency (c.f. $^{1}H=100$ MHz)	14.716	38.864	26.451	4.666
Quadrupole Moment (10^{-28} m^2)	-8×10^{-4}	-4.5×10^{-2}	0.12	5.5×10^{-2}

Table 2.2 Properties of selected alkali metal nuclei.[7]

The charge present in quadrupolar nuclei is no longer spherical but asymmetrically distributed, bringing about an electric quadrupolar moment capable of interacting with the electric field gradient (EFG).

When the nucleus is in a highly symmetrical environment, the EFG is low, or close to zero. The overall effect of the interaction between the nuclear quadrupole moment and the EFG gives the nuclei an additional relaxation mechanism, termed quadrupolar relaxation. Quadrupolar nuclei have shorter relaxation times (T_1 and T_2) than dipolar nuclei (e.g. ^{1}H and ^{13}C), but also the disadvantage of producing much broader lines, depending on the molecular environment, ranging from <1 Hz for $^{6}Li^{+}$ in H_2O to many kHz for ^{87}Rb-ionophore complexes. The line-widths for $^{23}Na^{+}$ and $^{39}K^{+}$ in aqueous solution are typically 10 to 13 Hz.

Quadrupolar relaxation is governed by the equation:

$$T_{1q}^{-1} = T_{2q}^{-1} = 3\pi^2/10.(2I+3)/I^2(2I-1).\chi^2.(1+\eta^2/3).\tau_C \qquad \text{Equation 2.8}$$

Here the asymmetry factor is defined from components of the EFG (q):

$$\eta = \frac{q_{yy} - q_{xx}}{q_{zz}} \qquad \text{Equation 2.9}$$

The strength of the quadrupolar interaction between the quadrupole moment (Q) and the EFG (q) is given by the quadrupolar coupling constant χ:

$$\chi = e^2.q_{zz}.Q/h \qquad \text{Equation 2.10}$$

Where:

I = Spin quantum number

χ = nuclear quadrupole coupling constant

τ_c = correlation time

c = charge on an electron

Q = quadrupole moment

q_{zz} = largest component of the electric field gradient

In solution some of the alkali metals are subject to relatively low quadrupolar interactions, with ^{6}Li and ^{133}Cs having the lowest known quadrupole moments. Quadrupolar effects tend to dominate ^{23}Na, ^{39}K, ^{85}Rb and ^{87}Rb spectra in many systems. In aqueous solution alkali metals are also heavily solvated. The exact pattern of water molecules around the central cation fluctuates very rapidly and may not exactly display spherical symmetry, but is always close to it. For the alkali metals in solution, with low quadrupole moments, dipolar relaxation mechanisms can account for between 75 % (^{7}Li) and 100 % (^{6}Li) of the relaxation.

In practice, ^{6}Li has low sensitivity and a low quadrupole moment and hence gives rise to sharp signals, whilst ^{7}Li has a higher quadrupole moment, gives broader lines and is highly sensitive. The

observed signal broadening of quadrupolar nuclei increases as a function of the quadrupolar moment and asymmetry of environment.

Biological NMR studies of ^{23}Na in tissues may be hindered by partial invisibility of ^{23}Na. This is due to static and/or dynamic quadrupolar effects encountered in the local microenvironment of Na^+ in the tissue.

2.5.2 The Halogens

All of the halogens are NMR active. Often there is more than one active isotope available. All halogen nuclei are quadrupolar, which, as with the alkali metals, subjects the nuclei to quadrupolar relaxation mechanisms. Chloride and bromide are the anions most frequently studied by NMR, using the isotopes ^{35}Cl, ^{37}Cl, ^{79}Br and ^{81}Br. All of these nuclei are quadrupolar, which has important effects when these nuclei are observed in conjunction with biological membranes. Experimentally, chloride and bromide in aqueous solution produce strong NMR signals and have relatively short relaxation times, but the line-widths are generally broad.

Nucleus	^{35}Cl	^{37}Cl	^{79}Br	^{81}Br
Spin-Quantum Number	3/2	3/2	3/2	3/2
Natural Abundance (%)	75.53	24.47	50.54	49.46
Receptivity (c.f. $^{13}C=1$)	20.2	3.8	226	277
Frequency (c.f. $^{1}H=100$ MHz)	9.8	8.16	25.05	27.00
Quadrupole Moment (10^{-28} m^2)	8.0×10^{-2}	6.32×10^{-2}	0.33	0.28

Table 2.3 Properties of selected halogen nuclei.[8]

The quadrupolar nature of the chloride and bromide nuclei causes line broadening (ca. 12 Hz for $^{35,37}Cl$, ca. 400 Hz $^{79,81}Br$, for Cl^- and Br^- in aqueous solution) and renders them almost invisible inside erythrocytes (ca. 700 Hz), thereby enabling NMR transport studies without the use of contrast reagents. Otherwise, the *isochronicity* phenomenon means that aqueous chemical shifts are essentially independent of the environment of a nucleus. This necessitates the use of a contrast reagent to distinguish the signals.

Riddell et al have used manganous ions as contrast reagents that operate by enhancing the relaxation processes of the nuclei that comprise the 'out' signal.[9] For example, in human erythrocytes, by

causing a very substantial broadening of the 'out' line (many kHz) the 'in' line (ca. 700 Hz) becomes visible.

References

1. Jeener, J., 1971 Ampere International Summer School, Basko Polje, Yugoslavia
2. A general introduction to modern multidimensional NMR techniques can be found in: (a) Derome, A. E., *Modern NMR Techniques for Chemical Research*, (1987), Pergamon, Oxford, (b) Sanders, J.K.M., Hunter, B.K., *Modern NMR Spectroscopy*, Oxford University Press, Second Edition, 1993, (c) Harris, R.K., 0Mann, B.E., *NMR and the Periodic Table*, Academic Press, 1978
3. Freeman, R., *Proceedings of the Royal Society of London.*, **A373**, 149-178, (1980)
4. Overhauser, A. W, *Physical Review*, **92**, 411-415, (1955)
5. Meier, B. H., Ernst, R. R, *Journal of the American Chemical Society*, **101**, 6441-6442, (1979)
6. Freeman, R, *A Handbook of Nuclear Magnetic Resonance, Longman*, Harlow, (1988)
7. Riddell, F. G., *Encyclopedia of Spectroscopy and Spectrometry*, Academic Press, London, Lindon, J. C., Tranter, G. E., Holmes, J. L., 1584-1593 (1999)
8. Riddell, F. G., *Encyclopedia of Spectroscopy and Spectrometry*, Academic Press, London, Lindon, J. C., Tranter, G. E., Holmes, J. L., 677-684 (1999)
9. Riddell, F. G., Zhou, Z., *Magnetic Resonance in Chemistry*, **33**, 66-69 (1995)

Chapter 3

Alkali Metal Transport Mediated By Lithium-Specific Ionophores

Chapter 3

Alkali Metal Transport Mediated By Lithium-Selective Ionophores

3.1 Introduction

Ionophores are useful research tools in experimental models of biological systems, and there is potential for their use in a pharmacological context. Ionophores that display selectivity for lithium have received a special interest due to the use of lithium in the treatment of manic-depressive illnesses. In addition, lithium-selective ionophores are often the active components of lithium-selective electrodes.

In Chapter 1 the main lithium-selective ionophore families consisting of crown ethers and polyether antibiotics were mentioned. The ionophores used in the current transport studies are of novel design. Both feature a single ring (cyclopentadienyl or cyclohexane) as the 'backbone' of the molecule, with 2 or 3 oxygen-containing cavity-forming ligands through which cation co-ordination can occur.

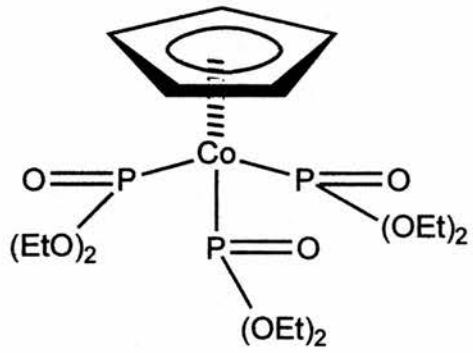

Figure 3.1 Lithium-selective Ionophore 1 [sodium (cyclopentadienyl) tris (diethylphosphite) cobaltate]

The first of these ionophores, **Ionophore 1**, $[(C_5H_5)Co[P(O)(OEt)_2]_3]^-$, (*sodium (cyclopentadienyl) tris-(diethylphosphite) cobaltate*, Figure 3.1, above), was synthesized in 1986[1], and the cation transport rates of the compound were measured in the same year by Shinar and Navon.[2] The active species in the transport process was found to have a 1:1 ligand to metal stoichiometry, and the apparent rate constants from transport experiments were found to be proportional to the ionophore concentration.

The rates of transport showed the preference for lithium over sodium, and were compared to the carboxylic ionophore monensin. The rate of lithium transport by monensin was twice that of Ionophore 1, whilst the rate of sodium transport by monensin was around a thousand times that of Ionophore 1. In competition experiments,

Ionophore 1 displays selectivity for lithium in favour of sodium by a factor of around 40. For comparison, ionophores previously considered to have high lithium-selectivity favoured lithium over the nearest other cations, e.g. sodium, by a factor of only around 13.

In 1981 Margalit and Eisenman[3] demonstrated that Simon's neutral, non-cyclic, lithium selective complex, *(N,N'-diheptyl-N,N'-5,5-tetramethyl-3,7-dioxanonanediamide, or ETH149*), bearing both imide and ether ligands, could carry monovalent cations across lipid bilayer membranes.

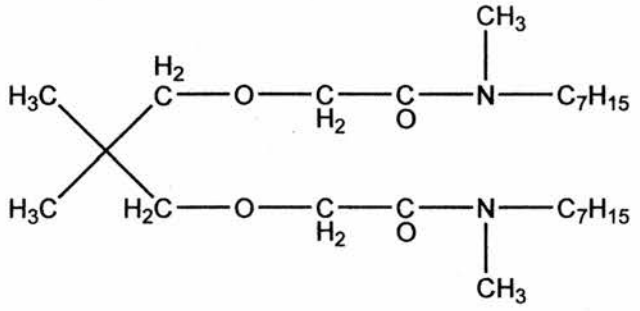

Figure 3.2 Ionophore ETH149 with imide and ether co-ordinating ligands

They claimed the compound showed a preference for lithium over the other alkali metal cations. They found the prevalent carrier / cation complex to have the ratio 2:1 at all but the lowest salt and carrier concentrations, where a 1:1 ligand to metal complex was formed. The selectivity sequence for ETH149 was given as: $Li^+ > Na^+ > K^+ > Rb^+ > Cs^+$.

A compound related to Ionophore 2 and shown below in Figure 3.3, AS701, was also shown to have anion-binding properties[4], although the cation complex was deemed to be the dominant permeant species in alkali chlorides, e.g. NaCl or LiCl. The experimentally determined selectivity sequence is as follows: *Li>Na>K>Rb>Cs.*

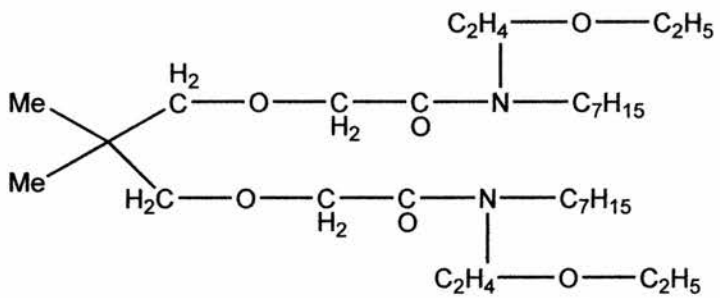

Figure 3.3 Shazner's Li^+-selective ionophore AS701.

In 1982 Erne and Ammann[5] et al reported the synthesis of a series of lipophilic *N, N, N', N'*- tetra-substituted diamides and examined their selectivity for alkali and alkaline earth metal cations in solvent potentiometric membranes. One of the compounds used in this study was the neutral non-cyclic *cis-N,N,N',N'-tetraisobutylcyclohexane-1,2-dicarboxamide* (ETH1644), **Ionophore 2**, Figure 3.4, *below.* Like ETH149, this compound has both imide and ether co-ordinating ligands, and shows a similar preference for lithium over the other alkali metal cations.

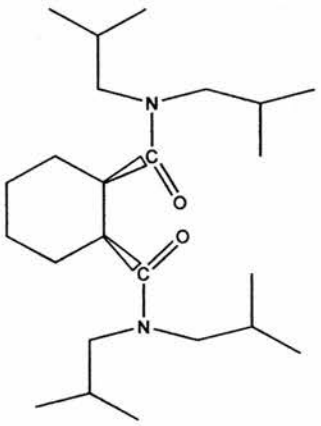

Figure 3.4 This lithium-selective Ionophore 2 (ETH1644 or cis-N,N,N',N'-tetraisobutylcyclohexane-1,2-dicarboxamide) was used in the present transport studies.

Ionophore 2 was designed as a Li^+ selective carrier with potential to aid Li^+ therapies for patients of manic depressive illnesses. It was found to induce selectivity in the membranes that was around 100 times greater for Li^+ than for other alkali metal cations (e.g. Na^+, K^+, Cs^+, Rb^+), and about 1000 times greater for Li^+ than the selectivity displayed towards other alkaline earth metal cations (e.g. Mg^{2+}, Ca^{2+}, Ba^{2+}, Sr^{2+}).

Zeevi and Margalit[6] carried out transport studies across lipid bilayer membranes with Ionophore 2 in 1985. They reported the formation of a 2:1 ligand to metal complex, and found diffusion across the membrane to be the rate-limiting step of the overall process. Based on structural studies and conductance data, the high affinity

for this ionophore towards lithium is believed to arise through a lowering of the affinities for other small cations, rather than an increase in affinity for lithium itself.

However, many of the contemporary alkali-metal specific carriers show a 1:1 ligand to metal ratio. Published studies[5] claimed that the rate-determining step was the diffusion of the complex across the membrane, and a ratio of 2:1 for the carrier: cation complex, but these finding were questioned after an unpublished study in the early 1990's showed a 1:1 complex in which formation and dissociation were the actual rate-determining steps.[7]

The current study aims to clarify outstanding issues such as the uncertainty in the molecularity of the transport process. It also uses techniques employed for the ionophoric antibiotics and so should permit comparison of the transport rates of these synthetic ionophores with those of the naturally occurring ones under identical conditions.

3.2 Kinetics of Ionophore-Mediated Transport Processes

3.2.1 Kinetics for First Order Ion Transport

The model adopted for the unimolecular transport process is that proposed by Painter and Pressman[8], as described in Figure 1.11, Page 25. The methodology used to calculate the dissociation and formation constants of the ligand-metal complex has been successfully used in earlier studies.[9, 10]

Despite the fact that complex formation and dissociation are multi-step processes, each can be represented by a single rate constant, k_f formation rate constant), and k_d (dissociation rate constant). This is the only system that tries to apply chemical kinetics to membrane transport processes in a rigorous manner. Using the model given in Figure 1.11, the transport process can be represented by the following set of equations:

$$1/k = K_m/V_m + [M+]/V_m \qquad \text{Equation 3.1}$$

$$V_m = k_d.k_{diff}/(k_d + 2k_{diff}) \qquad \text{Equation 3.2}$$

$$K_m = k_d/k_f = K_s^{-1} \qquad \text{Equation 3.3}$$

Where K_s is the stability constant for the ligand-metal complex.

Therefore if $k_d >> k_{diff}$ then $V_m = k_{diff}$

$$Slope = {(k_d + k_{diff})}/{k_d.k_{diff}} \qquad \text{Equation 3.4}$$

$$Intercept = {k_d.(k_d + k_{diff})}/{k_f.k_d.k_{diff}} \qquad \text{Equation 3.5}$$

$$1/T\ M^+_{in} = A.k_{diff}.k_d.[L]_T\ /\ V_{in}.(k_d + 2k_{diff}).([M^+] + k_d\ /\ k_f) \qquad \text{Equation 3.6}$$

Where:

$^TM^+_{in}$ = the lifetime of M^+ inside a vesicle

A = surface area

V_{in} = internal volume

$[L]_T$ = total concentration of ionophore

k_f = rate of formation of the complex

k_d = rate of dissociation of the complex

k_{diff} = diffusion coefficient of the complex

$[M^+]$ = metal ion concentration;

Substituting Equations 3.2 and 3.3 into Equation 3.6 gives a simplified rate equation:

$$1/T.M^{+}_{in} = A.V_{in}.[L]_t / V_{in}.(K_{in} + [M^{+}])$$ Equation 3.7

Processes that are first order in ionophore concentration and have a rate constant k' can be expressed as:

$$k' = A.V_{in} / V_{in}.(K_{in} + [M^{+}])$$ Equation 3.8

The rate constant k' is equal to the slope of the plot of k versus I/PC for each metal concentration. Therefore a plot of k' versus $[M^+]$ will have a slope of V_{in} / $A.V_m$ and an intercept of $V_{in}.K_m$ / $A.V_m$. The ratio of slope to intercept gives the stability constant of the ligand-metal complex in the membrane.

Equation 3.8 above is governed by two limiting conditions. If the diffusion co-efficient k_{diff} is very large with respect to the dissociation rate constant k_d then $V_m = k_d / 2$. In this instance, diffusion is not rate limiting and the slope is proportional to $1/k_d$ and the intercept to $1/k_f$. Alternatively, when k_{diff} is much smaller than k_d, then $V_m = k_{diff}$. Here diffusion is the slower rate-limiting step, hence the slope becomes proportional to $1/k_{diff}$ and the intercept to K_m/k_{diff}. When k_{diff} is of the order of k_d, the slope and intercept are more difficult to interpret, but their ratio still yields K_s. The measurement of the lifetime of an ion inside vesicles at varying metal ion and ionophore

concentrations should allow calculation of the transport rate constants.

3.2.2 Kinetics for Non-First Order Ion Transport

When there is no linear relationship in the plot of $[M^+]_{int}$ versus time the reaction is not first order, and the method described to obtain rate constants is no longer valid. The general rate law for the ion transport from the interior of the vesicle is given as:

$$d[Li^+]_{int}/dt = k[Li^+]_{int}^n \left([ionophore]/[lipid]\right)^m \qquad \text{Equation 3.9}$$

Where $[Li^+]_{int}$ is the mole fraction of Li^+ ions inside the vesicle with respect to the total $[Li^+]$, n is the order of the transport as regards the mole fraction of the total lithium inside the vesicles, and m is the order of the transport with respect to the concentration of ionophore in the membrane expressed as the *[ionophore]/[lipid]* or *[I] /[PC]* molar ratio, assuming that all the added ionophore is all dissolved in the bilayer.

If the kinetics do not follow a unimolecular mechanism then a different approach is needed. The order of the transport process can be obtained by measuring the initial rates (v) of the kinetics obtained for different ionophore concentrations. These rates were given from the tangents at time zero to the plots of $[M^+]_{int}$ as a function of time.

The kinetic order is equal to the slope (m), taken from the plot of ln (v) versus ln ([*ionophore*]/[*lipid*]).

This method of analysis of non-first order kinetics was used recently in a ^{23}Na and ^{35}Cl study of the ionophoric activity of the antibiotic peptaibol trichorzin PA VI, in which the kinetic order was found to be 3.1 ± 0.5 with respect to the peptaibol concentration.[11]

3.3 Ion Exchange and the Timecourse Experiment

In this procedure, the first spectrum, typically recorded 2-3 minutes after the addition of the ionophore into the NMR tube, is compared with all subsequent spectra (e.g. 25-50 spectra) collected over 1-2 hours. The increase or decrease of the peak sizes as shown in Figure 3.5 and 3.6 over time allows the rate of transport to be calculated. The rate constant k has units of sec^{-1}, and the inverse of the rate constant k' has units of *moles Ionophore, moles lipid*$^{-1}$ sec^{-1}. In each case a general trend in the increase or decrease of the peak heights can be followed.

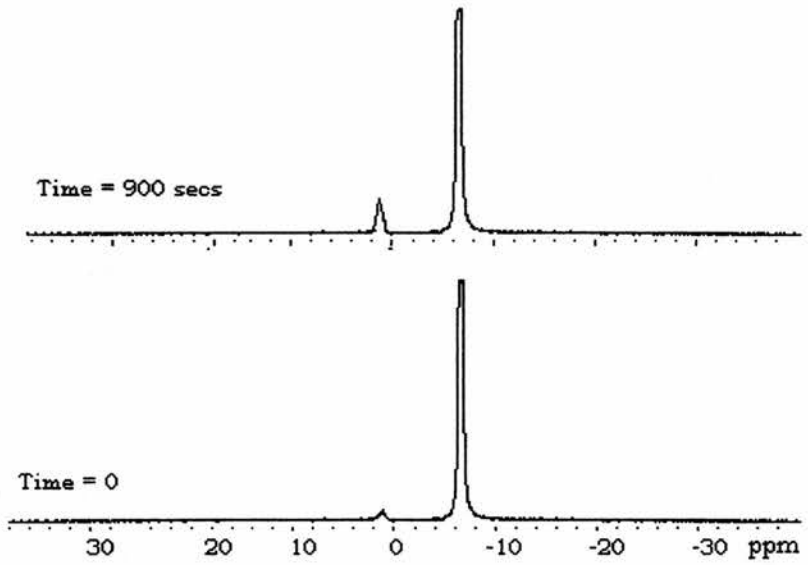

Figure 3.5 A 194.32 MHz ^{7}Li NMR spectrum showing the increase in the intensity of the intravesicular signal with time upon addition of 20 μl Ionophore 1. The signal separation is achieved using 15 μM $DyCl_3$.

The rate of passive diffusion into and out of the vesicles was measured by monitoring the changes in the intensity of the 'in' and 'out' signals over time when no ionophore was added, i.e. [I] = 0. In this situation it is assumed that the only way for ions to move across the membrane is by passive diffusion mechanisms, and that no ionophore-mediated transport occurs. Passive diffusion can be examined in this way until the vesicles begin to naturally decompose. The useable lifetime of vesicles prepared by dialytic detergent removal and in the presence of $DyCl_3$ / tripolyphosphate shift reagent is around 10-12 hours.

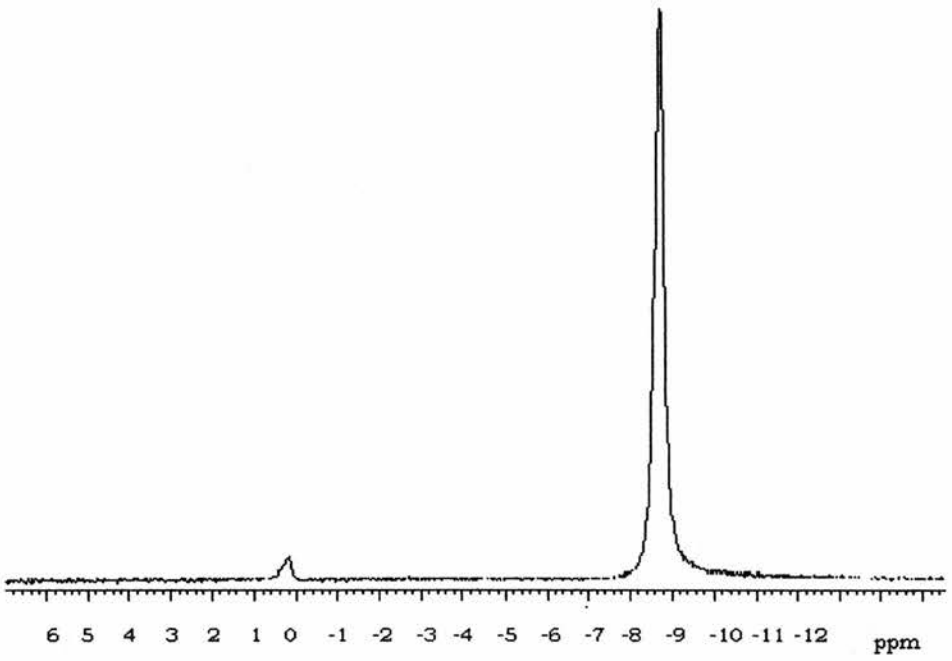

Figure 3.6 The 132.255 MHz ^{23}Na NMR spectrum of 1 cm^3 50 mM LiCl vesicles, 1 cm^3 10 mM Na_5PPP, and 10 μM $DyCl_3$ to generate the separation between intravesicular (left) and extravesicular (right) peaks

Each of the lithium / sodium exchange experiments began with lithium as the intravesicular ionic species. The addition of sodium tripolyphosphate sets up an equilibrium of lithium and sodium in both the intra and extravesicular environments. Thus it is possible to observe the NMR signal of ^7Li or ^{23}Na, as both are NMR active and have fairly high natural abundance.

The ionophores used in this study have been labelled lithium specific as they have previously been shown to favour lithium over

competing cations such as sodium or potassium. In the timecourse experiment, addition of a lithium specific ionophore into a vesicular medium as described above should result in an increase in the size of the intravesicular peak in the ^{7}Li NMR spectrum. In the ^{23}Na NMR spectrum, the addition of the same lithium specific ionophore invariably results in a decrease in the size of the intravesicular peak as sodium moves out in exchange for lithium moving in.

In each experiment, the concentrations of lithium and sodium and equal, i.e. concentrations are adjusted so that there should be one lithium ion present for every sodium ion. The following table shows the concentrations of lithium and sodium used in this transport studies:

[$^{7}Li+$] in mM as LiCl inside the vesicles	[$^{23}Na_5PPP$] in mM outside the vesicles	Average amount of [Dy^{3+}] to generate shift (mM)
50	10	4
100	20	5.5
150	30	7
200	40	8.5

Table 3.1 Relative concentrations of lithium and sodium in transport studies

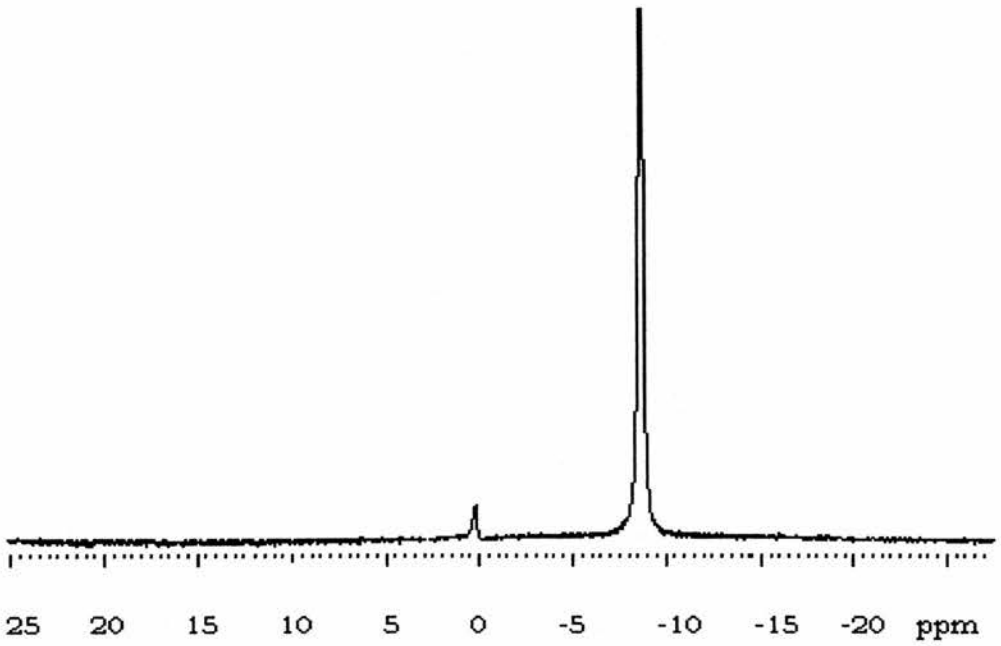

Figure 3.7 The 194.32 MHz ^{7}Li NMR spectrum of 1 cm^3 50 mM LiCl vesicles, 1 cm^3 10 mM Li_5PPP, and 8 μM $DyCl_3$ as shift reagent

The rates of ionophore-mediated transport are measured by adding carefully measured quantities of ionophore and following the reaction using the timecourse experiment. The exact concentration of ionophore can be varied to bring the rate of transport into a timescale that can be suitably studied using NMR. In the present case, using ionophore (1), 5, 10 and 20 μl amounts of a 15 mM solution (0.03573 g in 5 cm^3 methanol) were added to 1 cm^3 of X molar LiCl and 1 cm^3 of X/5 molar Na_5PPP, where X = 50, 100, 150, or 200. A few microliters of a 1 M solution of dysprosium chloride generates a 5-10 ppm shift

between 'in' and 'out' signals, which is sufficient to allow their individual measurement (See Table 3.1). All measurements were carried out at 298 K.

3.4 $Li^{+}_{(in)}$/ $Na^{+}_{(out)}$ Exchange Mediated by Ionophore 1

These studies involved **Ionophore 1** *(sodium (cyclopentadienyl) tris-(diethylphosphite) cobaltate),* obtained as a gift from Dr D. T. Richens (St. Andrews). The exchange of $^{7}lithium_{(in)}$ for (a) $^{23}sodium_{(out)}$, and (b) $^{6}lithium_{(out)}$ was followed using dynamic one-dimensional ^{23}Na and ^{7}Li NMR. The results are split into three sections.

^{23}Na / ^{7}Li exchange monitored by ^{23}Na NMR

^{23}Na / ^{7}Li exchange monitored by ^{7}Li NMR

^{6}Li / ^{7}Li exchange monitored by ^{7}Li NMR

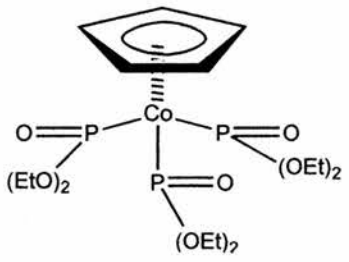

Figure 3.8 Ionophore (1) (sodium (cyclopentadienyl) tris-(diethylphosphite) cobaltate).

3.4.1 $^{7}Li_{(in)}$ /$^{23}Na^{+}_{(out)}$ Exchange Observed With ^{23}Na NMR Spectroscopy

The results of ^{23}Na NMR exchange experiments carried out at the four Li^{+} concentrations appear to show first-order kinetics in the concentration of ionophore. An immediate indication of this comes from the linear relationship between the change in signal intensity with time (see Figure 3.9). This suggests that the exchange occurs in 1:1 ratios for $lithium_{(in)}$: $sodium_{(out)}$, and implies that one ionophore molecule transports one ion in a single direction at a time.

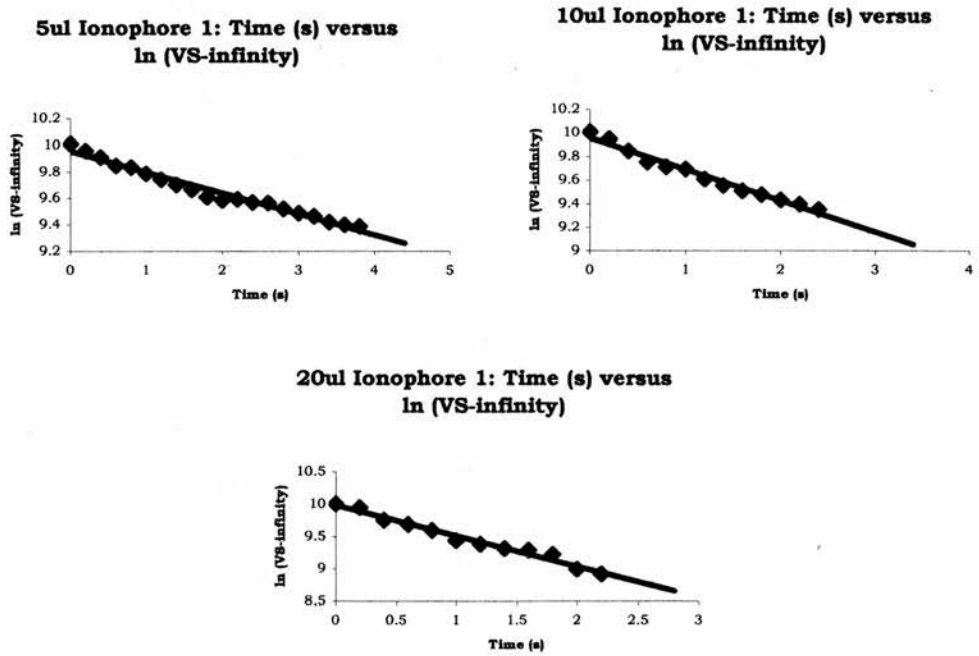

Figure 3.9 Plots of time versus ln(change in signal intensity-infinity) for Ionophore 1 mediated Li/Na exchange in 50 mM [LiCl] vesicles.

The slope of the plots of k versus [I]/[PC] for each metal ion concentration yielded k' values. These results are summarised in Table 3.2 below.

[LiCl] mM	[Na_5PPP] mM	Ionophore amount (μl)	[I]/[PC] ratios	k x 10^{-2} sec^{-1}	k' moles I, moles $lipid^{-1}$ sec^{-1}
50	10	5	0.00109	0.157	0.961
		10	0.00219	0.267	
		20	0.00438	0.474	
100	20	5	0.00113	0.089	0.762
		10	0.00226	0.155	
		20	0.00452	0.341	
150	30	5	0.00112	0.092	0.56
		10	0.00223	0.139	
		20	0.00446	0.276	
200	40	5	0.00116	0.085	0.464
		10	0.00232	0.147	
		20	0.00464	0.248	

Table 3.2 Results of Ionophore 1 mediated transport of lithium across EPC vesicle membranes, monitored using ^{23}Na NMR spectroscopy.

The plots of time versus ln(change in signal intensity-infinity) for Ionophore 1 mediated Li^+/Na^+ exchange observing ^{23}Na NMR at 100, 150 and 200 mM [LiCl] can be found in Appendix I.

Plotting k' against [M^+] should give a curve (Figure 3.10), whilst the plot of 1/k' versus [M^+] gives a straight line (Figure 3.11). In this plot the intercept is equal to $(k'_f)^{-1}$, and the slope is equal to $(k'_d)^{-1}$. This gives k'_f = 1.61 s^{-1}, and k'_d = 0.13 $M.s^{-1}$. The stability constant of the ionophore / ion complex in the membrane is given by K_s which is equal to k'_f / k'_d and in this case is equal to 12.1 M^{-1}.

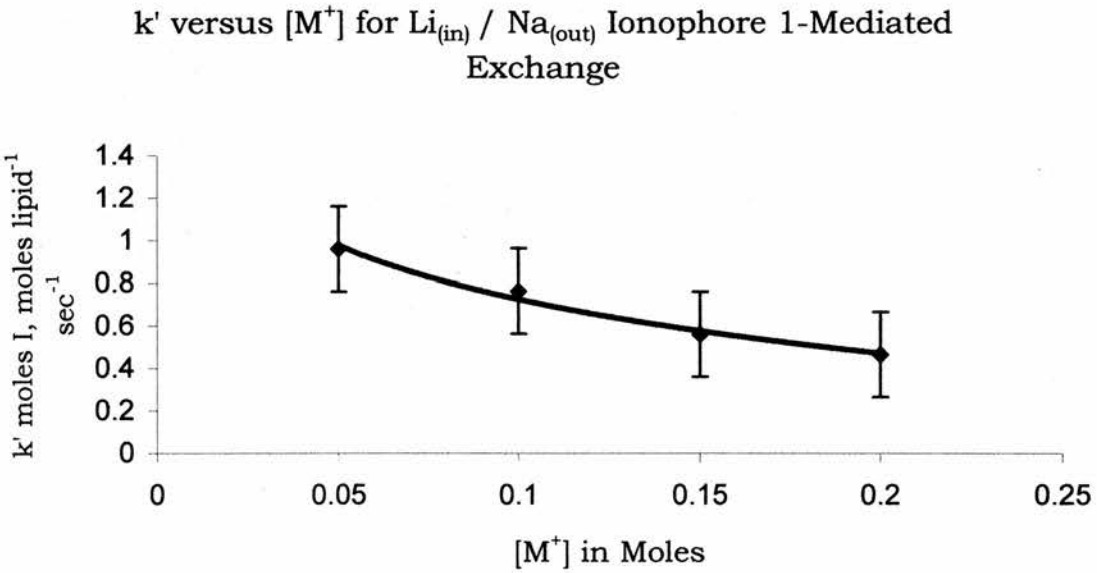

Figure 3.10 Plot of k' versus [M^+] for lithium / sodium exchange mediated by Ionophore 1 and observed using ^{23}Na NMR.

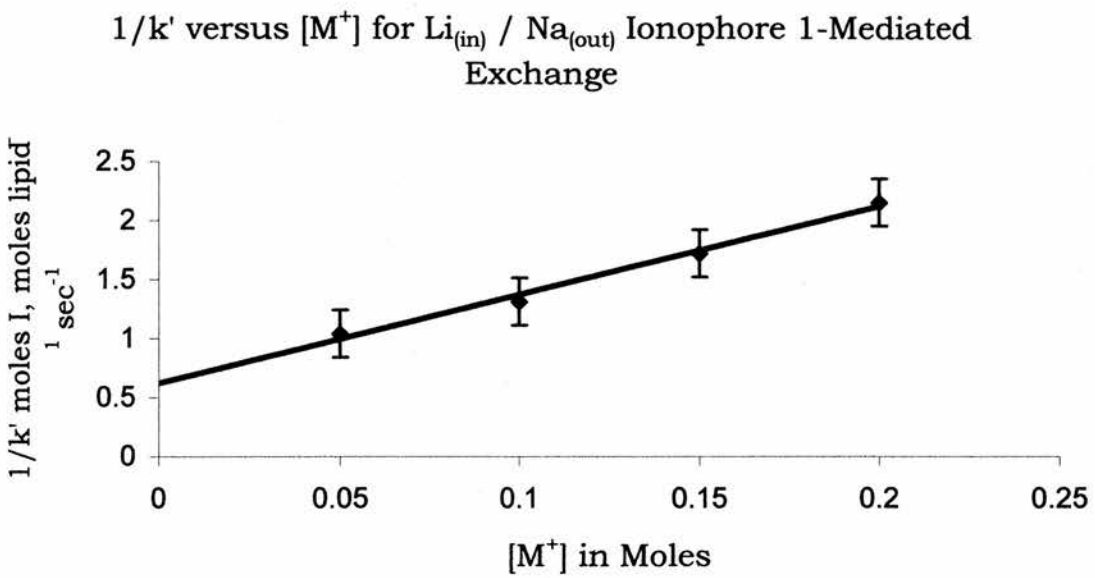

Figure 3.11 Plot of 1/k' versus [M+] for lithium / sodium exchange mediated by Ionophore 1 from which the formation, dissociation and stability constants are calculated.

3.4.2 $^{7}Li_{(in)}$ /$^{23}Na^{+}_{(out)}$ Exchange Observed With ^{7}Li NMR Spectroscopy

These experiments were carried out in an identical manner to the previous set, as described in Chapter 3.3.1. The only difference is that the experiment is followed using ^{7}Li NMR instead of ^{23}Na NMR. The results of the ^{7}Li NMR transport experiments with Ionophore 1 as shown in Table 3.3 below carried out at the four Li^{+} concentrations also appear to show first-order kinetics in the concentration of

ionophore, as with the ^{23}Na experiments. The plots of time versus ln(change in signal intensity-infinity) for Ionophore 1 mediated Li^+/Na^+ exchange observing ^7Li NMR at 50, 100, 150 and 200 mM [LiCl] can be found in Appendix II.

[LiCl] mM	[Na_5PPP] mM	Ionophore added (μl)	[I] / [PC] ratios	k x 10^{-2} sec^{-1}	k' moles I, moles $lipid^{-1}$ sec^{-1}
50	10	5	0.00117	0.109	1.113
		10	0.00234	0.230	
		20	0.00468	0.498	
100	20	5	0.00112	0.188	1.009
		10	0.00223	0.315	
		20	0.00446	0.528	
150	30	5	0.00114	0.26	0.705
		10	0.00228	0.336	
		20	0.00457	0.501	
200	40	5	0.00116	0.266	0.605
		10	0.00231	0.335	
		20	0.00463	0.476	

Table 3.3 – The results of Ionophore 1 mediated transport of lithium across EPC vesicle membranes, monitored using ^7Li NMR spectroscopy.

The graphs of k' versus [M+] and 1/k' versus [M+] can be found below in Figures 3.12 and 3.13. At constant [M+], doubling the ionophore concentration should result in a doubling in the rate of transport (or a halving of the time taken to transport *X* ions), i.e. there is a linear relationship. Again, this strongly suggests a 1:1 ligand-to-metal complex is active during the transport process.

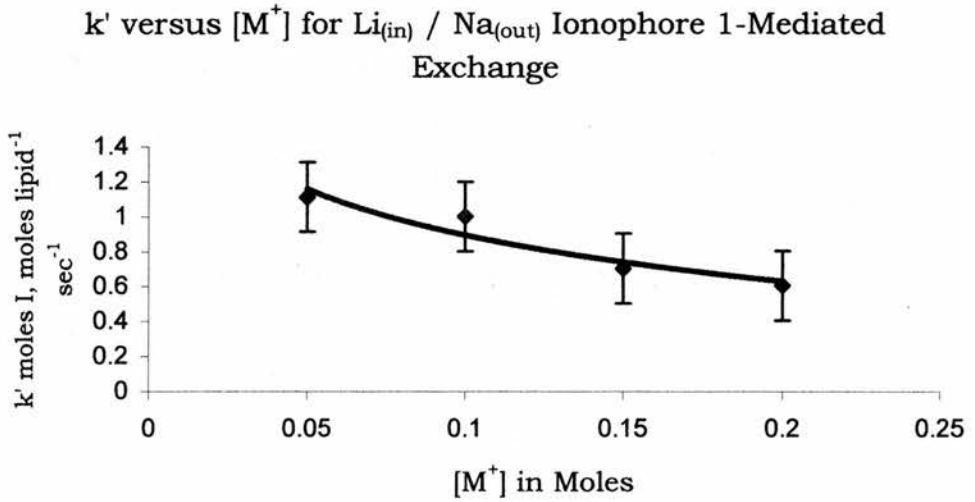

Figure 3.12 Plot of k' (moles I, moles lipid^{-1} sec^{-1}) versus [M+] for lithium / sodium exchange mediated by Ionophore 1 and observed with ^{7}-Li NMR.

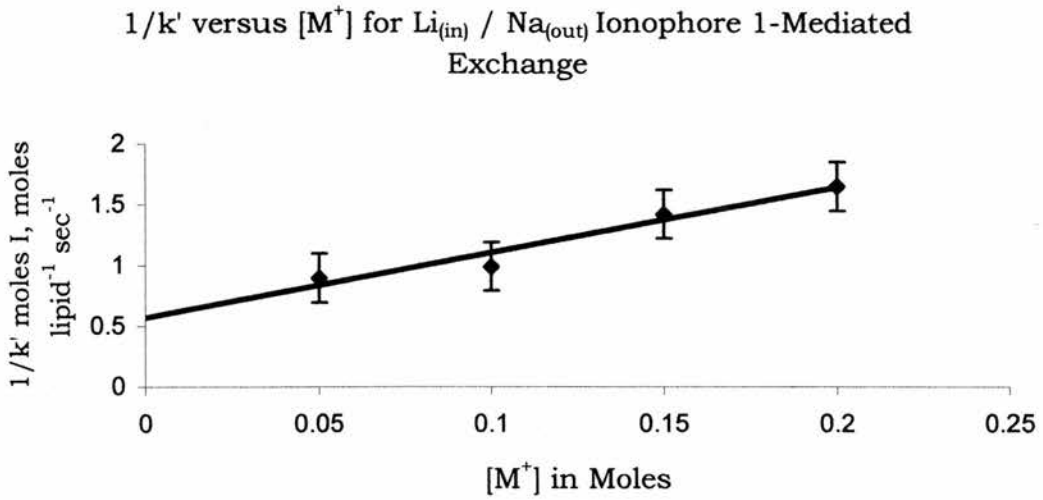

Figure 3.13 Plot of 1/k' (moles I, moles lipid^{-1}, sec^{-1}) for lithium / sodium exchange mediated by Ionophore 1 (observed with ^{7}-Li NMR) from which the formation, dissociation, and stability constants are calculated – see text for values.

Important conclusions regarding the transport mechanisms can be deduced from the observed kinetics. In all cases the exchange rate is directly proportional to the amount of ionophore added (See Appendix II). This implies that one ionophore molecule transports a single metal ion at a time in the rate-determining step. The transport is therefore probably unimolecular. Given that this ionophore is said to prefer lithium it is likely that the rate-determining step is the transport of sodium into the vesicle and that one ionophore carries one sodium cation at a time.

The rate variation with $[M^+]$ shows that as $[M^+]$ increases, the transport rate decreases. This is consistent with a model in which the ionophore is working at a set rate (c.f. an enzyme) and so takes twice as long to deal with a doubled metal ion concentration, seemingly halving the transport rate. A similar inverse dependence has been observed before in studies of naturally occurring ionophores such as monensin (See Figure 1.7).

Given this model the intercept in Figure 3.13 is $k'_f{}^{-1}$ and the slope is $k'_d{}^{-1}$. This allows evaluation of k'_f as 1.75 s^{-1}, and of k'_d as 0.19 M s^{-1}. The stability constant of the complex in the membrane surface (K_s) is given by k'_f / k'_d, and is 9.2 M^{-1}.

It is interesting to compare these values with those obtained for the ionophoric antibiotics e.g. monensin. The found value of K_s is around the typical values found for the ionophoric antibiotics, which typically range from around 2–100 M^{-1}. Rate constants for monensin mediated lithium transport in EPC vesicles[12] give k'_f = 1031 ± 145 s^{-1}, k'_d = 56 ± 5 $M.s^{-1}$, and K_s = 18.5 ± 3.4 M^{-1}.

The value of k'_f is around 0.02% of the value obtained for monensin, and the value for k'_d is 0.04% of the value in monensin. These much lower formation and dissociation constants rather than a lower stability are, therefore, responsible for the much slower transport

exhibited by this material. The value of K_s for monensin is around twice that of the value obtained for Ionophore 1, and can be accounted for through the differences in structures between Ionophore 1 and the larger and more flexible polyether antibiotic ionophores such as monensin. The carboxylic ionophores can usually supply more than 2 or 3 oxygen atoms for cation binding. The combination of greater molecular size and more co-ordinating oxygens allows (a) the charge present on the cation to be further stabilized, and (b) faster diffusion rates because of increased lipid solubility.

3.4.3 $^{7}Li_{(in)}$ / $^{6}Li_{(out)}$ Ionophore Mediated Exchange Observed with ^{7}Li NMR Spectroscopy

This set of experiments were mostly the same as the sodium / lithium exchange experiments, except the extravesicular ^{23}Na cation had been replaced by the isotope ^{6}Li, which was included in the extravesicular medium as $^{6}Li_5PPP$, the ^{6}Li analogue of sodium tripolyphosphate. As with the previous experiments, the concentration of ^{6}Li was adjusted to match the intra- and extravesicular ^{7}Li concentrations. As ^{6}Li moved into the vesicle there was a reduction in the signal intensity of the ^{7}Li 'in' peak, corresponding to ^{7}Li taken out of the vesicle in exchange for ^{6}Li going in.

This experiment should give k_f and k_d for lithium. The results show a greater k_f and k_d for lithium transport than in the previous set, adding to the evidence that sodium transport is the rate determining step in these experiments.

This explains why the stability constant for the complex in the membrane is higher than those obtained in Chapter 3.4.1 and 3.4.2. Using the data below, a plot of $1/k'$ versus $[M^+]$ gives a straight line with an intercept equal to 0.305 ($k'_f{}^{-1}$) and a slope of 4.7 ($k'_d{}^{-1}$). This gives k'_d of 0.22 M s^{-1}, and $k'_f = 3.28$. The ratio of k'_f / k'_d gives K_s, the stability constant, which comes out as 15.4 M^{-1}.

The significance of these experiments is that the exchange occurs between isotopes of lithium rather than different alkali metals. Since there is no significant ionic radius difference between ^6Li and ^7Li, this experiment allows the measurement of lithium transport rates in a non-competitive environment, i.e. with no other alkali metal cations present. This experiment can be followed using ^6Li or ^7Li NMR, but ^7Li NMR was used in this instance due to its having a much greater natural abundance.

We can conclude for this ionophore that the transporting species is a 1:1 complex, that lithium transport is faster than sodium transport and that lithium forms a more stable complex than sodium. The

stability constant in this case is much greater than it was when sodium was present as an exchanging species

The plots of time versus ln(change in signal intensity-infinity) for Ionophore 1 mediated $^{7}Li^{+}_{(in)}/^{6}Li^{+}_{(out)}$ exchange observing ^{7}Li NMR at 50, 100 and 150 mM [LiCl] can be found in Appendix III.

[$Li^{7}Cl$] mM	[$Li^{6}_{5}PPP$] mM	Ionophore added (µl)	[I] / [PC] ratio	k x 10^{-2} sec^{-1}	k' moles I, moles $lipid^{-1}$ sec^{-1}
50	10	5	0.00109	0.106	1.96
		10	0.00219	0.331	
		20	0.00438	0.753	
100	20	5	0.00113	0.189	1.22
		10	0.00226	0.404	
		20	0.00452	0.615	
150	30	5	0.00112	0.196	1.01
		10	0.00224	0.399	
		20	0.00448	0.555	

Table 3.4 – The results of Ionophore 1 mediated $^{7}Li_{(in)}$ / $^{6}Li_{(out)}$ exchange across EPC vesicle membranes, monitored using ^{7}Li NMR spectroscopy.

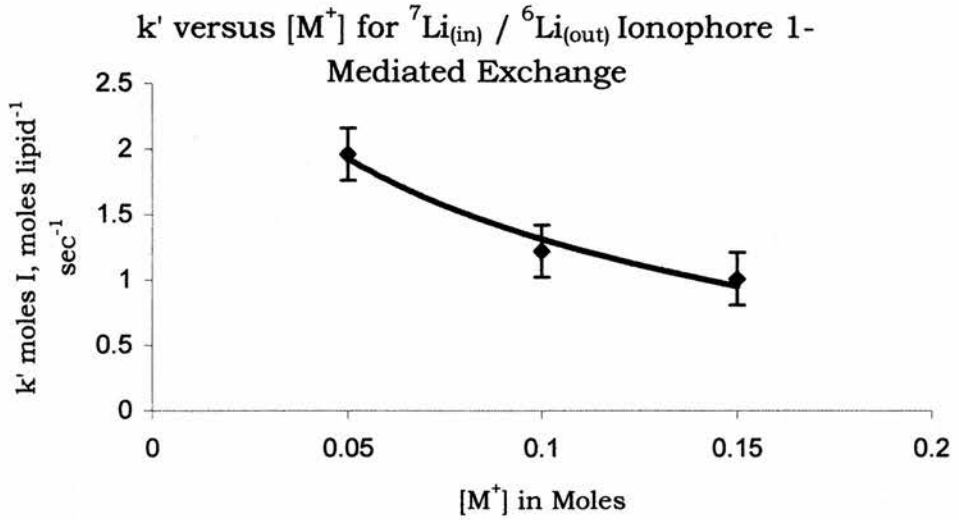

Figure 3.14 Plot of k' (*moles I, moles lipid^{-1} sec^{-1}* versus [M+] (*moles*)

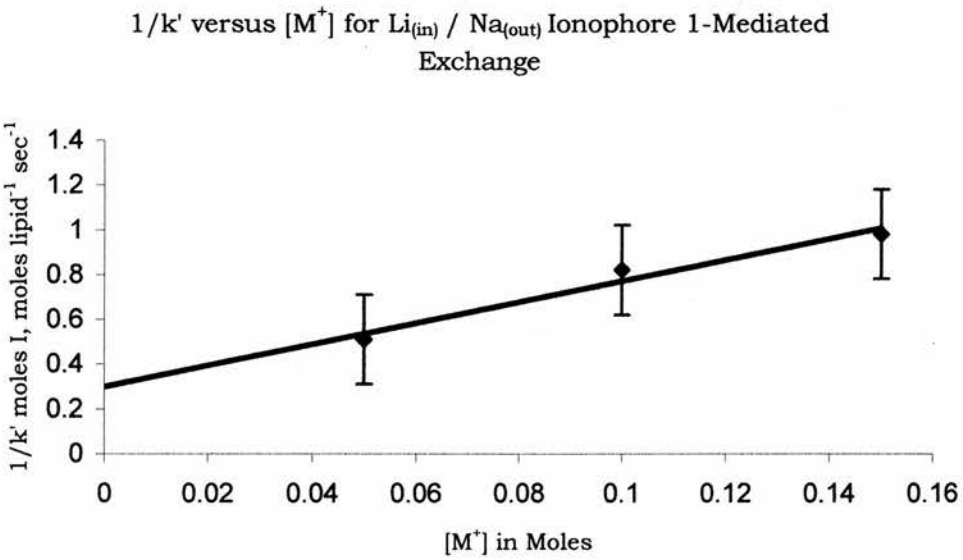

Figure 3.15 Plot of 1/k' (*moles I, moles lipid^{-1} sec^{-1}* versus [M+] (*moles*)

3.5 $Li^{+}_{(in)}$/ $Na^{+}_{(out)}$ Exchange Mediated by Ionophore 2

Ionophore 2, (*cis–N, N, N', N'-tetraisobutyl (dicarboxamide) cyclohexane*), shown in Figure 3.16 below, was synthesised according to the method given by Erne and Amman[5], described in Section 3.6.3. The relative transport rates were measured experimentally using the timecourse experiment in the manner previously described for Ionophore 1.

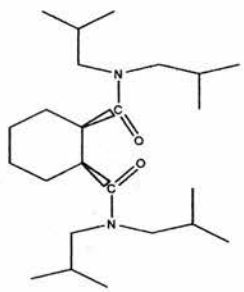

Figure 3.16 Ionophore 2 (cis –N, N, N', N'- tetraisobutyl (dicarboxamide) cyclohexane)

Initial studies[6] with this ionophore led to a proposed 2:1 ligand to metal ratio for the major active species in the transport process, with a 1:1 ratio only at very low salt and ionophore concentrations. These findings were called into question after later unpublished studies[7] with this compound, and it was felt that a more detailed study was required to conclusively define the transport ratios. For this reason,

the transport properties of ionophore 2 were examined through [M^+] from 50 to 200 mM observing ^7Li.

The synthesis of Ionophore 2 began with the ring opening of 1,2-cyclohexane dicarboxylic anhydride upon addition of diisobutylamine to give (1) in the reaction scheme below. This material was then reacted with dicyclohexylcarbodiimide and *p*-nitrophenol to give the monoester (2). The reflux of (2) with diisobutylamine and subsequent purification by chromatography and microdistillation gave the product (3).

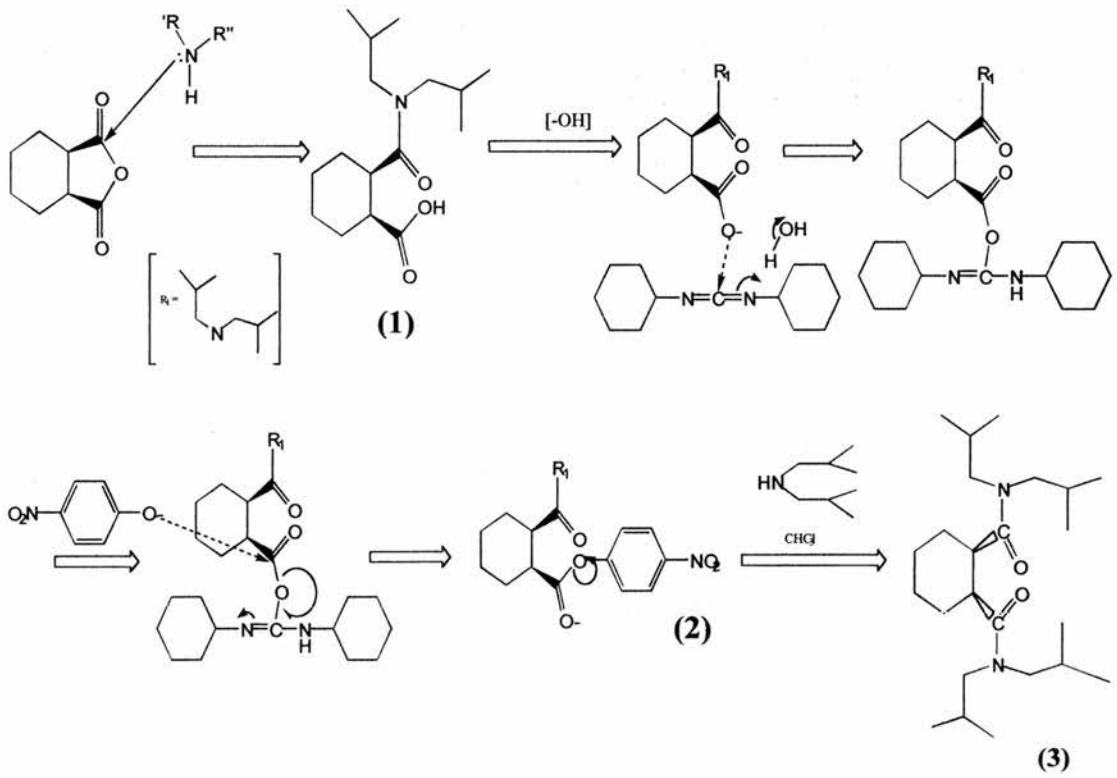

Figure 3.17 Reaction mechanism for the synthesis of *cis-N,N,N',N'*-tetraisobutylcyclohexane-1,2-dicarboxamide.

The absence of a linear relationship in the initial plot of $ln[M^+]_{int}$ *versus time (s)* is an indication that Ionophore 2 does not transport lithium by a 1:1 mechanism. This was confirmed in the plot of $1/ln[M^+]_{int}$ *versus time (s)* which could be fitted to a straight line. This is clearly different to the equivalent plots for Ionophore 1, in which a linear relationship between ionophore concentration and change in signal intensity was established.

The procedure used to analyse the non-first order kinetics[10] of Ionophore 2 mediated transport was described in Section 3.2. In this instance it is not possible to derive the formation, dissociation, and stability constants. The order of the kinetics is found from initial rate measurements using the tangents to the plots of $[M^+]_{int}$ at time=0. Data is collected at various concentrations of ionophore, and the slope of the plot of *ln (tangent) versus ln ([I]/[PC])* gives the order of the kinetics.

3.5.1 $^{7}Li_{(in)}$ /$^{23}Na^{+}_{(out)}$ Exchange Observed with ^{23}Na and ^{7}Li NMR Spectroscopy

The rates for Ionophore 2 mediated $^{7}Li_{(in)}/^{23}Na_{(out)}$ exchange were measured at 100 mM LiCl using ^{23}Na NMR, and at 150 mM and 200 mM LiCl using ^{7}Li NMR.

[LiCl] mM	[Na_5PPP] mM	Ionophore added (µl)	[I] / [PC] ratio	Tangent	Reaction / Kinetic Order (m)
100	20	20	0.00921	0.1429	3.1
		40	0.01843	0.1971	
		80	0.03685	0.2143	
150	30	20	0.00889	0.151	2.9
		50	0.01778	0.1687	
		75	0.02667	0.2125	
200	40	20	0.00901	0.1375	2.9
		40	0.01803	0.175	
		50	0.02704	0.201	

Table 3.5 – The results of Ionophore 2 mediated $^{7}Li_{(in)}$ / $^{23}Na_{(out)}$ exchange across EPC vesicle membranes, monitored using ^{7}Li and ^{23}Na NMR spectroscopy.

The following graphs are for 100 mM $lithium_{(in)}/sodium_{(out)}$ exchange using ^{23}Na spectroscopy. Graphs A-C show the reduction in

the size of the sodium$_{(in)}$ peak with time, as Na^+ moves out of the vesicles in exchange for Li^+ coming in. Graph D is a plot of ln([I]/[PC]) versus ln(tangent). The tangents are obtained from points 1 and 2 in graphs A and B, and from points 2 and 3 in graph C. As can be seen in Graph C, there is a lay-time during which there is no change in the intensity of the in peak. This is assumed to be due to poor dispersal of the ionophore throughout the vesicular medium. The graphs for 150 and 200 mM lithium$_{(in)}$/sodium$_{(out)}$ exchange using ^7Li NMR appear in Appendix IV. In these sets of graphs, there is an increase in the size of the lithium$_{(in)}$ peak as Li^+ is brought into the vesicles in exchange for Na^+ moving out.

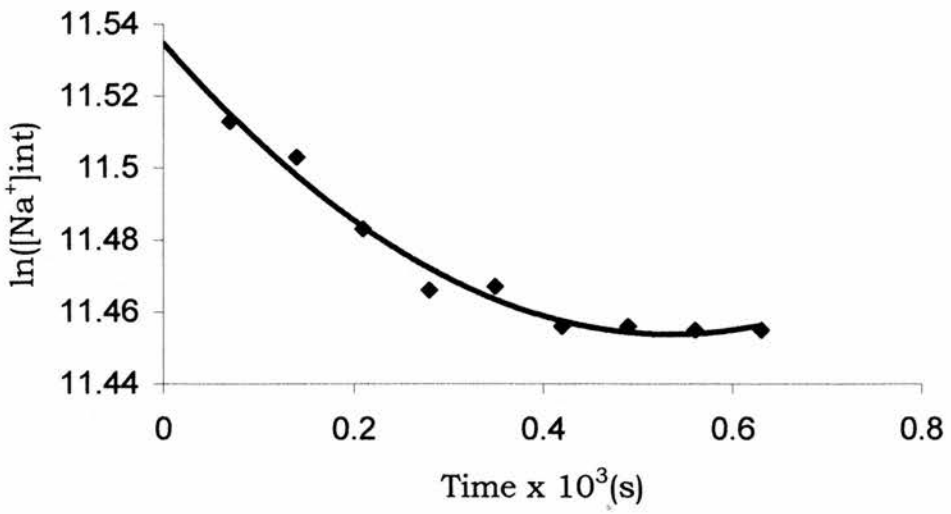

A

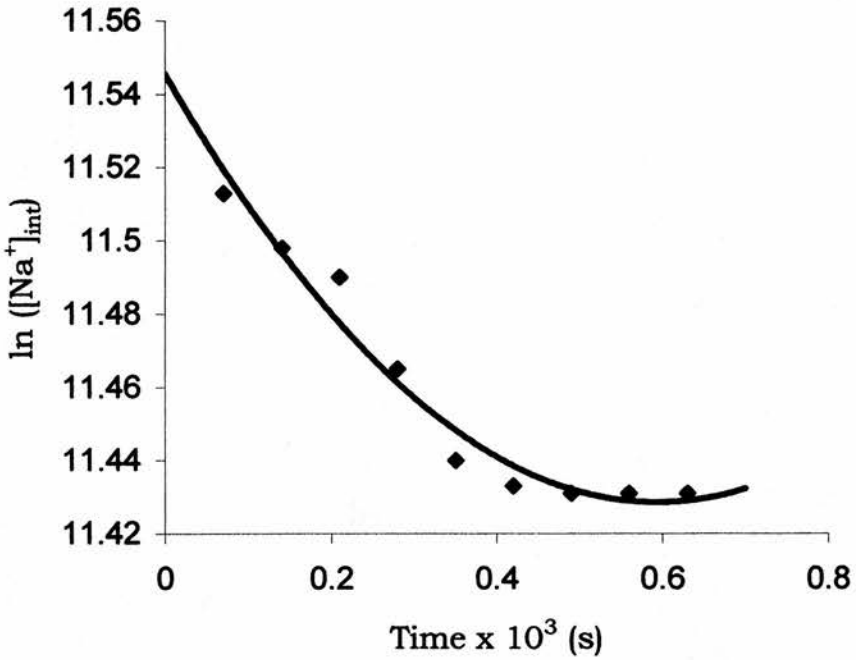
11.56
11.54
11.52
11.5
11.48
11.46
11.44
11.42
ln ([Na+]int)
0
0.2
0.4
0.6
0.8
Time x 10^3 (s)

B

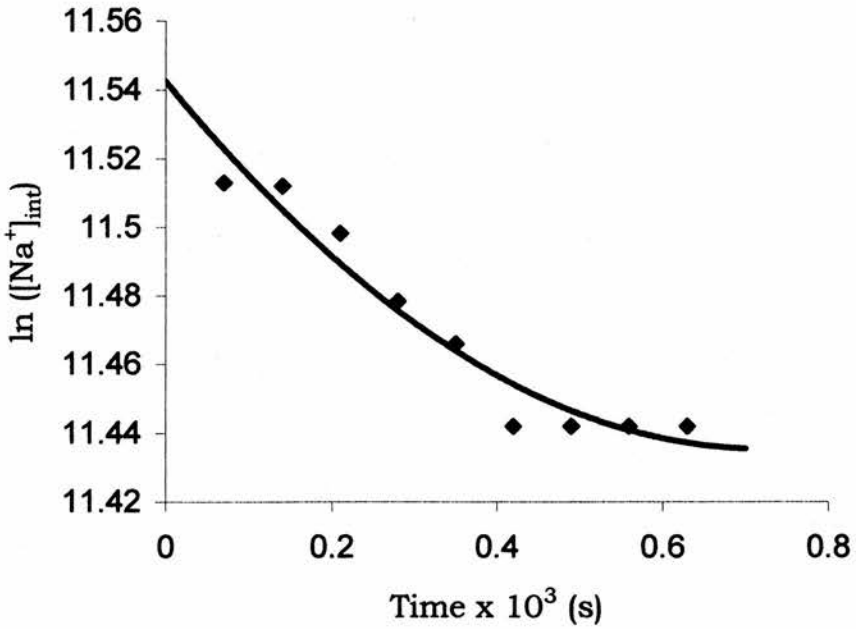
11.56
11.54
11.52
11.5
11.48
11.46
11.44
11.42
ln ([Na+]int)
0
0.2
0.4
0.6
0.8
Time x 10^3 (s)

C

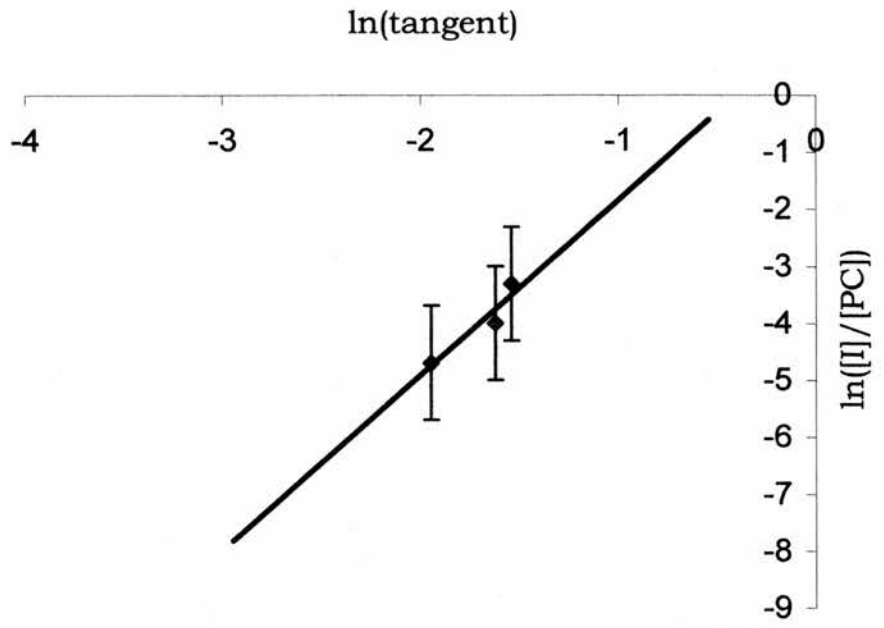

D

Figure 3.18 (A-C) Plots of $ln[Na^+]_{int}$ versus time x 10^{-3} (s) for Ionophore 2 mediated exchange of 100 mM $lithium_{(in)}$ for $sodium_{(out)}$, from which the tangents are obtained; (A) 20 μl Ionophore 2; (B) 40 μl Ionophore 2; (C) 80 μl Ionophore 2; (D) Plot ln(tangent) versus ln([I]/[PC]) for Ionophore 2 mediated exchange of 100 mM $lithium_{(in)}$ for $sodium_{(out)}$. The slope of the graph is equal to the order of the kinetic, and is 3.1.

Therefore, the kinetic order for the transport process at 100 mM LiCl is 3.1 with respect to ionophore concentration. Using the same process (see Appendix IV for graphs), the kinetic order at 150 mM LiCl was found to be 2.9, and at 200 mM the kinetic order was also 2.9. These results appear to indicate that the transport process is second

or third order. This means that two or three ionophore molecules may be involved in the transport of a single alkali metal cation.

Although sodium can have a co-ordination number of 6 in solution, lithium normally has a co-ordination number of 4 (or less) in solution. This would correspond to the situation in which two ionophore molecules transport a single lithium cation, depicted in Figure 3.19 below. Since the rate determining (slowest) step here is likely to be Na^+ transport, and because sodium is expected to be six co-ordinate, the third kinetic order obtained through transport studies fits with three Ionophore 2 molecules transporting a single sodium cation.

The bulkiness of the isobutyl and cyclohexane groups will ultimately limit the number of ionophore molecules that can co-ordinate around a single alkali metal cation. There is a 28% increase in ionic radius on going from lithium to sodium, providing a larger volume for the ionophore molecules to arrange themselves around.

Two ionophore molecules may adopt a tetrahedral arrangement around a lithium cation. Three ionophore molecules would presumably adopt an octahedral arrangement around the larger sodium cation.

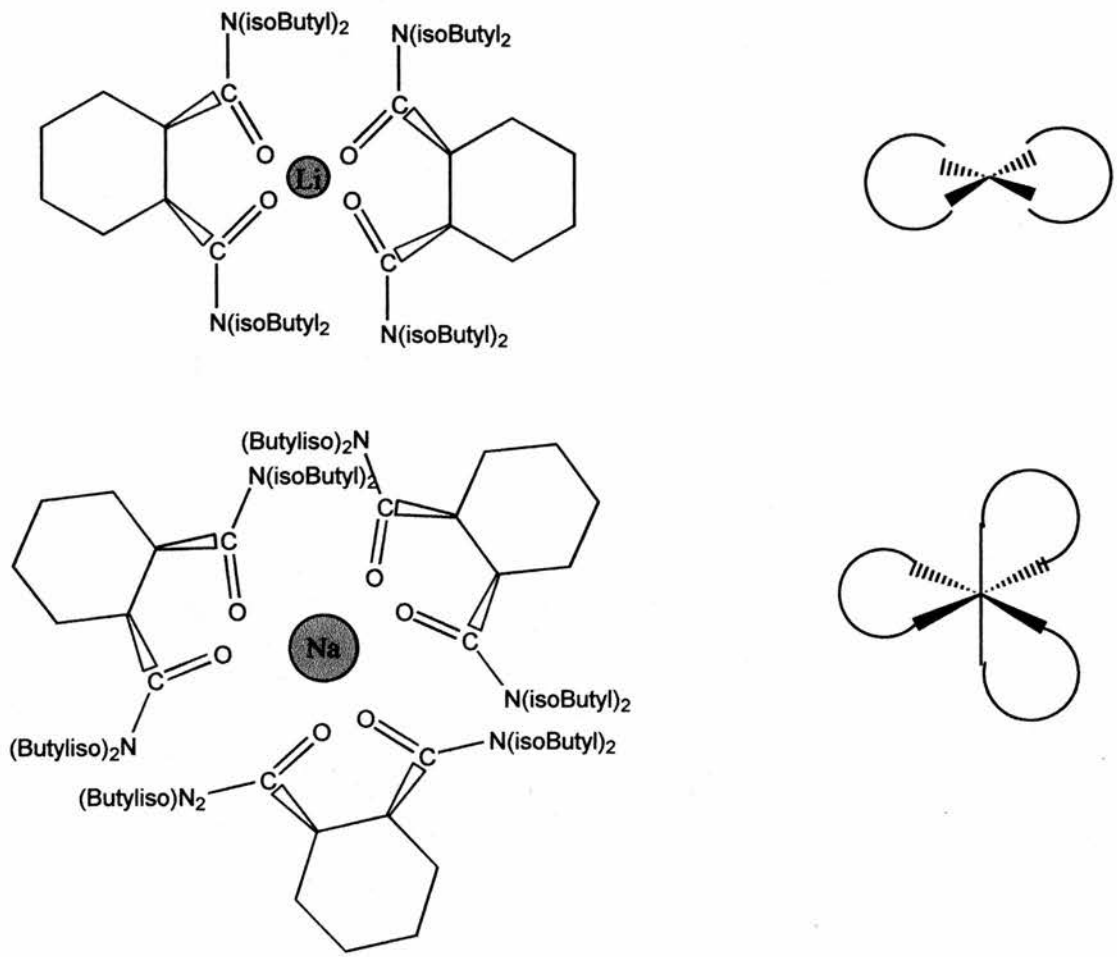

Figure 3.19 Hypothetical structures for the lithium and sodium complexes formed with Ionophore 2. Above - two ionophore molecules surround a single lithium cation in a tetrahedral arrangement. Below – three ionophore molecules surround a sodium cation in an octahedral arrangement.

The larger ionophoric antibiotics such as monensin and nigericin co-ordinate to cations using 5 or 6 oxygen atoms, although both prefer to bind to sodium rather than lithium, presumably because the

greater ionic radius of sodium allows a stronger interaction with the surrounding oxygens.

3.6 Experimental

3.6.1 Preparation of Large Unilamellar Phosphatidylcholine Vesicles Using the Dialytic detergent Removal Technique

This preparation is a modification of the dialytic detergent removal technique described by Reynolds et al[13]. The removal of detergent from mixed micelles of egg yolk phosphatidylcholine and n-octyl glucopyranoside leads to formation of large unilammelar phospholipid vesicles with a diameter of between 200 and 400 nm.

Egg yolk phosphatidylcholine (EPC, 516 μl, Lipid Products) was weighed into a clean round bottomed flask. The solvent was removed at the pump over three hours to give around 40 mg of dry EPC. An amount of n-octylglucopyranoside (260 mg, Sigma and Aldrich) was dissolved in 3 cm^3 of standard LiCl solution (100 mM). This solution was added slowly and with care to avoid introducing oxygen to the EPC solution. The mixture was stirred until the lipid had completely dissolved, then transferred quantitatively into a pre-soaked length of dialysis tubing and sealed. 2 – 2.5 L of 100 mM LiCl solution was preheated to 40°C in a thermostatically controlled dialysis vessel and

flushed with oxygen-free nitrogen for 12 hours. The dialysis tubing was attached inside the dialysis vessel at the end of this period. The solution in the dialysis vessel was changed every 12 hours for a total of 36 hours with more preheated and degassed 100 mM LiCl, and the dialysis tubing containing the EPC solution was inverted at least twice daily to ensure even mixing of the vesicles, otherwise they tended to settle slowly inside the dialysis tube.

Vesicles prepared in this manner generally require 2 full days to completely form. At the end of this period, large unilamelar vesicles will have formed, with the same concentration of lithium inside the vesicle as that in the external medium. Vesicles prepared using n-octylglucopyranoside have a diameter around ten times greater than vesicles prepared by sonication or from cholate-lipid mixed micelles. The sizes of the vesicles produced by the dialytic detergent removal technique are in the range 200 – 600 nm in diameter, averaging 400 nm.[14] Relative vesicle volumes were measured before the NMR experiment by comparing the integrated areas of the internal and external peaks.

It is important to maintain the same procedure for vesicle preparation otherwise there may be changes in the nature of the vesicles that form. For example the medium of the dialysis vessel

must be changed at regular intervals with a preheated solution of identical concentration, otherwise the size of the vesicles may not remain constant. In the present study, the size of the vesicles was 10-15% of the internal volume. The absolute sizes of the vesicles were measured from electron microscope images of freeze-fractured vesicles in previous studies.[14]

3.6.2 Preparation of Lithium Tripolyphosphate ($^6Li_5PPP$)

In the lithium / lithium exchange experiments, ^7Li is the intravesicular species and ^6Li is found in the extravesicular medium (in the form of $^6Li_5PPP$). Lithium tripolyphosphate was prepared from sodium tripolyphosphate by running the latter through an ion-exchange column charged in the H^+ form, then titrating the protonated tripolyphosphoric acid with ^6LiOH. The procedure is summarised below.

A cation exchange column is charged in the H^+ form by passing concentrated HCl through the column at a slow rate (e.g. 1-2 hours) until the pH of the effluent is between 1 and 2. The column is then flushed with distilled water until the pH at bottom of column has returned to between 5 and 6. In a separate beaker, 10 cm^3 40 mM ^6LiOH was measured out. The water in the column was drained to the top of the resin and a slurry of 0.75 g Na_5PPP dissolved in around

10 cm^3 water was added to the top of the column and ran down to the top of the resin. More (20-40 cm^3) distilled water was added, and run through the column until striations from the H_5PPP (tripolyphosphoric acid) appear at the bottom of the column. The H_5PPP is collected dropwise monitoring pH directly into beaker containing ^6LiOH. The addition of the acid stopped at pH 8.0. If the pH went below 8.0, small amounts of ^6LiOH were added. Water was removed by rotary evaporation and the 'dry' $^6Li_5PPP$ was collected. The ^6LiPPP was dissolved in distilled water as required.

3.6.3 Synthesis of cis-N,N,N',N'-tetraisobutylcyclohexane-1,2-dicarboxamide (Ionophore 2)

The following synthesis for Ionophore 2 was described in 1982 by Erne and Amman[5]:

Diisobutylamine (4.19 g, 5.66 cm^3, 0.0324 moles), 1,2-cyclohexane dicarboxylic anhydride (5 g, 0.0324 moles) and toluene (25 cm^3) were mixed and left overnight in a 100 cm^3 round bottomed flask. The solvent was removed at the pump, the remaining material was dissolved in diethyl ether, and the separated organic phase was washed with water. This solution was dried over magnesium sulphate, filtered, and the ether removed under vacuum.

Dicyclohexylcarbodiimide (6.68 g, 0.0324 moles) dissolved in ethyl acetate was added to a solution containing the material from above and p-nitrophenol (4.51 g, 0.0324 moles), also in ethyl acetate. This mixture was left to stir overnight, then filtered and concentrated under vacuum. After identification of the monoester, it was refluxed with diisobutylamine (11.32 g, 0.0648 moles) and chloroform overnight. The chloroform was later removed under vacuum, and a purification procedure using flash chromatography (3:7, ethyl acetate: hexane) with very fine grade silica. Microdistillation gave a fraction at occurred at 0.55 mm Hg, 150°C, leaving a dark amber coloured liquid.

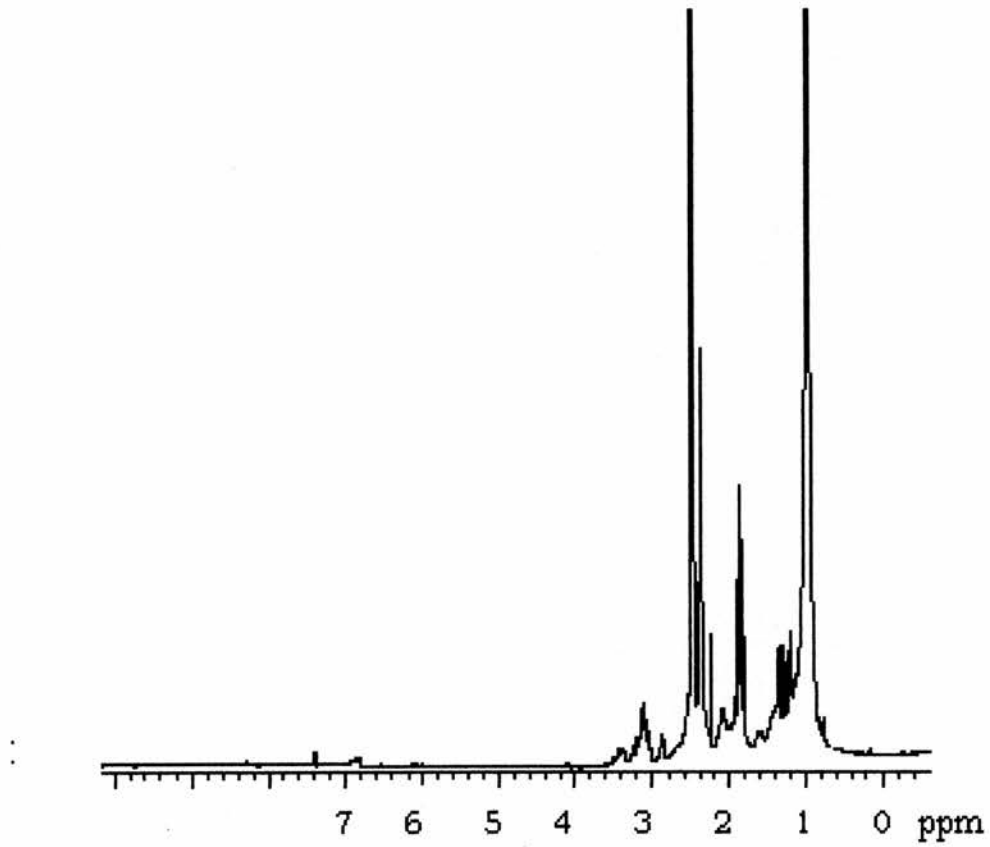

Figure 3.20 The 500 MHz ^{1}H NMR spectrum of *cis-N,N,N',N'*-tetraisobutylcyclohexane-1,2-dicarboxamide.

The formation of the product was confirmed by mass spectrometry. The peaks present in the mass spectrum and the ^{1}H NMR spectrum matched those quoted in the original synthetic paper by Erne and Amman.[5] ^{1}H NMR ($CDCl_3$): 0.87 (*d*, 24 H, 8 CH_3); 1-2.5 (br., 14 H, 4-ring-CH_2, 2-ring-CH, 4-CH); 2.5-3.4 (br., 8 H, 4 N-CH_2). M.S.: 394 (1,

M^+), 338 (1), 282 (1), 266 (100), 238 (6), 210 (13), 166 (4), 154 (6), 128 (11), 81 (6), 57 (18), 41 (8)

3.6.4 Sample Preparation

Sodium tri-polyphosphate solution (20 mM, 100 cm^3) was prepared with deionised water. A solution of Ionophore 1(15 mM, 0.03573 g, in 5 cm^3 HPLC-grade MeOH) and Ionophore 2(10 mM, 0.0175 g in 5 cm^3 HPLC-grade MeOH) were prepared. EPC-prepared LUV suspension (1 cm^3) and sodium tri-polyphosphate solution (1 cm^3) were added into a new top-grade 10 mm o.d. NMR tube (Wilmad) fitted with a coaxial insert containing D_2O. An amount of dysprosium chloride (1 M, 5-20 μl) was added to the NMR tube to produce a chemical shift difference between the intravesicular and extravesicular signals. The sample is now ready for NMR experiments to begin.

3.6.5 NMR Experimental and Analysis Procedure

The data for Ionophore 1 and Ionophore 2 was acquired using ^7Li and ^{23}Na one-dimensional NMR experiments. The samples were prepared as described above and the timecourse experiment (Chapter 3.3) was carried out over ~ one hour.

The transport data was interpreted using spectral subtraction subroutines built into Varian VNMR software on a Silicon Graphics Indy machine.

The first FID was acquired, and subsequent FID's were subtracted from the first using the subtraction process. This yielded a value equal to the change in the intensity of the 'in' (small) peak during the experiment. At the end of the experiment an excess of monensin was added into the NMR tube containing the vesicles. This drove the transport into the vesicles to its maximum within the time taken to acquire a single FID, and the intensity of the 'in' peak in this instance gave an infinity value ∞. In the case of Ionophore 1, plots of time (s) versus ln (change in signal intensity of 'in' peak – infinity) produced straight lines with slope equal to k x 10^{-2} sec^{-1}. For Ionophore 2, plots of time (s) versus ln (change in signal intensity of 'in' peak – infinity) gave curved lines. These are indications of first order and non-first order kinetic processes respectively, and the data was from here on treated in the appropriate manner as described in Chapter 3.2.

Both ^{7}Li and ^{23}Na NMR were used with Ionophore 1 in separate $^{7}Li_{(in)}$ / $^{23}Na_{(out)}$ exchange experiments, allowing the reproducibility of the procedure to be demonstrated. The values of the association and

dissociation rate constants and the stability constant of the complex in the membrane were very close in both cases.

Transport experiments were conducted at 50, 100, 150 and 200 mM LiCl concentrations. Increasing the metal ion concentration led to an increase in the amount of shift reagent required to separate the intravesicular and extravesicular signals, i.e. at 100 mM LiCl, 7.5 x 10^{-3} M $DyCl_3$ would provide approximately a 10 ppm shift between the two signals, whereas at 200 mM salt concentrations, 12.5-15 x 10^{-3}M $DyCl_3$ was needed. This is presumably due to their being a greater number of ions present in solution.

Nucleus	Transients / FID	d_1 delay between pulses (s)
^{7}Li	8-16	15-30
^{23}Na	200-400	0.5-1.0

Table 3.6 Some of the parameters used in ^{7}Li and ^{23}Na NMR transport experiments with EPC vesicles.

3.7 Discussion and Conclusions

$^{7}Li^{+}_{(in)}/^{23}Na^{+}_{(out)}$ exchange mediated by Ionophore 1 [sodium (cyclopentadienyl) tris- (diethylphosphite) cobaltate]:

Observing ^{7}Li NMR:	$k'_f = 1.79\ s^{-1}$
	$k'_d = 0.19\ M.s^{-1}$
	$K_s = 9.6\ M^{-1}$
Observing ^{23}Na NMR:	$k'_f = 1.423\ s^{-1}$
	$k'_d = 0.15\ M.s^{-1}$
	$K_s = 9.7\ M^{-1}$
$^{6/7}$Li Exchange Observing ^{7}Li:	$k'_f = 3.28\ s^{-1}$
	$k'_d = 0.22\ M.s^{-1}$
	$K_s = 15.4\ M^{-1}$

The stability constant K_s of the metal / ionophore complex in the membrane surface is highest when lithium is the only cationic species present in both the intra and extravesicular medium, i.e. in isotope exchange experiments. The formation rate constant is greatest when lithium alone is present, being around double that of the sodium / ionophore complex under competitive conditions. The formation and stability constants reflect the preference of the ionophore for lithium. The more rapid formation rate and the greater stability of the lithium complex appears to be the main reason for the differences is transport rates, as the dissociation rates are more closely comparable.

Ionophore 1 is a monoanionic tridentate ligand half-sandwich compound in which three phosphite oxygen donor atoms co-ordinate to a single metal cation. This ionophore is much smaller than, for example, the polyether antibiotics, which co-ordinate to the metal with 5 or 6 oxygen atoms. The physical differences in binding and co-ordination are reflected in the stability constants.

Early kinetic studies with vesicles revealed transport rate selectivity some 20 to 40 times greater for the lithium complex compared to the sodium.[2] Ionophore 1 is closer in structure and size to some of the smaller spirotetrahydrofuran analogues and the crown ethers than the polyether antibiotics such as monensin or nigericin.

It is possible to compare the rates of lithium transport under identical conditions by other ionophores such as monensin. The rates of Ionophore 1 mediated transport of lithium (a) in the presence of an equal concentration of sodium, and (b) under isotope exchange conditions (i.e. only ^{6} & ^{7}Li), obtained using ^{23}Na and ^{7}Li NMR spectroscopy are compared to rates of lithium transport by monensin, from Riddell, Arumugam, and Cox[15] in tables 3.7 and 3.8 below.

[Monensin]/[PC] x 10^3 at 75mM LiCl	$k_{(in-out)}$ x 10^4 s^{-1}	[Ionophore1]/[PC x 10^3 at 50mM LiCl (^{23}Na NMR)	$k_{(in-out)}$ x 10^2 s^{-1}	[Ionophore1]/[PC] x 10^3 at 100mM LiCl (^{23}Na NMR)	$k_{(in-out)}$ x 10^2 s^{-1}
0.0	0.0	0.0	0.0	0.0	0.0
1.604	0.46	1.09	0.157	1.13	0.089
2.3208	0.86	2.19	0.267	2.26	0.155
4.6417	1.85	4.38	0.474	4.52	0.341

Table 3.7 Comparison of the rates of lithium / sodium transport by Ionophore 1 with the rates of lithium transport by monensin.[15]

[Monensin]/[PC] x 10^3 at 75mM LiCl	$k_{(in-out)}$ x 10^4 s^{-1}	[Ionophore1]/[PC] x 10^3 50mM LiCl (^{7}Li NMR)	$k_{(in-out)}$ x 10^2 s^{-1}	[Ionophore1]/[PC] x 10^3 100mM LiCl (^{7}Li NMR)	$k_{(in-out)}$ x 10^2 s^{-1}
0.0	0.0	0.0	0.0	0.0	0.0
1.604	0.42	1.09	0.106	1.13	0.189
2.3208	0.76	2.19	0.331	2.26	0.404
4.6417	1.79	4.38	0.753	4.52	0.615

Table 3.8 Comparison of the rates of lithium transport by Ionophore 1 obtained using ^{7}Li NMR with the rates of lithium transport by monensin.[15]

The rates of lithium transport by monensin are on average about 500 times greater than those obtained for Ionophore 1 in the presence of an equivalent concentration of sodium (i.e. when lithium and sodium compete for Ionophore 1), but only around 250 times greater

than the rate of lithium transport mediated by ionophore 1 when there is no sodium present (when ^{6}Li and ^{7}Li compete for Ionophore 1). However, the rates for monensin were measured using the line-broadenings as opposed to the spectral subtraction procedures used with Ionophore 1.

This is further evidence (a) that the transport of sodium is the rate-determining step, and (b) that Ionophore 1 has a much greater affinity for lithium than for sodium.

$^{7}Li^{+}_{(in)}/^{23}Na^{+}_{(out)}$ exchange mediated by Ionophore 2 (cis-N,N,N',N'-tetraisobutylcyclohexane-1,2-dicarboxamide]:

[LiCl] and [NaCl] mM	Kinetic Order with respect to Ionophore 2 Concentration
100	3.1
150	2.9
200	2.9

Table 3.9 Summary of the kinetic orders for Ionophore 2

The results in Table 3.9 above appear to validate the findings of Zeevi and Margalit,[6] who proposed a 2:1 ionophore – cation complex for the active species and found diffusion across the membrane to be the rate-limiting step.

References

1. Roman, E. E., Tapia, F. C., Hernandez, S. M., *Tetrahedron*, **5**, 3, 917-920 (1986)
2. Shinar, H., Navon, G., *Journal of the American Chemical Society*, **108**, 5005-5006 (1986)
3. Margalit, R., Eisenman, G., *Journal of Membrane Biology*, **61**, 209-219 (1981)
4. Margalit, R., Shanzer, A., *Biochimica et Biophysica Acta*, **649**, 441-448 (1981); Margalit, R., Shanzer, A., Pflugers Archive, **395**, 87-92 (1982)
5. Erne D., Ammann D., Zhukov A. F., Behm F., Pretsch E., Simon W., *Helevetica Chimica Acta*, **65**, 2, 538-545 (1982)
6. Zeevi A., Margalit R., *Journal of Membrane Biology*, **86**, 61-67 (1985)
7. McMillan F., Senior Honours Report, Department of Chemistry, University of St Andrews (1984)
8. Painter, G.R., Pressman, B.C., Top. Curr. Chem., **101**, 83-100 (1982)
9. Riddell, F. G., Arumugam, S., Brophy, P. J., Cox, B. G., Payne, M. C. H., Southon, T. E., *Journal of the American Chemical Society*, **110**, 734-738 (1988)
10. Riddell, F. G., Tompsett, S., *Biochimica et Biophysica Acta*, **1034**, 193-196 (1990)
11. Duval, D., Riddell, F. G., Rebuffat, S., Platzer, N., Bodo, B., *Biochimica et Biophysica Acta*, **1372**, 370-378 (1998)

12. Riddell, F. G., Arumugam, S., *Biochimica et Biophysica Acta,* **945**, 65-72 (1988)

13. Reynolds, J. A., Mimms, L. T., Zampighi, G., Nozaki, Y., Tanford, C., *Biochemistry*, **20**, 833-840 (1981)

14. Riddell, F. G., Hayer, M. K., *Biochimica et Biophysica Acta,* **817**, 313-317 (1985)

15. Riddell, F. G., Arumugam, S., Cox, B. G., *Journal of the Chemical Society, Chemical Communications*, 1890 (1987)

Chapter 4

Anion Transport Mediated By A Cholic Acid Based Anionophore

Chapter 4

Anion Recognition and Transport by a Cholic Acid-Based Anionophore

4.1 Introduction

Although more than two thirds of all biological enzymes act on negatively charged substrates, anion co-ordination, recognition and transport have only recently attracted attention because of its biological relevance. Transport of the chloride ion, as discussed earlier, has become a focus for many transport studies, since abnormalities in the chloride transport process can have serious health consequences, e.g. cystic fibrosis. Many of the proteins involved in transport, such as Band 3 protein for chloride, perform vital tasks.

In the early 1980s the carrier-facilitated phase-transfer of anions from an aqueous phase to an organic phase was demonstrated with a series of alkylammonium salts and cationic metal complexes.[1] The phase-transfer catalyst (Q^+X^-) is usually a quaternary ammonium halide ($R_4N^+X^-$), such as tetrabutylammonium halide, $(CH_3CH_2CH_2CH_2)_4\ N^+\ X^-$, which can catalyse the transport of a nucleophile (e.g. CN^-) as an ion pair [Q^+CN^-] into the organic phase, as

shown in Figure 4.1 below. No reaction occurs without the phase-transfer catalyst because the nucleophile alone cannot enter the organic phase.

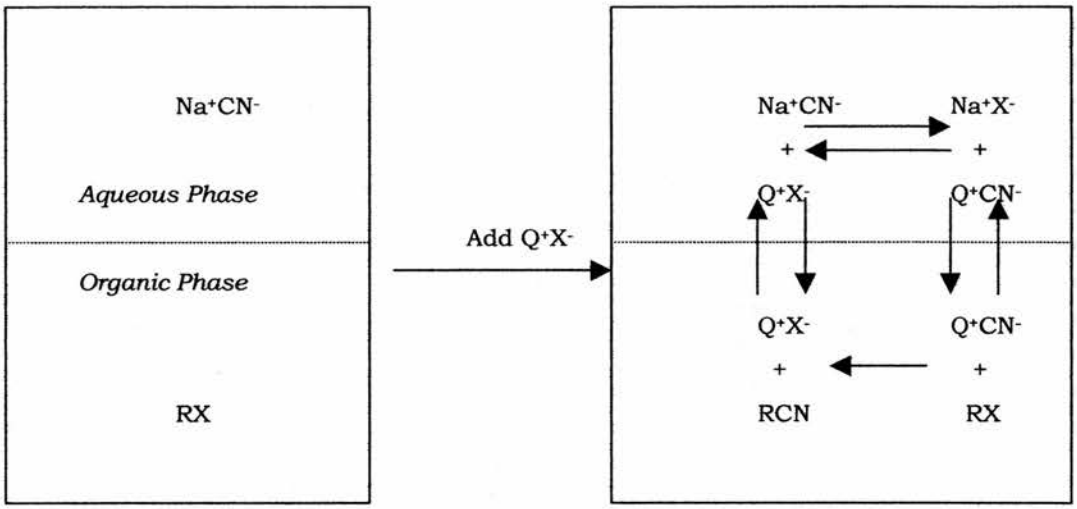

Figure 4.1 Phase-transfer catalysis of the S_N2 reaction between sodium cyanide and an alkyl halide.

It was also shown that in each case the transported anion was bound to the carrier through electrostatic interactions. Anion transport selectivity is determined largely by the free energy of transfer of the anion moving from an aqueous to an organic phase. Lipophilic anions are usually extracted and transported at a greater rate than hydrophobic anions.

Researchers in the field of molecular recognition aim to create synthetic organic receptor molecules designed for the selective and efficient binding of ions and simple organic or biological substrates. When looking for suitable receptor molecules, certain general criteria exist: such a molecule should have a rigid backbone (with flexible functional groups attached that allow the ready ingress and egress of the substrate), be easily accessible and cheap, allow for additional functionalisation, and have a well-understood chemical background.

The cholic acid skeleton fits the criteria given above, with the added benefit of being amphiphilic. The molecule (Figure 4.2) also has three hydroxyl groups pointing onto the α-face of the molecule that are relatively easily transformed into other functional groups. Cholic acid and many of its derivatives are said to be contrafacially amphiphilic, as one face of the molecule is polar, while the other face is non-polar.

A typical amphiphile such as phospholipid can organise itself such that polar-polar and non-polar-non-polar contacts are maintained, keeping the polar headgroups hydrated, and the lipophilic tails unhydrated. Many contrafacial amphiphiles, however, have too rigid a structure to allow the close packing of the molecules in the way phospholipids can line up and form self-sealing vesicles.

4.2 Background to Steroid-Based Ionophores for Halide Anions

Contrafacial amphiphiles with segregated polar functionality may be able to diffuse through lipid bilayers provided a sufficiently large hydrophobic surface is exposed to the hydrocarbon interior of the lipid bilayer. The development of contrafacial amphiphiles has led to hopes that they could be used as drug-delivery systems for intracellular targets.

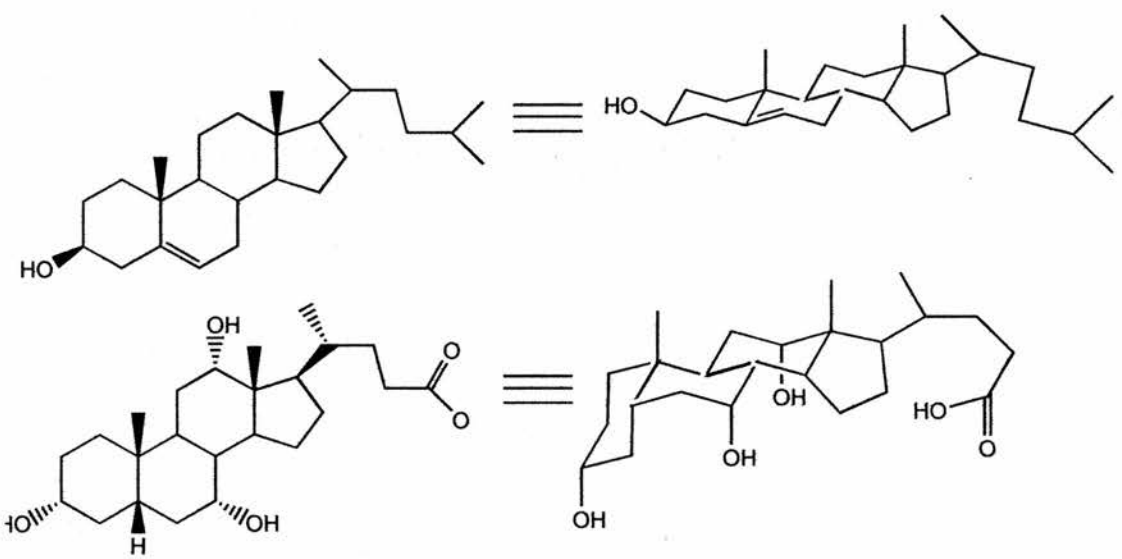

Figure 4.2 The structures of cholesterol (above) and cholic acid show many similarities. Both are inexpensive and readily available, and thus make good starting materials for more elaborate frameworks.

Anion carriers make use of the co-operative action of neutral hydrogen bond donor groups. These groups are chosen to be acidic for the promotion of strong anion binding, whilst at the same time minimizing intramolecular hydrogen bonding. The acidity and size of the functional groups can be varied to allow selective binding with the target anion.

Cryptand molecules contain several side-arm amino functionalities that when protonated are capable of complexing with an anion, have found application as anion binding receptors. The anion / protonated cryptand complex bears a net positive charge which lowers the lipid solubility, but this can be partially overcome by inclusion of a large lipophilic anion, such as dinonylnapthalene sulphonate (DNNS-), into the membrane.[2]

In 1989 Davis and Bonar-Law[3] from Trinity College in Dublin used the basic cholic acid framework to create the macrocyclic cholaphane ring system, shown below in Figure 4.3. They also noted that such systems had potential for molecular recognition, since the ring and cavity sizes could be adjusted using various functional groups and spacer groups positioned between each cholic acid unit. The dimeric cholaphane ring with inwards pointing functional groups shown in Figure 4.3 bears a resemblance to the structures of some of the

polyether antibiotic ionophores, in which head-to-tail buttoning occurs as a single ionophore forms a complex with a small cation.

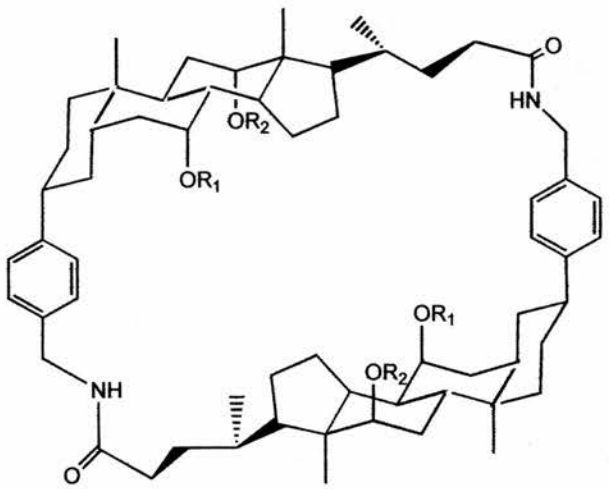

Where (a) R_1, R_2 = Ac
(b) R_1, R_2 = PhCO
(c) R_1=Ac, R_2=$PhCH_2$

Figure 4.3 Steroidal cyclodimers or 'cholaphanes' synthesized from cholic acid.

Several important modifications to the functionality of the cholic acid skeleton led to increased amphiphilicity.[4] Glycosylation of the axial hydroxyl groups at C7 and C12 left the hydrophobic face much the same but greatly increased the hydrophilicity of the opposite face. In 1993 Davis and Bonar-Law[5] used cholic acid as an architectural component for biomimetic and molecular recognition chemistry, and in doing so generated a new series of cholaphanes, with a variety of function groups incorporated into the assembly.

Davis[6] also used the steroid / cholaphane framework to organise functional group arrays or clusters. The resulting system contained a cavity between 40-50 $Å^3$ surrounded by six polar functional groups in a 3D arrangement, and was shown to be suitable as a receptor for small organic molecules. As with the cryptand family, the size of the cavity is primarily responsible for the observed ion selectivity, making such molecules useful as anion receptors and anionic ionophores.

The potential, in the areas of molecular recognition, of the cholic acid skeleton became more fully realised as derivatives became more readily accessible and applications for such molecules grew. In 1996 Davis and Walsh[7] continued work on the cholaphane system and by modifying the cavity sizes, prepared another series of receptors with inward-directing polar functional groups.

The macro-tri-lactam (Figure 4.4 below) consists of two steroidal molecules and a variable fragment Y. When Y was varied, the cavity size and framework flexibility were also altered, which in turn affected the solubility or catalytic properties of the molecules.

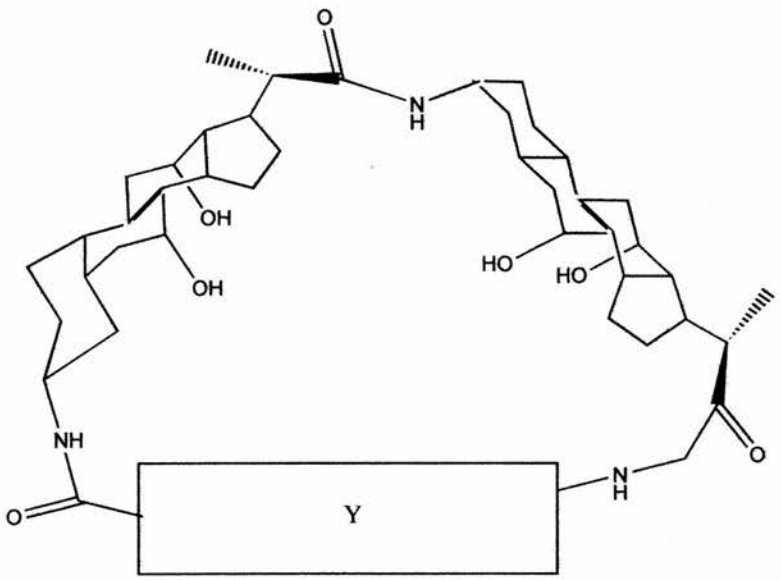

Figure 4.4 One of a series of receptors with inward-directing polar functional groups and a variable fragment Y.

In 1997 Davis, Perry and Williams[8] observed that for strong and selective binding, anion receptors rely on the co-operative action of neutral hydrogen bond donors. When the donor groups were made more acidic and complementary to the target ion, the hydrogen bonding was maximised. Cryptand and crown ether structures have previously been used in molecular recognition studies, and new receptors based on the podand-type architecture were shown to have a much greater affinity to chloride in non-polar organic solvents.

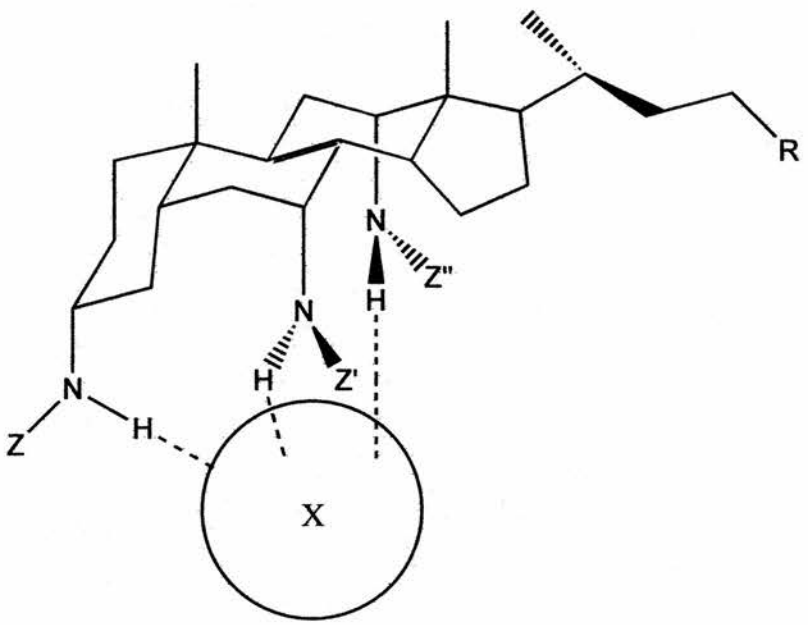

Where : X is an ionic substrate

: Z, Z', Z" are electron withdrawing groups such as:

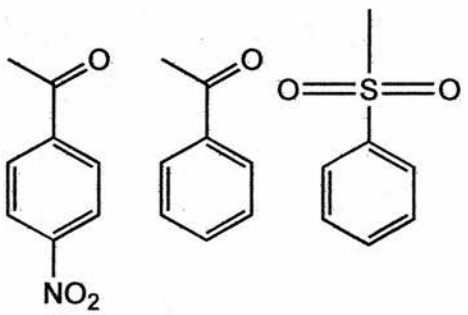

Figure 4.5 Co-operative action of hydrogen-bond donor groups allows strong and selective binding between receptor and target ion.

In Figure 4.5, the anion recognition is achieved through three NH containing groups at C3, C7, C12, with the average hydrogen-bond distance from proton to anion around 2.5Å. The protons of the NH groups are made more acidic by the presence of the electron-

withdrawing groups Z, Z' and Z". This means that the relative acidity of the NH's can be fine tuned by the three Z groups.

In 1997 Davis[9, 10] created new cholaphanes / steroid based macrocycles with increased solubility and controlled flexibility. This new system incorporated externally directed alkyl chains to promote solubility in organic solvents and reduce conformational freedom through the cropping of the steroidal side-chain. In 1998, Davis, Broderick and Williams[11] created the triamino steroid from cholic acid, replacing each hydroxyl with an amino group and substituting the side-chain hydroxyl for an ester (Figure 4.6). The amino groups retain the hydrogen bond donating ability after acylation, thus increasing the hydrophilicity when protonated.

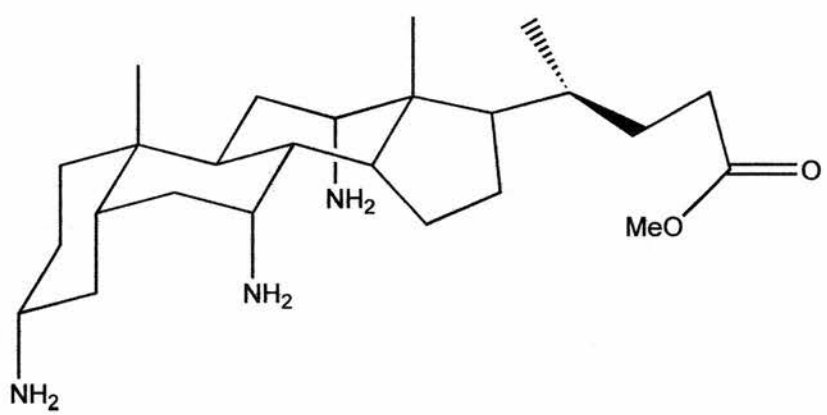

Figure 4.6 The triamino steroid created from cholic acid

This tris-deoxa-tris-aza analogue of methyl cholate was thought to have potential as a facial amphiphile, as it has suitable transport properties in biphasic media, i.e. phospholipid membranes. Davis, Perry, and Wareham[12] used alkyl cholates as neutral ionophores related to natural products. The resultant molecule displayed preference for tridentate oxoanions, bound by hydrogen bonding with the three hydroxyl groups, as shown in Figure 4.7 below.

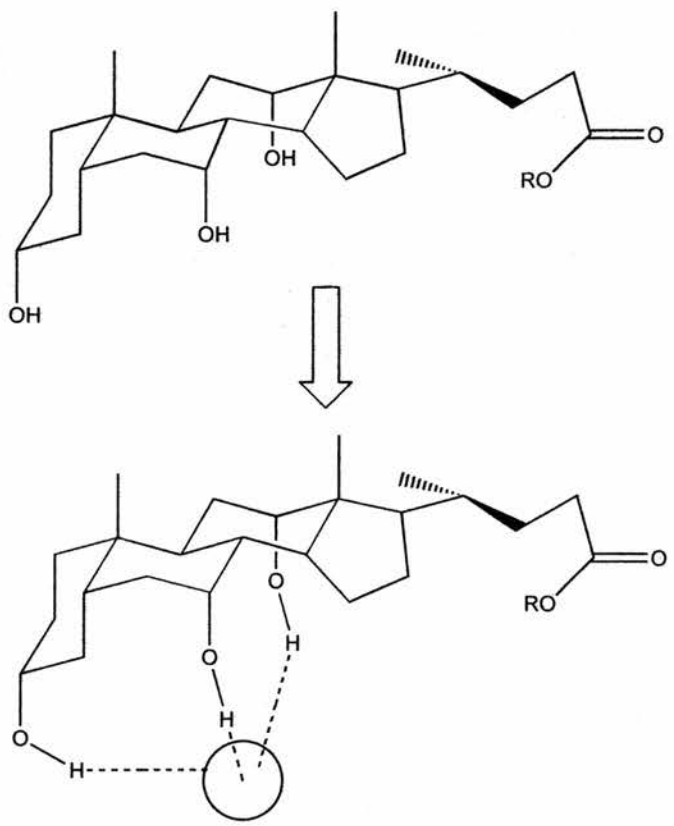

Figure 4.7 Hydrogen bonding between three hydroxyl groups and a tridentate oxoanion.

The methyl groups on the hydrophobic face (β, upper) aid binding and increase the solubility of the cholic acid derivative / anion complex in aqueous media. The functionalised face (α, lower) is used in recognition of polar species in non-polar media, or hydrocarbon solvents. The affinity between the oxoanion and the new alkyl cholates is likely to be limited primarily by the hydrogen-bond donating ability of the hydroxyl groups. In 1999 Davis et al[13] modified the cholic acid unit again and used the new material as a starting point for combinatorial libraries, as an aid in the search for biologically active molecules, receptors, catalysts, and ionophores. The molecule shown in Figure 4.8 was essentially a trifunctional steroid-based unit, to be used as a scaffold in combinatorial chemistry.

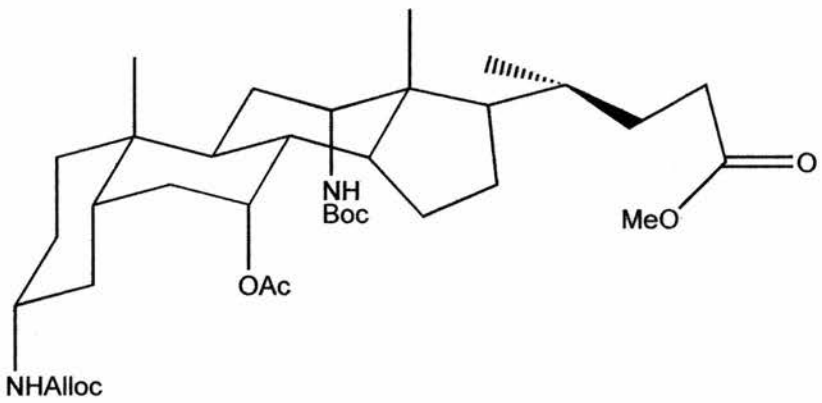

Figure 4.8 The tri-functional steroid-based unit for use in combinatorial chemistry

The latest in these compounds has been labelled Broderick 1. Using a new method for measuring affinity based on the extraction of tetra-alkylammonium salts from water into chlorofom, the binding constant to chloride and bromide is of the order of 10^7 M^{-1}. Broderick 1 is shown below in Figure 4.9.

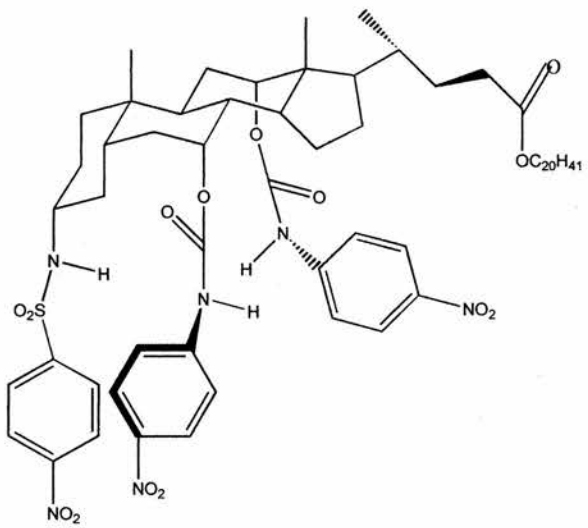

Figure 4.9 Broderick 1 [Eicosyl-3a-(p-nitrophenylsulfonylamino)-7a,12a-(nitrophenylamino-carbonyloxy) cholanate].

4.3 Results of Transport Studies with Broderick 1

The results of Broderick 1 mediated $chloride_{(in)}$ / $bromide_{(out)}$ at 200, 250, 300 and 350 mM [Cl^-] are presented below in Table 4.1. The changes in the signal intensity of the 'in' peak over time were obtained

after the addition of aliquots of Broderick 1 and at different metal ion concentrations.

$[M^+]$ mM	$[I]/]PC] \times 10^{-4}$	$k_{mediated} \times 10^{-2}$	$k_{passive} \times 10^{-4}$	k'_{med}
200	10.025	0.092	0.128	1.961
	20.233	0.335	0.140	
	40.649	0.701	0.145	
250	8.463	0.099	0.079	1.412
	17.079	0.335	0.125	
	34.313	0.487	0.099	
300	7.643	0.114	0.025	1.205
	15.425	0.331	0.047	
	30.989	0.420	0.076	
350	9.955	0.100	0.037	1.091
	20.090	0.212	0.056	
	40.362	0.432	0.070	

Table 4.1 Broderick 1-mediated transport study rates.

All of the initial plots of ln (change in signal intensity) versus time could be fitted to a straight line (see Appendix V). This indicates first-order kinetics. The slopes from these plots are equal to $k_{med.}$ A plot of k_{med} versus I/PC gives a straight line with slope equal to k'_{med}. The plot of k'_{med} versus $[M^+]$ (Figure 4.10) has a slightly curved slope, and the plot of $1/k'_{med}$ versus $[M^+]$ (Figure 4.11) gives a straight line. The intercept of this line is equal to $(k'_f)^{-1}$ and the slope of this line is equal to $(k'_d)^{-1}$.

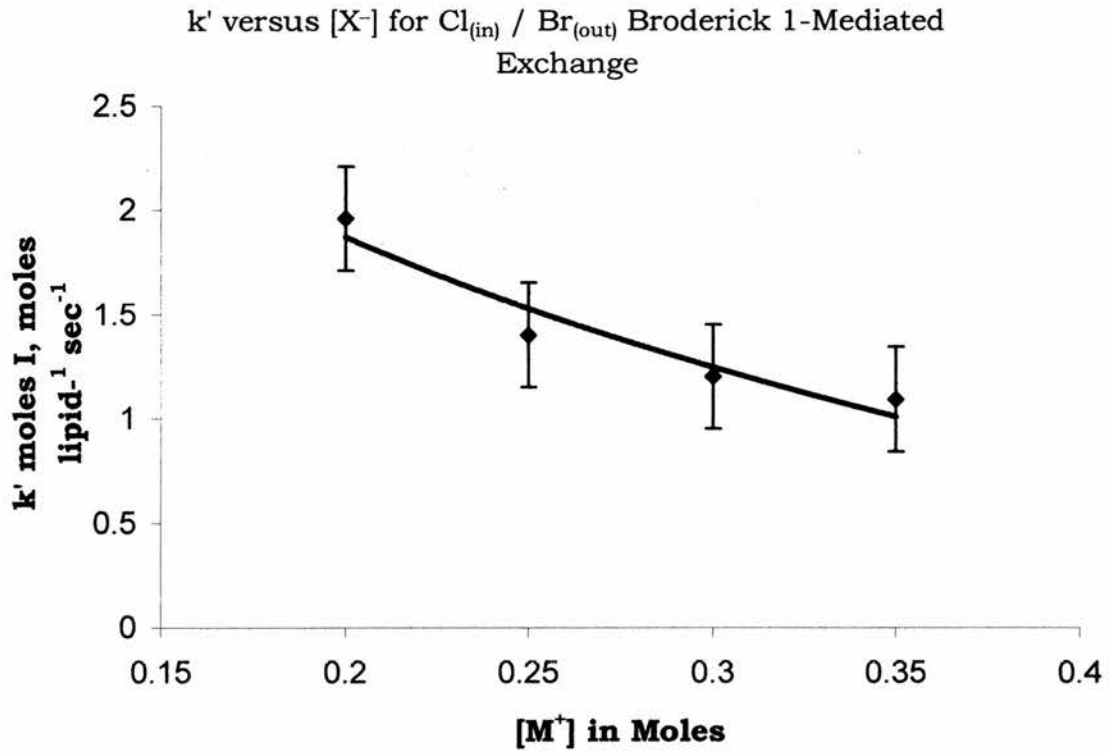

Figure 4.10 A plot of k' versus $[M^+]$ in M^{-1} for Broderick 1 mediated transport.

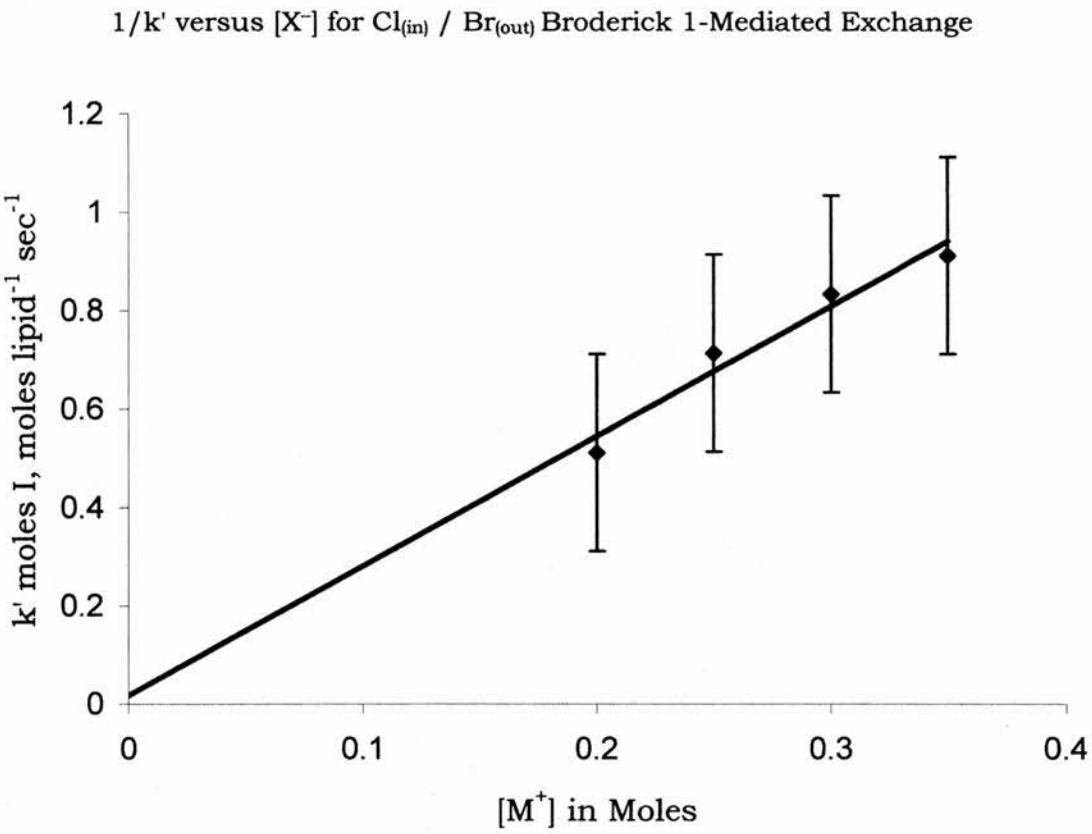

Figure 4.11 A plot of 1/k' versus [M⁺] in M⁻¹ from which values for k'_f and k'_d are obtained.

As seen in the cation transport studies with Ionophore 1 in Chapter Three, the linear variation of transport rate with ionophore concentration is again a suggestion of a first-order kinetic relationship between ligand and ion, and implies that the active transport species is a 1:1 complex. This means that the formation and dissociation rate constants and an overall stability constant for the complex in the

membrane can be obtained in the manner described for Ionophore 1 in Chapter 3

From the plot of 1/k' versus [M^+] the intercept (0.019) is equal to $(k'_f)^{-1}$ and the slope (2.638) is equal to $(k'_d)^{-1}$. This gives a value of 52.6 s^{-1} for k'_f, and 0.4 $M.s^{-1}$ for k'_d. The stability of the complex in the membrane, K_s, is given by the ratio of the formation and dissociation constants, k'_f / k'_d, and in this case is 139 M^{-1}.

These results indicate that a single anionophore transports a single anion at a time during the rate-determining step. Broderick 1 is said to have a high affinity for chloride, so it is possible that the transport of bromide into the vesicle is the rate-determining step. If the transport of bromide is indeed rate-determining, then the rate constants k_f, k_d, and K_s have a significant contribution from the bromide/anionophore complex, as well as from the chloride/anionophore complex.

Alternatively, the dissociation rate constant for the chloride complex is low, indicating that the dissociation step is probably slow, and therefore may be rate-determining.

The value obtained for K_s indicates that the complex is relatively stable. The formation constant is high, reflecting the high affinity this anionophore has for the anion. The low dissociation rate suggests

that the anion is not readily released. A high formation rate and a low dissociation rate for an ionophore usually indicate a stable complex, as the ratio of the rates k'_f / k'_d gives the stability constant of the complex in the membrane.

Comparison of these results with others is difficult because very few anionophore-mediated transport studies using vesicles and NMR have been done. The rates of anionophore-mediated transport for three compounds related to Broderick 1 were given in the Ph.D. Thesis of Sina Sareth (St. Andrews, 1998).[17] These studies were carried out at 200 mM [X^-] and a first-order kinetic relationship was found for two of the anionophores, shown below in Figure 4.12. As the transport rates were not measured at other [X^-], the formation and dissociation rate constants and the stability constant could not be calculated, and so cannot be used here for comparison.

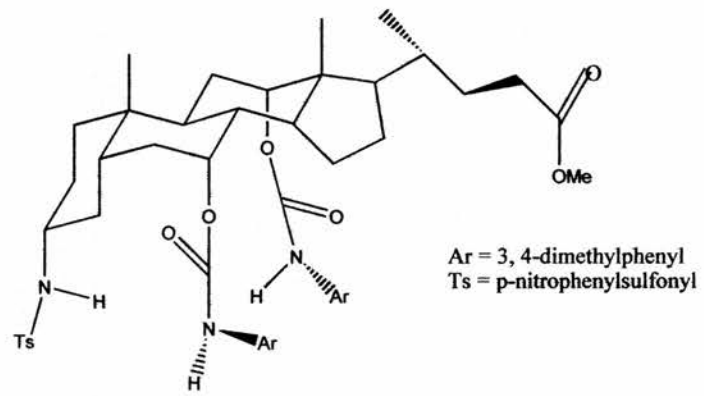

Methyl-3α-(p-nitrophenylsulfonylamino)-7α, 12α-(3, 5-dimethylphenyl) cholanate

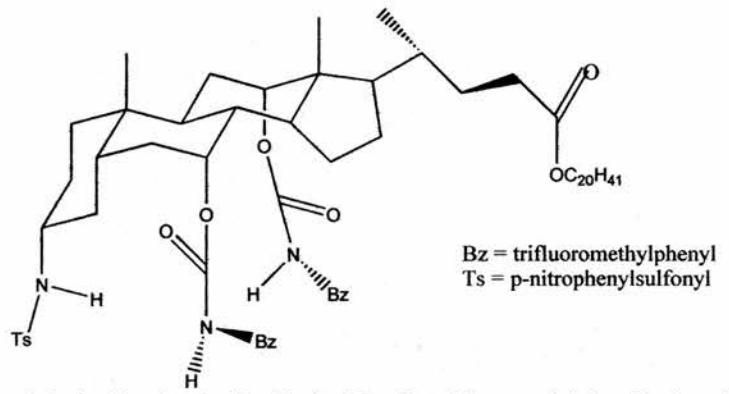

Eicosyl-3α-(p-nitrophenylsulfonylamino)-7α, 12α-trifluoromethylphenylaminocarbonyloxy) cholanat

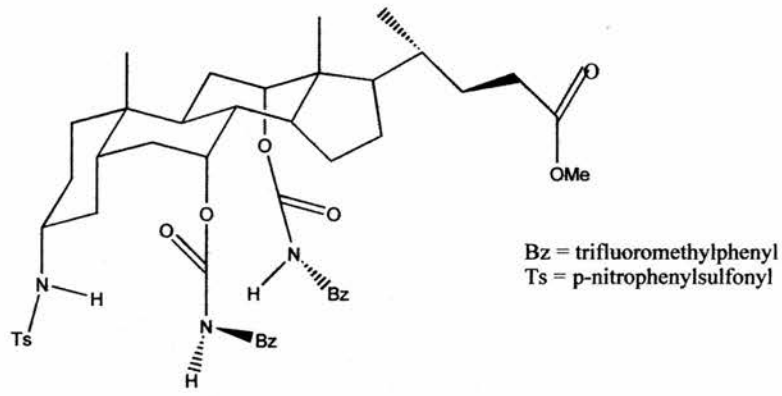

Methyl-3α-(p-nitrophenylsulfonylamino)-7α, 12α-trifluoromethylphenylaminocarbonyloxy) cholanat

Figure 4.12 Three Broderick 1-related compounds previously used in anion transport studies.[17]

4.4 Experimental

4.4.1 Preparation of Large Unilamellar Phosphatidylcholine Vesicles using the Dialytic Detergent Removal Technique

This preparation is a modification of the dialytic detergent removal technique described by Reynolds et al[13]. The removal of detergent from mixed micelles of egg yolk phosphatidylcholine and n-octyl glucopyranoside leads to formation of large unilamelar phospholipid vesicles with a diameter of between 200 and 400 nm.

Egg yolk phosphatidylcholine (EPC, 516 μl, Lipid Products) was weighed into a clean round bottomed flask. The solvent was removed at the pump over three hours to give around 40 mg of dry EPC. An amount of n-octylglucopyranoside (260 mg, Sigma and Aldrich) was dissolved in 3 cm^3 of standard NaCl solution (100 mM). This solution was added slowly and with care to avoid introducing oxygen to the dry EPC. The mixture was stirred until the lipid had completely dissolved, then transferred quantitatively into a pre-soaked length of dialysis tubing and sealed. The dialysis procedure for the preparation of LUVs suitable for anion transport is carried out in a cold room at 4 °C, and leads to the formation of vesicles with smaller diameters than thosose prepared at 40 °C for cation transport experiments.

2 – 2.5 L of 100 mM NaCl solution was precooled to 4 °C in a dialysis vessel and flushed with oxygen-free nitrogen for 12 hours. The dialysis tubing was attached inside the dialysis vessel at the end of this period. The solution in the dialysis vessel was changed every 12 hours for a total of 60 hours with more preheated and degassed 100 mM NaCl, and the dialysis tubing containing the EPC solution was inverted at least twice daily to ensure even mixing of the vesicles, otherwise they tended to settle slowly inside the dialysis tube.

Vesicles prepared in this manner generally require 3 full days to completely form. At the end of this period, large unilamelar vesicles suitable for anion transport experiments will have formed, with the same concentration of chloride inside the vesicle as that in the external medium. Relative vesicle volumes were measured before the NMR experiment by comparing the integrated areas of the internal and external peaks.

4.4.2 Sample Preparations

The anionophore known as Broderick 1 [*Eicosyl-3a-(p-nitrophenylsulfonylamino)-7a,12a-(nitrophenylamino-carbonyloxy) cholanate,* Figure 4.13 below] was obtained as a gift from Professor Anthony Davis, Trinity College, Belfast.

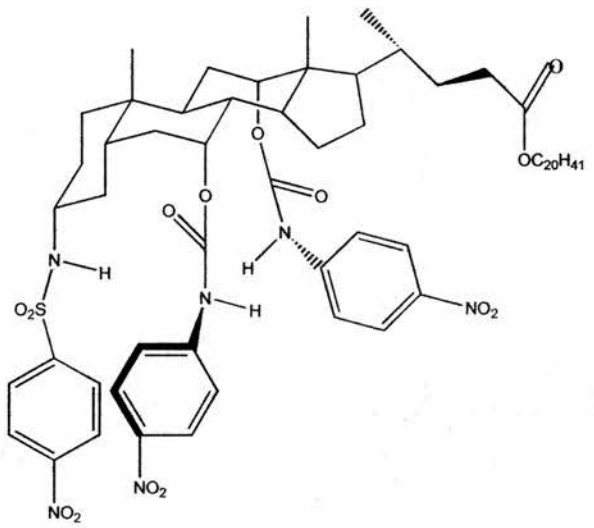

Figure 4.13 Broderick 1 [Eicosyl-3a-(p-nitrophenylsulfonylamino)-7a,12a-(nitrophenylamino-carbonyloxy) cholanate].

A solution of Broderick 1 (15 mM, 0.0905 g, in 5 cm^3 HPLC-grade MeOH) was prepared. From this, 5, 10 and 20 μl amounts were taken and added directly into the NMR tube containing the vesicle suspension.

Bromide was chosen to be the extravesicular species and was added as sodium bromide in the same volume and concentration as sodium

chloride. This allows the $Cl^-_{(in)}$ / $Br^-_{(out)}$ exchange rates to be measured without any concentration gradient between intra and extravesicular ion concentrations.

LUV suspension (1 cm^3) and sodium bromide solution (1 cm^3) were added into a new 10 mm o. d. NMR tube fitted with a coaxial insert containing D_2O. An amount of $MnCl_2$ (1 M, 10-25 μl) was added to the NMR tube to substantially flatten the out signal, leaving the in signal sharp and clearly visible. Once the signals can be clearly discriminated, the sample is ready for the experiment to begin.

4.4.3 NMR Experimental and Analysis Procedure

The rates of passive and Broderick 1-mediated transport were obtained at 200, 250, 300, and 350 mM chloride ion concentrations. The passive exchange rates were subtracted from the mediated transport rates to account for the natural leakage from vesicles prepared for anion transport. The data obtained at low (200 mM) chloride concentrations were more difficult to interpret than at higher (≥250 mM) chloride concentrations. This may be due to the inherent low natural receptivity of $^{35}Cl^-$, or to there being a fewer number of ^{35}Cl atoms at the low Cl^- concentrations and thus a weaker NMR signal, giving smaller peaks for which it can be harder to obtain a precise volume.

The data for Broderick 1 was acquired using ^{35}Cl NMR one-dimensional NMR experiments. The samples were prepared as described above and the rates of passive diffusion were measured over ~ 30 minutes. At the end of this period, the anionophore was added and the timecourse experiment (as described in Chapter 3.3) was carried out over 30 to 60 minutes. All experiments and measurements were made at 298 K. Figure 4.10 below shows a typical ^{35}Cl NMR spectrum from a chloride transport experiment.

The transport data was interpreted using an analysis procedure very similar to the one described in Chapter 3.6.5 (p. 132). Spectral subtraction routines built into Varian VNMR software were employed using a Silicon Graphics Indy workstation. As before, the first FID was acquired, and subsequent FID's were subtracted from the first using the subtraction process. This gives a value equal to the change in signal intensity of the 'in' peak (the tall sharp signal in the middle of the substantially broadened 'out' signal) of the first FID and the *n*th FID. Plots of ln (change in signal intensity of 'in' peak) versus time (s) produced straight lines. This is a preliminary indication that transport occurs through first order processes.

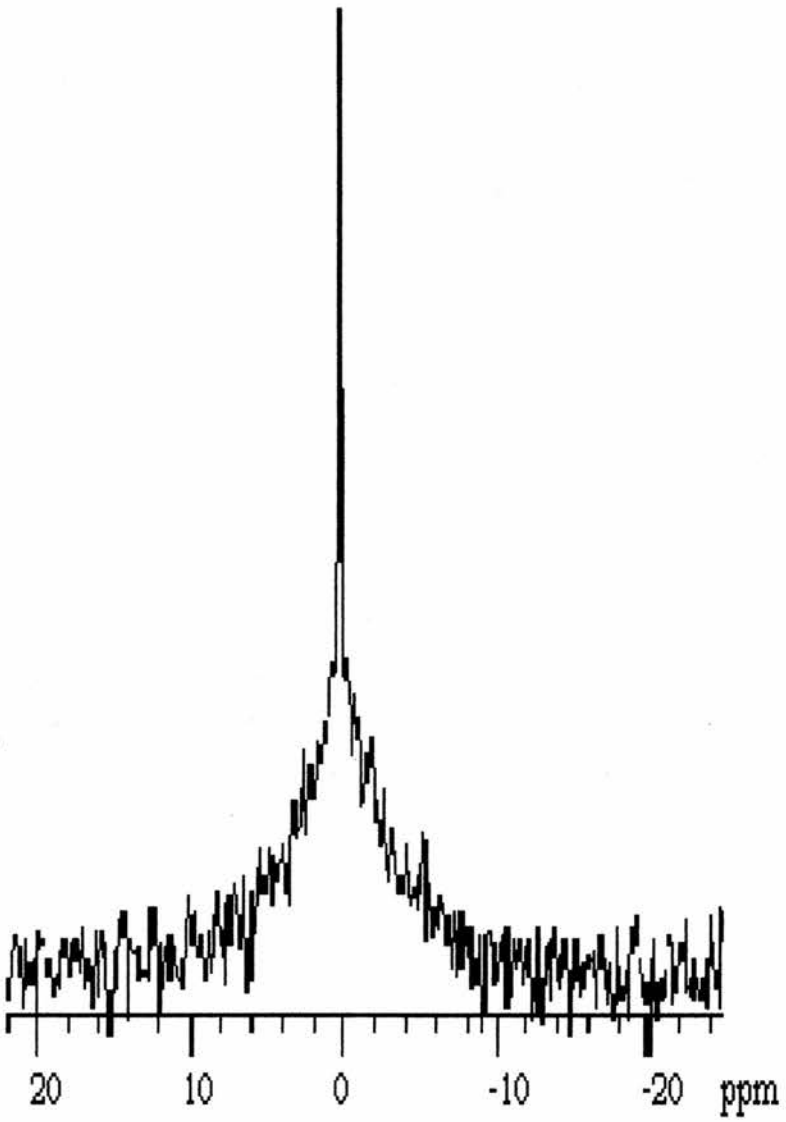

Figure 4.15 A 48.99 MHz ^{35}Cl NMR spectrum of 1 cm^3 150 mM NaCl EPC vesicles, 1 cm^3 150 mM NaBr, and 10 mM $MnCl_2$ to generate the separation between intravesicular and extravesicular signals.

The transport data was interpreted using spectral subtraction subroutines built into Varian VNMR software on a Silicon Graphics Indy machine. The first FID was acquired, and subsequent FID's were subtracted from the first using the subtraction process. This yielded a value equal to the change in the intensity of the 'in' (small) peak during the experiment. Plots of time (s) versus ln (change in signal intensity of 'in' peak – infinity) produced straight lines with slope equal to k x 10^{-2} sec^{-1}. This is an indication of a first-order kinetic relationship between anion and anionophore and the data was from here on is treated in the manner described in Chapter 3.2.

4.4.4 Contrast Agents for NMR Anion Transport Studies

There are very few NMR contrast agents available for anions compared to the large numbers available for cations. Riddell et al have published some of the only work done on anion contrast agents suitable for use with large unilamellar vesicles, using Mn^{2+} as a relaxation agent for $^{35}Cl^-$.

Shakar-Hill and Schulman[14] described the use of Co^{2+} as both a shift agent and a relaxation agent for $^{35}Cl^-$. The major disadvantage of using Co^{2+} is that it considerably broadens the shifted resonance. When relaxation is paramagnetic in origin, the linewidth (Hz) of the signal increases with the square of the magnetic field, but the shift

(Hz) varies only linearly. Therefore, increasing the magnetic field means higher concentrations of Co^{2+} are required to separate intra- and extravesicular signals. Strong magnetic fields increase the rates of paramagnetic relaxation processes, which also increases the linewidth of the relaxed signal. At high field strengths, Co^{2+} is only a moderate shift agent, but an efficient relaxation agent.

In the experiments with Broderick 1, the relaxation agent used was 1 M $MnCl_2$. This was added to the vesicle suspension in 10-20 μl amounts and considerably broadened the extravesicular signal, leaving the intravesicular signal clearly visible.

4.5 Future Work

The condensation of cholic acid and spermine has been shown to yield an ion conductor or *quasi*-ionophore that forms membrane-spanning channels (resembling gramicidin, see Figure 1.12) through phosphatidylcholine bilayer membranes of varying thickness with high specificity.[15] An increase in the activity of this ionophore by factors of 30 000 when the length of the carbon chains comprising the interior of the membrane changed from 14 to 18 carbons was found. This offers the possibility of using these compounds to make use of the differences in membrane thickness between mammalian and bacterial

or fungal cells and deliver ions or drugs specifically to a site recognised by its own membrane thickness.

This *quasi*-ionophore represents the new series of synthetic ionophores that exhibit membrane as well as ion selectivity.[15, 16] The motivation for this type of work arose from the hypothesis that such ionophores could be used to kill bacterial and fungal cells by destroying the barrier properties of their plasma membranes, without the need to enter the cell.

The development of cobalt (II) triglycine as a shift reagent (see Chapter 5) offers an interesting alternative to $MnCl_2$ as a relaxation agent.

References

1. Lamb, J. D., Christensen, J. J., Oscarson, J. L., Nielsen, B. L., Asay, B. W., Izatt, R. M., *Journal of the American Chemical Society*, **102**, 6820-6824 (1980); Maruyama, K., Tsukube, H., Araki, T., *Journal of the American Chemical Society*, **104**, *19*, 5197-5203, (1982)

2. Dietrich, B., Fyles, T. M., Wais Hosseini, M., Lehn, J. M., Kaye, K. C., *Journal of the Chemical Society, Chemical Communications*, 691-692, (1988)

3. Davis, A.P., Bonar-Law, R. P., *Journal of the Chemical Society, Chemical Communications*, 1050-1052, (1989)

4. Cheng Y., Ho, D. M., Gottlieb, C.R., Kahne, D., *Journal of the American Chemical Society*, **114**, 7318-7319, (1992)

5. (a) Bonar-Law, R. P., Davis, A. P., *Tetrahedron*, **49**, 9829-9844 (1993); (b) Ibid, 9845-9854; (c) Ibid, 9855-9866

6. Davis, A. P., *Chemical Society Reviews*, 243-253 (1993)

7. (a) Davis, A. P., Walsh, J. J., *Chemical Communications*, 449-452 (1993); (b) Ibid, 453-455

8. Davis, A. P., Perry, J. J., Williams, W. P., *Journal of the American Chemical Society*, **119**, 1793-1794 (1997)

9. Davis, A. P., Dresen, S., Lawless, l. J., *Tetrahedron*, **38**, 24, 4305-4308

10. Bhattarai, K. M., Davis, A. P., Perry, J. J., Walter, C. J., *Journal of Organic Chemistry*, **62**, 8463-8473 (1997)

11. Broderick, S., Davis, A. P., Williams, R. P., *Tetrahedron Letters*, **39**, 6083-6086 (1998)

12. Davis, A. P., Perry, J. J., Williams, R. P., *Tetrahedron Letters*, **39**, 4569-4572 (1998)

13. Barry, J. F., Davis, A. P., Perez-Payan, M. N., et al, *Tetrahedron Letters*, **40**, 2849-2852 (1999)

14. Shachar-Hill Y., Shulman R.G., *Biochemistry*, **31**, 27, 6273-6278 (1992)

15. Deng, G., Dewa, T., Regen, S. L., *Journal of the American Chemical Society*, **118**, 8975-8976 (1996)

16. Merritt, M., Lauier, M., Deng, G., Regen, S. L., *Journal of the American Chemical Society*, **120**, 8494-8501 (1998)

17. Sareth, S., Ph. D. Thesis, University of St. Andrews, 1998

Chapter 5

New NMR Shift Reagent For Anions

Chapter 5

New NMR Shift Reagent for Anions

5.1 Introduction

The use of NMR to investigate cellular phenomena was at first inhibited by the inability to discriminate between intracellular and extracellular resonances, from alkali metal cations such as lithium, sodium and potassium, and from anions such as chloride, bromide and iodide. The NMR signals of these nuclei frequently overlap in spectra and become obscured, as the aqueous chemical shifts of such ions are essentially independent of the ion's surroundings. For example, ^{35}Cl signals from inside and outside a cell or vesicle in the absence of paramagnetic species will appear at almost the same chemical shift position. In 1982 Gupta and Gupta[1] provided a means of separating two compartmentalised signals. They showed that intra and extracellular ^{23}Na signals in human erythrocytes could be differentiated using dysprosium tripolyphosphate as a shift reagent. Since then a variety of compounds known as *contrast reagents* have been made to perform the same basic function.[2, 3]

5.2 Signal Differentiation Using Relaxation and Shift Reagents

There are two general ways of separating a pair of partitioned signals, e.g. signals arising from nuclei inside and outside cells or vesicles. Both methods involve the addition of a contrast reagent to one of the compartments, e.g. extracellular / extravesicular. The contrast reagent only exerts an effect on the nuclei it comes into close contact with, i.e. the intracellular / intravesicular nuclei are unaffected.

Relaxation agents are usually paramagnetic in nature (having unpaired electrons) and artificially relax nearby nuclei through substantial paramagnetic or quadrupolar interactions. Such molecules are designed to be non-interactive with and impenetrable to cells or vesicles, and therefore only exert their effect on nuclei comprising the 'out' signal. The observed signal (in cases where vesicles or cells are used, and depending on the nucleus under study) features a very broad hump with a tall and sharp peak somewhere close to the centre, corresponding to the broad relaxed extracellular (vesicular) and the sharp intracellular (vesicular) signals respectively (See Figure 5.1 below).

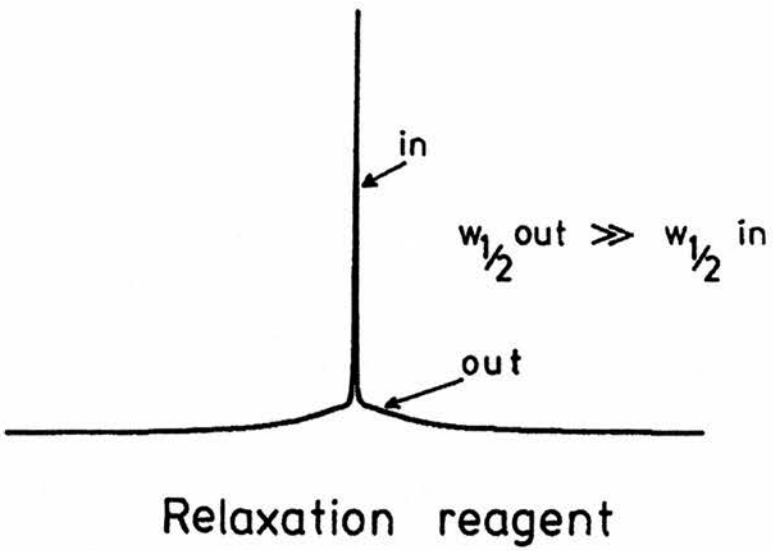

Figure 5.1 Diagrammatic representation of the effects of a relaxation agent on the 'out' signal (broad hump), leaving the 'in' signal sharp and clearly visible.

The other method of separating these signals is to move one of the signals so it does not fall directly on top of the other signal in a spectrum. *Chemical shift agents* such as $DyCl_3$ and $TbCl_3$ generally (in conjunction with a suitable ligand) cause the 'out' signal to be slightly broadened but substantially shifted to higher or lower frequency through interactions between extra-vesicular nuclear spins and the unpaired electron density associated with the paramagnetic lanthanide atom. The intravesicular or 'in' signal remains at its usual position, since the shift reagent does not cross the biological or artificial membrane (See Figure 5.2 below).

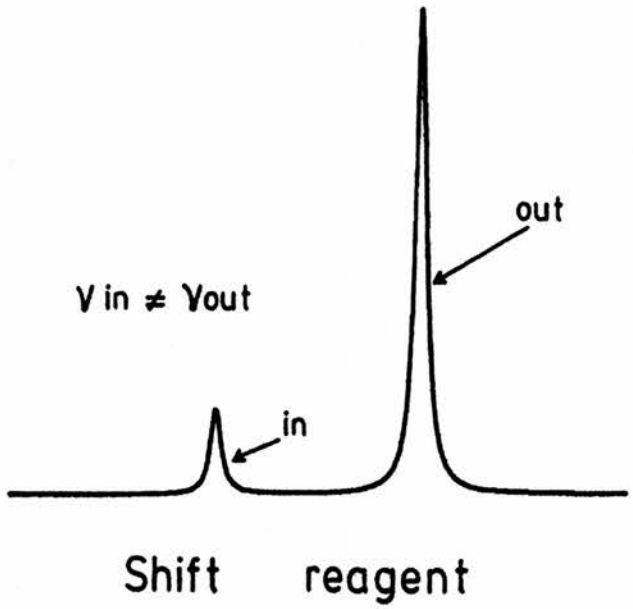

Figure 5.2 Diagrammatic representation of a shift agent, leaving the small 'in' peak on the left at its original chemical shift position, but shifting the large 'out' signal upfield, typically by around 10 ppm.

5.3 How do Contrast Reagents Work?

Lanthanide-induced shifts Δ of a ligand upon co-ordination to a Ln^{3+} cation can be expressed as the sum of three terms, diamagnetic (Δd), contact (Δc), and pseudocontact (Δp) shifts:

$$\Delta = \Delta d + \Delta c + \Delta p \qquad \text{Equation 5.1}$$

The diamagnetic contribution is usually small, and is often neglected. It originates from sources such as conformational changes, inductive effects, and direct field effects.

Contact shifts arise from the through bond transmission of unpaired electron spin density from the Ln *f*-orbital to the nucleus under study. Contact shifts can quickly decrease in magnitude as the number of bonds between the Ln^{3+} cation and the nucleus under study increases. The largest contact shifts are observed from directly Ln^{3+}-bound donor sites.

Pseudo-contact or dipolar shifts are a result of the local magnetic field induced in the nucleus under study by the magnetic moment of the Ln^{3+} ion. Pseudo-contact shift is a *through-space* effect and for lanthanides, is usually the predominant effect.

Shift and relaxation reagents essentially operate through a combination of the above effects. A positively charged lanthanide atom surrounded by ligands that are able to donate nonbonding pairs can attract positively charged cations such as alkali metals to the complex and interaction with unpaired electron density in the paramagnetic ion results in a significant chemical shift change. This interaction can occur as a *through-bond* effect (contact shift) between the paramagnetic lanthanide atom and protons from the substrate, or as a *through- space* effect (pseudo-contact) the secondary field around the protons generated by the rotating paramagnetic centre.

The ligand used to co-ordinate with the Ln^{3+} or transition metal atom has a significant effect on the ability of the complex to exert a shifting or relaxing effect. If the ligand bears a high negative charge, the Ln^{3+}-ligand complex may maintain enough electron density to attract cations (e.g. Li^+, Na^+). If there is only a small negative charge present on the ligand, the Ln^{3+}-ligand complex may be able to attract anions.

The broadening of the shifted resonances for the tripolyphosphate shift / relaxation agents has been shown to be largely due to quadrupolar rather than paramagnetic interactions.[2] Almost any paramagnetic species can be used to provide additional relaxation pathways (nuclear-electron interactions become dominant instead of heteronuclear dipole-dipole interactions) for carbon nuclei and / or protons. The only limiting factor is that the contrast reagent must not in any way interact with any organic substrate present in the sample.

In a sample, the presence of a paramagnetic species such as oxygen O_2 is important, as these nuclei have relatively large magnetic moments and can give rise to broadened lines. In practice, very low oxygen concentrations do not change the T_1 and / or T_2 significantly in most samples, although degassing of samples under oxygen-free nitrogen is a routine part of sample preparation.

5.4 Uses of Contrast Reagents

5.4.1 Contrast Reagents in MRI

Paramagnetic compounds containing lanthanide atoms have been used for some time in magnetic resonance imaging (MRI). In such cases the substance causes relaxation differences between various tissues or organs through its lack of permeability. Images recorded using non-toxic contrast agents such as Gd-DTPA (Gadolinium diethylenetriaminepentaacetic acid, Figure 5.3, below) or $GdCl_3$ can in many cases provide better data for doctors to base their diagnoses on, as a variety of images of varying grey-scale can be obtained. This can 'shed light', as it were, on features that may be otherwise difficult to see, or on features that may require separate and specific pulse sequences in order to be highlighted.

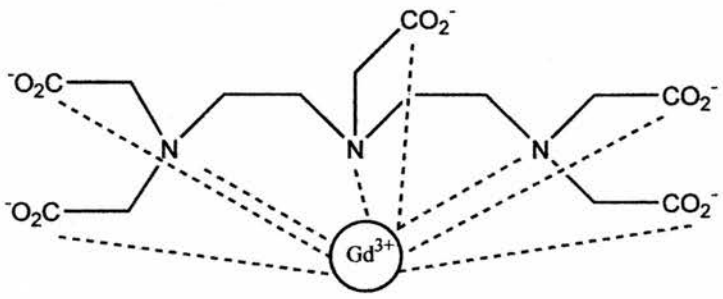

Figure 5.3 The contrast reagent gadolinium DTPA (diethylene triaminepentaacetic acid) binds to eight of the nine co-ordination sites of the Gd atom (represented by dashed lines). A water molecule may occupy the ninth site.

5.4.2 One Dimensional Liquid and Solid State NMR

Other paramagnetic substances using transition metal atoms and bulky negatively charged ligands are routinely used in liquid and solid state NMR to bring about artificial relaxation, hence reducing spin-lattice relaxation times (T_1) and allowing experiments to be carried out in a shorter space of time. An example of a relaxation agent used in solid state NMR are the transition metal / $(acac)_3$ complexes, including $Cr(acac)_3$, $Ti(acac)_3$, $V(acac)_3$, where $(acac)^-$ is the acetylacetonate ligand.

For *in-vivo* experimentation the complex must be non-toxic in the prescribed amounts. The shift reagent dysprosium tripolyphosphate ($DyPPP_2$) can be used for *in-vitro* studies, such as ion transport

involving vesicles or in studies of some cellular systems such as erythrocytes, but is not safe enough to be used in living systems. Similar compounds such as $TmDOTP^{5-}$ (Thulium 1, 4, 7, 10-teraazacyclodecane-1, 4, 7, 10-tetrakismethylenephosphonate) in Figure 5.4 below are preferred, as they give signal separation and are non-toxic.

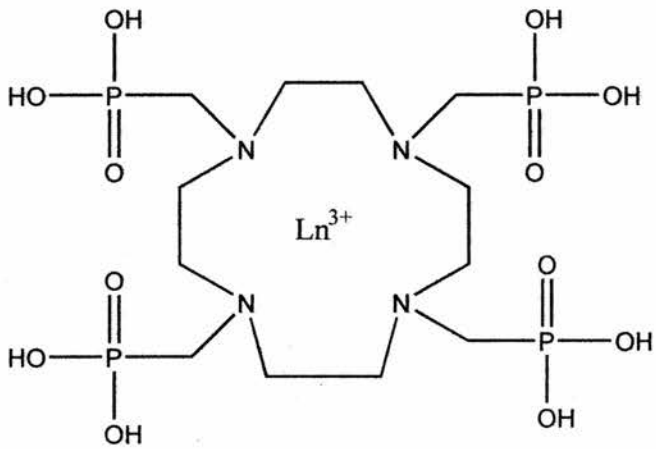

Figure 5.4 The structure of the DOTP ligand used as a lanthanide shift reagent.

The octadentate DOTP ligand co-ordinates to Ln^{3+} ions in a square prismatic (SAP) arrangement via the four nitrogen atoms of the macrocyclic ring and four phosphonate oxygens of the pendant arms. The DOTP ligand co-ordinates to trivalent Ln^{3+} ions to produce anionic complexes of various net charges.

5.4.3 Chiral Contrast Reagents

Lanthanide (III) metals bound to chiral ligands can give chiral shift reagents[4, 5] in the manner already discussed. The use of chiral shift reagents allows the resolution of enantiomer signals. A recently reported chiral shift reagent for α-amino acids and N-protected oligosaccharides based on europium (III) is capable of resolving the B-protons in a ^1H spectrum of (R, S)-alanine.[6] The interaction between europium (III) complex (no net charge) and α-amino acids is weak at neutral pH. This is due to monodentate co-ordination through a single carboxylate oxygen. A welcome effect of the weak interaction is that enantiomer signals can be observed without significant signal broadening. A recently developed chiral shift reagent allows the determination of the enantiomeric purity of ruthenium (II) organometallic complexes.[7]

5.5 Aqueous Shift Reagents for Cations

There are currently several types of shift reagents for alkali metal NMR spectroscopy.[2-5] These reagents are mostly used to provide signal separation in membrane transport experiments, with artificial membrane systems, or with, for example, red blood cells or erythrocytes. Lanthanide (III) cations complexed with a variety of

ligands have been shown to be successful at separating compartmentalised signals. Examples include lanthanum[2], dysprosium[3], and thulium triphosphates and chlorides, e.g. $Ln(PPP)_2^{7-}$, $DyCl_3$, etc The relative orders of cation complexation for $Dy(PPP)_2^{7-}$ is: $Li^+ > Na^+ \geq K^+$.

Effective shift reagents use a large ligand to exclude mono-atomic cations from the primary co-ordination sphere. This ensures that the cation / metal interaction is not strong enough to adversely affect the spectrum, while at the same time producing shifts large enough to leave a clear baseline between the peaks of interest. Figure 5.5 below shows a hypothetical solution structure[4] for $Dy(PPP)_2^{7-}$ at pH 7.5. Cations are attracted to the $Dy(PPP)_2^{n-}$ complex due to its net negative charge and so are brought close to the paramagnetic Dy^{3+} atom. The presence of the lithium cations neutralizes the –7 charge on the complex.

The nature of the complex formed is pH dependent. At low pH, the protonated triphosphate predominates, and cation / metal interaction is low. As pH increases, the protonated sites decrease in number and exchange with cations can occur quickly. This has the effect of broadening lines due to intermolecular ligand exchange processes.

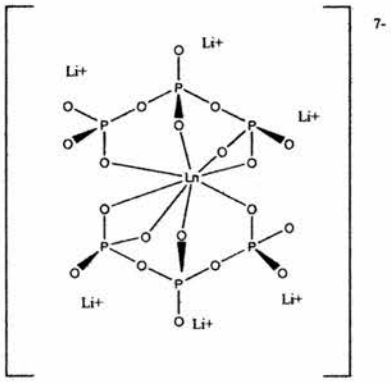

Figure 5.5 Proposed structure[7] of $Dy(PPP)_2^{7-}$ at pH7.5. Obtained through multinuclear NMR studies[4] on $Dy(PPP)_2^{7-}$

The maximum shifts generated by $Dy(PPP)_2$ are: $^{7}Li^{+}$ ~ 40 ppm; ^{23}Na ~ 20 ppm; ^{39}K ~ 10 ppm; ^{81}Rb ~ 2-3 ppm, but this is smaller than the line widths. For Cs^{+} the shift is slightly anion dependent.

5.6 NMR Shift Reagent for Anions Based on Cobalt (II) Triglycine

In 1992 Shachar-Hill and Schulman[8] used cobalt (II) as a shift reagent for ^{35}Cl NMR of chloride with vesicles and cells. They added 16 mM $CoCl_2$ into a suspension of lipid vesicles in 40 mM KCl and observed a ~20 ppm shift in intravesicular and extravesicular signals.

In 1996 Mota de Freitas and Lin[9] published an account of chloride ion distribution and transport in human red blood cell (RBC)

suspensions. They were able to observe intracellular and extracellular chloride using ^{35}Cl NMR. They tested several shift reagents as a means of separating the two chloride resonances, and found that Co (II) glycine, $[Co(Gly)_3]^-$ was the best shift reagent. Co (II) glycine gave the greatest shifts and the narrowest line widths at half-height for both intra- (673 Hz) and extracellular (200 Hz) signals. At 40 mM $[Co(Gly)_3]^-$ the extracellular Cl^- signal was shifted by 34.5 ppm. The solubility of most Co (II) complexes confines the concentration range to a maximum of ~ 200 mM. The formation constant expressed as the log *K* value for the $[Co(Gly)_3]^-$ complex as calculated below is 23.91

$$Co^{2+} + 3\ Gly^- \rightleftharpoons [Co(Gly)_3]^-$$

$$K = [Co(Gly)_3]^- / ([Co^{2+}][Gly^-]^3)$$

Of the Co (II) complexes studied, $[Co(Gly)_3]^-$ was the most stable. When glycine is used as the ligand there is probably very little free Co^{2+} is solution. This and the absence of direct chloride binding in the primary co-ordination sphere accounts for the narrow line widths observed at half height.

Mota de Freitas and Lin[9] showed that the lanthanide shift reagents were ineffective as anion shift reagents even thought they are routinely used for separating alkali metal signals. This was believed to be due to the repulsion created between the chloride ions and the

highly negatively charged $Dy(TTHA)^{3-}$ and $HTmDOTP^{4-}$ complexes. In such a situation, the paramagnetic effect of the unpaired electrons is not felt by the chloride ions, simply because they are kept at a distance through electron-electron repulsion.

The range of contrast reagents available until now has meant that, in most cases, a shift reagent is used in conjunction with alkali metal transport studies[2-5] and relaxation or shift reagents[6-8] are used for anion transport studies. Despite its many advantages the shifts generated by $[Co(gly)_3]^-$ are not strong enough to prevent residual overlap between the two resonances. A clear baseline between the intra and extracellular resonances is essential when observing ion transport with NMR. A powerful new shift reagent for use with anions has been developed and studied in detail. The new complex is cobalt (II) triglycine. It is related to $[Co(II)(gly)_3]^-$ introduced by Mota de Freitas, discussed earlier.

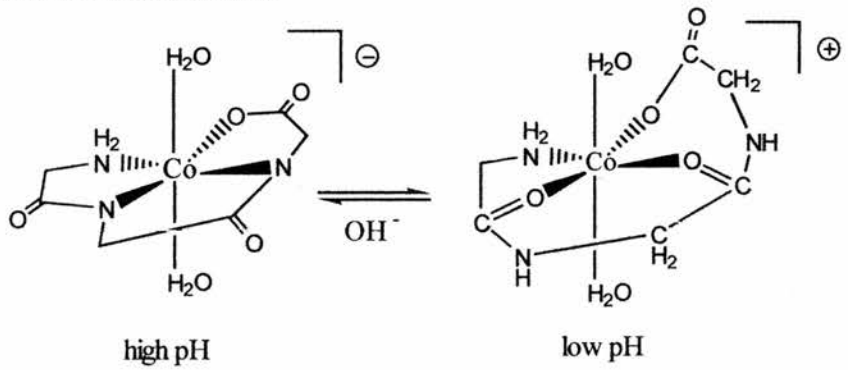

Figure 5.6 A hypothetical structure for [Cobalt (II) triglycine]

The structures in Figure 5.6 have two water molecules associated with the metal atom. These should be very labile and exchange rapidly with free chloride ions in solution at and around neutral pH. This would bring the chloride ions into close contact with the metal centre, and may account for the observed effects.

Gillard and Phipps[10] and Evans et al[11] showed that the binding sites for triglycine and cobalt (II) included the terminal amino group, the adjacent deprotonated amide nitrogens, and the carbonyl oxygen of the central glycyl residue of the tripeptide. Changes in the co-ordination pattern are observed with increasing pH. Triglycine can co-ordinate using two of its carbonyl oxygens and one of the carboxyl oxygens instead of the deprotonated amide nitrogens (see Figure 5.6). Changes can also be seen at higher pH values (pH9.5 and upwards) as cobalt (II) changes to cobalt (III) in the presence of oxygen.

Cobalt (II) triglycine is made by addition of $CoCl_2$ to one equivalent of triglycine, mixing, and balancing the pH to neutral with NaOH. Other Co (II) salts (bromide and nitrate) were prepared with both triglycine and glycine, and tested as NMR contrast agents. [Co(trigly)] gives substantially greater shifts than $[Co(gly)_3]^-$ at the expense of greater line widths for the shifted resonance. It also acts as a shift reagent for a wide variety of inorganic anions.

The intra and extracellular ^{35}Cl NMR signals in human can be distinguished in RBC (and LUV) suspensions through interaction between Co^{2+} and extracellular Cl^-. This generates two magnetically different compartments and gives rise to two ^{35}Cl NMR resonances, corresponding to an 'in' and an 'out' signal.

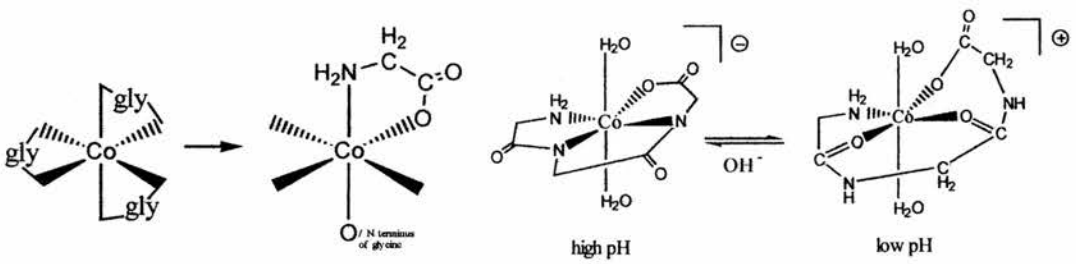

Figure 5.7 Cobalt (II) (glycine)$_3$ and cobalt (II) triglycine

Importantly, in the triglycine complex, cobalt has two sites out of six that are not required in the bonding with the ligand. These two sites are normally occupied by water molecules (pH dependent), but can undergo rapid exchange with chloride anions. Thus, chloride ions come into closer contact with the cobalt nucleus with the triglycine complex than with the (glycine)$_3^-$ complex. If the chloride anions can exchange at these two sites, the increased interactions result in bigger shifts and shorter relaxation times with the triglycine reagent than with the (glycine)$_3^-$ reagent.

5.7 Nuclei Studied in Shift Reagent Experiments

It was possible to observe a range of NMR-active nuclei (^{14}N, ^{15}N, ^{35}Cl, ^{37}Cl, ^{79}Br, ^{81}Br) in testing both cobalt (II) shift reagents. The advantages and disadvantages of using particular isotopes of these nuclei are discussed, and some of the relevant NMR properties of the nuclei are considered below in Table 5.1. Based on factors such as natural abundance, ^{14}N, ^{35}Cl and ^{81}Br were the nuclei chosen for study by NMR.

Isotope	NMR Frequency in a 500 MHz ^{1}H field	Natural Abundance (%)	Spin
^{14}N	36.12	99.63	1
^{15}N	50.685	0.37	½
^{35}Cl	48.99	75.53	3/2
^{37}Cl	40.78	24.47	3/2
^{79}Br	125.27	50.54	3/2
^{81}Br	135.03	49.46	3/2

Table 5.1 Some of the spin properties of the nuclei used in shift reagent experiments.[12]

5.7.1 Nitrogen, ^{14} & ^{15} N

Two isotopes of nitrogen, ^{14}N and ^{15}N, are of interest. When more than one isotope is available, usually the isotope with the highest

natural abundance is used, as the higher receptivity should give greater signal-to-noise in the spectrum. The natural abundance of ^{14}N is 99.63 %, but ^{14}N has $I=1$, and is therefore quadrupolar. For nitrogen containing anions, $T_1=T_2$, and quadrupolar relaxation pathways and mechanisms are dominant for ^{14}N and the anions generally have high symmetry. As a consequence, ^{14}N signals for simple anions are not difficult to detect, and the experiments can be done in a relatively short space of time (since relaxation times are between 0.1 to 10 ms). However, where symmetry is lacking quadrupolar interactions can often make the lines broad.

^{15}N is a dipolar nucleus, not subject to quadrupolar interactions, but of such low natural abundance (0.36 %) and receptivity to the NMR experiment that it has not been fully exploited in areas of NMR research such as protein structural studies. With the negative magneto-gyric ratio, γ, the ^{15}N nucleus gives a negative nuclear Overhauser enhancement. The relaxation behaviour of ^{15}N has been likened to that of ^{13}C, with T_1 values typically between 1 and 100 seconds. ^{15}N T_1 values are often dependent on concentration, temperature and pH.

5.7.2 Chlorine, ^{35} & ^{37}Cl, and Bromine, ^{79} & ^{81}Br

Both isotopes of chlorine and bromine have I=3/2, and are subject to quadrupolar interactions. Both ^{35} & ^{37}Cl have relatively low quadrupole moments, but ^{79} & ^{81}Br have larger quadrupole moments and therefore give broader lines, (ca. 400 Hz for ^{79} & ^{81}Br in H_2O, ca. 10-15 Hz for ^{35} & ^{37}Cl in H_2O.

The nuclear quadrupole moment allows these nuclei to relax very efficiently (quickly). The disadvantage of quadrupolar nuclei is that the NMR signals obtained from them are often several kilohertz wide, and in some cases me be so broad they are unobservable. ^{35}Cl is usually favoured over ^{37}Cl due to its greater natural abundance (75.5 % compared to 24.5 %), but for bromine there is just over 1 % difference in natural abundance between the two isotopes. Since both Cl^- and Br^- are spherical anions, the quadrupolar relaxation contribution is relatively small despite the high values of Q. Thus, in this instance the signals were relatively sharp and easy to detect.

5.8 Experimental

5.8.1 Sample Preparation

Cobalt (II) triglycine was freshly prepared on the day of use in 1:1 cobalt (II):triglycine ratios. Amounts that would create x mM (where x is 30, 60, 90) in 10 cm^3 were placed in a small sample vial. Approximately 7 cm^3 water was added, the pH was adjusted to 7.0, then the total volume made up to 10.0 cm^3. Cobalt (II) glycine was made in 1:3 cobalt (II) : glycine ratios, (i.e. three molecules of glycine for every molecule of triglycine) in the same manner.

5.8.2 NMR Experiments

The shift reagent was tested in two ways. In each case the tip of a coaxial insert for a 10 mm o. d. NMR tube was filled with an almost saturated solution of NaCl (or NaBr, $NaNO_3$, etc.) dissolved in D_2O. This signal was assigned to 0 ppm. The outer 10 mm tube into which the coaxial insert fits contained the shift reagent solution. For nitrate, chloride and bromide, the respective ^{14}N, ^{35}Cl and ^{81}Br spectra show a large signal at 0ppm, corresponding to the concentrated volume in the insert, and a smaller signal from the external tube shifted to high frequency (left hand side of spectrum) by the presence of unpaired electrons from Co (II) ions.

The observed changes in chemical shifts are mainly determined by the concentration of shift reagent, but they also show pH dependency, with the largest shifts occurring at the lowest pH. The first set of experiments involved simply measuring the chemical shifts and line-widths (Hz). The second set of experiments involved altering the pH of the samples, then measuring the chemical shifts and line-widths. The samples were retained and the chemical shifts measured again at the end of the experiment to check the reproducibility of the results and to partially examine the rate at which the shift reagent decomposed and was no longer effective.

Experiments were carried out with 30, 60 and 90 mM samples of cobalt triglycine and cobalt $(glycine)_3^-$ prepared from $CoCl_2$, $CoBr_2$ and $Co(NO_3)_2$. The samples were freshly made on the day of use and the NMR experiments were carried out at 298 K. The nuclei observed by simple one dimensional NMR were ^{14}N, ^{35}Cl and ^{81}Br.

5.9 Results

The results of experiments to measure the chemical shifts produced by cobalt (II) $(glycine)_3$ and cobalt (II) triglycine are presented in three sections. The first shows the relationship between the induced chemical shift and the cobalt (II) concentration. The second section shows the variation of the induced chemical shift with pH. The final part involves the testing of cobalt (II) triglycine with EPC vesicles.

5.9.1 Shifts at Varying Cobalt (II) Concentrations

[Co(II)triglycine] and $[Co(II)(glycine)_3]^-$ complexes made from $CoCl_2$, $CoBr_2$, and $Co(NO_3)_2$ were prepared in 30, 60 and 90 mM quantities. The results are presented as graphs and tables and clearly show that cobalt (II) triglycine provides greater shifts than cobalt (II) glycine. Furthermore, cobalt (II) triglycine prepared from $CoCl_2$ had a stronger shifting effect than shift reagents prepared from $CoBr_2$ or $Co(NO_3)_2$. The powerful shifting effect produced by cobalt (II) triglycine prepared from $CoCl_2$ is in part due to the greater electronegativity displayed by chloride compared to bromide or nitrate. The rapid exchange of water molecules with chloride ions also accounts for the greater shifting effect when the shift reagent is prepared from $CoCl_2$. The exchange of water and chloride or other anions is based on the structure of the complex, as outlined by Gillard and Phipps[10] and Evans et al.[11]

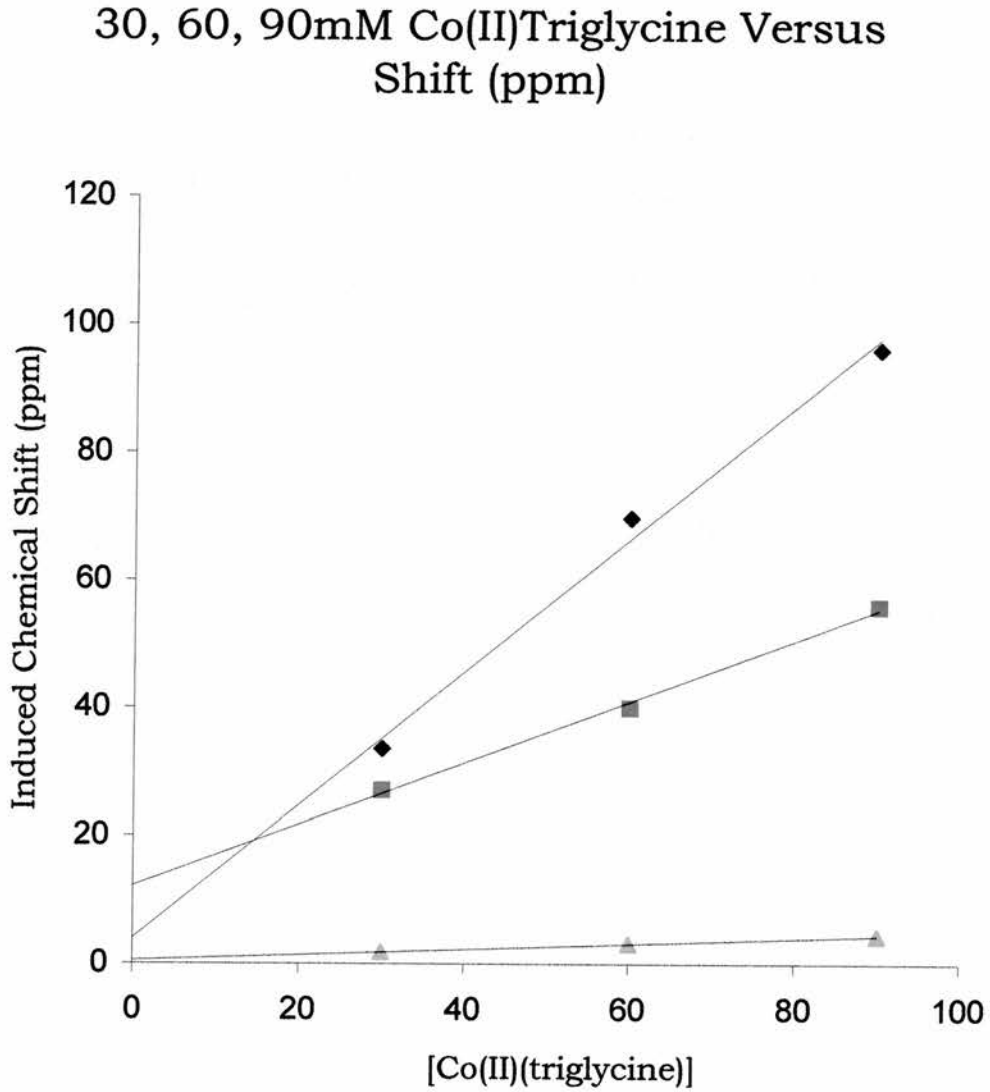

Figure 5.8 Plot of 30, 60, 90mM cobalt (II) triglycine versus Induced Chemical Shift (ppm). Diamond = $CoCl_2$; Square = $CoBr_2$; Triangle = $Co(NO_3)_2$;

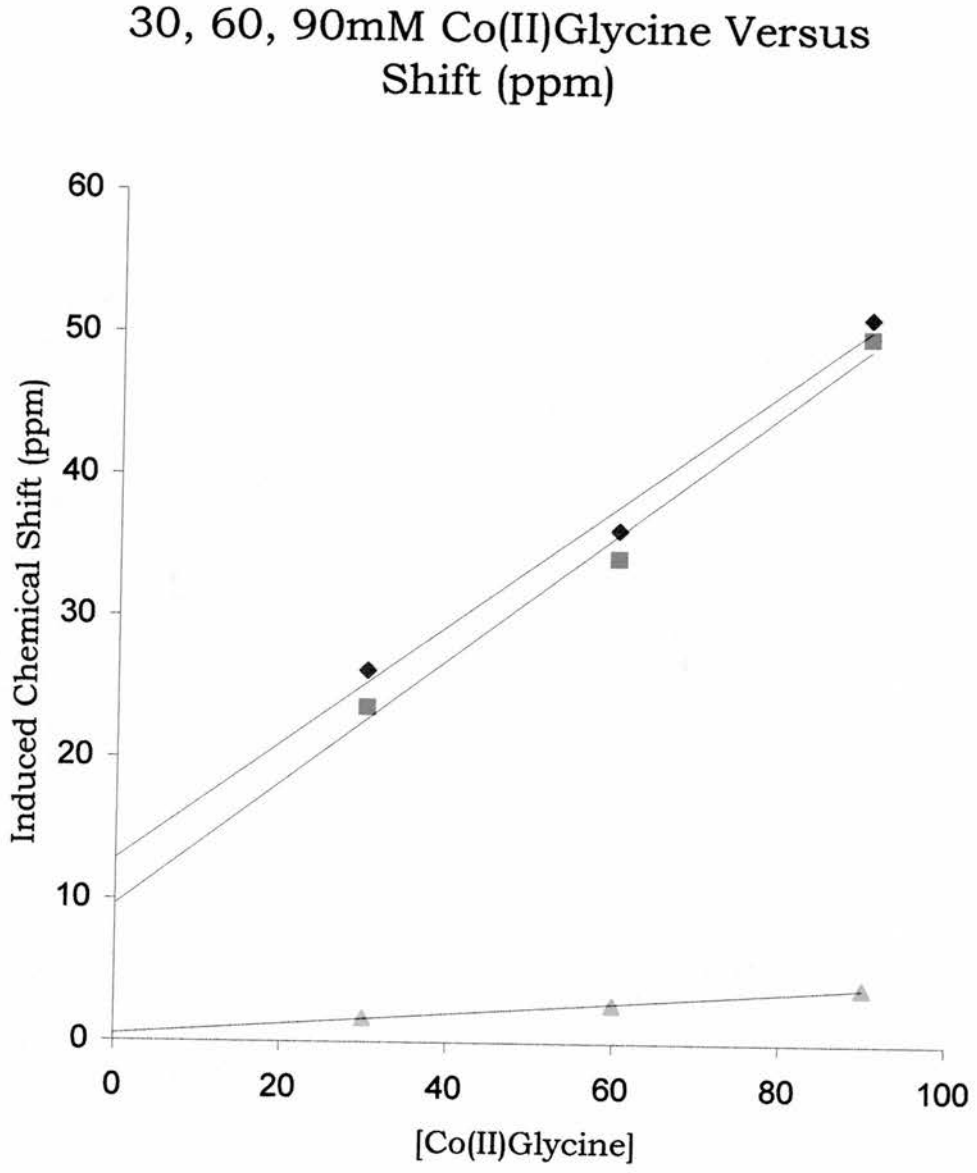

Figure 5.9 Plot of 30, 60, 90mM cobalt (II) (glycine)$_3$ versus Induced Chemical Shift)ppm). Diamond = $CoCl_2$; Square = $CoBr_2$; Triangle = $Co(NO_3)_2$;

30 mM [Co]	Shift (ppm)	ω ½ (Hz)
$CoCl_2$ / triglycine	33.6	654
$CoCl_2$ / 90 mM glycine	26.2	90
$CoBr_2$ / triglycine	27.1	1465
$CoBr_2$ / 90 mM glycine	23.6	611
$Co(NO_3)_2$ / triglycine	1.8	6
$Co(NO_3)_2$ / 90 mM gly	1.7	11

Table 5.2 Shifts in ppm for various combinations of cobalt salts with glycine and triglycine at 30 mM [Co].

60 mM[Co]	Shift (ppm)	ω ½ (Hz)
$CoCl_2$ / triglycine	69.7	1311
$CoCl_2$ / 180 mM gly	36.2	90
$CoBr_2$ / triglycine	40	2222
$CoBr_2$ / 180 mM gly	34.2	867
$Co(NO_3)_2$ / triglycine	3.2	10
$Co(NO_3)_2$/180 mM gly	2.7	25

Table 5.3 Shifts in ppm for various combinations of cobalt salts with glycine and triglycine at 60 mM [Co].

90 mM[Co]	Shift(ppm)	ω ½ (Hz)
$CoCl_2$ / triglycine	96.08	2226
$CoCl_2$ / glycine	51.24	260
$CoBr_2$ / triglycine	55.9	2900
$CoBr_2$ / glycine	49.9	1071
$Co(NO_3)_2$ / triglycine	4.443	15
$Co(NO_3)_2$ / glycine	3.9895	39

Table 5.4 Shifts in ppm for various combinations of cobalt salts with glycine and triglycine at 90mM[Co].

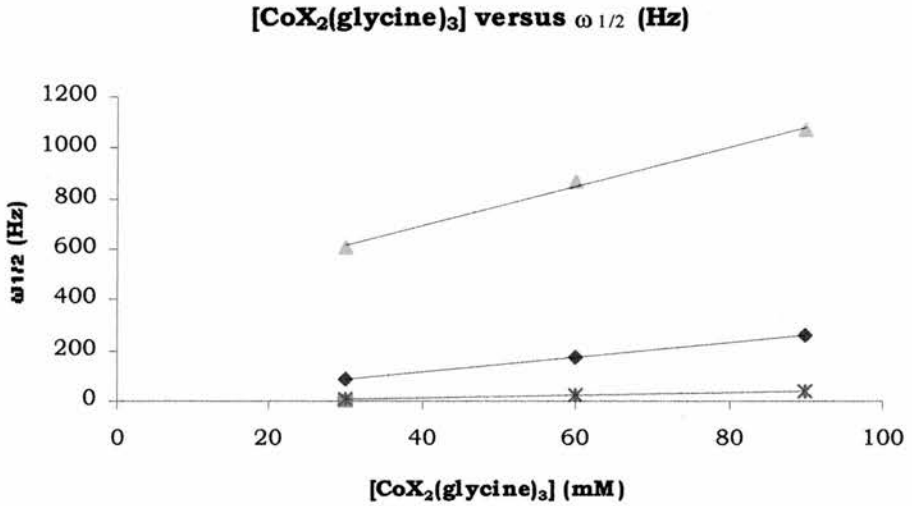

Figure 5.10 $[CoX_2(gly)_3]^-$ versus ω½ (Hz). Diamond = $CoCl_2$; Triangle = $CoBr_2$; Square = $Co(NO_3)_2$;

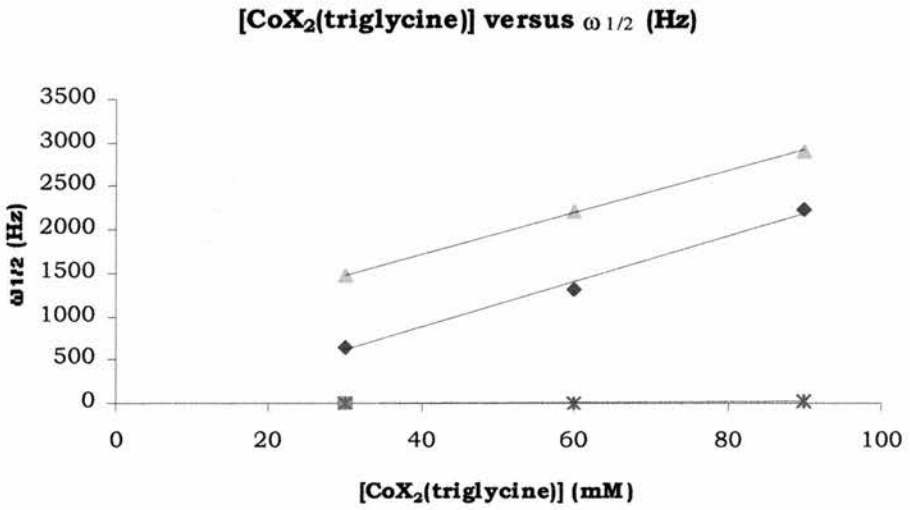

Figure 5.11 [CoX_2(triglycine)] versus ω½ (Hz). Diamond = $CoCl_2$; Triangle = $CoBr_2$; Square = $Co(NO_3)_2$;

The Co(II) nitrate / triglycine complexes were tested with sodium nitrate and sodium nitrite as a single sample. It was shown that Co(II) nitrate / triglycine could shift nitrate and nitrite signals, although the shifts induced were weak. ^{15}N-labelled sodium nitrite was used to allow the nitrogen NMR signals to be more easily identified.

5.9.2 Experiments at Varying pH

The Co (II) based contrast reagents were tested at varying pH by adding aliquots of dilute NaOH such that the pH of the Co (II) salt solution was between 5 and 8, in steps of 0.5. The shifts produced by specific amounts of reagent were plotted against increasing pH, and

the pH sensitivity of Co (II) salts as contrast reagents examined. The triglycine / $CoCl_2$ samples changed colour from purple to blue between pH 8.5 and 9.0, and the chemical shift difference between the two peaks dropped by half at this point. Cobalt (II) complexes are known to form pink / purple complexes with glyclglycinate chelated by the amino nitrogen and amide carbonyl oxygen. Near pH 10, Co^{2+} substitutes for the peptide hydrogen on two ligands to give the light blue bis tridentate complex.[12]

Also, between pH 8.5 and 9.0, a precipitate formed, which limits any potential biological applications of triglycine / $CoCl_2$ as a shift reagent. The precipitate (the last point in Figure 5.6 below) is thought to form when a weakly labile proton in triglycine dissociates in this pH range. Whether or not this is the case, there must be a major change in the chemistry around pH 8.5 – 9.0, with the formation of a different species

The results of this work are given below as graphs and tables.

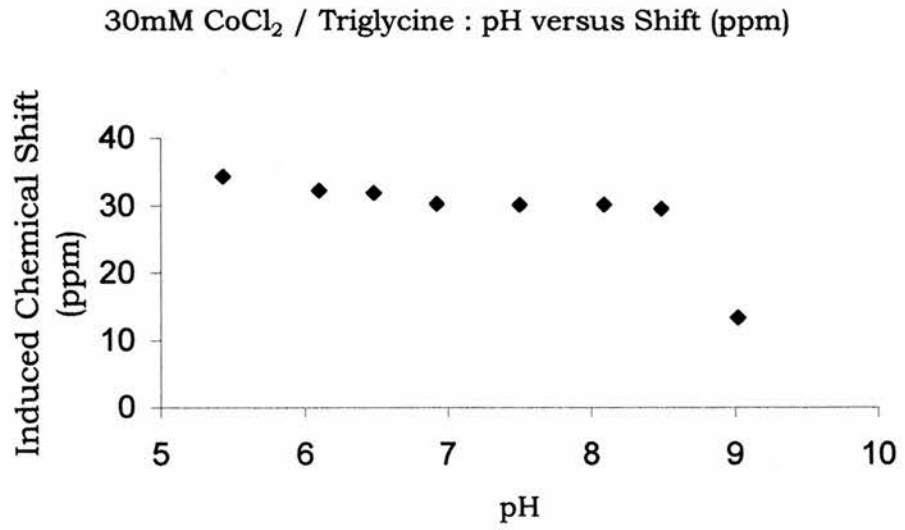

Figure 5.12 30 mM $CoCl_2$ / 30 mM Triglycine pH versus Shift (ppm)

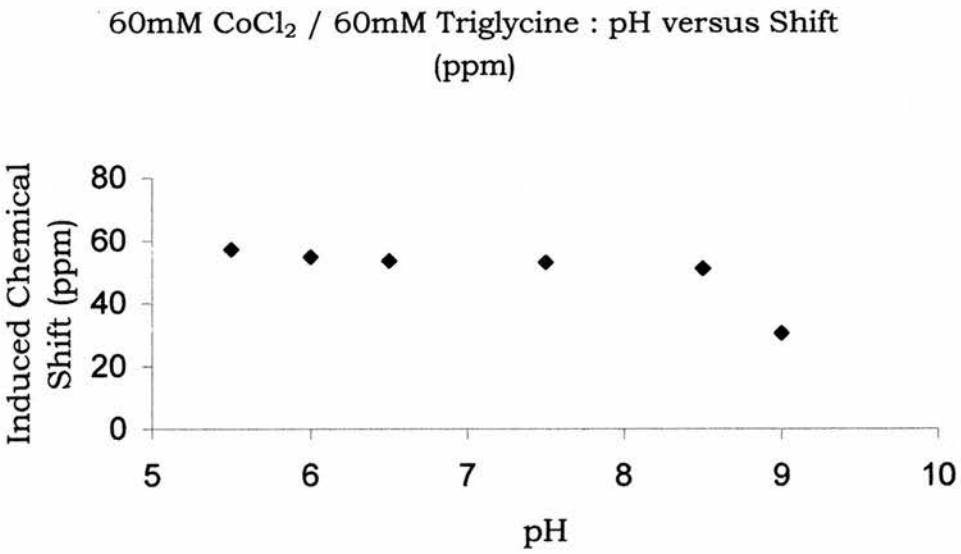

Figure 5.13 60 mM $CoCl_2$ / 60 mM Triglycine pH versus Shift (ppm)

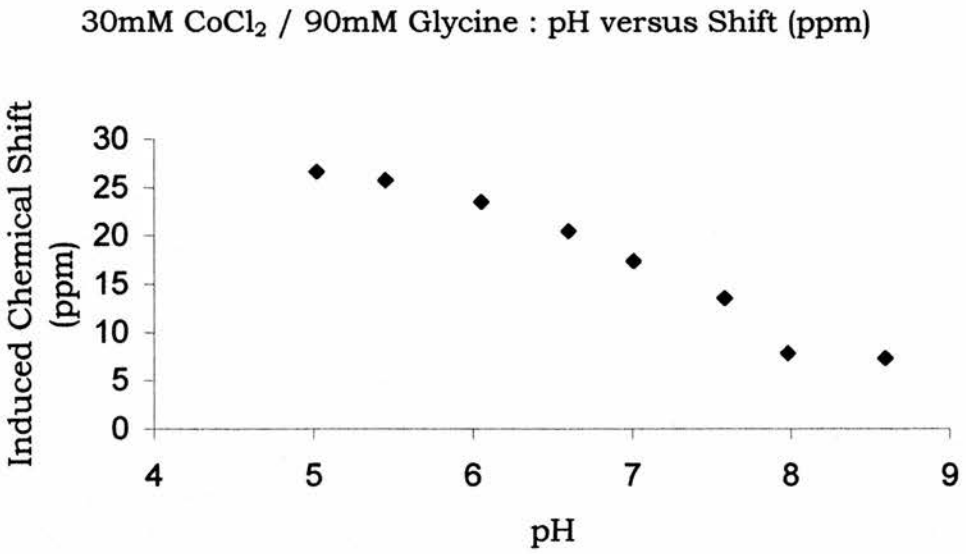

Figure 5.14 30 mM $CoCl_2$ / 90 mM glycine pH versus Shift (ppm)

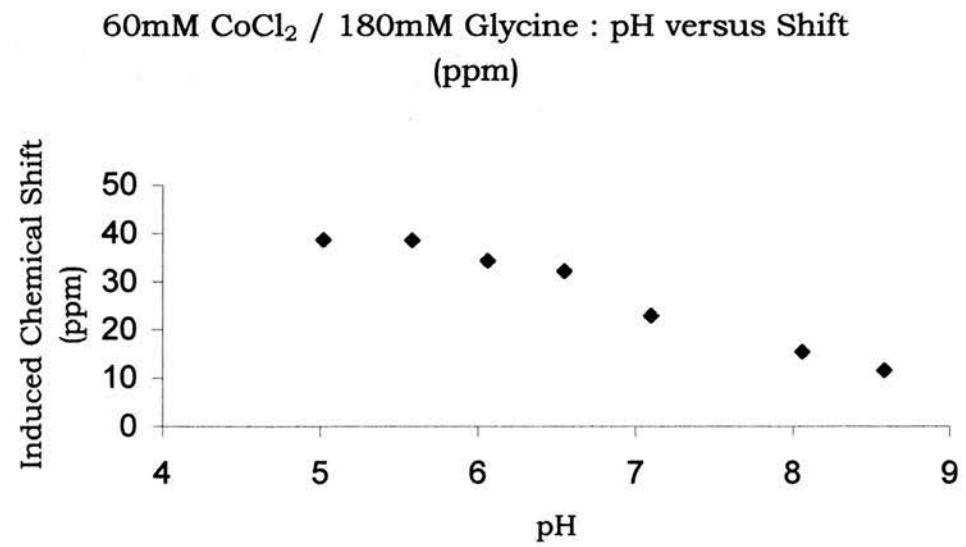

Figure 5.15 60 mM $CoCl_2$ / 180 mM glycine pH versus Shift (ppm)

30 mM pH	Induced Shift (ppm)
5.43	34.3
6.1	32.2
6.48	31.8
6.92	30.2
7.5	30.1
8.09	30.1
8.49	29.5
*9.02	13.4

Table 5.5 30 mM $CoCl_2$ / 30 mM Triglycine pH versus Shift (ppm) data

60 mM pH	Induced Shift (ppm)
5.5	57.3
6.0	54.7
6.5	53. 7
7.5	53.1
8.5	51.2
9.0	30.4

Table 5.6 60 mM $CoCl_2$ / 60 mM Triglycine pH versus Shift (ppm) data

30 mM pH	Induced Shift (ppm)
5.02	26.6
5.45	25.8
6.05	23.5
6.6	20.5
7.01	17.3
7.58	13.5
7.98	7.9
8.59	7.3

Table 5.7 30 mM $CoCl_2$ / 90 mM Glycine pH versus Shift (ppm) data

60 mM pH	Induced Shift (ppm)
5.02	38.7
5.58	38.5
6.06	34.3
6.55	32.2
7.1	22.9
8.06	15.4
8.58	11.6

Table 5.8 60 mM $CoCl_2$ / 180 mM Glycine pH versus Shift (ppm) data

5.9.3 Experiments With Vesicles

The graph below shows the linear relationship between the amount of cobalt (II) triglycine added to a 100 mM NaCl vesicle suspension and the induced shift of the external signal to higher field. The addition of shift reagent began at 200 μl, and continued in 25 μl amounts up to 400 μl. This stage of testing also demonstrated the suitability of cobalt (II) triglycine shift reagents for use in transport experiments with phosphatidylcholine vesicles.

No ionophore was added to the sample while the shift reagent was being tested. Simply leaving the sample in the spectrometer and acquiring a series of spectra over a 12-hour period examined the tolerance of the vesicles to cobalt (II) triglycine. At the end of this time, there were still two peaks in the spectrum, corresponding to the intravesicular (small) peak and the extravesicular (large) peak. The presence of the intravesicular signal suggests that the vesicles had not decomposed or burst through contact with cobalt (II) triglycine. It was therefore assumed that the vesicles could tolerate the shift reagent.

Furthermore there was no real change over time in the size of the intravesicular signal, which implies that the shift reagent does not penetrate the vesicles at an appreciable rate.

Amount of Shift Reagent Added (μl)	Induced Shift (ppm)
200	9.9
225	11.0
250	11.2
275	11.9
300	12.5
325	13.3
350	14.0
375	14.8
400	15.7

Table 5.9 Shifts induced upon additions of 30 mM Co(II)Triglycine to a 100 mM NaCl vesicle suspension.

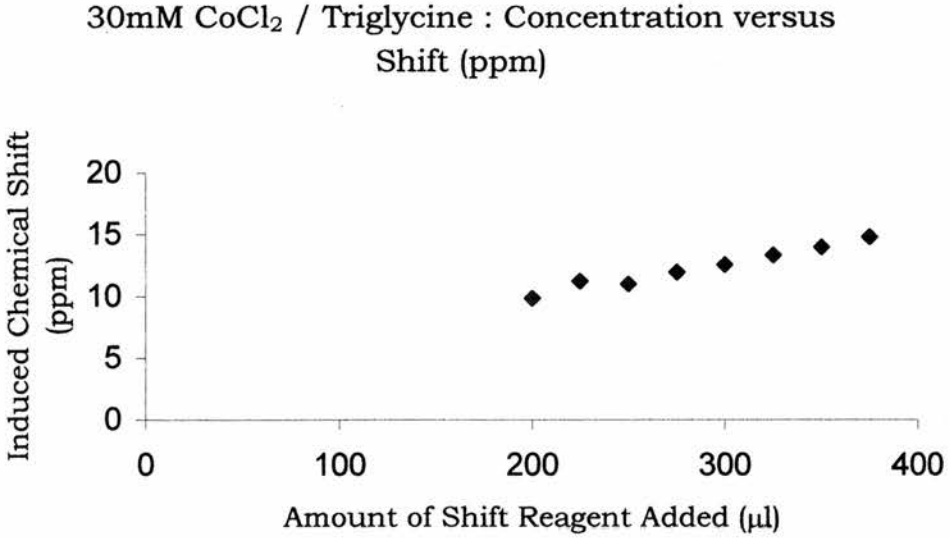

Figure 5.16 The shifts induced between intra and extravesicular ^{35}Cl signals upon addition of aliquots of 30 mM Co(II)Triglycine.

5.10 Summary

1. Cobalt (II) triglycine is an effective shift reagent for chloride, bromide, nitrate, and nitrite.

2. Vesicles made with the dialytic detergent removal technique are stable in the presence of cobalt (II) triglycine. The shift reagent has also been successfully used in ionophore mediated anion transport studies using vesicles.

3. The greatest shifts are produced when the pH of the cobalt (II) triglycine is unaltered, i.e. around pH 5.25.

4. Cobalt (II) triglycine produced from $CoCl_2$ provides a greater shift than cobalt (II) triglycine prepared from $CoBr_2$ or $Co(NO_3)_2$.

5. Cobalt (II) $(glycine)_3$ is also effective as a shift reagent but is not as powerful as cobalt (II) triglycine. At pH 5.43, the triglycine gave a shift of 34.27ppm, whereas the $(glycine)_3$ produced a shift of 25.77ppm.

6. This shift reagent would have offered an interesting alternative for the earlier chloride transport experiments with vesicles.

References

1. Gupta, R. K., Gupta, P., *Biophysical Journal*, **37**, 76a (1982)
2. Riddell, F.G., Southon T.E., *Inorganica Chimica Acta*, **136**, 133-137 (1987)
3. Pike, M. M., Springer, C. S. Jr., *Journal of Magnetic Resonance*, **46**, 348-353 (1982)
4. Ramasamy, R., Espanol, M. C., Long, K. M., Mota de Freitas, D., *Inorganica Chimica Acta*, **163**, 41-52 (1989)
5. Nieuwenhuizen, M. S., Peters, J. A., Sinnema, A., Kieboom, A. P. C., van Bekkum, H., *Journal of the American Chemical Society*, **107**, 12-16 (1985)
6. Watanabe, M., Hasegawa, T., Miyake, H., Kojima, Y., *Chemistry Letters*, 4-5 (2001)
7. Monchaud, D., Lacour, J., Coudret, C., Fraysse, S., *Journal of Organometallic Chemistry*, **624**, 388-391 (2001)
8. Shachar-Hill Y., Shulman R.G., *Biochemistry*, **31**, 27, 6273-6278 (1992)
9. Mota de Freitas, D., Lin, W., *Magnetic Resonance in Chemistry*, **34**, 768-772 (1996)
10. Gillard, R. D., Phipps, D. A., *Journal of the Chemical Society (A)*, 1074-1082 (1971)
11. Evans, E.J., Grice, J. E., Hawkins, C. J., Heard, M. R., *Inorganic Chemistry*, **19**, 3496-3502 (1980)
12. Riddell, F. G., *Encyclopedia of Spectroscopy and Spectrometry*, Academic Press, London, Lindon, J. C.,

Tranter, G. E., Holmes, J. L. 677-684 (1999); Merbach, A. E., Toth, E., (Editors), *The Chemistry of Contrast Agents in Medical MRI*, 2001John Wiley & Sons, Ltd.

13. Sigel, H., Martin, R. B., *Chemical Review*, **82**, 385 (1982)

Chapter 6

The Assignment of the ^{1}H NMR Spectra of the Alkali Metal Salts of Nigericin

Chapter 6

The Assignment of the ^{1}H NMR Spectra of the Alkali Metals Salts of Nigericin

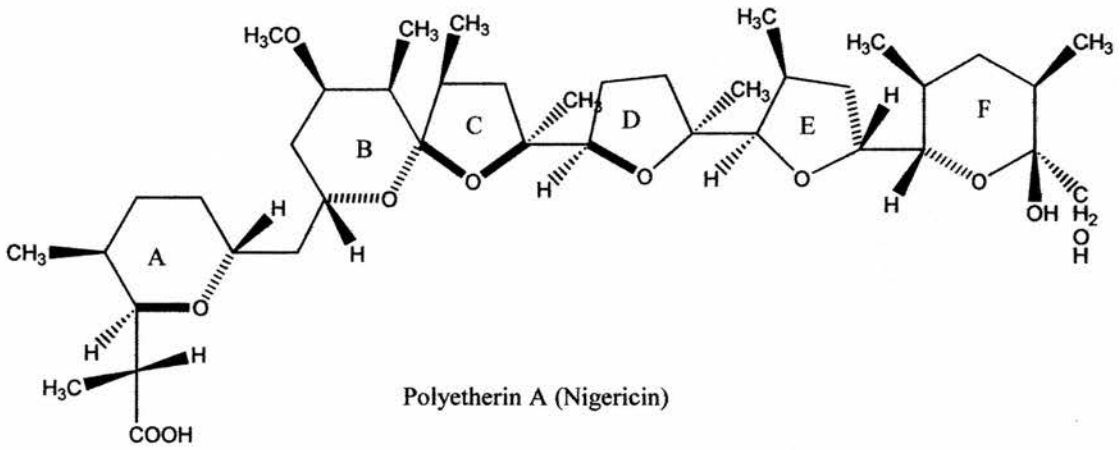

Polyetherin A (Nigericin)

Figure 6.1 – Nigericin free-acid

6.1 Introduction

Nigericin is an ionophoric mono-carboxylic polyether with antibiotic properties, and is capable of forming complexes with alkali metal cations. Nigericin was isolated from the culture of *Streptomyces hygroscopicus* strain E749 in 1968.[1] Like many similar ionophores such as monensin and valinomycin, nigericin was found to be active as an antibiotic[2] (against Gram positive bacteria, including mycobacteria, and phytopathogenic fungi).

X-ray crystallographic studies[3-7] and NMR techniques[8-12] were used to elicit information about the structures and conformations of this and other ionophores, thereby furthering understanding of the complexation mechanism, and providing insight into biologically important transport process at atomic and molecular levels.

6.2 NMR Structural and Conformational Studies

Some of the possible solution state conformations of Nigericin in both the free-acid and sodium salt forms, along with an almost complete assignment of the 300 MHz ^{1}H NMR spectrum were published in 1977 by Rodios and Anteunis.[9] Both forms displayed almost identical structural and conformational features. Head-to-tail buttoning of the molecule, as predicted by x-ray crystallographic data, was confirmed.[9, 10] In complexed forms hydrogen bonding between the tertiary hydroxyl group (OH-9) and one of the carboxylate oxygens maintains the head-to-tail-buttoning. At least five oxygen atoms are implicated in the coordination of cation. These are O1, O5, O11, O6 and O7, and participation of O8 cannot be ruled out.

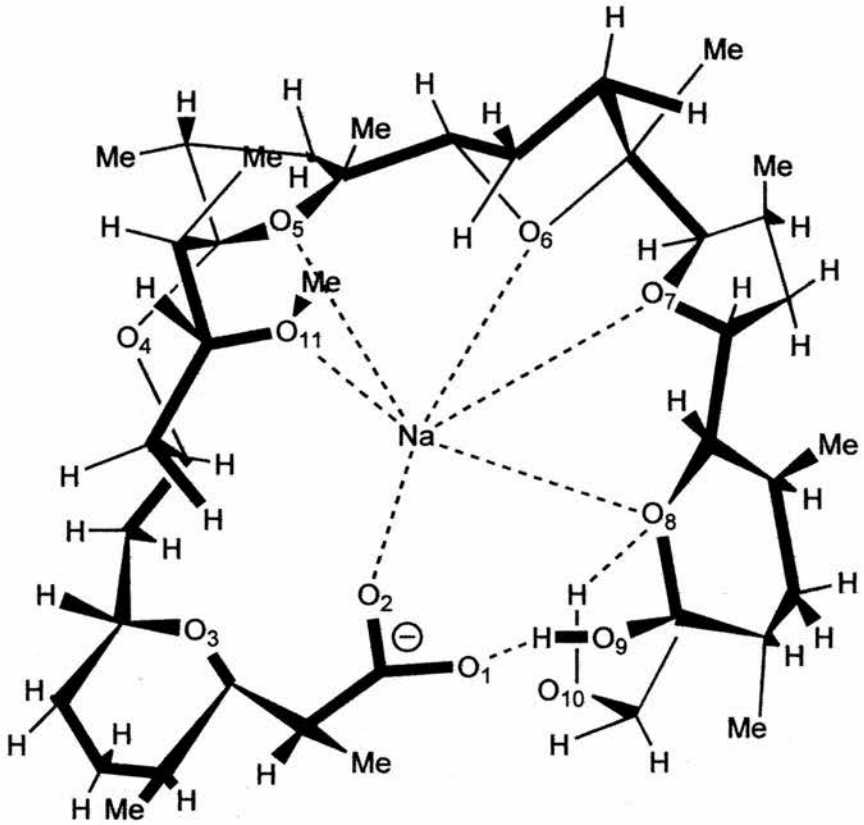

Figure 6.2 A stereodrawing of sodium nigericin, showing the oxygen atoms involved in cation binding. The image was copied from solid state x-ray diffraction data.[4]

Rodios and Anteunis noted that both monensin and nigericin are open non-pseudocyclic conformers in protic solvents such as methanol.[10] Significant changes in the intensity of peaks, and much smaller changes in chemical shift were observed in the region 1.0 to 4.5 ppm in the ^1H spectrum of both ionophores upon heating, and

when the spectrum was recorded more than 48 hours after the sample was prepared.[10]

The stoichiometry of the nigericin / cation complex[13] has been shown to change with pH; such that an acidic pH promotes a transition from dimeric 2 : 1 nigericin : cation stoichiometry to the trimeric form. While the dimeric and trimeric forms of nigericin may indeed exist (at very low metal ion concentrations and at low pH), there is overwhelming evidence for the 1:1 monomeric complex from X-ray crystallographic studies[3-4], and NMR structural[9-12] and transport studies (see Table 6.1 below).

Sample of nigericin-potassium complex	Nigericin/K^+ ratio
1. Untreated	1.21 ± 0.01
2. Adjusted to pH 6 to 8	2.02 ± 0.02
3. Adjusted to pH 4	3.08 ± 0.17

Table 6.1 The stoichiometry of nigericin-potassium varies with pH. The 1:1 stoichiometry is observed when the pH is unadjusted.[13]

Toro et al[13] likened the ^1H shifts for the free-acid to those of the Na^+ salt, as reported by Rodios and Anteunis.[9] The work reported within this Thesis finds the proton shifts of the Na^+ salt to be

significantly closer to those of the K^+ salt than to those of the free-acid.

In 1994 Beloeil et al[11] used ROESY NMR (Rotating Frame Overhauser Effect Spectroscopy) to obtain inter-atomic distances and dihedral angle constraints (using the assignments provided by Rodios and Anteunis[9]) as part of a conformational analysis of the sodium and potassium salts of nigericin. They concluded that the potassium salt has a wider cage than the sodium salt and that calculated structures were more compact for the sodium salt than for the potassium salt, as expected with the increasing ionic radius from Na^+ to K^+, and in agreement with x-ray data. This can be seen in Table 6.2 below.

Metal Ion	Radius (pm)	Percentage Increase (%)
Li^+	90	-
Na^+	116	28
K^+	152	31
Rb^+	166	9
Cs^+	188	13

Table 6.2 Increase in ionic radius (pm) going down Group 1. The percentage increase in ionic radius for successively heavier metals is also given.

6.3 X-ray Crystallographic Studies

The crystal structure of the silver salt of Polyetherin A ($C_{40}H_{68}O_{11}$), derived from 3D *X*-ray diffraction methods, was published in 1968.[3] In 1970 the same Japanese researchers gave a more detailed account of the structure of the silver salt of Polyetherin A[4], which proved to be identical to that of nigericin, and bore a strong resemblance to the structure of monensin. Furthermore the torsion angles within the complexes show that a large part of both nigericin and monensin (rings A to E) have the same conformations. Indeed, nigericin has been described as the archetypal potassium carrying carboxylic ionophore, with monensin being its sodium-favouring counterpart.

The main differences between nigericin and monensin lie in the way in which they co-ordinate to the metal cation and the hydrogen-bonding scheme used to hold the complex together. Nigericin uses a combination of five oxygens (from ether, hydroxyl and carboxylate groups) during cation co-ordination, whereas monensin uses 6 oxygens, the extra one coming from ring A.

The naturally occurring carboxylic ionophores have several general structural features, the most apparent being the connected tetrahydrofuran and tetrahydropyran ring systems which house the oxygen atoms used during co-ordination with the metal cation. These

ionophores also have terminal hydroxyl group(s) at one end, and one or more carboxyl groups at the other.

Crystal structure studies show head-to-tail hydrogen bonding between the terminal carboxylic group(s) and the hydroxyl function(s) of the terminal tetrahydrofuran rings. This allows the ionophore to encapsulate the metal cation in a snug cavity and protects it from unfavourable interaction with hydrophobic media. The extra tetrahydropyran ring in nigericin forces a carboxyl group directly into the cation complexation cavity, thereby involving this group in cation co-ordination. The oxygen atoms from monensin and nigericin that participate in cation co-ordination are indicated in Figure 6.3 below.

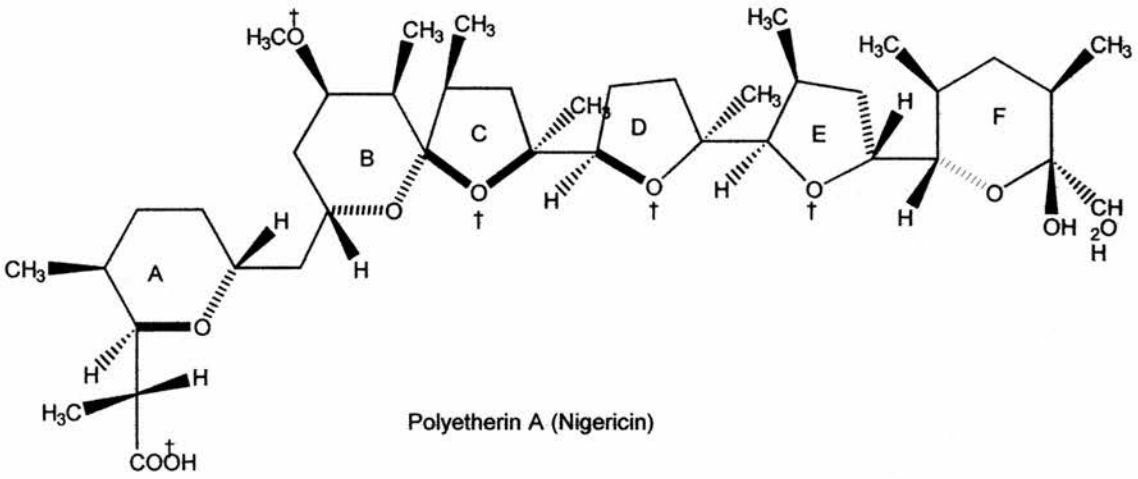

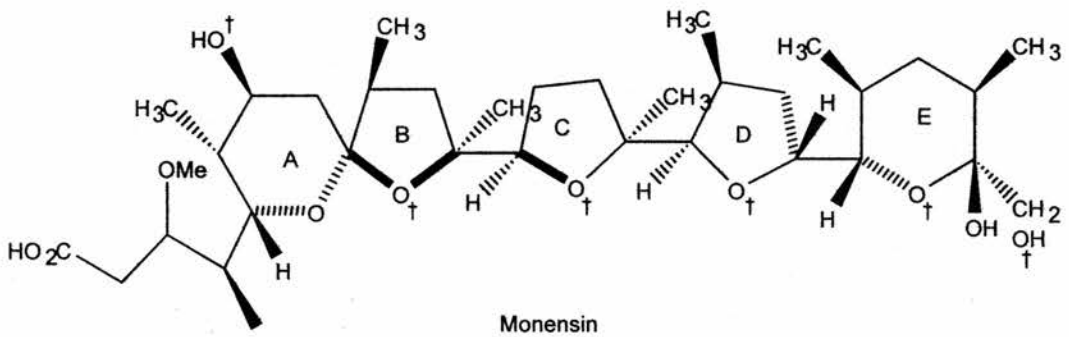

where † indicates an oxygen atom involved in cation coordination

Figure 6.3 – The ligating oxygen atoms of nigericin and monensin

The conformations of the free acid and the salt forms have been shown to be significantly different, with changes both to the carboxylic functionality, a tetrahydrofuran ring, and the hydrogen-bonding scheme responsible for head-to-tail connectivity. The structures of the sodium and potassium salts of nigericin have been studied and show an increase in cavity size in accord with the increasing ionic radii.

Nigericin has been shown to form stable complexes with lithium and caesium.[12]

6.4 Nigericin-Mediated Cation Transport

There are several stages to the complexation of a small metal cation by a carboxylic ionophore such as nigericin. At physiological pH the terminal carboxylic acid will be dissociated. First, the ionophore is believed to sit inside the membrane with its terminal carboxylate group projecting into the external medium. It is one of the oxygen atoms in this group that initially makes contact with the solvated metal cation. The cation becomes engulfed as the water molecules associated with the metal cation are stripped away one at a time. When the last water molecule has been displaced, the zwitterionic complex diffuses to the other side of the membrane and releases the cation, which resolvates, again in a stepwise manner.

The now negatively charged ionophore can either pick up another metal cation or a proton, diffuse back into the membrane, and release the species at the first interface, thereby restoring the original conditions. The net result of these electrically neutral processes is exchange of a singly charged cation for another.

Pressman and Painter[2] showed that at concentrations below 10^{-7} M and at neutral pH, the transport of sodium and potassium catalysed by nigericin occurs through monomeric 1:1 electrically neutral complexes. At ionophore concentrations above 10^{-7} M, cation transport across lipid membranes proceeds via dimeric forms of nigericin. Toro et al[13] showed that at concentrations above 10^{-7} M nigericin and at acid pH, nigericin aggregates into trimers to transport K^+ across the hydrophobic membrane interior in a process that involves a net charge transfer. Importantly, untreated samples of the nigericin-potassium complex in $CDCl_3$ show the familiar 1:1 stoichiometry.

The results of nigericin-mediated transport of sodium and potassium ions through phosphatidylcholine bilayer membranes studied by ^{23}Na and ^{31}K NMR was published in 1988 by Riddell et al.[16] They found that nigericin actually transported sodium more quickly than potassium under the experimental conditions used. This was a consequence of the nigericin / Na complex having a more rapid dissociation rate than monensin / Na, which in turn leads to a reduction in the rate of sodium transport caused by competing potassium (Tables 6.3 and 6.4 below). It was also shown that membrane transport under the conditions employed occurred through a 1:1 complex for Na^+ and K^+.

$[Na^+]$ (M)	Monensin mediated k x 10^{-4} (mol PC.mol monensin^{-1}.s^{-1})	Nigericin mediated k x 10^{-4} (mol PC.mol nigericin^{-1}.s^{-1})
0.100	1.274	2.23
0.150	0.869	1.70
0.200	0.612	1.52

Table 6.3 Rate constants for sodium transport in EPC vesicles by monensin and nigericin. [14, 16]

$[K^+]$ (M)	Monensin mediated k x 10^{-4} (mol PC.mol monensin^{-1}.s^{-1})	Nigericin mediated k x 10^{-4} (mol PC.mol nigericin^{-1}.s^{-1})
0.075	1.685	1.18
0.100	1.533	0.9

Table 6.4 Rate constants for potassium transport in EPC vesicles by monensin and nigericin.[14, 16]

The activation energy E_a for the overall process of monensin and nigericin mediated transport of sodium was determined by following the temperature variation of the line width of the $sodium_{(in)}$ signal. Line broadenings at various temperatures were calculated from the observed line width minus the natural line width of the same sample at that temperature. The activation energy can then be derived from

the Arrhenius equation. For monensin E_a was 7.8 ± 0.13 kcal.mol^{-1}, and for nigericin E_a was 8.21 ± 0.28 kcal.mol^{-1}.

The stability constants at room temperature for lithium, sodium, potassium, rubidium and caesium nigericin salts are given in Table 6.5 below. The stability constants are very dependent on the solvent polarity.

Nigericin–Alkali Metal Complex	Log K_s	ΔG^o(kcal/mol^{-1})
Lithium	4.16 ± 0.3	-5.62
Sodium	3.91 ±0.2	-5.34
Potassium	3.70 ± 0.1	-5.05
Rubidium	3.70 ± 0.2	-5.05
Caesium	3.82 ± 0.3	-5.27

Table 6.5 Stability constant K_s and ΔG^o values for nigericin-alkali metal cation complexes.[12] The measurements were made with nigericin-free acid dissolved in a 1, 4-dioxane / H_2O homogenous solution using potentiometric titration at room temperature.

Of the naturally occurring polyether antibiotics, (including nigericin, monensin, valinomycin, salinomycin, dianemycin, lasalocid, and grisorixin) the structure of nigericin most closely resembles that of grisorixin[17-18] and monensin[10, 19-21] as can be seen in Figure 6.4 below.

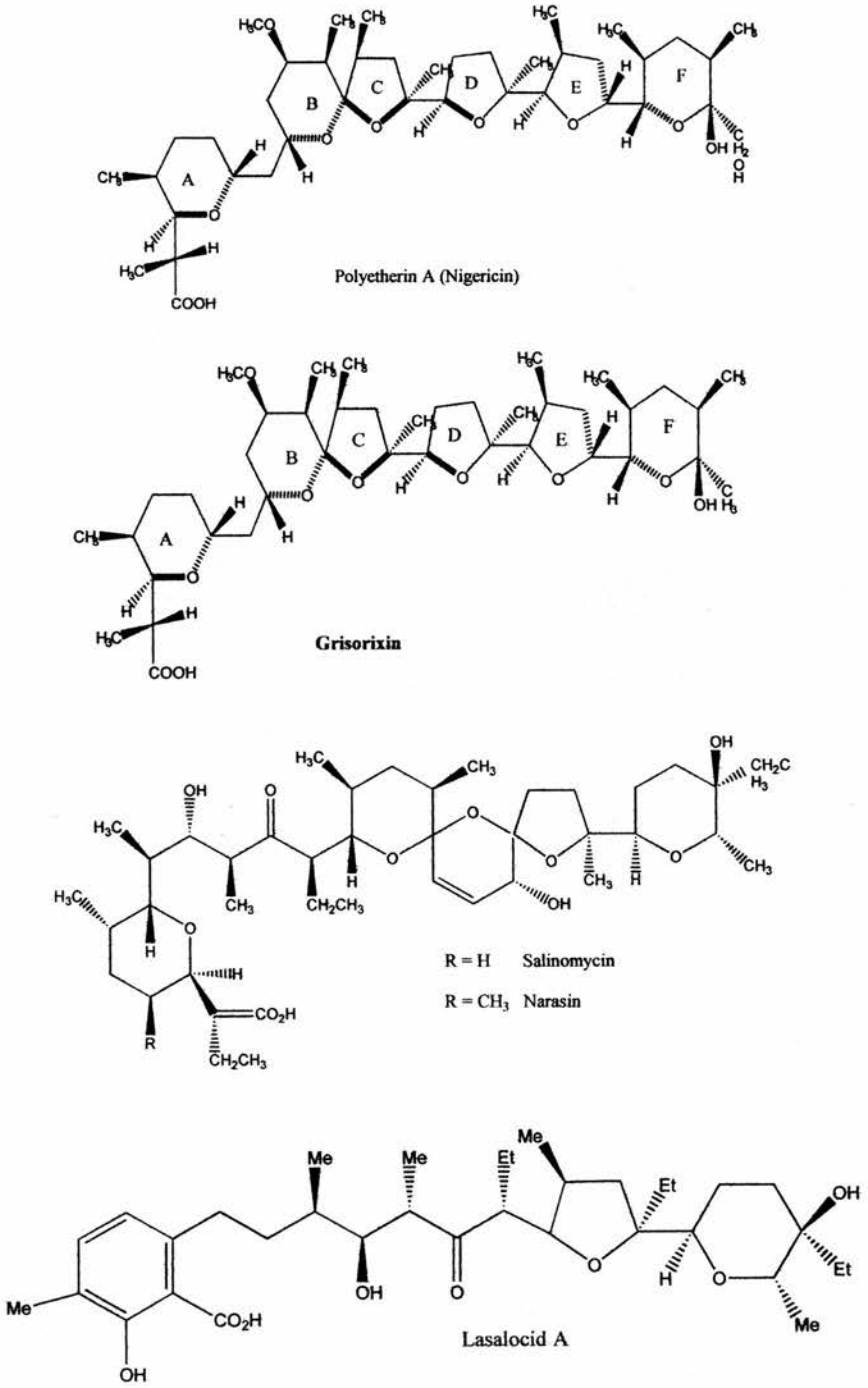

Figure 6.4 – Some of the naturally-occurring polyether antibiotics.

The results of ionophore-mediated transport of sodium and potassium by six of the polyether antibiotics allowed the extraction of rate constants for complex formation and dissociation and an overall stability constant for each ionophore-cation complex.

	Sodium			Potassium		
Ionophore	$K_f \times 10^4 s^{-1}$	$K_d \times 10^4 M s^{-1}$	Ks M^{-1}	$K_f \times 10^4 s^{-1}$	$K_d \times 10^4 M s^{-1}$	Ks M^{-1}
Nigericin	7.84	0.35	22.0	9.61	0.10	96.0
Monensin	4.88	0.15	32.6	2.30	0.43	5.3
Salinomycin	2.61	0.43	6.1	28.3	1.39	20.4
Narasin	5.86	0.54	11.0	14.7	1.67	8.8
Cationomycin	1.88	0.16	12.1	10.5	0.17	62.9
Tetronasin	20.52	0.86	24.0	5.65	0.80	7.0

Table 6.6 The dissociation and formation rate constants and the stability constants for the sodium and potassium complexes of some polyether antibiotics.[14]

6.5 Experimental

6.5.1 NMR Sample Preparation of Nigericin salts

The nigericin sodium salt was obtained from Sigma Aldrich Co. Ltd. 5 mg amounts were dissolved in 1 cm^3 of $CDCl_3$. To this 2 cm^3 of a saturated aqueous lithium chloride or sodium/ potassium carbonate solution was added and the mixture was stirred for 1 hour in a small

glass bottle containing a small magnetic stirrer bar at a vigorous speed. After stirring the mixture was allowed to settle for approximately 15 minutes. During this time a lengthened Pasteur pipette was plugged with a small piece of cotton that had been soaked in the appropriate metal solution. To this, a small quantity of anhydrous metal chloride / carbonate was added, and the tip of the pipette was placed into the NMR tube, held upright in a clamp.

The dissolved nigericin salt collected in the bottom organic layer of the sample tube, with the aqueous layer above. The $CDCl_3$ layer was then dropped into the Pasteur pipette filter in the NMR sample tube. The remaining aqueous layer was washed with a small amount of $CDCl_3$ which was then filtered and dried. More $CDCl_3$ was added to top up the solution in the NMR sample tube to around 6 cm. The NMR sample tube containing the $CDCl_3$ solution was degassed by lengthening a Pasteur pipette to a capillary tube, attaching it to an oxygen-free N_2 gas bottle, and allowing N_2 gas to bubble through. After bubbling for approximately five minutes the tube was sealed with a plastic cap and thereafter kept refrigerated.

6.5.2 NMR Spectra of Nigericin

One-dimensional ^1H NMR spectra of the lithium, sodium, potassium, rubidium and caesium salts of nigericin in $CDCl_3$ were recorded at 303 K on Varian 300 MHz and Varian 500 MHz spectrometers in the Department of Chemistry, University of St Andrews. Two-dimensional COSY and NOESY experiments (see Chapter Two for descriptions) were carried out on all five nigericin complexes. Using the assignments[2, 3] from Rodios and Anteunis, most of the peaks in the one-dimensional ^1H spectra were identified, and where necessary, the chemical shifts were corrected.

The cross peaks in the COSY spectra were assigned to specific protons in nigericin. This enabled the pattern of scalar couplings to be deduced, and following this the NOESY cross peaks were identified and integrated to establish the relative distances between protons through space. Starting with the assignments and scalar coupling patterns from sodium nigericin, proton chemical shifts for the remaining salts were derived through COSY experiments.

The ^1H NMR spectra for the lithium, sodium, potassium, rubidium and cesium nigericin salts are given below. They are followed by the 500 MHz COSY spectra of the lithium, sodium, potassium and rubidium complexes.

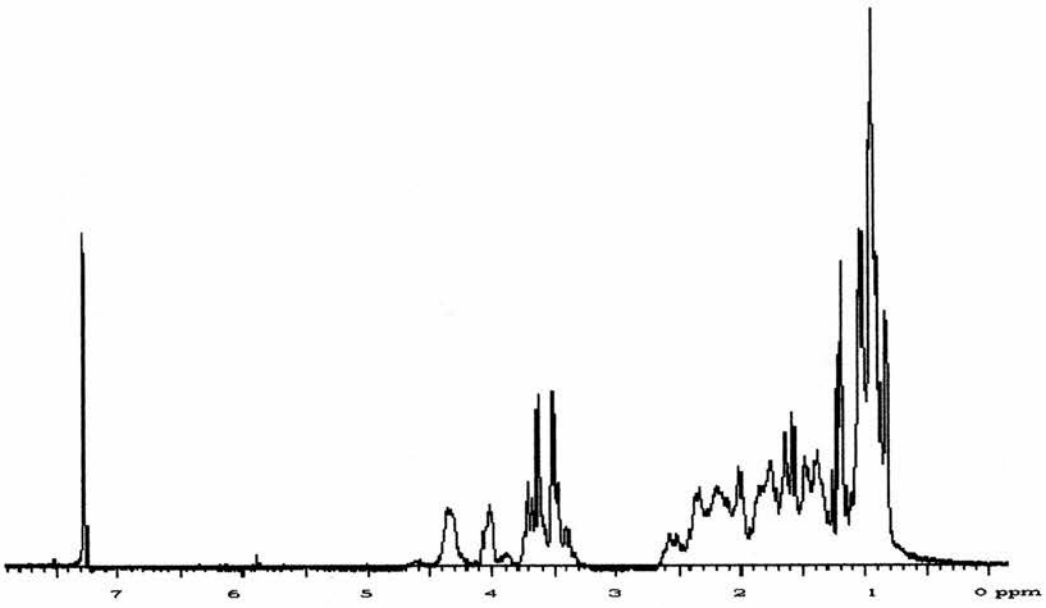

Figure 6.5 The 300 MHz ^{1}H NMR spectrum of lithium nigericin

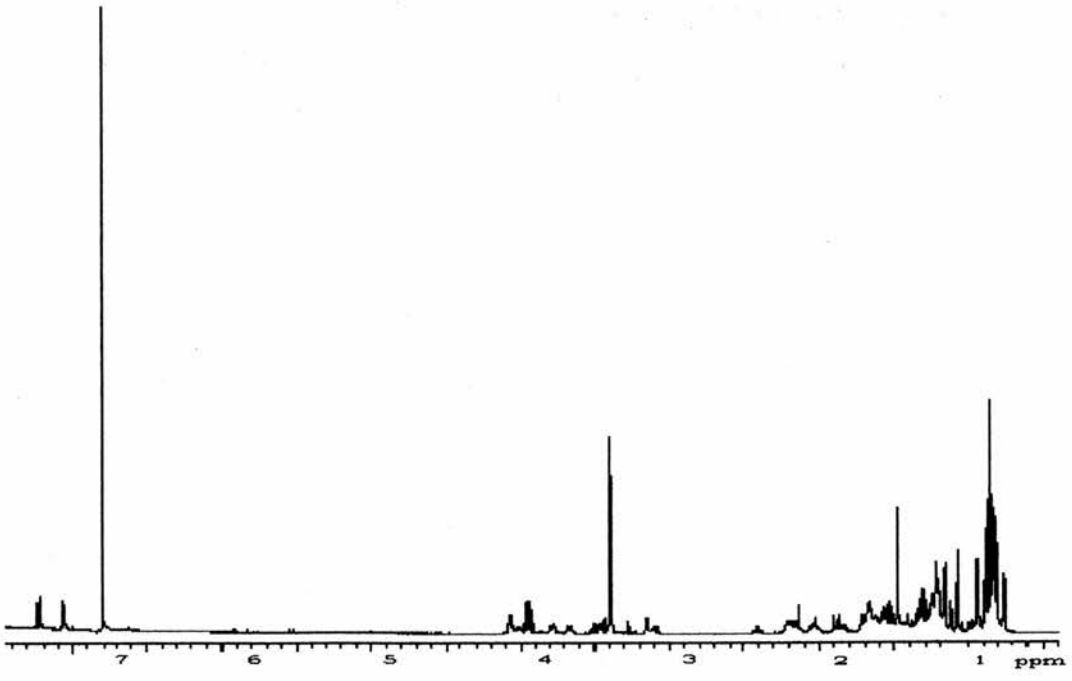

Figure 6.6 The 500 MHz ^{1}H NMR spectrum of sodium nigericin

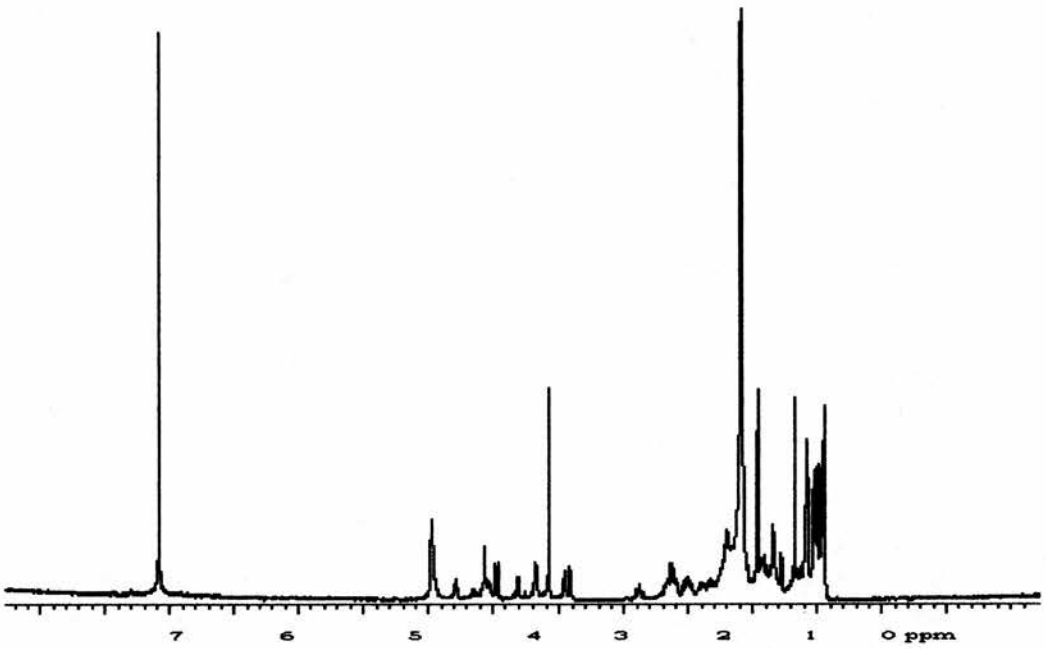

Figure 6.7 The 500 MHz ^{1}H NMR spectrum of potassium nigericin

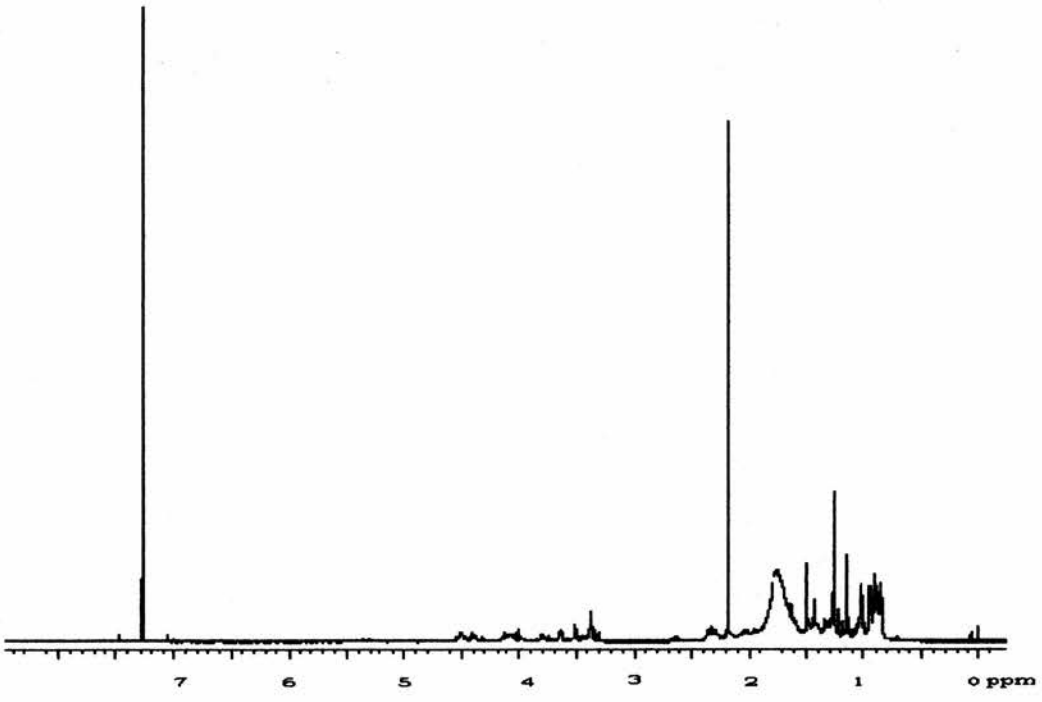

Figure 6.8 The 300 MHz ^{1}H NMR spectrum of rubidium nigericin

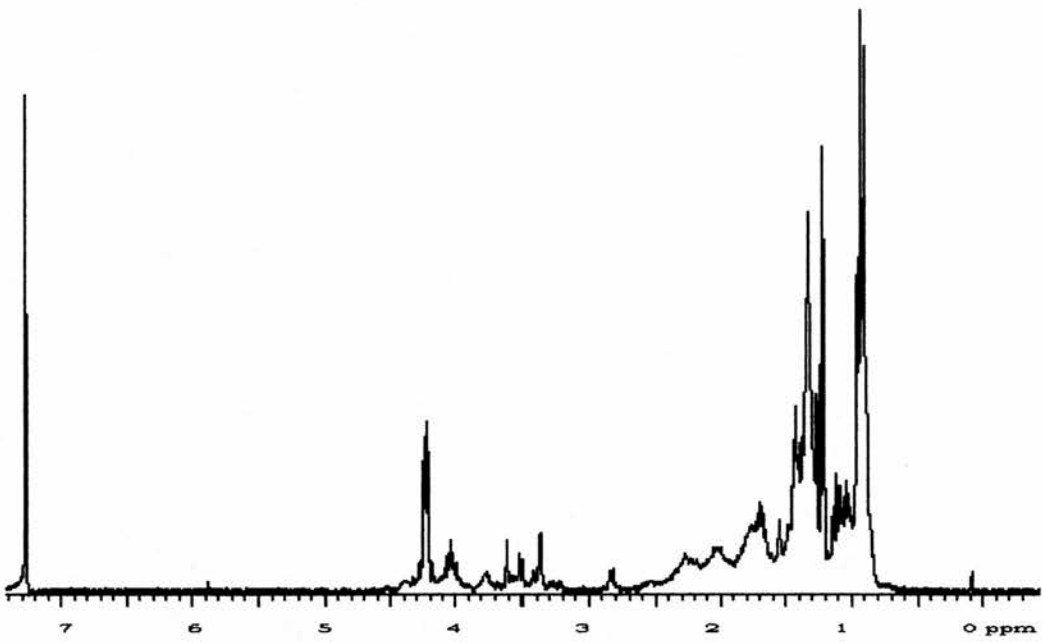

Figure 6.9 The 300 MHz ^{1}H NMR spectrum of cesium nigericin

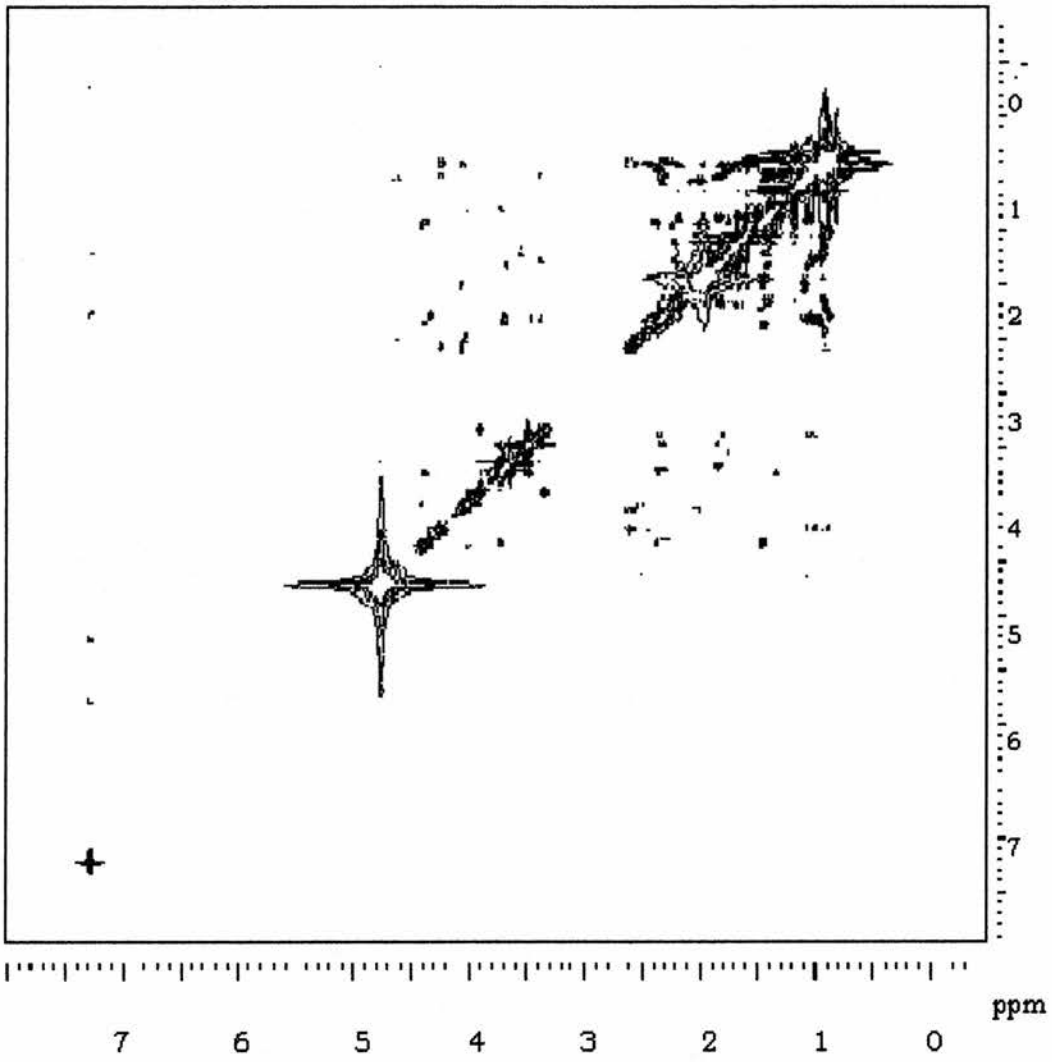

Figure 6.10 The 500 MHz COSY spectrum of lithium nigericin

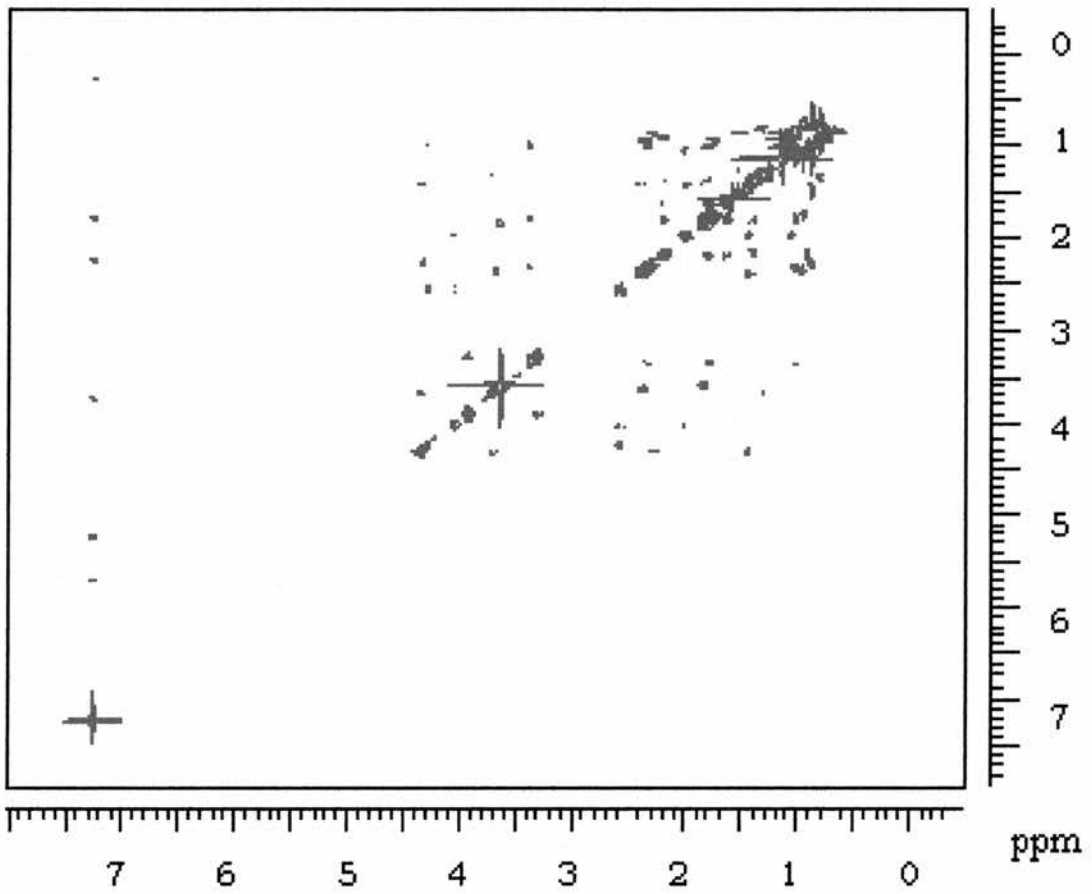

Figure 6.11 An expanded region of the 500 MHz COSY spectrum of sodium nigericin.

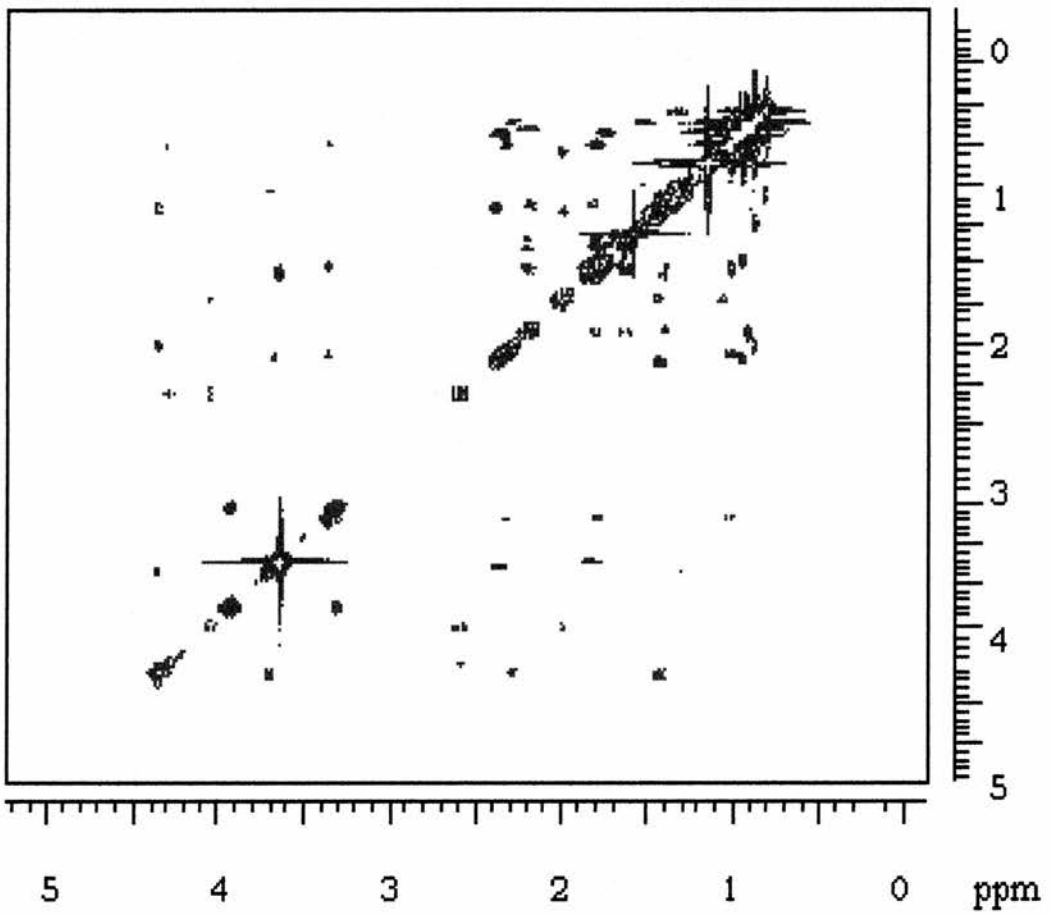

Figure 6.12 An expanded region of the 500 MHz COSY spectrum of potassium nigericin.

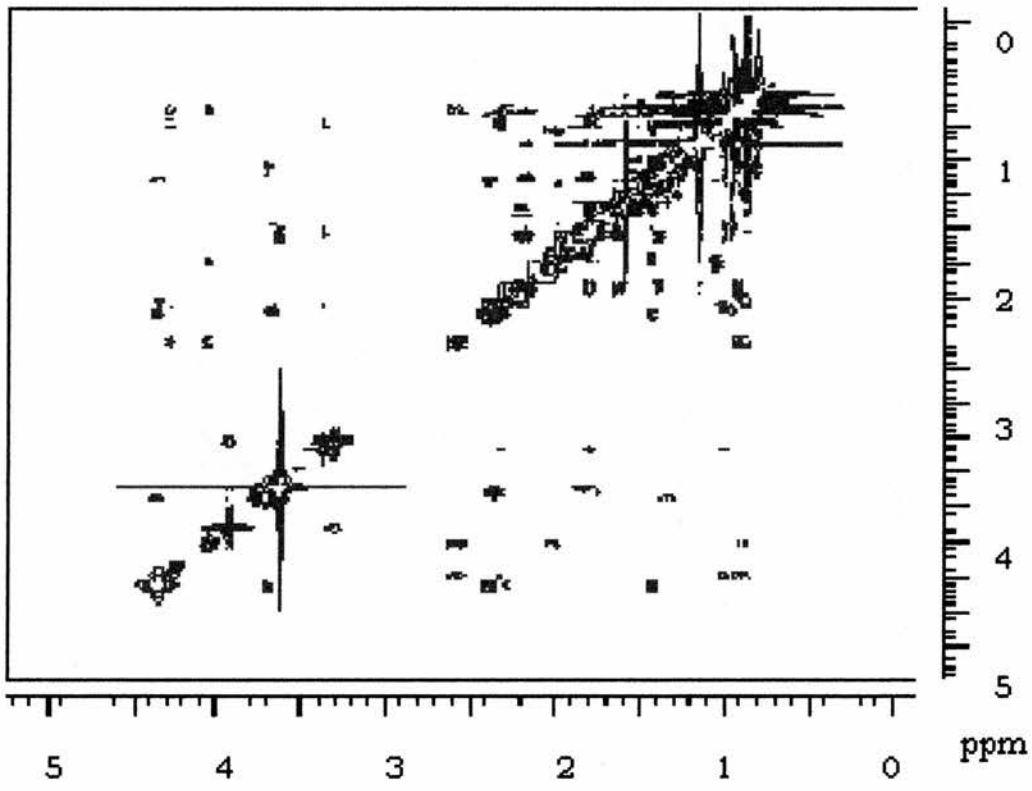

Figure 6.13 The 500 MHz COSY spectrum of rubidium nigericin.

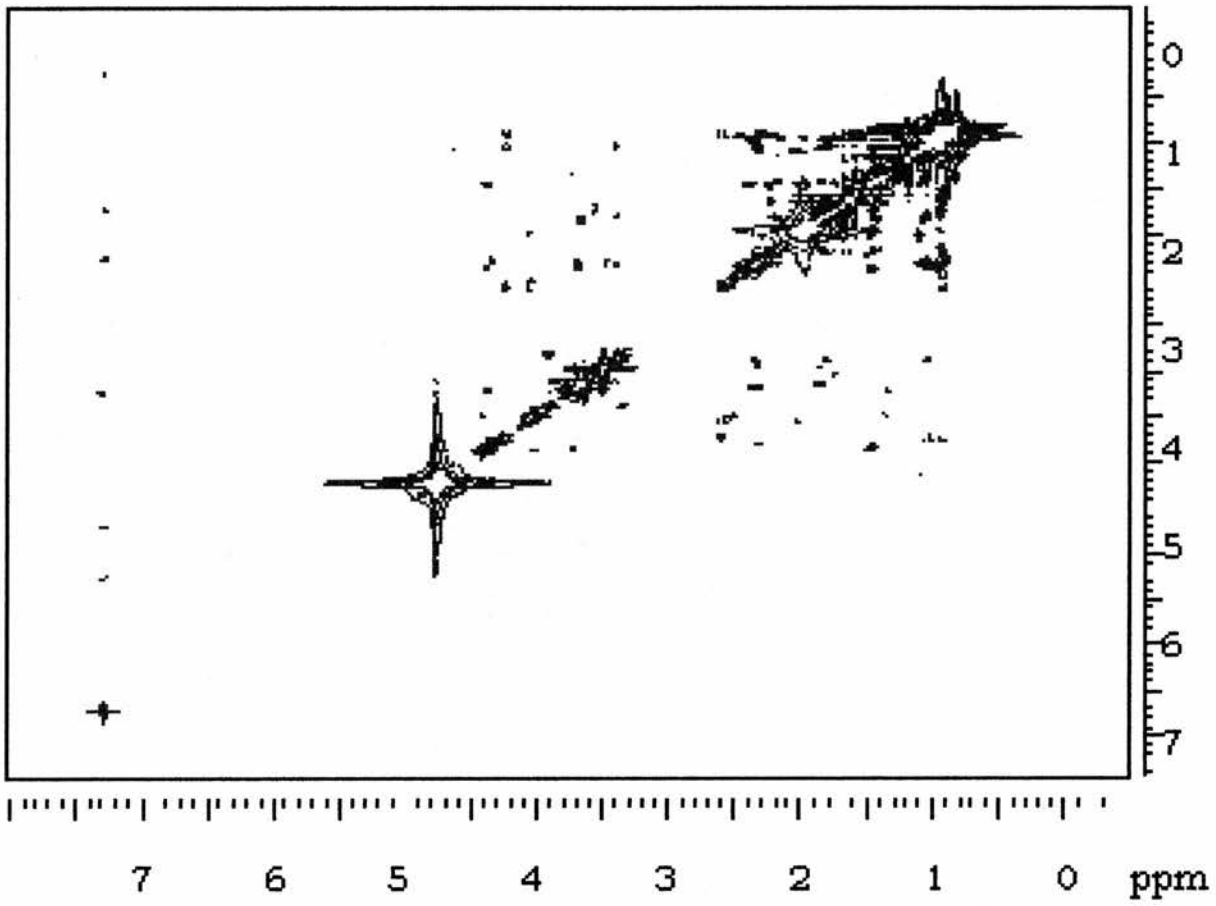

Figure 6.14 The 500 MHz COSY spectrum of cesium nigericin.

6.5.3 Parameters for 2D NMR Experiments

All spectra were analysed using Varian VNMR software on a Silicon Graphics INDY machine in the Department of Chemistry, University of St. Andrews. Some of the important parameters such as delay times and 90^0 pulse lengths are quoted in Table 6.7.

Experiment	Pulse Sequence	Relaxation Delay (sec^{-1})	Acquisition Time (sec)
1D ^1H	90^0_x	10.000	1.926
COSY	D_1-90^o_x-t_1-90^o_x-t_2	1.559	0.241
NOESY	D_1-90^o_x-t_1-90^o_x-τ_{mix}-90^o_x-t_2	1.200	0.241

Table 6.7 Values for some of the important parameters in COSY and NOESY experiments.

A typical 1D ^1H NMR spectrum was recorded at 298 K with a 90^0 pulse of 7.3 μs. The spectral width was around 4500 Hz, the number of data points used was 16 k, and the sequence was repeated sixteen times.

The 2D COSY experiments used a matrix of 4096 x 2048 data points, 1024 increments, and 16 repetitions. The 2D NOESY experiments used a mixing time of 400 ms and a matrix of 4096 x 2048 data points to record the spectrum. The number of increments

was 2048 and the sequence was repeated eight times. Both COSY and NOESY experiments were recorded at 298 K.

6.6 Strategy for Assignment

The assignments from Rodios and Anteunis[2] for the nigericin-H and nigericin-Na complexes provided the initial entry into the present assignments of 2D COSY and NOESY spectra of the five nigericin-alkali metal salts. Most of the peaks along the diagonal of the 2D COSY spectrum were identified using the network of ^3J couplings, which were revealed through positions of the cross peaks. The NOESY spectrum allowed identification of nearby proton pairs. Each cross peak was identified and the volume of the cross peak measured by integration using Varian VNMR and NMR View software.

6.7 Proton Chemical Shifts for Alkali Metal Nigericin Salts Derived from 2D COSY Experiments

The assignment of the 500 MHz COSY NMR spectrum of the nigericin salts was straightforward. Starting with Na-nigericin, the H30 A (3.92 ppm) and B (3.32 ppm) protons were identified as they only show cross-peaks to each other. The distinctive peak next to H30B was found to be H11e (3.38 ppm), and from here the protons of

rings A and B were identified as follows. H11e shows cross-peaks to H12A (1.79 ppm), H10B (1.07 ppm) and H10Ae (2.33 ppm). H 10Ae correlates to H9A (4.29 ppm), which in turn correlates to H8A (2.58 ppm) and this leads on to ring A, with H7e (4.05 ppm) connected with H6Aa (2.01 ppm), connected with H6Be (1.44 ppm).

H2 (2.38 ppm) and H3a (3.68 ppm) were relatively easy to identify, with H2 showing only one cross-peak to Me38 (0.95 ppm).

The identification of H24 (4.37 ppm) opens up a trail to H23B (1.41 ppm), which connects to H23A (2.38 ppm). H23A shows a small cross-peak very close to the diagonal which links with H22 (2.30 ppm). H22 then correlates to H21 (4.36 ppm).

H17 (3.64 ppm) shows a cross-peak to H18A (1.81 ppm), but the positions of the H19 A and B protons could not be ascertained. Rodios and Anteunis[9] did not find a value for these protons in $CDCl_3$, but did find values when the solvent was changed to benzene.

It was not possible to assign protons H5, H15 and H28 (no inter-proton connections). No details about the two hinges between rings C and D and rings D and E could be revealed, again due to the lack of inter-proton connectivity.

The assignment of the remaining peaks was based on the chemical shifts quoted by Rodios and Anteunis[9]. The assignment of the four

other salts proceeded in a more or less similar manner to that outlined above.

The 500 MHz ^{1}H NMR chemical shifts for the lithium, sodium, potassium, rubidium and cesium complexes of nigericin are given below in Table 6.8. Assignments for the free acid and the sodium salt at lower field strength (300 MHz) were available, and the shifts for sodium-nigericin are provided for reference.[9] A model of nigericin featuring the numbering scheme used by Rodios and Anteunis[9] and in the present study is also given.

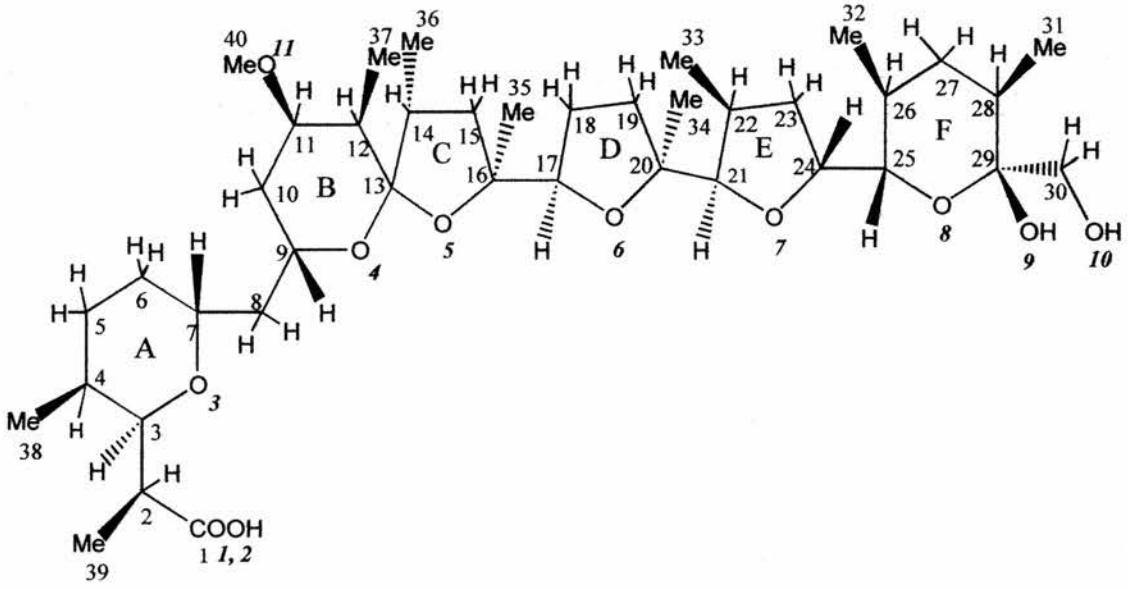

Figure 6.15 A model of nigericin showing the atomic numbering scheme used.[9] The oxygen atoms are numbered in bold italics. The carbon atoms are numbered in normal type. The hydrogen atoms are also shown in this figure.

Proton	Sodium Literature	Sodium	Lithium	Potassium	Rubidium	Caesium
OH10	5.539					
H24	4.358	4.37	4.40	4.40	4.40	4.37
H21	4.345	4.36	4.37			4.34
H9a	4.283	4.29	4.24	4.13	4.12	4.24
H7e	4.408	4.05	4.06	4.07	4.08	4.09
H30A	3.936	3.92	3.90	4.00	4.01	4.00
H25a	3.69	3.71	3.72	3.64	3.64	3.89
H3a	3.675	3.68	3.69	3.81	3.80	3.79
H17	3.64	3.64	3.63	3.52	3.63	3.65
H11e	3.367	3.38	3.37	3.37	3.37	3.37
H30B	3.306	3.32	3.33	3.31	3.32	3.31
H8A	2.588	2.58	2.58	2.64	2.65	2.65
H23a	2.37	2.38	2.39	2.38	2.37	2.37
H2	2.36	2.38	2.37	2.31	2.32	
H10Ae	2.33	2.33	2.32	2.33	2.28	2.28
H22	2.27	2.30	2.33	2.29		
H14d	2.18	2.19	2.21	2.16		2.17
H6Aa	1.99	2.01	1.99	2.03	2.03	1.99
H18A	1.80	1.81	1.79		1.82	
H12a	1.78		1.74	1.80	1.77	
H4e	1.74	1.75	1.75	1.75	1.75	
Me35f	1.591	1.54	1.58			
H28a	1.48	1.44(i)	1.52	1.47	1.50	
H6Be	1.46	1.44(ii)	1.455	1.46		1.46

Proton	Sodium Literature	Sodium	Lithium	Potassium	Rubidium	Caesium
H23B	1.40	1.41	1.44	1.43	1.43	1.42
H26	1.32	1.35	1.34	1.34	1.27	1.32
Me34f	1.144	1.15	1.16	1.14	1.13	
H10Ba	1.03	1.07	1.08	1.01	1.02	
Me37	1.019	1.02	1.02	1.02		
Me38	0.945	0.95	0.935	0.94	0.94	
Me36d	0.916	0.92	0.93	0.92		
H8B	0.89		0.92	0.88		
Me33	0.880	0.87	0.88	0.86		
Me31d	0.87		0.88	0.85	0.86	
Me32	0.815	0.82	0.83	0.84		

Table 6.8 500 MHz proton chemical shifts (ppm) for lithium, sodium, potassium, rubidium and cesium nigericin complexes.

The blanks in the table above indicate protons that could not be unambiguously assigned to a specific chemical shift. This was due to the overlap of some of the signals in the crowded region around 2.0-0.75 ppm, the area in which the methyl resonances fall. Nigericin has eight methyl groups that give rise to signals in this region.

The 2D COSY spectra for the Cs^+-nigericin complex was of lower quality than the spectra of the other four salts, and could not be

repeated due to time limitations. The reduction in quality may be due to the small quantities of nigericin (5 mg) used to make up the samples. As a result, there are far fewer assignments for the cesium salt.

6.8 Conformational Variations Identified by Changes in Chemical Shift

The areas in which conformational changes are expected are the 'hinge' regions connecting the tetrahydrofuran and tetrahydropyran rings together, as the cage formed by nigericin gets bigger in order to accommodate ions with increasingly larger diameter as for the alkali metals. In nigericin there are four such regions of interest.

Positions 7-8-9 connecting ring A and B: The literature value for H8A in Na-nigericin is close to the values found for Li- and Na-nigericin, but on going to K-nigericin there is a change in chemical shift of around 0.06 ppm. The literature Na-nigericin value for H8B lies between the found values for the lithium and potassium analogues, with Li-nigericin being higher than the quoted literature value and K-nigericin being lower. These are indications that there may be conformational change in this area on going from Li and Na to K, Rb, and Cs, as would be expected with the changes in ionic radius. H9a

chemical shift values for Li- and Na-nigericin are comparable to that for the sodium salt given in the literature, but the values for the K- and Rb-nigericin complexes are lower than those for the lithium and sodium complexes by around 0.1 ppm. There is also a large increase from K and Rb to Cs, bringing the chemical shift value back to the values of the Li complex.

H25a: The Li- and Na-nigericin chemical shift values for H25a are slightly higher than the values quoted by Rodios and Anteunis for Na-nigericin, but the K- and Rb-nigericin chemical shift values for H25a are slightly lower than the literature Na-nigericin value. The Cs-nigericin H25a value is around 0.2ppm greater than any of the other values. This may reflect a change in the conformation of ring F when cesium, the largest alkali metal, is complexed. *H24*: The chemical shift values for the Li, K and Rb nigericin complexes are higher than literature Na values by 0.04 ppm. The chemical shift of H24 in Cs-nigericin becomes only 0.01 ppm greater than the literature Na-nigericin value. This is more evidence of conformational changes around H24 – H25 when cesium is the guest cation.

H30A and H30B are attached to the hydroxyl end of the molecule involved in the head to tail buttoning on the molecule. For H30A the chemical shift values for Li- and Na-nigericin are lower than the

literature Na-nigericin value, then the K, Rb, and Cs-nigericin values are 0.1 ppm greater than the Li-nigericin value. The changes in the chemical shift values for H30B are less pronounced than for H30A, with the biggest change found for the Li complex, which is around 0.02 ppm greater than the other shifts.

H21 lies at the hinge between rings D and E, and the chemical shifts for this proton appear to show a steady decreasing trend from 4.37 for Li to 4.34 for Cs. A similar downward trend is observed for the chemical shifts for Me-34, which lies at the hinge area of ring D (connecting to ring E). In this case the Li-nigericin complex chemical shift is 1.16, and this decreases to 1.13 for Rb, in steady steps of 0.01 ppm.

Proton H3a lies at the carboxylic end of the molecule where it connects to ring A. The Li- and Na-nigericin chemical shift values for H3a are closely comparable with the Na literature value, but there is a sharp jump in chemical shift values of 0.1 ppm on going to K, Rb, and Cs. H3a lies at a terminal end of nigericin and although not directly involved in the head to tail buttoning shut of the molecule, or in binding to the cation, its position may change as the conformation of this region changes as cations of increasing ionic radius are accommodated.

In the current study, seventeen of the thirty-four chemical shift assignments for sodium nigericin are within 0.01 ppm of the values quoted for the same salt by Rodios and Anteunis[9] in 1971. The remaining assignments vary mostly by less than 0.02 ppm, with the greatest variance being the resonance for Me-35f, quoted as 1.59 ppm and found to be 1.54 ppm.

No details could be revealed for two important torsions, C_{16}-C_{17} and C_{20}-C_{21}, as there are no inter-proton ^3J connections between the carbon centres. Rodios and Anteunis[9] reported the local conformations of the ring systems in sodium nigericin in $CDCl_3$. Ring D is close to a half chair form, and ring F is in the chair form. The conformation of ring C could not be examined due to the inherent lack of proton connectivity.

Proton connections are a problem in the areas C_{16}-C_{17} and C_{20}-C_{21}. There are no directly bound hydrogens on C_{16} or on C_{20}, and consequently no COSY connectivities.

All chemical shift positions quoted in this section were derived from 500 MHz COSY NMR spectra of the alkali metal salts of nigericin. There are several sophisticated computer programs that can be used to extract further information from the spectra, such as the coupling

constants between scalar-coupled protons. This, however, would be beyond the scope of the current study.

6.9 Future Work

More information could be derived from the 2D NOESY NMR spectra acquired for the five nigericin-alkali metal salts. The integrated cross-peak volumes obtained for the sodium-nigericin complex were not used in molecular modelling studies due to time limitations. The data derived from the NOESY experiments will be used in molecular dynamics / modelling simulations, in the University of Szeged, Hungary, by a Hungarian colleague and a member of the Riddell research group who works in St Andrews. None of the data obtained from NOESY experiments is included in this thesis.

The missing assignments from Table 6.8 above could be revealed using DEPT and COSY-45 techniques, and this work will be carried out in St. Andrews. A higher concentration of nigericin could be used in making up the cesium–nigericin sample, and the COSY and NOESY experiments could be re-done to obtain further proton assignments. The poor resolution and low signal to noise ratio in the cesium-nigericin COSY spectrum is due to the small quantity of nigericin (<5 mg) available at the time.

Two things are predicted to become more apparent after a closer inspection of the NOESY spectra for the five salts. There are signs that one or more pairs of protons may be exchanging in the NOESY spectrum of the lithium salt. An immediate indication of this comes from the 2D spectra, which show a much greater number of cross-peaks when exchange processes occur. From previous studies it would be reasonable to expect some significant conformational changes as the cavity formed by nigericin expands to accommodate increasing larger cations. Molecular dynamics and molecular modelling simulations could be used to produce structures for each of the nigericin complexes. Conformational changes may be more easily recognised and rationalised when detailed 3D models of the five nigericin salts are available.

Although research in ionophore-related fields continues unabated, much work has gone into the carboxylic ionophore group, featuring monensin, nigericin, grisorixin, and lasalocid. Transport studies using these molecules have been carried out in several different ways, and it appears that little useful information remains to be elucidated from structural studies. The main work done in this area in the future will most likely involve organic synthesis, as some of the naturally-occurring structural features that give rise to the antibiotic properties displayed by some of these ionophores are exploited and

recreated in synthetic molecules designed for increasingly specific roles.

References

1. Shoji J., Kozuki S., Matsutani S., Kubota T., Nishimura H., Mayama M., Motokawa K., Tanaka Y., Shimaoka N., Oisuka H., *Journal of Antibiotics*, **21**, 402-409, (1968)

2. (a) See, for example, articles in: Metal Ions in Biological Systems, Sigel, H., Ed., Marcel Decker, New York, Vol. 19 (1985); (b) Painter G.E., Pressman, B.C., *Topics In Current Chemistry*, **101**, 83-110, (1982); (c) Westley, J. W., Polyether Antibiotics, Volume 2, Marcel Dekker (1983);

3. Kubota, T., Matsutani S., Shiro M., Koyama H., *Journal of the Chemical Society, Chemical Communications,* 1541-1543, (1968)

4. Shiro M., Koyama H., *Journal of the Chemical Society (B)*, 243-253, (1970)

5. Alleaume M., Hickel D., *Journal of the Chemical Society, Chemical Communications*, 1422-1423, (1970)

6. Barrans, P.Y., Alleaume M., David L., *Acta Crystallographica,* **B36**, 936-938, (1980)

7. Geddes A.J., Sheldrick B., Stevenson W.T.J., *Biochemical and Biophysical Research Communications*, **60**, *4*, 1245-1251, (1974)

8. Kasuga, N.C., Kuboniwa, H., Nakahama, S., Yamaguchi, K., *Journal of the American Chemical Society*, **117**, 7238-7224, (1997)

9. Rodios N.A., Anteunis M.J.O., *Bull.Soc.Chim.Belg.*, **86**, 12, 917-929, (1977)

10. Rodios N.A., Anteunis M.J.O., *Bull.Soc.Chim.Belg.*, **89**, 7, 537-550, (1980)

11. Beloeil J.C., Biou V., Dauphin G., Garnier J., Morellet N., Vaufrey F., *Magnetic Resonance in Chemistry*, **32**, 83-86, (1994)

12. Alva R., Lugor. A., Arzt E., Cerbon J., Rivera B. E., Toro M., Estradao. S., *Journal of Bioenergetics and Biomembranes*, **24**, *1*, 125-129, (1992)

13. Toro M., Artz E., Cerbon J., Algeria G., Alva R., Meas Y., Estrada-O. S., *Journal of Membrane Biology*, **95**, 1-8, (1987)

14. S. Tompsett, Ph.D. Thesis, University of St. Andrews, UK, (1991)

15. Riddell, F.G., Arumugam S., Patel A., *Inorganic Chemistry*, **29**, 2397-2398, (1990)

16. Riddell, F.G., Arumugam S., Brophy, P. J., Cox, B. G., Payne, M. C. H., Southon, T. E., *Journal of the American Chemical Society*, **110**, 734-738, (1988)

17. Gahcon, P., Kergomard, A., Veschambre H., *Journal of the Chemical Society, Chemical Communications*, 1421-1422, (1970)

18. Alleaume M., Hickel D., *Journal of the Chemical Society, Chemical Communications*, 175-176, (1972)

19. Pinkerton M., Steinrauf L. K., *Journal of Molecular Biology*, **49**, 533-546, (1970)

20. Lutz W. K., Winkler F. K., Dunitz J. D., *Helevetica et Chimica Acta*, **54**, 1103-1108, (1971)

21. Daux W. L., Smith G. D., Strong P. A., *Journal of the American Chemical Society*, **102**, *22*, 6725-6729 (1980)

Appendices

Appendix I

Plots of time x 10^{-2} (s) versus ln(signal intensity-infinity) for Ionophore 1 mediated $^{7}Li^{+}_{(in)}/^{23}Na^{+}_{(out)}$ exchange in 50, 100, 150 and 200 mM LiCl vesicles observed with ^{23}Na NMR

<u>50 mM</u>

50 mM 5 µl [I]/[PC] = 0.00109

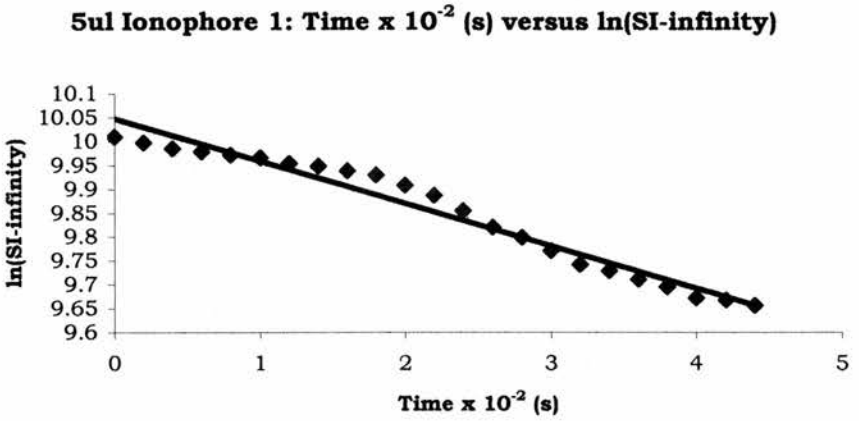

50 mM 10 µl [I]/[PC] = 0.00219

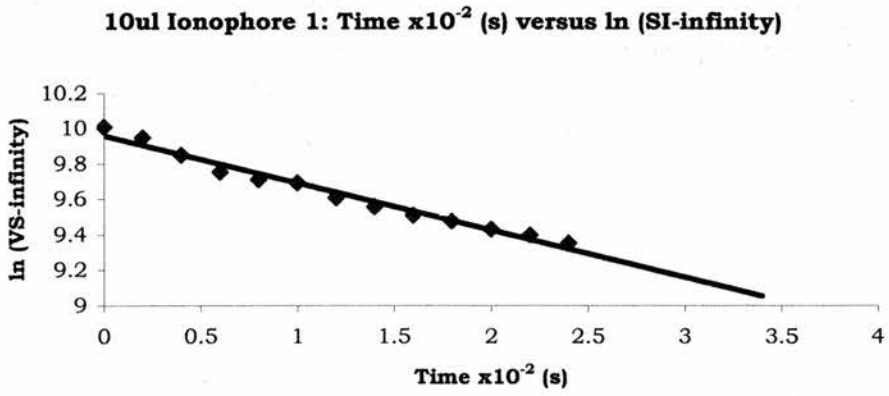

50 mM 20 µl [I]/[PC] = 0.00438

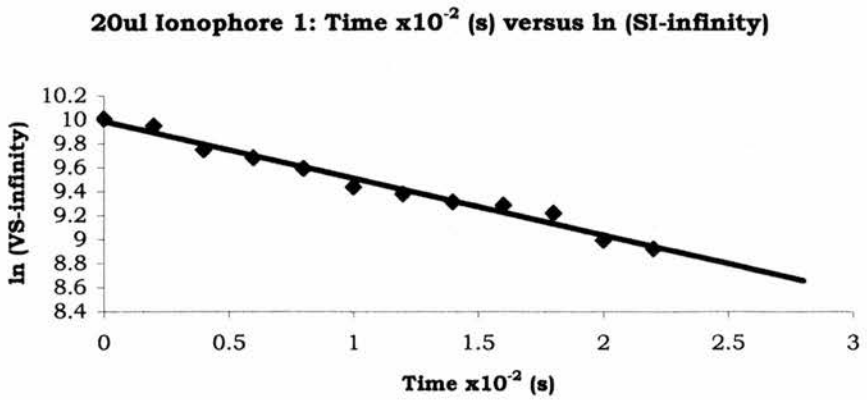

100 mM

100 mM 5 µl [I]/[PC] = 0.00113

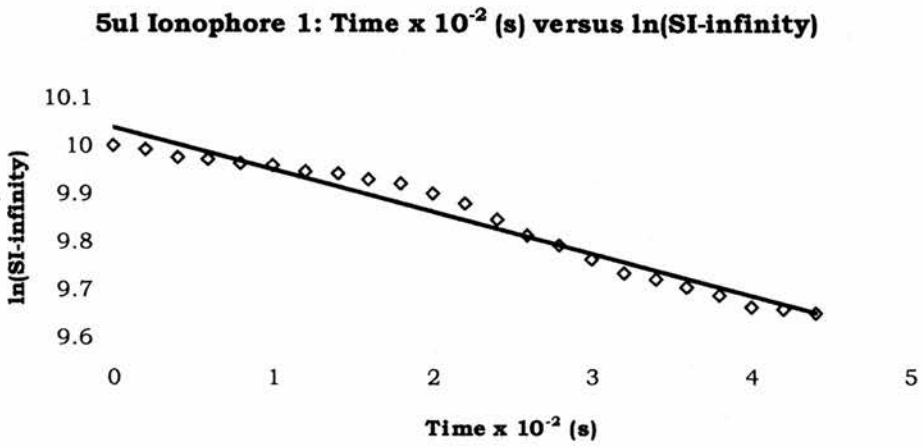

100 mM 10 µl [I]/[PC] = 0.00226

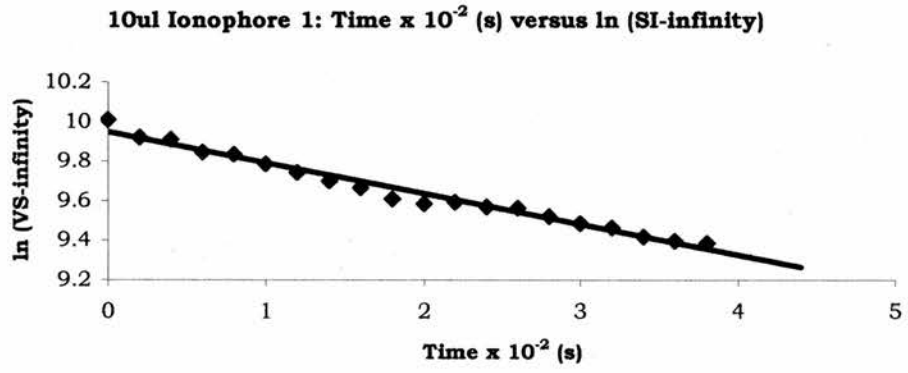

100 mM 20 µl [I]/[PC] =0.00452

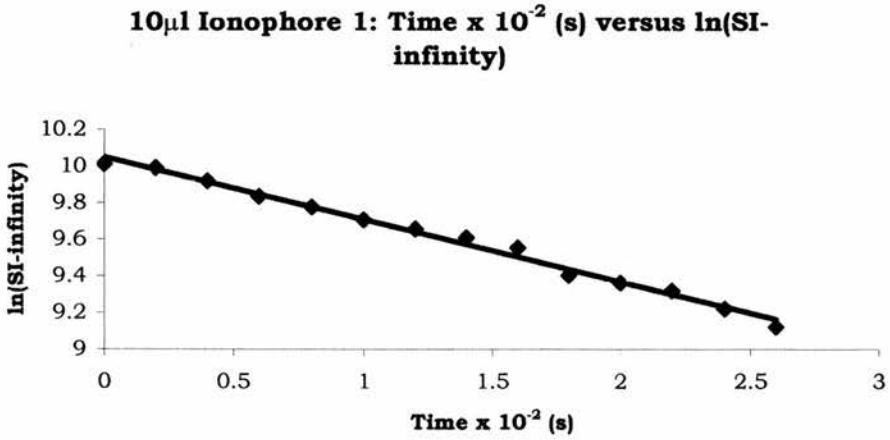

<u>150 mM</u>

150 mM 5 µl [I]/[PC] =0.00112

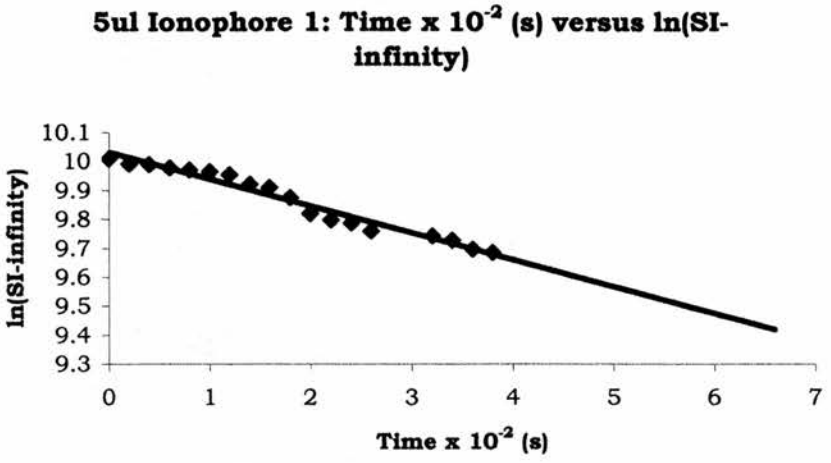

150 mM 10 µl [I]/[PC] =0.00223

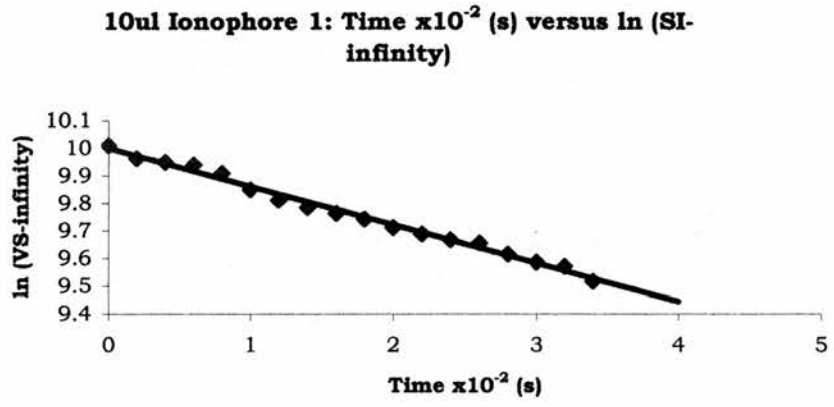

150 mM 20 µl [I]/[PC] =0.00446

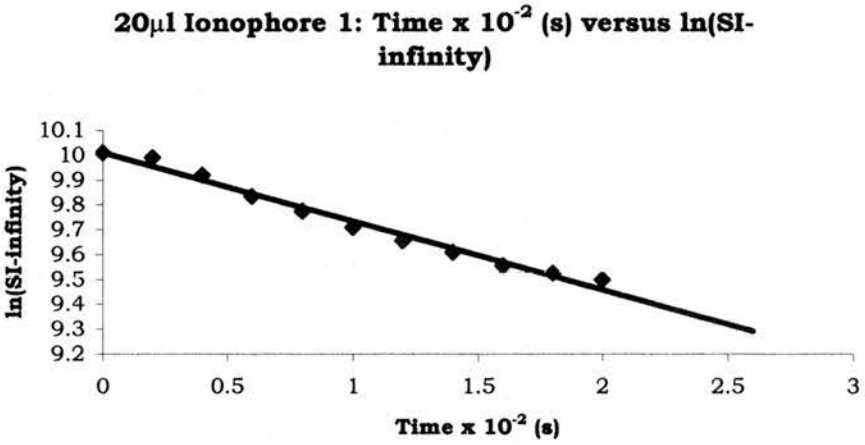

<u>200 mM</u>

200 mM 5 µl [I]/[PC] = 0.00116

5ul Ionophore 1: Time x 10^{-2} (s) versus ln(SI-infinity)

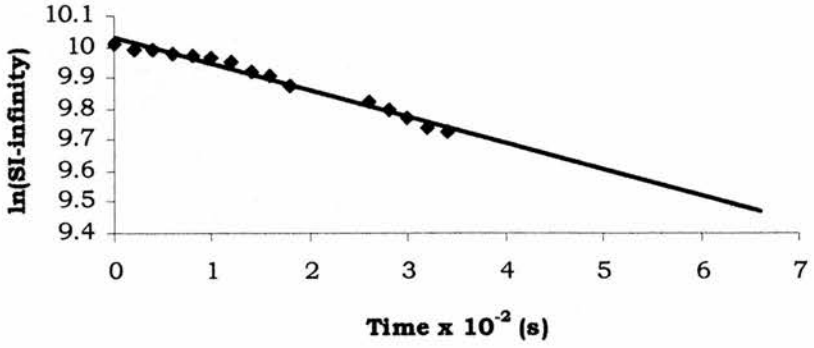

200 mM 10 µl [I]/[PC] = 0.00232

10ul Ionophore 1: Time x10^{-2} (s) versus ln (SI-infinity)

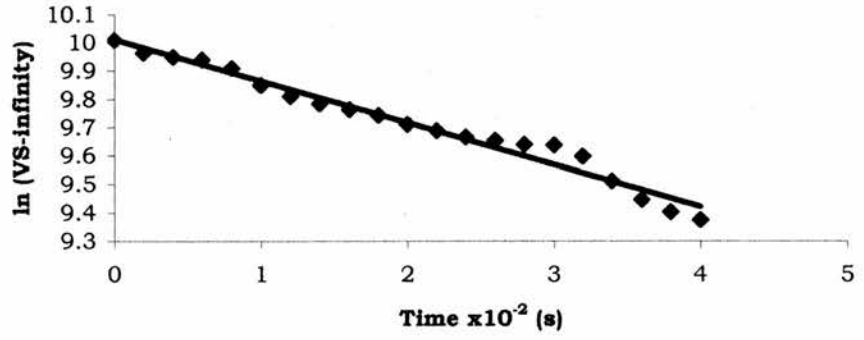

200 mM 20 µl [I]/[PC] = 0.00464

20µl Ionophore 1: Time x 10^{-2} (s) versus ln(SI-infinity)

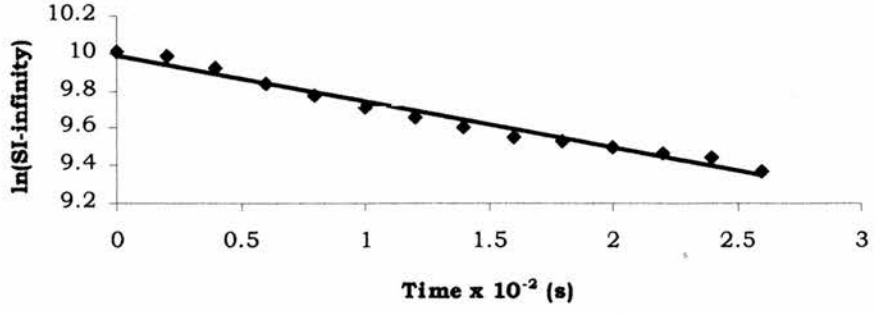

Appendix II

Plots of Time x 10^{-2} (s) versus ln(Signal Intensity-Infinity) for Ionophore 1 mediated $^{7}Li^{+}_{(in)}/^{23}Na^{+}_{(out)}$ exchange in 50, 100, 150 and 200 mM LiCl vesicles observed with ^{7}Li NMR

<u>50 mM</u>

50 mM 5 µl [I]/[PC] = 0.00117

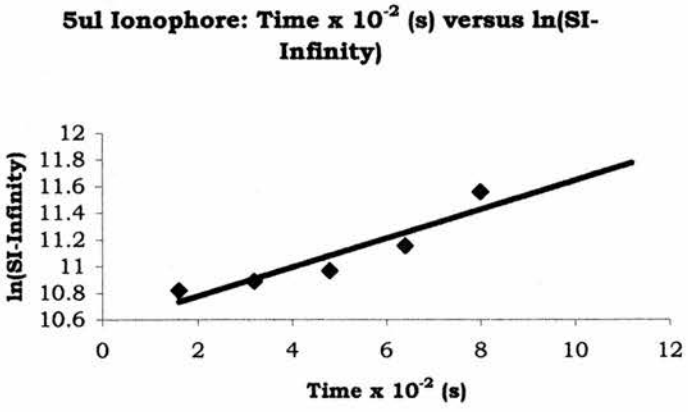

50 mM 10 µl [I]/[PC] = 0.00234

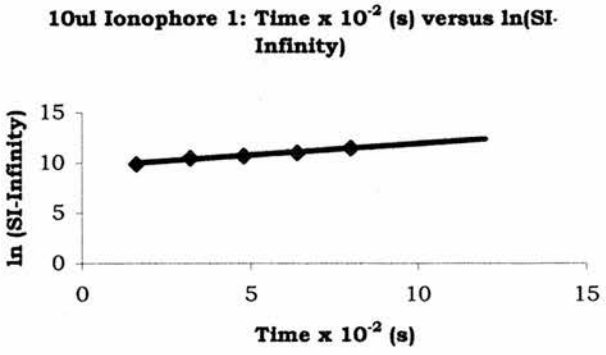

50 mM 20 µl [I]/[PC] = 0.00468

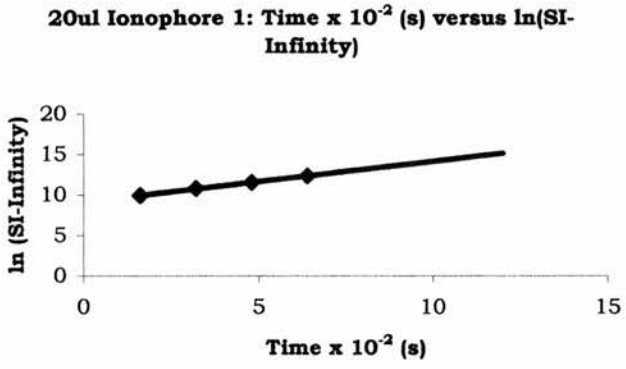

100 mM

100 mM 5 µl [I]/[PC] = 0.00112

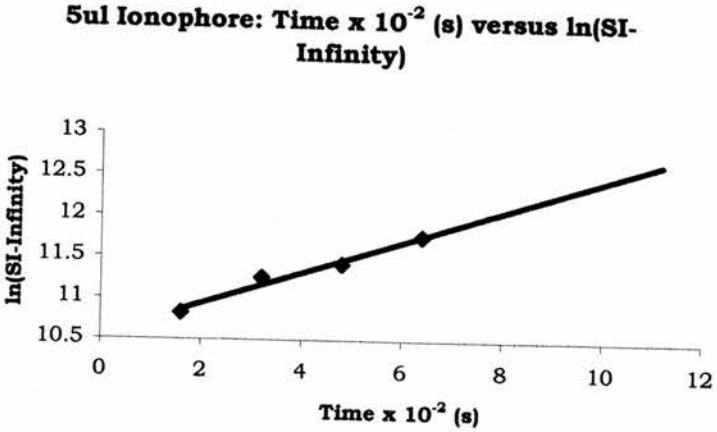

100 mM 10 µl [I]/[PC] = 0.00223

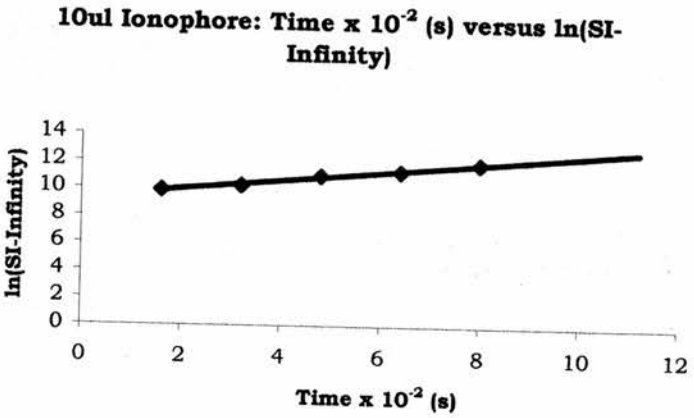

100 mM 20 µl [I]/[PC] = 0.00446

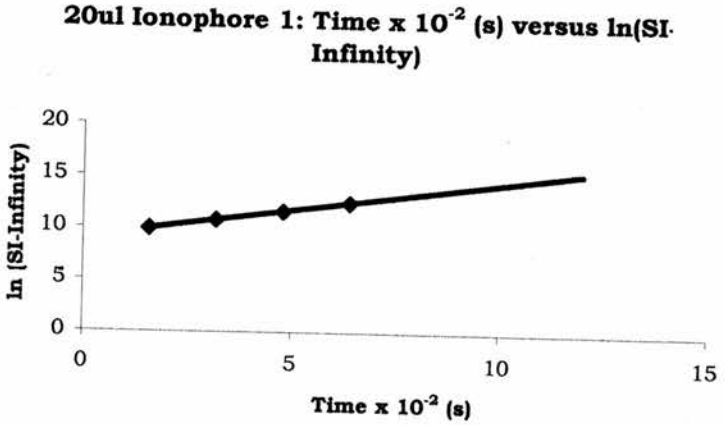

150 mM

150 mM 5 µl [I]/[PC] = 0.00114

5ul Ionophore: Time x 10^{-2} (s) versus ln(SI-Infinity)

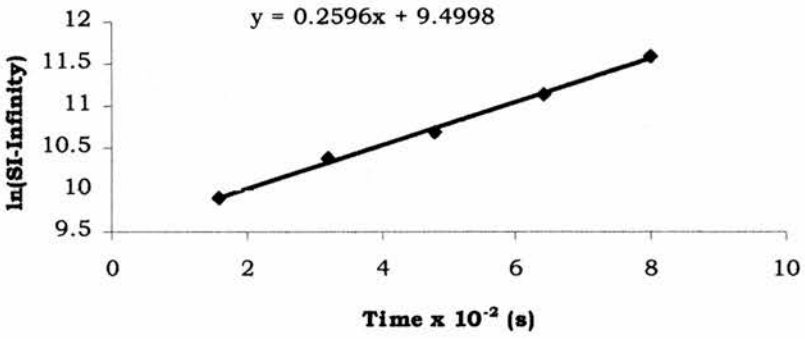

150 mM 10 µl [I]/[PC] = 0.00228

10ul Ionophore: Time x 10^{-2} (s) versus ln(SI-Infinity)

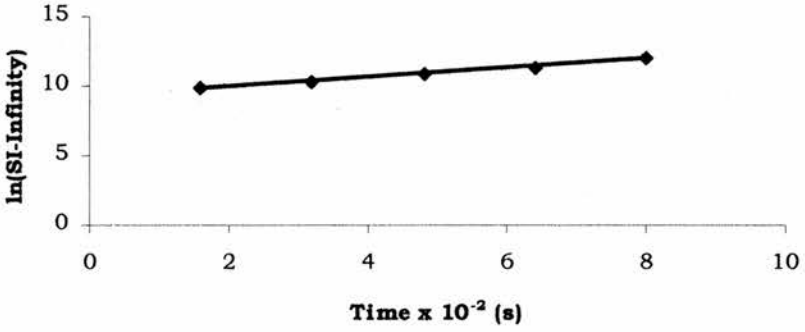

150 mM 20 µl [I]/[PC] = 0.00457

20ul Ionophore: Time x 10^{-2} (s) versus ln(SI-Infinity)

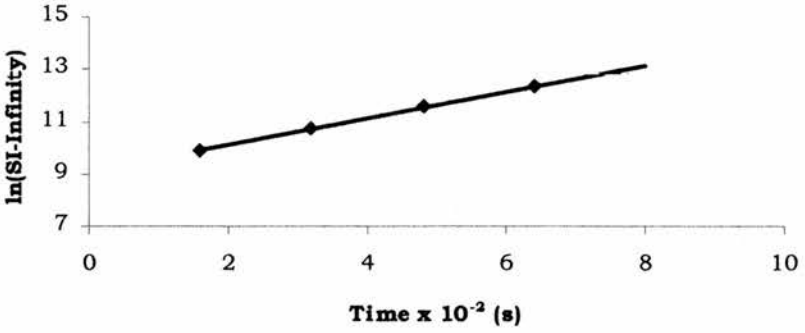

200 mM

200 mM 5 µl [I]/[PC] = 0.00116

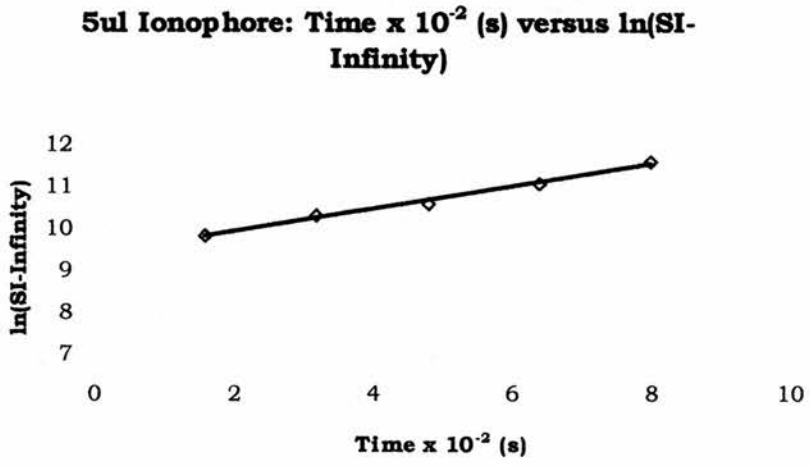

200 mM 10 µl [I]/[PC] = 0.00231

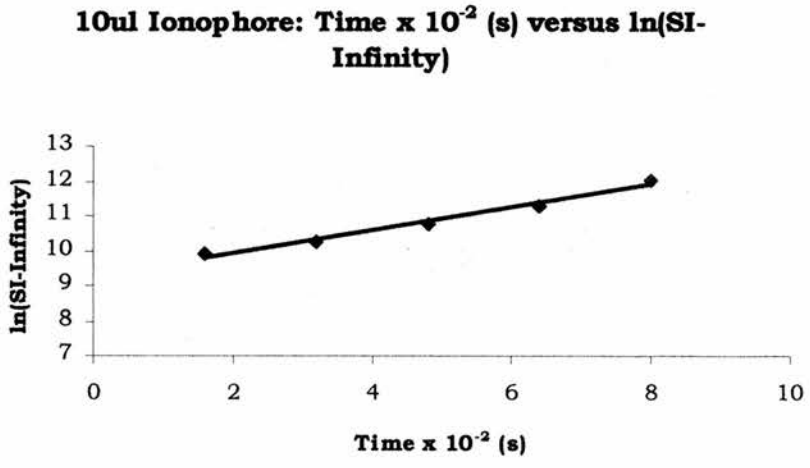

200 mM 20 µl [I]/[PC] = 0.00462

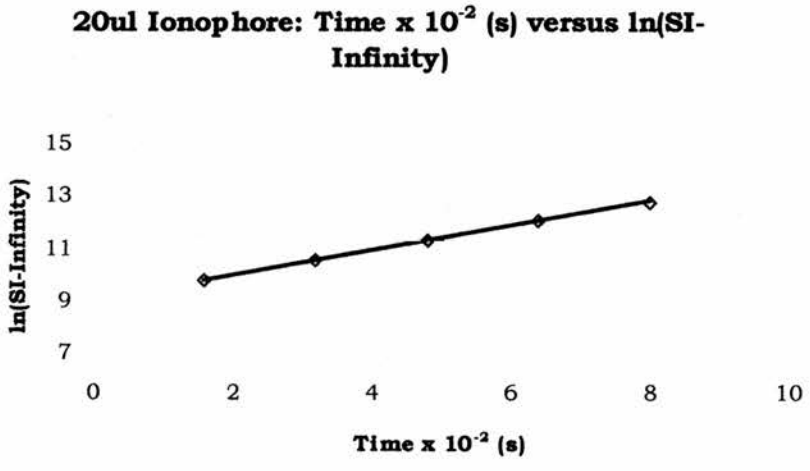

Appendix III

Plots of Time x 10^{-2} (s) versus ln(Signal Intensity-Infinity) for Ionophore 1 mediated $^{7}Li^{+}_{(in)}/^{6}Li^{+}_{(out)}$ isotope exchange in 50, 100, and150 mM LiCl vesicles observed with ^{7}Li NMR

<u>50 mM</u>

50 mM 5 µl [I]/[PC] = 0.00109

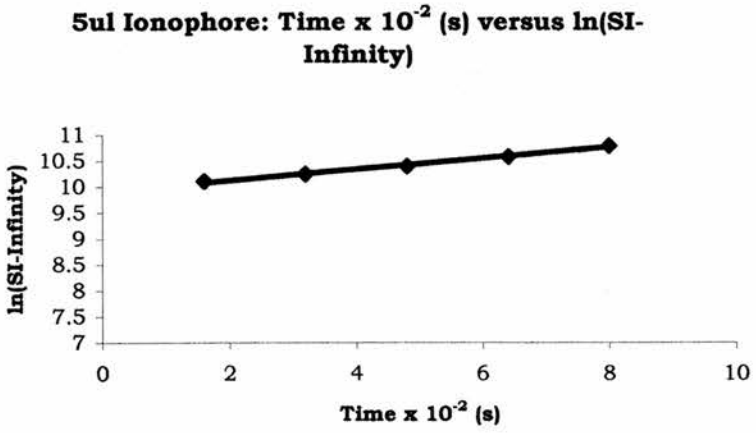

50 mM 10 µl [I]/[PC] = 0.00219

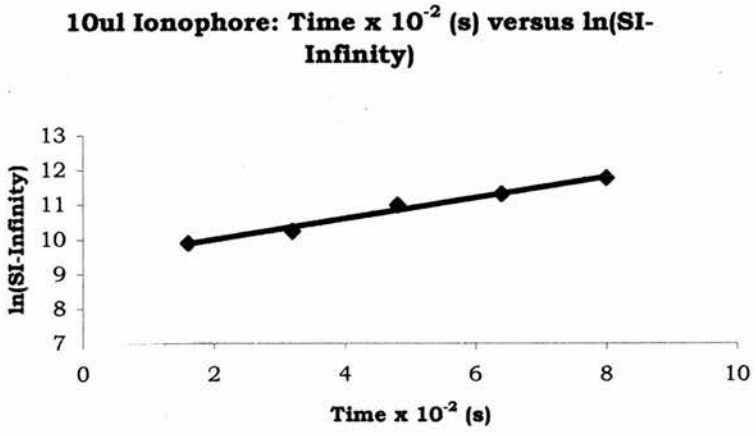

50 mM 20 µl [I]/[PC] = 0.00438

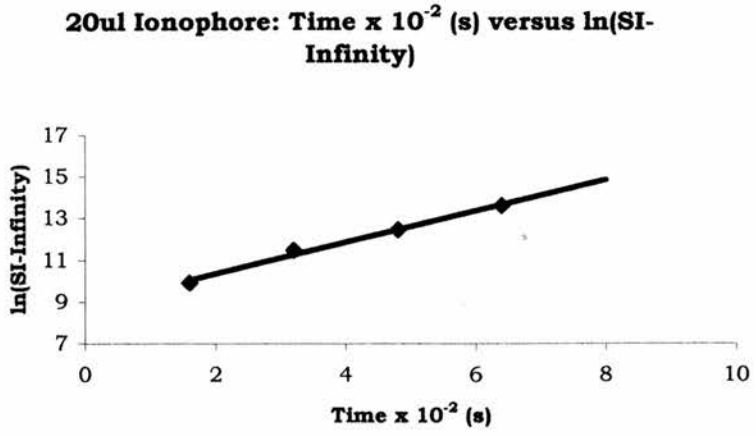

<u>100 mM</u>

100 mM 5 µl [I]/[PC] = 0.00113

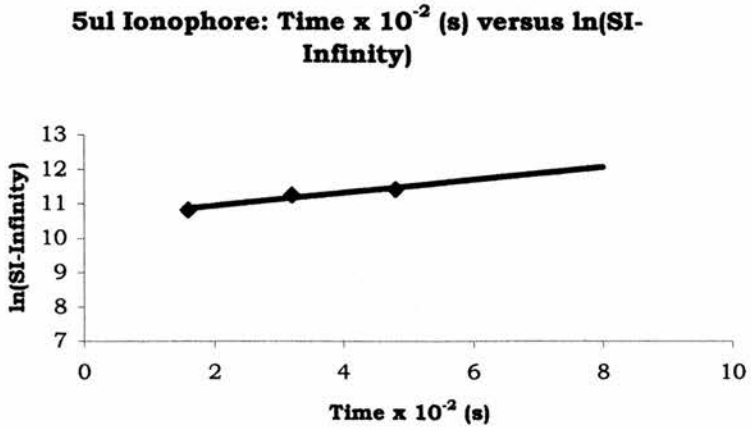

100 mM 10 µl [I]/[PC] = 0.00226

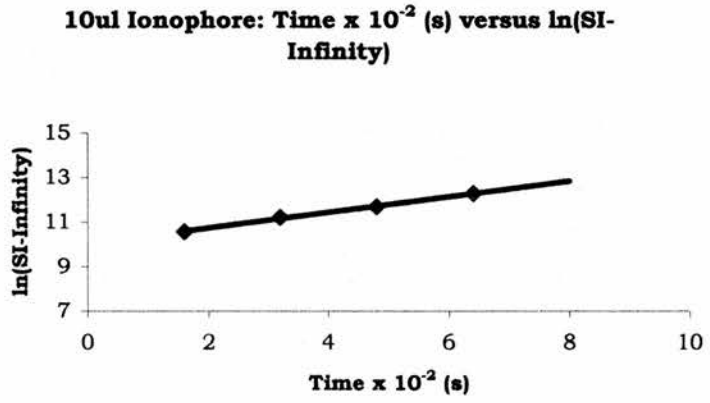

100 mM 20 µl [I]/[PC] = 0.00452

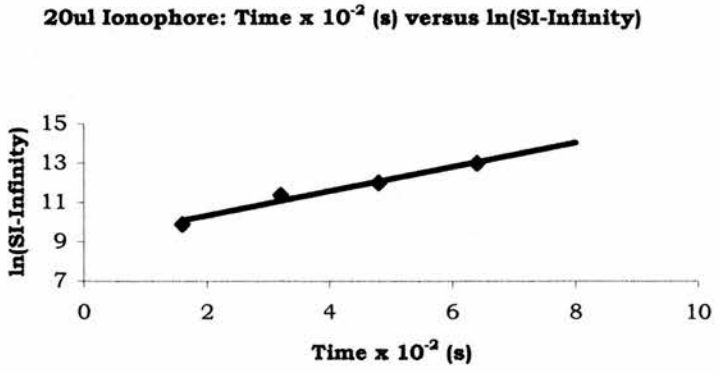

<u>150 mM</u>

150 mM 5 µl [I]/[PC] = 0.00112

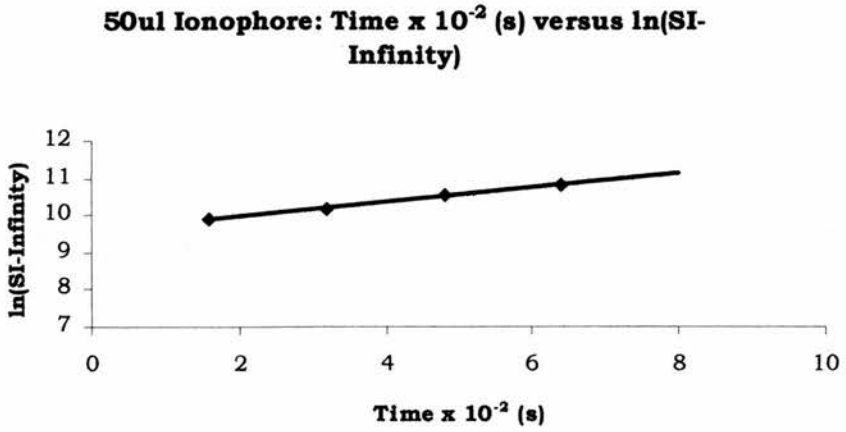

150 mM 10 µl [I]/[PC] = 0.00224

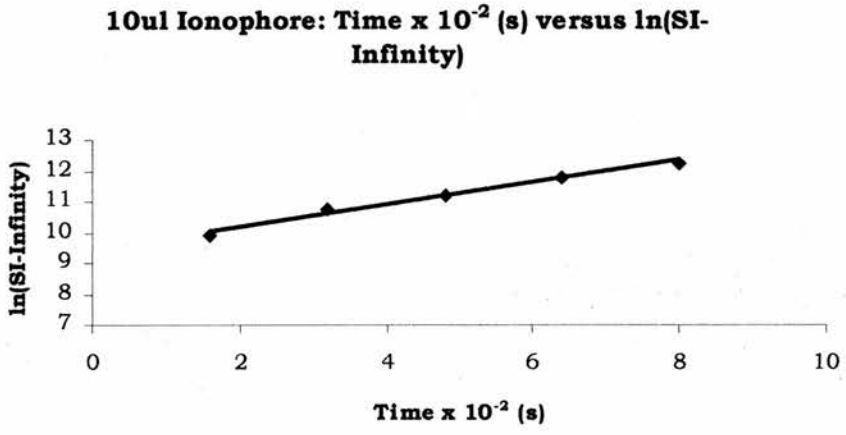

150 mM 20 µl [I]/[PC] = 0.00448

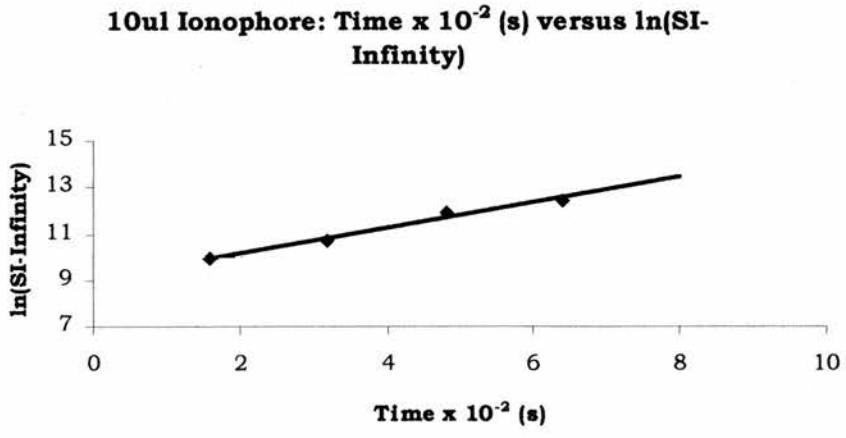

Appendix IV

(a) Transport Results for Ionophore 2 Mediated Exchange of 150 mM $Li_{(in)}/Na_{(out)}$ Observed with ^7Li:

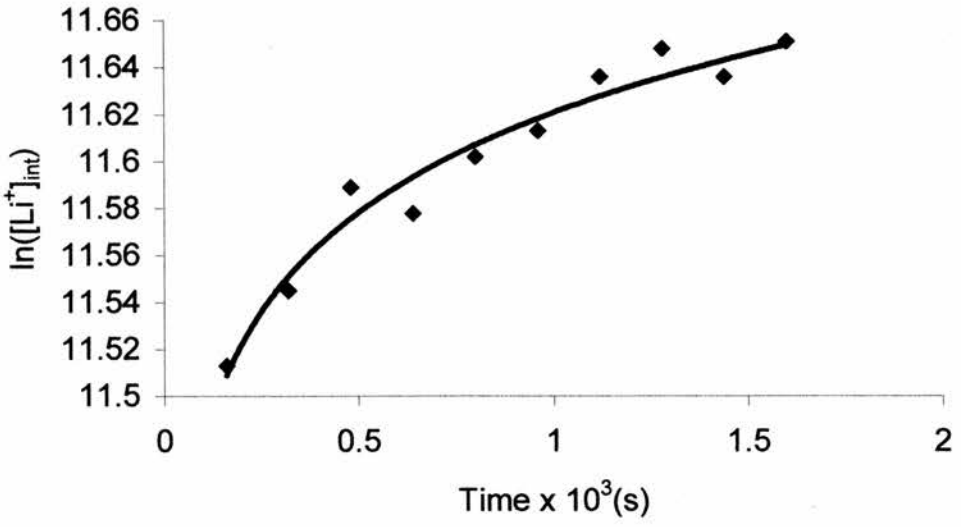

A

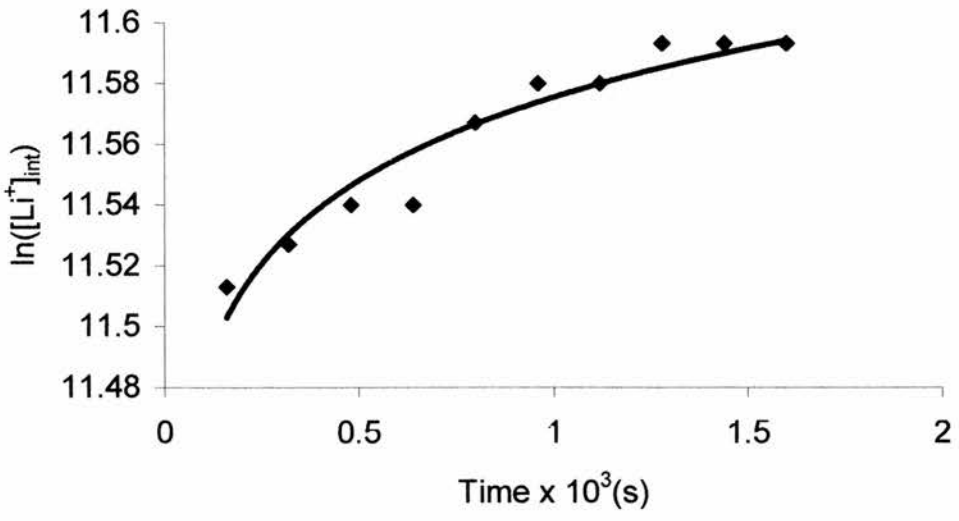

B

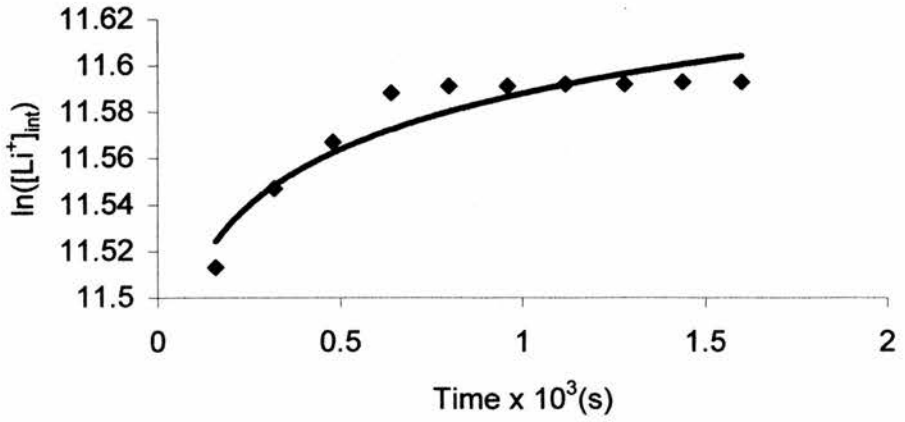

C

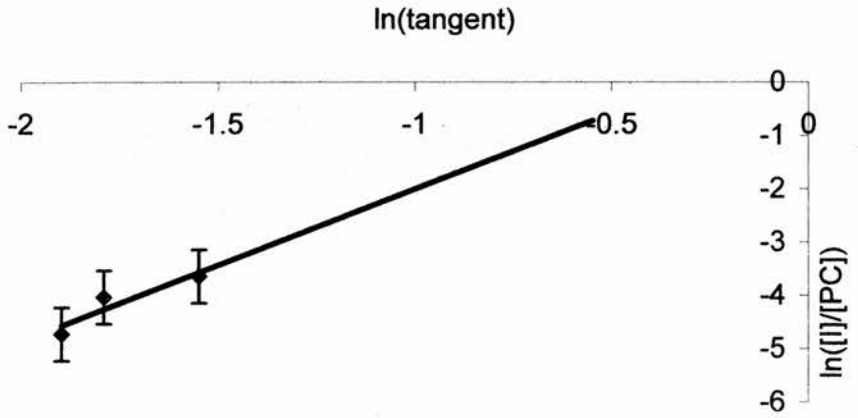

D

Figure 1 (A-C) Plots of $\ln[Li^+]_{int}$ versus time x 10^{-3} (s) for Ionophore 2 mediated exchange of 150 mM $lithium_{(in)}$ for $sodium_{(out)}$, from which the tangents are obtained; (A) 20 µl Ionophore 2; (B) 50 µl Ionophore 2; (C) 75 µl Ionophore 2; (D) Plot ln(tangent) versus ln([I]/[PC]) for Ionophore 2 mediated exchange of 150 mM $lithium_{(in)}$ for $sodium_{(out)}$. The slope of the graph is equal to the order of the kinetic, and is 2.9 ± 0.5.

(b) Transport Results for Ionophore 2 Mediated Exchange of 200 mM $Li_{(in)}/Na_{(out)}$ Observed with ^7Li:

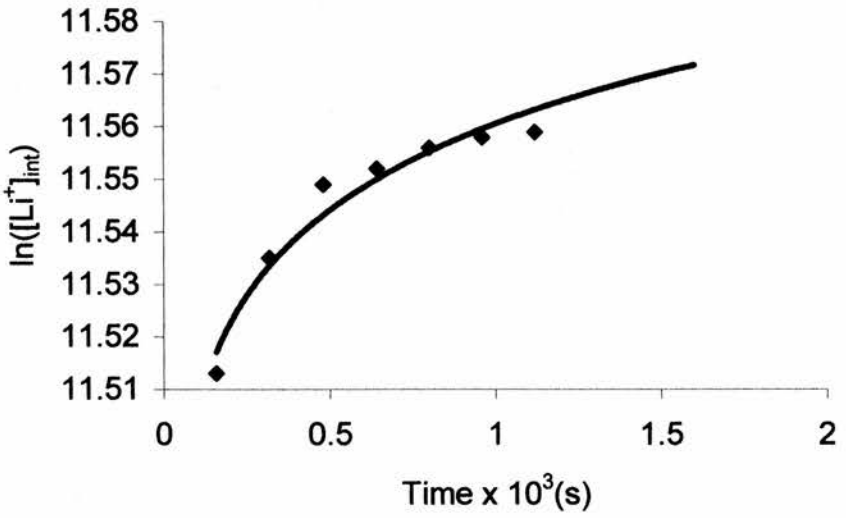

A

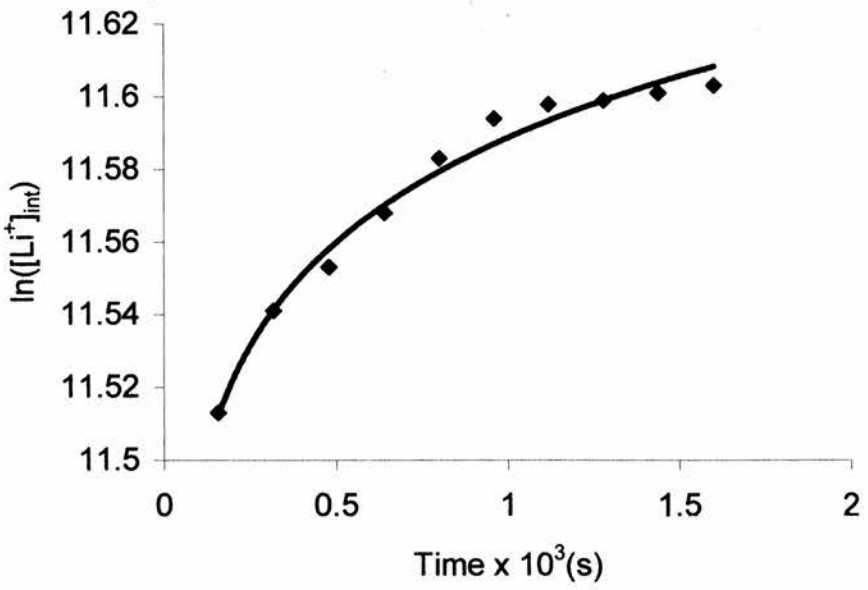

B

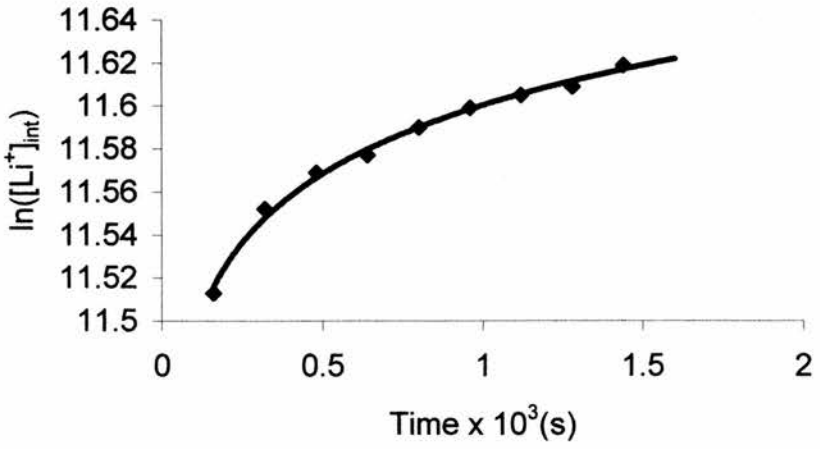

C

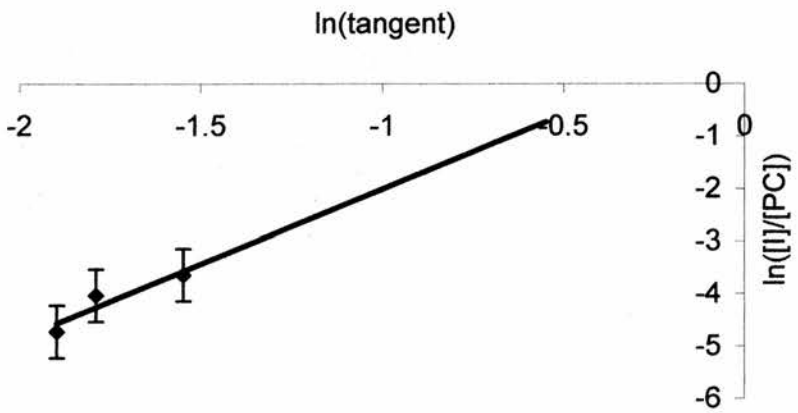

D

Figure 1 (A-C) Plots of $\ln[Li^+]_{int}$ versus time x 10^{-3} (s) for Ionophore 2 mediated exchange of 200 mM $lithium_{(in)}$ for $sodium_{(out)}$, from which the tangents are obtained; (A) 20 µl Ionophore 2; (B) 40 µl Ionophore 2; (C) 80 µl Ionophore 2; (D) Plot ln(tangent) versus ln([I]/[PC]) for Ionophore 2 mediated exchange of 200 mM $lithium_{(in)}$ for $sodium_{(out)}$. The slope of the graph is equal to the order of the kinetic, and is 2.9 ± 0.5.

Appendix V

Plots of Time x 10^{-2} (s) versus $\ln(k_{med})$ for Broderick 1 mediated $^{35}Cl^-_{(in)}/^{79}Br^-_{(out)}$ exchange in 200, 250, 300 and 350 mM NaCl vesicles observed with ^{35}Cl NMR

200 mM 5 µl [I]/[PC] = 0.00100

5µl Broderick: Time x 10^{-2} (s) versus $\ln(k_{med})$

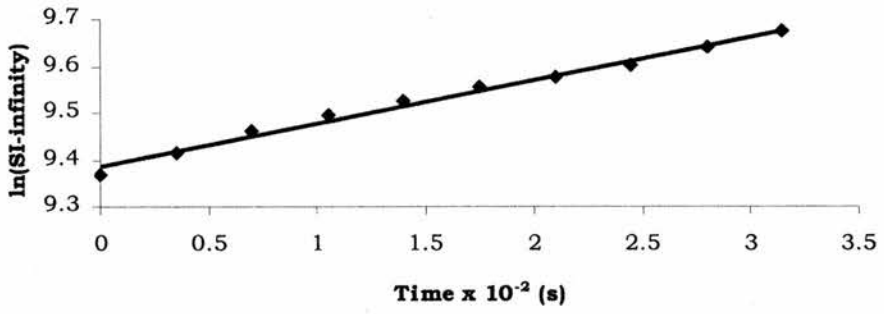

200 mM 10 µl [I]/[PC] = 0.00202

10µl Broderick: Time x 10^{-2} (s) versus ln(SI-infinity)

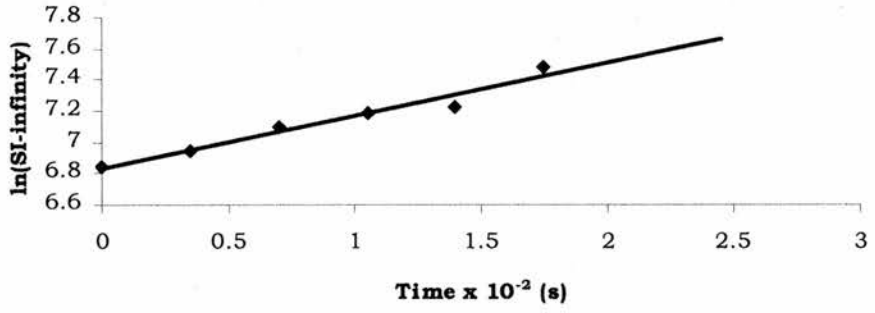

200 mM 20 µl [I]/[PC] = 0.00406

20µl Broderick: Time x 10^{-2} (s) versus ln(SI-infinity)

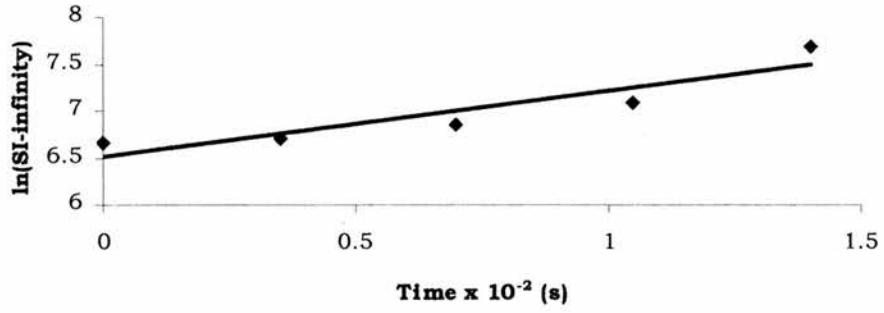

250 mM

250 mM 5 µl[I]/[PC] = 0.00085

5µl Broderick 1 : Time x 10^{-2} (s) versus ln(k_{med})

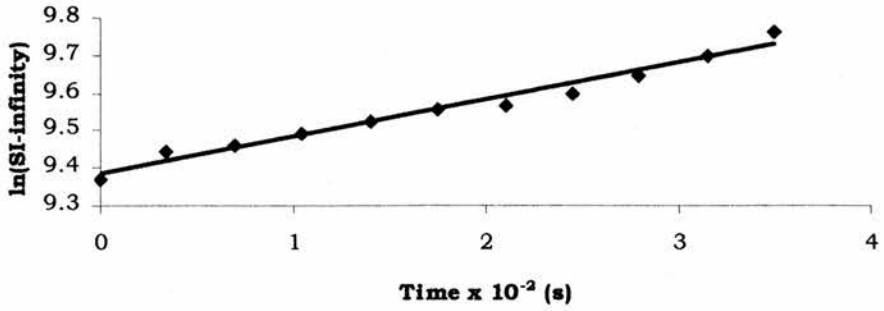

250 mM 10 µl [I]/[PC] = 0.00171

10µl Broderick 1: Time x 10^{-2} (s) versus ln(k_{med})

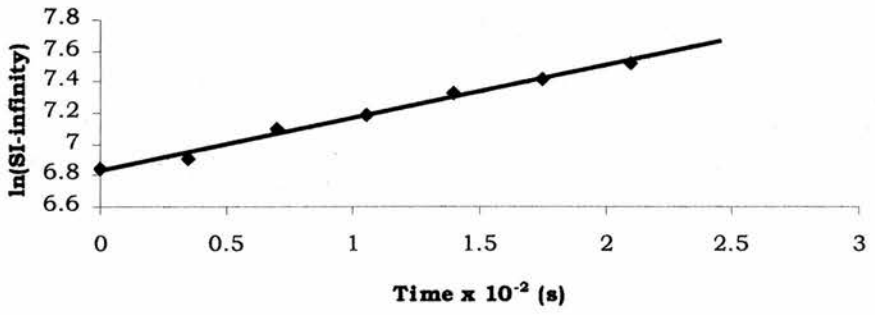

250 mM 20 µl [I]/[PC] = 0.00343

20µl Broderick 1: Time x 10^{-2} (s) versus ln(k_{med})

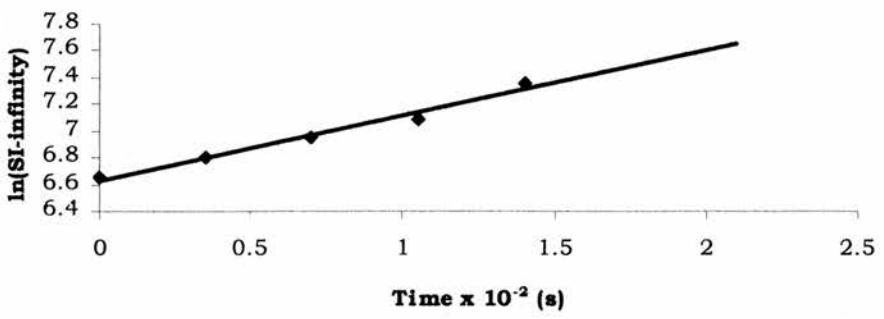

<u>300 mM</u>

300 mM 5 µl [I]/[PC] = 0.00076

5µl Broderick 1: Time x 10^{-2} (s) versus ln(k_{med})

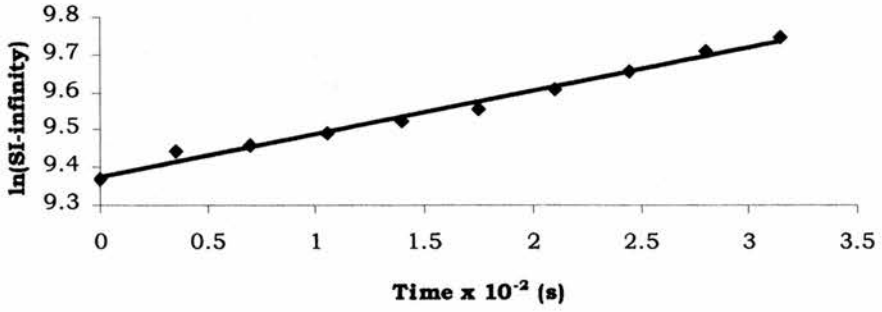

300 mM 10 µl [I]/[PC] = 0.00154

10µl Broderick 1: Time x 10^{-2} (s) versus ln(k_{med})

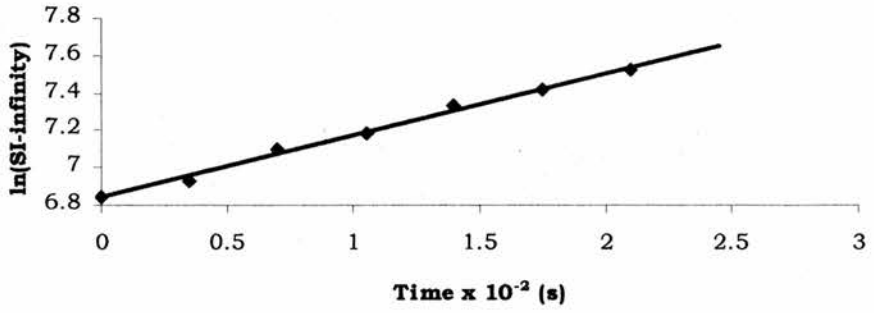

300 mM 20 µl [I]/[PC] = 0.0031

20µl Broderick 1: Time x 10^{-2} (s) versus ln(k_{med})

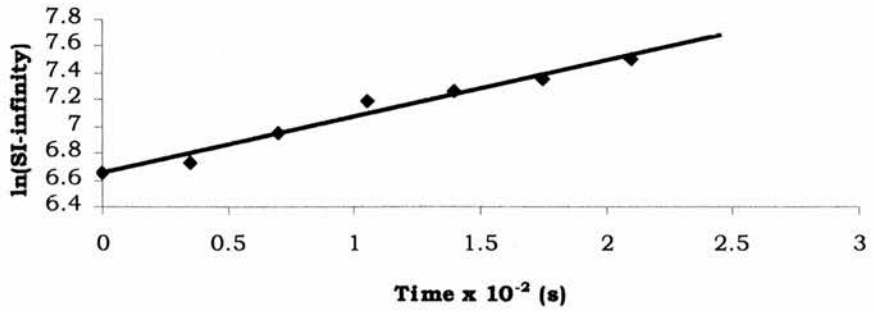

<u>350 mM</u>

350 mM 5 µl [I]/[PC] = 0.00099

5µl Broderick 1: Time x 10^{-2} (s) versus ln(k_{med})

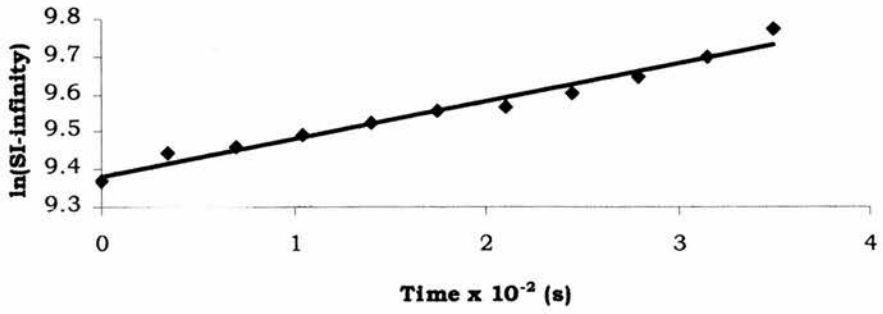

350 mM 10 µl

10µl Broderick 1: Time x 10^{-2} (s) versus ln(k_{med})

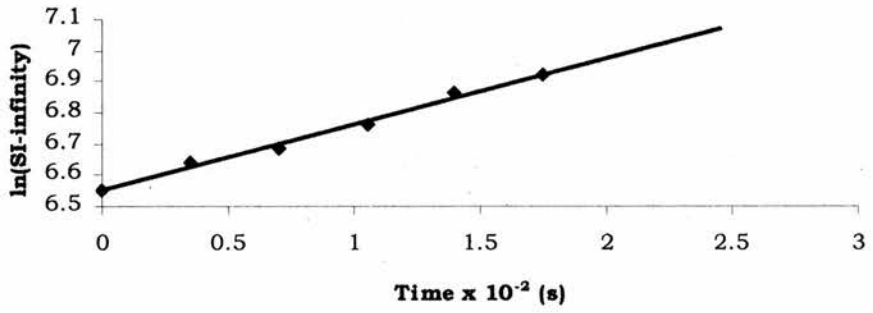

350 mM 20 µl

20µl Broderick 1: Time x 10^{-2} (s) versus ln(k_{med})